

Rechargeable Zinc Batteries and Capacitors *via* Electrodes and Electrolyte Engineering

by

Zhixiao Xu

A thesis submitted in partial fulfillment of the requirements for the degree of

Doctor of Philosophy

in

Chemical Engineering

Department of Chemical and Materials Engineering
University of Alberta

© Zhixiao Xu, 2023

Abstract

With advantages of high capacity, water compatibility, suitable redox potential, high safety, and low cost, Zn-based aqueous energy storage devices are promising for grid-level energy storage. However, Zn metal reversibility is challenged with dendritic growth, low Coulombic efficiency (CE), metal corrosion, and hydrogen evolution. That is why excessive amount of Zn has often been used for cells, which however also reduces cell-level energy densities. Besides challenges to the anode, cathode materials suffer from metal dissolution and poor conductivity in batteries or limited capacitance in capacitors. Overall, achieving high depth of discharge (DOD) in Zn, low negative-to-positive (N/P) ratios, high loading cathodes, lean electrolyte, and wide-temperature operation is essential for the commercialization of rechargeable Zn batteries and capacitors. However, the development of these devices is still in the early stages. Furthermore, sustainable development requires recycling/upcycling of spent zinc batteries. To that end, this thesis aims to achieve practical Zn batteries and supercapacitors through electrode, electrolyte, and binder engineering, including i) making of ultrafast, long-life, high-loading, and wide-temperature zinc metal capacitors, ii) construction of a 3D hierarchical zincophilic carbon host for efficient zinc plating/stripping, iii) design of ultrafast, durable, and high-loading Zn-metal-free organic anodes, and iv) upcycling of primary alkaline batteries into secondary Zn-MnO₂ batteries.

The first work described in this thesis focuses on optimizing the electrolyte and binder towards high-performance zinc metal capacitors. As the benchmark, commercial activated carbon with hierarchical pores and large surface area was rationally selected as the cathode material. An aqueous binder enhances electrode-electrolyte wettability enabling high-mass-loading electrode, and concentrated electrolytes give high Zn stripping/plating efficiency, high ionic conductivity as well as suppressed hydrogen bonding interaction in water realizing ultralow freezing temperature.

The optimal combination unlocks unprecedented zinc metal capacitors with a large capacitance of 436 F g^{-1} , ultrahigh rate up to 200 A g^{-1} , ultralong cycles (0.3 million), ultrahigh loadings (10 mg cm^{-2}) in lean electrolyte ($8.8 \mu\text{L mg}^{-1}$), and wide-temperature operation (-60 to $60 \text{ }^\circ\text{C}$).

To further increase cell-level energy densities, a 3D carbon host was constructed to regulate highly efficient Zn plating/stripping under a high DOD. Through theoretical calculation, monomer selection, polymer assembly, and carbon fabrication, an oxygen- and nitrogen-codoped carbon superstructure was synthesized as an efficient host for high-DOD Zn metal anodes. With microscale 3D hierarchical structures, microcrystalline graphitic layers, and zincophilic heteroatom dopants, a flower-shaped carbon (C_{flower}) host could guide Zn nucleation and growth in a heteroepitaxial mode, affording horizontal plating with high CE and long life. As a demonstration, the C_{flower} -hosted Zn anode was paired with both battery and supercapacitor cathodes and delivered high performance, outclassing hostless Zn-based devices.

It is still challenging to achieve high rates and ultra-long cycles in C_{flower} -hosted Zn metal anodes. Alternatively, an ultrafast, stable, and high-loading polymer anode was developed for aqueous Zn-ion batteries and capacitors (ZIBs and ZICs) by engineering both the electrode and electrolyte. The anode polymer was rationally prepared to have a suitable electronic structure and a large π -conjugated structure, whereas the electrolyte was manufactured based on the superiority of triflate anions over sulfate anions, as analyzed and confirmed via experiments and simulations. This dual engineering results in an optimal polymer anode with a low discharge potential, near-theoretical capacity, ultrahigh-loading capability ($\approx 50 \text{ mg cm}^{-2}$), ultrafast rate (100 A g^{-1}), and ultralong lifespan (one million cycles). When the polymer anode is coupled with cathodes for both ZIB and ZIC applications, corresponding devices demonstrate ultrahigh power densities and ultralong lifespans, surpassing those of Zn-metal-based devices.

To achieve sustainable development, spent alkaline batteries were upcycled into rechargeable Zn metal batteries through a simple thermal treatment of electrode waste. The regenerated Zn powder anode showed super-zincophilicity and low overpotentials even under fast rates (8 mA cm^{-2}) and high DOD (50 %), which can be ascribed to coating of hydroxyl-rich organic layer with abundant nucleation sites as well as high orientation of favorable (002) plane and induced horizontal plating behavior. The regenerated cathode composed of MnO_2 and MnOOH had enhanced capacity in comparison to pristine ones. Under a low N/P capacity ratio of 3.8 and high loading of $\sim 10 \text{ mg cm}^{-2}$, the regenerated electrodes were paired to fabricate zinc metal batteries which demonstrate high energy and power densities (94 Wh kg^{-1} , 1349 W kg^{-1}), holding potential for practical applications.

Preface

This thesis focuses on engineering electrodes, electrolyte, and binder towards rechargeable zinc batteries/capacitors. The body of this thesis is based upon published works. The research presented in Chapters 3, 4, 5, 6, along with their supporting information, is my original work.

Chapter 3:

Zhixiao Xu, Rujiao Ma, Xiaolei Wang*, Ultrafast, long-life, high-loading, and wide-temperature zinc ion supercapacitors. *Energy Storage Materials*, 2022, 46, 233-242.

Contributions: I designed and conducted experiments and wrote the original draft. Ms. Ma assisted with some experiment (the making of hydrogel and soft-packaged pouch cells) and corresponding writing. Dr. Wang, as the supervisor author, assisted with conceptualization, discussion, and manuscript reviewing/editing.

Chapter 4:

Zhixiao Xu, Song Jin, Nianji Zhang, Wenjing Deng, Min Ho Seo, Xiaolei Wang*, Efficient Zn Metal Anode Enabled by O, N-Codoped Carbon Microflowers. *Nano Letters*, 2022, 22, 1350-1357.

Contributions: I designed and conducted experiments and wrote the original draft. Mr. Jin and Dr. Seo conducted DFT calculations. Mr. Zhang and Ms. Deng assisted with some experiments (the making of cathode materials). Dr. Wang and Dr. Seo supervised the research and reviewed/edited the manuscript.

Chapter 5:

Zhixiao Xu, Matthew Li, Wenyuan Sun, Tian Tang, Jun Lu,* and Xiaolei Wang*, An Ultrafast, Durable, and High-loading Polymer Anode for Aqueous Zinc-Ion Batteries and Supercapacitors. *Advanced Materials*, 2022, 34, 2200077.

Contributions: I designed and conducted experiments including sample preparation, structural characterizations, and electrochemical measurements, and wrote the original draft. Dr. Li assisted with some experiments and manuscript reviewing/editing. Dr. Sun and Dr. Tang conducted DFT calculations and MD simulations. Dr. Wang and Dr. Lu supervised the research and reviewed/edited the manuscript.

Chapter 6:

Zhixiao Xu, Nianji Zhang, Xiaolei Wang, Upcycling spent alkaline batteries into rechargeable Zn metal batteries, *Nano Energy*, 2022, 102, 107724.

Contributions: I designed and carried out the experiments, collected and analyzed the data, and wrote the manuscript. Mr. Zhang assisted with experiments and validation. Dr. Wang, as the supervisor author, contributed to conceptualization, discussion, and manuscript reviewing/editing.

In addition to the above publications, I also first-authored or co-first-authored four publications (not included in this thesis due to different topics):

Zhixiao Xu, Wenjing Deng, Xiaolei Wang*, 3D Hierarchical Carbon-Rich Micro/Nano-Materials for Energy Storage and Catalysis. *Electrochemical Energy Reviews*, 2021, 4, 269-335.

My contribution is the literature search, figures organization, and manuscript writing.

Zhixiao Xu⁺, Song Jin⁺(co-first author), Min Ho Seo, Xiaolei Wang*. Hierarchical Ni-Mo₂C//N-doped Carbon Mott-Schottky Array for Water Electrolysis. *Applied Catalysis B: Environmental*, 2021, 292, 120168.

My contribution: I designed and conducted experiments, analyzed data, and wrote the manuscript.

Zhixiao Xu⁺, Luyao Xu⁺, Zhixin Xu⁺(co-first author), Zhiping Deng, Xiaolei Wang*, N, O-codoped Carbon Nanosheet Array Enabling Stable Lithium Metal Anode. *Advanced Functional Materials*, 2021, 31, 2102354.

My contribution is experiments, data analysis, and manuscript writing.

Xiaolan Gao⁺, Zhixiao Xu⁺ (co-first author), Ge Li*. MOF-driven ultrafine Co₉S₈ Nanocrystals embedded in N, S-Codoped Multilayer-Assembled Carbon Nanoplates for Efficient Bifunctional Oxygen Electrocatalysis. *Chemical Engineering Journal*, 2022, 431, 133385.

My contribution is conceptualization and manuscript review/editing.

Besides above publications, I also co-authored several publications (not included in this thesis) in which my contribution is manuscript review and editing:

Wenjing Deng, Zhixiao Xu, Xiaolei Wang*. High-donor electrolyte additive enabling stable aqueous zinc-ion batteries. *Energy Storage Materials*, 2022, 52, 52-60.

Zhiping Deng, Zhixiao Xu, Wenjing Deng, Xiaolei Wang*. Ultrafine Li₄Ti₅O₁₂ Nanocrystals as Building Blocks for Ultrahigh-Power Lithium-Ion Battery Anodes. *Journal of Power Sources*, 2022, 521, 230970.

Nianji Zhang, Wenjing Deng, Zhixiao Xu, Xiaolei Wang*. Upcycling of Spent LiCoO₂ Cathodes via Nickel- and Manganese-Doping. *Carbon Energy*, 2023, 5, e231.

Wenjing Deng, Zhixiao Xu, Zhiping Deng, Xiaolei Wang*. Enhanced Polysulfides Regulation via Honeycomb-Like Porous Carbon with Inlaid Catalytic MoC for Lithium-Sulfur Batteries. *Journal of Materials Chemistry A*. 2021, 9, 21760-21770.

Acknowledgements

First of all, I would like to thank my supervisor, Dr. Xiaolei Wang and supervisor committee member, Dr. Ge Li, for giving me the opportunity to pursue doctoral studies at University of Alberta. Dr. Wang's insightful guidance helped me overcome countless difficulties in my research, and his wisdom and tolerance inspired me to continuously grow as a better person. Without their support, this work would be impossible to complete.

I would also like to thank Dr. Min ho Seo, Mr. Song Jin, Dr. Tian Tang, Dr. Wenyuan Sun, Dr. Luyao Xu, Dr. Hao Zhang, and Mr. Yue Li for their calculation and simulation support, Dr. Jun Lu, Dr. Matthew Li, Dr. Zhixin Xu, Dr. Douglas Ivey, Mr. Jiayao Cui, Dr. Zhengyu Bai, Ms. Wenjie Han, Dr. Dongqing Wu, Dr. Xin Xi, and nanoFAB staff for their experimental and characterization support.

I am also grateful to our group members. Wenjing, Zhiping, Xiaolan, Nianji, Rujiao, Qiuji, Pengcheng, Xuzi, Yimei, Yan, Zhiqing, Hangxuan, Yicheng, Ziwei, Jialiang, Han, Anil, Mahrima, Sara, it is my pleasure to work with such talented and kind-hearted people like you.

I am deeply thankful to my parents. Thank you for the unconditional love and all the hardships you had to endure to give me this carefree life.

Financial support from the Natural Sciences and Engineering Research Council of Canada (NSERC), Canada First Research Excellence Fund as part of the University of Alberta's Future Energy Systems research initiative (FES-T06-Q03) are gratefully acknowledged.

Table of Contents

Preface.....	v
Acknowledgements.....	viii
List of Tables	xiii
List of Figures.....	xiv
Chapter 1 Introduction	1
1.1 Research Background.....	1
1.2 Research Objectives	2
1.3 Thesis Structure.....	3
Chapter 2 Literature Review.....	5
2.1 Zinc-based Energy Storage Devices	5
2.2 Anode Materials	8
2.2.1 Zinc metal and its electrochemistry	8
2.2.2 Dendrite-free Zn metal construction.....	10
2.2.3 Zn-metal-free anodes (chalcogenides, oxides, and organics).....	13
2.3 Cathode Materials	17
2.3.1 Cathodes for Zn-based batteries.....	17
2.3.2 Storage mechanisms.....	17
2.3.3 Hierarchical porous carbons for Zn-based capacitors.....	22
2.4 Electrolyte Engineering (Solvent, Salt, Concentration and Additives).....	25
Chapter 3 Ultrafast, Long-life, High-loading, and Wide-temperature Zinc Ion Supercapacitors	29
3.1 Introduction	29
3.2 Experimental Section	32
3.2.1 Materials.....	32

3.2.2 Characterization.....	32
3.2.3 Electrochemical measurement.....	33
3.2.4 Calculation.....	35
3.3 Results and Discussion.....	37
3.3.1 Structural characterization of activated carbon	37
3.3.2 Optimization of binder and electrolyte.....	39
3.3.3 Ultrahigh rates, ultralong cycles, and kinetics analysis.....	43
3.3.4 Storage mechanism analysis.....	46
3.3.5 The influence of mass loadings on capacitor performance	49
3.3.6 Extremely low- and high-temperature performance.....	52
3.3.7 Soft-packaged ZIC pouch cells.....	55
3.4 Summary	56
3.5 Supporting Information.....	57
Chapter 4 Efficient Zn Metal Anode Enabled by O, N-Codoped Carbon Microflowers	79
4.1 Introduction	79
4.2 Experimental Section	81
4.2.1 Samples preparation	81
4.2.2 Characterization.....	82
4.2.3 Electrochemical measurement.....	83
4.2.4 Theoretical calculation	85
4.3 Results and Discussion.....	86
4.4 Summary	97
4.5 Supporting Information.....	98
Chapter 5 An Ultrafast, Durable, and High-loading Polymer Anode for Aqueous Zinc-Ion Batteries and Supercapacitors	116

5.1 Introduction	116
5.2 Experimental Section	118
5.2.1 Chemicals and materials preparation.....	118
5.2.2 Characterization.....	119
5.2.3 Electrochemical measurements.	120
5.2.4 Calculation of gravimetric energy and power densities	122
5.2.5 Molecular dynamics simulation and DFT calculation.....	123
5.3 Results and Discussion.....	123
5.3.1 Anode material design and selection	123
5.3.2 Electrolyte engineering and molecular dynamics simulation.....	127
5.3.3 Fast and stable cycling, high loadings, and kinetics analysis.....	131
5.3.4 Storage mechanism analysis.....	134
5.3.5 Application of PI-1/CNT as Zn-free anode for ZIBs and ZICs.....	138
5.4 Summary	142
5.5 Supporting Information	143
Chapter 6 Upcycling Spent Alkaline Batteries into Rechargeable Zn Metal Batteries	174
6.1 Introduction	174
6.2 Experimental Section	176
6.2.1 Regeneration of anode and cathode materials.	176
6.2.2 Characterization.....	176
6.2.3 Electrochemical measurement.....	177
6.2.4 Calculation.....	178
6.3 Results and discussion.....	179
6.3.1 Anode regeneration and structural characterization	179
6.3.2 Cathode regeneration and structural characterization	181

6.3.3 Electrochemical performance and deposition morphology of regenerated anode	183
6.3.4 Electrochemical performance of regenerated cathode materials	186
6.3.5 Regenerated anode and cathode for full cells	189
6.4 Summary	192
6.5 Supporting Information	192
Chapter 7 Conclusions and Perspective	206
7.1 Conclusions	206
7.2 Perspective	208
References	211

List of Tables

Table S3.1 Comparison of high-rate electrode materials for zinc ion capacitors.....	75
Table S3.2 Comparison of high-rate electrode materials for zinc ion batteries.....	76
Table S3.3 Comparison of high-mass-loading electrode materials for zinc ion capacitors.....	77
Table S3.4 Comparison of low-temperature zinc ion capacitors.....	78
Table S4.1 Binding energies of Zn atom on pristine, O-doped, and N-doped GNS.....	112
Table S4.2 Modified Zn anode and corresponding electrochemical performance in Zn/Cu half cells.....	113
Table S4.3 A survey of modified Zn anodes and corresponding electrochemical properties in Zn Zn symmetric cells.	114
Table S4.4 Comparison of DOD values of reported Zn metal in full cells.....	115
Table S5.1 Performance comparison between electrode materials for zinc ion batteries.....	169
Table S5.2 Performance comparison of Zn-free anode materials for rocking-chair type ZIBs...	171
Table S5.3 Comparison of rocking-chair type ZIBs (energy density, power density, and life cycles)	172
Table S5.4 Performance comparison of aqueous zinc ion hybrid supercapacitors.....	173
Table S6.1 Comparison of DOD values of reported Zn metal in symmetric cells and full cells.....	204
Table S6.2 Comparison of full cells with regards to discharge voltage, power density, and energy density.....	205

List of Figures

Figure 2.1 Zinc-based Energy Storage Devices. (A) Milestones for Zn-based energy storage devices, Schemes illustrating (B) ZMB with Zn metal anode and intercalative cathode, (C) ZIB with intercalative anode and cathode, (E) ZMC with Zn metal anode and intercalative cathode, and (F) ZIC with intercalative anode and cathode, Ragone plots of (D) Zn batteries and (G) Zn capacitors.....	6
Figure 2.2 Zinc metal and its electrochemistry. (A) Pourbaix diagram of a Zn/H ₂ O system when taking HER overpotential into consideration. (B) The free energy diagram of the zinc nucleation process. (C) A typical voltage profile for zinc deposition. Simulation of (D) electric field and (E) ion distribution under different nucleation conditions.....	9
Figure 2.3 Construction of Dendrite-free Zn Anodes. (A-C) Surface modification. (A) Scheme showing Zn deposition on (B) bare Zn electrode and (C) PA coated Zn. (D-E) Host construction. (D) Zn plating/stripping on CC or CNT/CC electrode and (E) corresponding nucleation overpotential on bare CC or CNT/CC. (F-I) Structural design. (F) Illustration and (G) morphology of hierarchical Zn. SEM images for (H) Zn/CNT paper and (I) Zn/CC.....	11
Figure 2.4 Zn-metal-free Anodes for ZIBs. The timeline showing the development of metal sulfides (Mo ₆ S ₈ , Zn ₂ Mo ₆ S ₈ and Na _{0.14} TiS ₂), metal oxides (h-MoO ₃), and organics (9,10-AQ and PTCDI/rGO) as Zn-free anodes for rocking-chair type ZIBs.....	13
Figure 2.5 Cathode Materials and Storage Mechanisms in Zn Batteries. (A) Brief development history of the cathode materials and energy storage mechanism of aqueous rechargeable ZMBs. (B) Discharge voltage-capacity plots of various Zn battery cathode materials. (C-E) Different energy storage mechanisms for aqueous Zn batteries with different cathode materials. (C) Zn ²⁺ insertion/extraction into/from MnO ₂ . (D) H ⁺ insertion chemistry in HATN. (E) H ⁺ /Zn ²⁺ coininsertion/extraction into/from NaV ₃ O ₈ ·1.5H ₂ O.....	18
Figure 2.6 Preparation of Hierarchical Porous Carbon Cathodes. (A) Strategies for fabricating HPCs. (B) Schematic illustration for PSC samples preparation and corresponding (C) electrochemical performances at different mass loading. (D) Scheme showing the synthetic process of HNPC. (E) DFT calculation of binding energy between Zn and heteroatoms dopants. (F) Ragone plot and (G) the LED board powered by ZIC.....	22

Figure 2.7 Electrolyte Engineering. (A) Schematic illustration of Zn batteries with liquid electrolyte, (B) electrolyte regulation strategies for addressing ZIBs issues.....	26
Figure 3.1 Structural characterization of AC. (a) SEM image, (b) EDX mapping, (c) isotherm adsorption/desorption curve and its corresponding pore size distribution, high-resolution XPS (d) C 1s, (e) O 1s, and (f) N 1s spectrum.....	37
Figure 3.2 Optimization of binder and electrolyte. (a) CV curves of AC-SA and AC-PVDF. (b) Plot of capacity against current density of AC-SA and AC-PVDF in different electrolyte. (c) Cycling performance of AC-SA in 1.0/2.0/3.0M ZnSO ₄ at the current density of 5 Ag ⁻¹ . (d) Contact angles of 3M ZnSO ₄ electrolyte on the surface of pristine SSM, AC-PVDF coated SSM, and AC-SA coated SSM. (e) pH values, viscosity, and ionic conductivity of ZnSO ₄ electrolyte with different concentration. (f) Coulombic efficiency of Zn metal plating/stripping in different electrolyte (1.0/2.0/3.0M ZnSO ₄).....	39
Figure 3.3 High-rate performance and kinetics. (a) Charge-discharge curves of the AC-SA electrode at high current densities from 10 to 200 Ag ⁻¹ . (b-d) Long cycling performance of AC-SA electrodes at (b)100 and 200 Ag ⁻¹ , (c) 20 Ag ⁻¹ , and (d) 45 Ag ⁻¹ . (e) CV profiles of AC-SA electrode at scan rates from 0.1 mVs ⁻¹ to 5.0 mVs ⁻¹ . (f) The linear fitting between log (current) and log (scan rate) at redox peaks. (g) capacitive contributions at different scan rates.....	43
Figure 3.4 Storage mechanism of AC-SA for ZICs. (a) Charge-discharge profiles containing different colored points indicating electrodes under different states. (Yellow: discharged to 0.8V, green: discharged to 0.15V, blue: charged to 1.2V, purple: charged to 1.8V). (b-c) XRD patterns of (b) AC and (c) Zn electrode under different charge/discharge states. (d-g) SEM images of AC-SA electrode at different states: (d) discharged to 0.8V, (e) discharged to 0.15V, (f) charged to 1.2V, (g) charged to 1.8V. (h) SEM EDX elemental mapping of zinc sulfate hydroxide covered AC electrode. (i) normalized CV curves and (j) voltage-capacity profiles of AC-SA electrode in different electrolyte.....	46
Figure 3.5 High-loading performance. (a) 3D profiles for the capacity-current density-mass loading relationship. (b) Charge-discharge curves, (c) rate performance, and (d) cycling performance (at 1.0 A g ⁻¹) of the high-loading AC-SA electrode (10 mg cm ⁻²). (e) Plots for the areal capacity vs. the mass loading. (f) Areal capacity versus areal current density of AC-SA electrode with different mass loadings.	49

Figure 3.6 Low/high-temperature performance. (a) 3D plot showing the ZIC capacity against temperature and current density. Charge-discharge curves of ZICs under different rates at (b) -60 °C and (d) 60 °C. (c) Long-cycling performance of ZICs at low/high temperatures (60, 0 °C, -20 °C, -40 °C, and -60 °C). (e) energy and power density of AC-SA electrodes at different temperatures.....52

Figure 3.7 Performance of soft-packaged pouch cells. (a) Rate and cycle performance of a Zn-AC pouch cell. (b) Charge/discharge profiles of pouch cells bent at different angles. (c) Self-discharge test and inset shows the open-circuit voltage change with time. (d) Voltage-time profiles of single ZIC and three ZICs connected in series. (e) The digital photo showing two ZICs in series powering one blue LED.....55

Figure S3.1 Structural characterization of AC. (a) SEM image, (b) Raman spectrum, (c) XRD pattern, and (d) XPS full spectrum.....57

Figure S3.2 Digital photos of AC-SA electrodes in different solution: (a) deionized water, (b) 3M ZnSO₄, and (c) 3M ZnSO₄ for 10 days.....57

Figure S3.3 Rate performance of AC-SA and AC-PVDF electrodes in different electrolyte (0.5M, 1M, 2M, 3M ZnSO₄).....58

Figure S3.4 Electrochemical performance of AC electrodes in 2M ZnCl₂ electrolyte: (a,b) AC-PVDF electrode using SSM as the current collector, (c, d), AC-SA electrode using SSM as the current collector, (e, f) AC-SA electrode using carbon cloth as the current collector.....58

Figure S3.5 Electrochemical performance of AC-SA electrode in 2M Zn(OTf)₂ electrolyte.....59

Figure S3.6 (a) H-cell setup for the testing of corrosion behavior of Zn foil in which only one chamber is filled with 3M ZnSO₄ electrolyte and the Zn foil was put in between two chambers so that only one side is exposed to the electrolyte. (b) Tafel polarization curve of Zn electrode tested in a three-electrode system with 3M ZnSO₄ (pH=3.4) as the electrolyte, Zn foil (diameter: 1.6 cm) as the working electrode, and Ag/AgCl (saturated KCl) as the reference electrode.....59

Figure S3.7 Cycling performance of AC-PVDF electrode in 2M ZnSO₄ electrolyte at a high rate of 20 Ag⁻¹.....60

Figure S3.8 SEM images of Zn anode after 80000 cycles at 20 Ag⁻¹. Hexagonal flakes can be found which may be composed of zinc hydroxide sulfate. Zn dendrites may be underneath zinc hydroxide sulfate.....60

Figure S3.9 Electrochemical performance of AC-SA electrode under ultrahigh-rate cycling using thin Zn foils (30 μm thickness). (a) Rate performance, (b) Charge/discharge profiles, (c) cycling at 100 Ag^{-1}	61
Figure S3.10 Redox peaks for calculating b values in AC-SA electrode.....	61
Figure S3.11 Capacitive contributions of AC-SA electrode under different scan rates.....	62
Figure S3.12 The kinetics analysis of AC-PVDF electrode. (a) CV curves, (b) b value plot, and (c) capacitive contributions at different scan rate.....	62
Figure S3.13 Capacitive contributions of AC-PVDF electrode under different scan rates.....	63
Figure S3.14 Electrochemical performance of AC-PVDF electrodes under different mass loadings. (a) rate performance and corresponding (b) charge-discharge curves of AC-PVDF with a 3.9 mg cm^{-2} loading. (a) rate performance and corresponding (b) charge-discharge curves of AC-PVDF with a 10 mg cm^{-2} loading.....	64
Figure S3.15 Electrochemical performance of low-loading AC-SA electrode (3.2 mg cm^{-2}).....	65
Figure S3.16 Electrochemical performance of low-loading AC-SA electrode (4.1 mg cm^{-2}).....	65
Figure S3.17 Electrochemical performance of medium-loading AC-SA electrode (5.0 mg cm^{-2}).....	66
Figure S3.18 Electrochemical performance of medium-loading AC-SA electrode (7.6 mg cm^{-2})	66
Figure S3.19 Electrochemical performance of high-loading AC-SA electrode (9.5 mg cm^{-2}).....	67
Figure S3.20 Cycling performance of high-loading AC-SA electrode (10 mg cm^{-2}) showing the failure of the capacitor after 42 cycles.....	67
Figure S3.21 Morphology of after-cycling zinc electrode in Figure S3.20 indicating the presence of Zn dendrites.....	68
Figure S3.22 Energy density and power density of AC-SA electrodes with different mass loadings. (a) gravimetric energy/power densities and (b) areal energy/power densities. The calculation is based on the active mass of the AC-SA electrode.....	68
Figure S3.23 Electrochemical performance of AC-SA electrode at low temperatures ($0 \text{ }^{\circ}\text{C}$ and $-20 \text{ }^{\circ}\text{C}$) in 3M ZnSO_4 electrolyte.....	69
Figure S3.24 DSC curves of electrolyte. (a) 3M ZnSO_4 , (b) 5.5M ZnCl_2	69
Figure S3.25 Charge-discharge curves of AC-SA electrode at different current densities under low temperatures ($0 \text{ }^{\circ}\text{C}$, $-20 \text{ }^{\circ}\text{C}$, $-40 \text{ }^{\circ}\text{C}$, and $-60 \text{ }^{\circ}\text{C}$) in 5.5M ZnCl_2 electrolyte.....	70

Figure S3.26 Storage mechanism of AC-SA electrode for ZICs in 5.5 M ZnCl₂ at -60 °C. (a) normalized CV curves of AC-SA electrode in different electrolyte. (b) Charge-discharge profiles indicating electrodes under different states. (purple: discharge to 0.8V, blue: discharge to 0.15V, yellow: charge to 1.2V, red: charge to 1.8V). (c) XRD patterns of AC electrodes under different charge/discharge states. (d-f) SEM images of AC-SA electrode at different states: (d) DC 0.8V, (e) DC 0.15V, (f) C1.2V, (g) C1.8V. (h-i) SEM EDX elemental mapping of AC-SA electrode under (h) DC 0.15V and (i) C 1.8V.....70

Figure S3.27 Electrochemical performance of AC-SA electrode in 3M ZnSO₄ electrolyte at high temperatures. (a) Rate performance at 60 °C and (b) cycling performance at 10 Ag⁻¹ at 80 °C.....72

Figure S3.28 Electrochemical performance of AC-SA and AC-PVDF electrode in organic electrolyte (0.5M Zn(OTf)₂-DMF) at room temperature (20 °C). (a, d) charge-discharge curves, (b, e) rate performance, (c, f) cycling performance of (a-c) AC-SA and (d-f) AC-PVDF electrodes.72

Figure S3.29 Electrochemical performance of AC-SA electrode in organic electrolyte (0.5M Zn(OTf)₂-DMF) at 60 °C. (a) rate performance, (b) charge-discharge curves, (c) cycling performance at 5 Ag⁻¹.....73

Figure S3.30 Electrochemical performance of AC-SA electrode in organic electrolyte (0.5M Zn(OTf)₂-DMF) at 80 °C. (a) rate performance, (b) charge-discharge curves, (c) cycling performance at 10 Ag⁻¹.....73

Figure S3.31 Electrochemical performance of high-loading AC-SA electrode (6.96 mg) tested under harsh conditions including thin Zn foil (30 μm thick, 1.13 cm², 28.5 mg) and lean electrolyte (70 μL 3M ZSO, 98.8 mg).....74

Figure 4.1 (a) Modeling of oxygen/nitrogen-doped graphene. (b) Summary of the calculated binding energies of Zn atoms with all possible configurations of pristine, O- and N-doped graphene. (c-e) model structure for the most stable adsorption sites of Zn atoms and (f-h) charge density differences of (c, f) pristine, (d, g) O-doped and (e, h) N-doped graphene, respectively. (i) Scheme showing the ideal transition from monomers to polyimide precursor, polyimide, and derived O/N-codoped carbon.....87

Figure 4.2 SEM images of (a) C_{flower}, (b) C_{disk}, (c) C_{sphere} and TEM images of (d) C_{flower}, (e) C_{disk}, (f) C_{sphere}. High-resolution XPS spectra of (g) C 1s, (h) O 1s, and (i) N 1s.....88

Figure 4.3 Zn/Cu half-cell tests. (a) Coulombic efficiency of Zn stripping/plating onto different substrates (pure Cu, $C_{\text{flower}}/\text{Cu}$, $C_{\text{disk}}/\text{Cu}$, and $C_{\text{sphere}}/\text{Cu}$) at 0.5 mA cm^{-2} and 0.25 mAh cm^{-2} . (b) CE of the $C_{\text{flower}}/\text{Cu}$ electrode at different current rates and capacities and (c) corresponding discharge/charge profiles. (d) Zn plating profiles of $C_{\text{flower}}/\text{Cu}$ and pure Cu at 10 mA cm^{-2} and 50 mAh cm^{-2} . (e-h) SEM images of deposited Zn morphology onto (e, f) pure Cu and (g, h) $C_{\text{flower}}/\text{Cu}$.
91

Figure 4.4 Symmetric cells based on Zn metal anodes with or without carbon coating. a) Voltage profiles of symmetric cells using $C_{\text{flower}}/\text{Zn}$ and pure Zn electrodes at 0.5 mA cm^{-2} . b) Comparison of voltage profiles of symmetric cells based on $C_{\text{flower}}/\text{Zn}$, $C_{\text{disk}}/\text{Zn}$, and $C_{\text{sphere}}/\text{Zn}$ at 2 mA cm^{-2} . d) Rate performance of symmetric cells based on $C_{\text{flower}}/\text{Zn}$ electrodes at current densities from 1.0 to 20 mA cm^{-2} with plating capacities from 0.5 mAh cm^{-2} to 2.5 mAh cm^{-2} . e) Long-term cycling performance of $C_{\text{flower}}/\text{Zn}$ electrodes-based cell at a high rate of 5 mA cm^{-2} .
93

Figure 4.5 Zn metal-based full cells. a) charge/discharge profiles of $C_{\text{flower}}/\text{Zn}/\text{MnO}_2$ batteries at different current densities ($0.1\sim 5 \text{ Ag}^{-1}$). Rate performance comparison between $C_{\text{flower}}/\text{Zn}$ -based cells and pure Zn-based cells with limited Zn: (b) 1 mAh and (c) 2 mAh . d) charge/discharge profiles of $C_{\text{flower}}/\text{Zn}/\text{AC}$ capacitor vs. Zn/AC capacitor at different current densities ($1, 5, \text{ and } 10 \text{ Ag}^{-1}$). e) Rate and cycling performance of $C_{\text{flower}}/\text{Zn}$ -based and pure Zn-based capacitor with limited Zn amount of 5 mAh .
95

Figure S4.1 Possible configurations of Zn atom adsorption on (a) pristine, (b) O-doped, and (c) N-doped GNS for searching the most stable adsorption site (described as yellow round).
98

Figure S4.2 Defined configurations of (a) pristine, (b) O-doped, and (c) N-doped GNS which shows the most stable adsorption with Zn atom among the possible adsorption sites.
98

Figure S4.3 Density of state of (a) pristine, (b) O-containing and (c) N-containing graphene, respectively.
98

Figure S4.4 The projected-density of state of (a) pristine, (b) O-doped, and (c) N-doped GNS, respectively.
98

Figure S4.5 Schematic illustration of the synthetic process of different polymer and carbon micro/nanostructure. (a) pre-polymerization reaction, (b) solvothermal polymerization under high pressure, (c) wet polymerization under stirring and atmospheric pressure, (d) precipitation polymerization, (e) carbonization.
100

Figure S4.6 SEM images of (a, b) PI _{flower} , (c, d) PI _{disk} , and (e, f) PI _{sphere}	102
Figure S4.7 FTIR spectra and XRD patterns of PI _{flower} , PI _{disk} , and PI _{sphere}	102
Figure S4.8 TGA curves of PI _{flower} , PI _{disk} , and PI _{sphere} tested at a ramp rate of 10 °C min ⁻¹ in the N ₂ atmosphere.....	103
Figure S4.9 SEM image and EDX mapping of (a-d) C _{flower} , (e-h) C _{disk} , and (i-l) C _{sphere}	103
Figure S4.10 Structural characterization of C _{flower} , C _{disk} , and C _{sphere} . (a) XRD patterns, (b) Raman spectra of different carbon materials (C _{flower} , C _{disk} , and C _{sphere}). (c) Nitrogen adsorption/desorption curves of C _{flower} , C _{disk} , and C _{sphere} . For clear comparison, the curve for C _{flower} and C _{disk} is shifted positively along the y axis with a value of 100 and 50 cm ³ g ⁻¹ , respectively. (d) corresponding pore size distribution curves of different carbons.....	104
Figure S4.11 XPS survey spectra of different carbon materials. Only C, N, and O elements can be detected in all samples.....	105
Figure S4.12 Discharge/charge profiles of b) C _{flower} /Cu, C _{disk} /Cu and c) C _{sphere} /Cu, pure Cu at different cycles, corresponding to Figure 4.3a.....	105
Figure S4.13 Plot for voltage and current density versus cycling time.....	106
Figure S4.14 Plating profiles of Zn onto C _{flower} /Cu vs. pure Cu substrate at a current density of 0.2 mA cm ⁻² and a capacity of 2.0 mAh cm ⁻²	106
Figure S4.15 Cycling performance of symmetric cells using Zn foils coated with different carbon materials (activated carbon, Super P, and C _{flower}). Test condition: 1 mA cm ⁻² , 0.5 mAh cm ⁻²	107
Figure S4.16 Plots of current density against overpotential in symmetric cells.....	107
Figure S4.17 Rate performance of symmetric cells based on pure Zn electrodes at current densities from 1.0 to 3 mA cm ⁻² with plating capacities from 0.5 mAh cm ⁻² to 1.5 mAh cm ⁻²	108
Figure S4.18 Structural characterization of cathode materials. (a-c) XRD patterns of (a) MnO ₂ , (b) AC, and (c) I ₂ /AC and (d-f) SEM images of (d) MnO ₂ , (e) AC, and (f) I ₂ /AC.....	108
Figure S4.19 Cycling performance of Zn//MnO ₂ batteries based on 2 mAh of Zn and 1.5 mg of MnO ₂ . The green line resperent C _{flower} /Zn-based battery while yellow line is Cu/Zn-based battery	109
Figure S4.20 Zn//MnO ₂ batteries using 10 mAh (ca. 12.2 mg) of Zn and 1.5 mg of MnO ₂ . Charge/discharge profiles of b) C _{flower} /Zn//MnO ₂ battery and c) Cu/Zn//MnO ₂ battery at different current densities.....	109

Figure S4.21 Electrochemical performance of Zn/SSM half cells. (a, b) Coulombic efficiency of Zn plating/stripping onto SSM-based substrates ($C_{\text{flower}}/\text{SSM}$ vs. pristine SSM) at a current density of 0.5 mA cm^{-2} and a capacity of 1.0 mAh cm^{-2} . Charge/discharge curves of Zn plating/stripping on (c) $C_{\text{flower}}/\text{SSM}$ and (d) pristine SSM at different cycles.....	110
Figure S4.22 Rate performance of $C_{\text{flower}}/\text{Zn}/\text{AC}$ and $\text{SSM}/\text{Zn}/\text{AC}$ capacitors based on 2 mAh (ca. 2.44 mg) of Zn anode and 2 mg of AC cathode.	111
Figure S4.23 $C_{\text{flower}}/\text{Zn}/\text{I}_2/\text{AC}$ full cell constructed by 5 mAh (~6.1 mg) of Zn, 1.5 mg of I_2/AC composite, and 100 μL of 3M ZnSO_4 electrolyte. (a) Charge/discharge profiles based on iodine only and (b) iodine/AC composite. (c) Rate and cycling performance.....	111
Figure S4.24 Full cell performance. (a-c) Charge/discharge curves of $C_{\text{flower}}/\text{Zn}$ -based full cells, capacity and current rate is based on the total mass of Zn metal and cathode materials. And corresponding (d-f) Ragone plot of these devices.....	112
Figure 5.1 Electrode Engineering and Structural Characterization of PI-1 and PI-1/CNT. (A) Electronic structure of different molecules and polymers, (B) Cycling performance of different organic electrodes at 0.1 A g^{-1} , (C) FTIR spectra, (D) XRD patterns, and (E) TGA profiles of PI-1/CNT and PI-1. (F) SEM image, (G-H) TEM images, and (I) HAADF image and elemental mapping images of PI-1/CNT.....	126
Figure 5.2 Electrolyte Engineering and Molecular Dynamics Simulation. (A) Capacity values of PI-1/CNT in different electrolyte at current densities from 0.2 to 5 A g^{-1} . (B) Voltage–capacity profiles of PI-1/CNT in 1.0 M $\text{Zn}(\text{OTf})_2$ and 1.0 M ZnSO_4 at low (0.2 A g^{-1}) and high (5.0 A g^{-1}) current rates. (C) Electrochemical impedance spectra (EIS) of PI-1/CNT in 1.0 M $\text{Zn}(\text{OTf})_2$ and 1.0 M ZnSO_4 . (D) Capacity and Capacity retention of PI-1/CNT in different electrolytes after ultralong cycling. (E) Cycling performance and CE profiles of PI-1/CNT in 1.0 M $\text{Zn}(\text{OTf})_2$ and 1.0 M ZnSO_4 tested at 5.0 A g^{-1} . (F) Ionic conductivities, viscosities, and pH values of different electrolytes. (G) MD-simulated distribution of ions and water near cathode surface. (H) Number density profiles of water and Zn^{2+} along normal direction of cathode surface.....	129
Figure 5.3 Optimized electrochemical performance and kinetics analysis of PI-1/CNT electrode. (A) Voltage–capacity profiles of PI-1/CNT at different current densities from 0.2 to 100 A g^{-1} . (B) Ultralong cycle life of PI-1/CNT at different current densities (10 or 50 A g^{-1}). (C) Million-cycle life of PI-1/CNT at 100 A g^{-1} . (D) Comparison of rate and cycling performance between different	

ZIB electrode materials. (E–G) High-loading PI-1/CNT electrodes: (E) Rate and cycling performance of PI-1/CNT with high loading of 4.08 mg cm^{-2} , (F) Cycling performance of ultrahigh-loading PI-1/CNT electrodes, inset of F shows the optical image of the 19.7 mg cm^{-2} electrode, (G) Plots of areal capacity against mass loadings. (H) CV curves of PI-1/CNT at different scan rates from 0.3 mV s^{-1} to 5 mVs^{-1} and corresponding (I) kinetics profiles of different redox peaks (A, B, C).....131

Figure 5.4 Ion storage mechanism of PI-1/CNT Electrode. (A) CV profiles of PI-1/CNT in different Zn/Na-based electrolytes. (B) SEM mapping images of PI-1/CNT electrode discharged to 0.1 V in 0.5 M $\text{Zn}(\text{OTf})_2$ -DMF. (C) CV profiles of PI-1/CNT in different aqueous electrolytes with controlled pH values. (D) SEM images of PI-1/CNT electrode discharged to 0.1 V (upper part) and charged back to 1.1 V (downside part). (E) *Ex situ* XRD patterns of PI-1/CNT electrode at pristine and discharged status. (F) SEM image and corresponding elemental mapping images of PI-1/CNT electrode discharged to 0.1 V in 1.5 M $\text{Zn}(\text{OTf})_2$. (G–H) *In situ* ATR-FTIR spectra of PI-1/CNT at different discharge/charge states. *Ex situ* high-resolution (I) *C1s* and (J) *O1s* XPS spectra of PI-1/CNT electrode at pristine, DC0.1V, and C1.1V statuses.....136

Figure 5.5 Application of PI-1/CNT as Zn-metal-free Anode for ZIBs and ZICs. (A) Galvanostatic charge and discharge potential profiles of PI-1/CNT// Zn_xMnO_2 at different current rates. (B) Rate performance of PI-1/CNT// Zn_xMnO_2 and corresponding CE values. (C) Ragone plots of PI-1/CNT// Zn_xMnO_2 and documented rocking-chair type ZIBs (energy and power densities are based on total active material mass of cathode and anode). (D) Cycling comparison between PI-1/CNT// Zn_xMnO_2 and Zn// MnO_2 with equal MnO_2 mass at current density of 2.0 A g^{-1} . (E) Long cycle performance of PI-1/CNT//AC and Zn//AC at high current density of 10 A g^{-1} . (F) Ultrafast and stable cycling of PI-1/CNT//AC capacitor (N/P mass ratio=1.15). (G) Capacity retention against cycle numbers for different materials in reported papers.....140

Figure S5.1 FTIR spectra of a) PTCDA, PTCDI, PI-1 and b) PI-1/CNT, PI-2/CNT, PI-3/CNT..142

Figure S5.2 XRD patterns of a) PTCDA, PTCDI, PI-1 and b) PI-1/CNT, PI-2/CNT, PI-3/CNT.....143

Figure S5.3 SEM images of (a-b) PTCDA, (c-d) PTCDI, (e-f) PI-1, (g-h) PI-1/CNT, (i-j) PI-2/CNT and (k-l) PI-3/CNT.....144

Figure S5.4 HRTEM images of PI-1/CNT. The crystal lattice can be assigned to CNT.....145

Figure S5.5 ZIB performance of PTCDA. a) Charge-discharge profiles. b) Rate performance. c) cycling performance and Coulombic efficiency at 0.1 Ag ⁻¹	145
Figure S5.6 ZIB performance of PTCDI. a) Scheme showing the synthesis of PTCDI. b) Charge-discharge profiles. c) cycling performance and Coulombic efficiency at 0.1 Ag ⁻¹	146
Figure S5.7 The digital photo showing the solubility of different samples in hot water (60 °C) after two days.....	146
Figure S5.8 ZIB performance of PI-2/CNT. a) Scheme showing the synthesis of PI-2. b) Voltage-capacity profiles. c) cycling performance and Coulombic efficiency at 0.1 Ag ⁻¹	147
Figure S5.9 ZIB performance of PI-3/CNT. a) Scheme showing the synthesis of PI-3. b, d) Voltage-capacity profiles. c, e) cycling performance and Coulombic efficiency at 0.1 Ag ⁻¹ . (b-c) is tested in the voltage window of 0.01-1.3 V while (d-e) is tested in 0.08-1.1 V.....	147
Figure S5.10 ZIB performance of CNT. a) Voltage-capacity profiles. b) cycling performance and Coulombic efficiency at 0.1 Ag ⁻¹	148
Figure S5.11 ZIB performance of PI-1/CNT in different aqueous electrolyte. Rate performance in a) ZnSO ₄ and b) Zn(OTf) ₂ electrolyte from 0.2 A g ⁻¹ to 5 A g ⁻¹ . c) comparison of different electrolyte at different rates. d) Cycling performance and Coulombic efficiency at 5 A g ⁻¹	148
Figure S5.12 MD simulation of ions and water in an electrical double layer model under different electrolytes and potentials. Simulation models for (a) 1M ZnSO ₄ electrolyte containing 32 ZnSO ₄ and 1598 H ₂ O molecules and (b) 1M Zn(OTf) ₂ electrolyte containing 32 Zn(OTf) ₂ and 1390 H ₂ O molecules.....	149
Figure S5.13 Radial distribution function (RDF) of (a) water oxygen around Zn ²⁺ (Zn-Ow), S of OTF ⁻ around Zn ²⁺ (Zn-S(OTF)), and O of OTF ⁻ around Zn ²⁺ (Zn-O(OTf)) in system T-0.5; (b) water oxygen around Zn ²⁺ (Zn-Ow), S of SO ₄ ²⁻ around Zn ²⁺ (Zn-S), and O of SO ₄ ²⁻ around Zn ²⁺ (Zn-Os) in system S-0.5; (c) water oxygen around S of OTF ⁻ (St-Ow), water oxygen around O of OTF ⁻ (Ot-Ow), water oxygen around C of OTF ⁻ (Ct-Ow), and water oxygen around F of OTF ⁻ (Ft-Ow) in system T-0.5; (d) water oxygen around S of SO ₄ ²⁻ (S-Ow), and water oxygen around O of SO ₄ ²⁻ (Os-Ow) in system S-0.5.....	150
Figure S5.14 Relative number density of water in systems (S-0.5, S-1.1, T-0.5, T-1.1). The densities were normalized with respect to the bulk values at Z = 6 nm.....	151

Figure S5.15 Number density of (a) Zn^{2+} and (b) anions in the systems (S-0.5, S-1.1, T-0.5, T-1.1).....	151
Figure S5.16 Cycling performance of PI-1/CNT in 1.5 M $Zn(OTf)_2$ at a low rate of $0.1 A g^{-1}$..	152
Figure S5.17 High-rate cycling performance of PI-1/CNT at $50 A g^{-1}$	152
Figure S5.18 Electrochemical performance of free-standing PI-1/CNT electrode with an ultrahigh loading of $12.5 mg cm^{-2}$ under lean electrolyte of $6.3 \mu L mg^{-1}$. (a-c) gravimetric capacities and (d-f) areal capacities. (a, d) charge-discharge profiles at different rates, (b, e) rate performance, (c, f) cycling performance and Coulombic efficiency changes.....	152
Figure S5.19 Electrochemical performance of free-standing PI-1/CNT electrode with an ultrahigh loading of $19.7 mg cm^{-2}$ under lean electrolyte of $4.0 \mu L mg^{-1}$. (a-c) gravimetric capacities and (d-f) areal capacities. (a, d) charge-discharge profiles at different rates, (b, e) rate performance, (c, f) cycling performance and Coulombic efficiency changes.....	153
Figure S5.20 Free-standing PI-1/CNT electrode with the loading of $19.7 mg cm^{-2}$. (a) Digital photos, (b-d) cross-sectional (b) and top-view SEM images (c-d). Digital photos show the green-shiny color and dense packing of PI-1/CNT powders. The thickness of the high-loading electrode is measured to be $\sim 150 \mu m$ and the electrode surface is extremely smooth.....	153
Figure S5.21 Electrochemical performance of free-standing PI-1/CNT electrode with an ultrahigh loading of $30.1 mg cm^{-2}$ under lean electrolyte of $2.62 \mu L mg^{-1}$. (a-c) gravimetric capacities and (d-f) areal capacities. (a, d) charge-discharge profiles at different rates, (b, e) rate performance, (c, f) cycling performance and Coulombic efficiency changes. Of note, Zn foil with a thickness of $100 \mu m$ was used as the anode.....	154
Figure S5.22 Electrochemical performance of free-standing PI-1/CNT electrode with an ultrahigh loading of $50 mg cm^{-2}$ under lean electrolyte of $1.58 \mu L mg^{-1}$. (a-c) gravimetric capacities and (d-f) areal capacities. (a, d) charge-discharge profiles at different rates, (b, e) rate performance, (c, f) cycling performance and Coulombic efficiency changes. Of note, Zn foil with a thickness of $100 \mu m$ was used as the anode.....	154
Figure S5.23 Digital photos of disassembled ZIB electrodes after 600 cycles. (a) free-standing PI-1/CNT electrode ($19.7 mg cm^{-2}$) and (b) Zn metal electrode.....	155
Figure S5.24 Characterization of the $30.1 mg cm^{-2}$ electrode after cycling. (a) A digital photo of the disassembled PI-1/CNT electrode showing its intact feature. (b, c) Top-view SEM images	

showing the ultrasmooth surface with layered products covering on the surface without dendrites. (d-f) Cross-sectional SEM images showing the dense packing of PI-1/CNT.....155

Figure S5.25 Characterization of the 50 mg cm⁻² electrode after cycling. (a) A digital photo showing the intact feature of the disassembled PI-1/CNT electrode after continuous washing by water (Video S2). (b, c) Top-view SEM images showing the nanosheet-like products covering on the surface without dendrites. (d-f) Cross-sectional SEM images showing the dense packing of PI-1/CNT.....156

Figure S5.26 Electrochemical performance comparison between high-loading PI-1 and PI-1/CNT electrodes. (a) Capacities of PI-1 electrodes (9.95 and 20 mg cm⁻²) at different rates (0.05-2.0 A g⁻¹). (b) Capacities of PI-1/CNT electrodes (12.5-50 mg cm⁻²) at different rates (0.05-2.0 A g⁻¹). (c) Capacity retentions after hundreds of cycles in PI-1 and PI-1/CNT electrodes under lean electrolyte.156

Figure S5.27 Electrochemical performance of free-standing PI-1 electrode with an ultrahigh loading of 9.95 mg cm⁻² under lean electrolyte of 7.94 μL mg⁻¹. (a-c) gravimetric capacities and (d-f) areal capacities. (a, d) charge-discharge profiles at different rates, (b, e) rate performance, (c, f) cycling performance and Coulombic efficiency changes.....157

Figure S5.28 Electrochemical performance of free-standing PI-1 electrode with an ultrahigh loading of 20.0 mg cm⁻² under lean electrolyte of 3.94 μL mg⁻¹. (a-c) gravimetric capacities and (d-f) areal capacities. (a, d) charge-discharge profiles at different rates, (b, e) rate performance, (c, f) cycling performance and Coulombic efficiency changes.....157

Figure S5.29 Capacitive contribution ratio of PI-1/CNT electrode at different scan rates.....158

Figure S5.30 Two-electrode CV test in H₂SO₄ (pH=1) electrolyte with the PI-1/CNT as working electrode and Zn metal as counter/reference electrode.....158

Figure S5.31 Set-up for *in situ* ATR-FTIR test during battery charging/discharging.....159

Figure S5.32 CV curves of polymer based ZIBs (PI-1/CNT//Zn_xMnO₂) in the first five cycles with a scan rate of 0.5 mV s⁻¹.....159

Figure S5.33 Electrochemical performance of Zn//MnO₂ battery. (a) Charge-discharge curves and (b) rate performance at different current densities.....160

Figure S5.34 The electrochemical performance of rocking-chair PI-1/CNT//Zn_xMnO₂ full cells with a N/P mass ratio of ~2.5. (a) charge-discharge curves and (b) rate performance.....160

Figure S5.35 Cycling of PI-1/CNT//Zn _x MnO ₂ and Zn//MnO ₂ batteries at 2 Ag ⁻¹ with the same amount of MnO ₂ (1.32 mg) but different amount of anode materials.....	161
Figure S5.36 Digital photographs of disassembled ZIBs after long cycles. (a-b) PI-1/CNT//Zn _x MnO ₂ battery after 50,000 cycles and (c-d) Zn//MnO ₂ battery after 16,000 cycles...	161
Figure S5.37 Structural characterization of after-50k-cycle PI-1/CNT electrode in the PI-1/CNT//Zn _x MnO ₂ battery. (a-d) SEM images and (e) XRD patterns.....	162
Figure S5.38 Structural characterization of Zn anode in the Zn//MnO ₂ battery. (a-d) SEM images of the Zn anode after 16k cycles.....	162
Figure S5.39 Structural characterization of cathode materials in the PI-1/CNT//Zn _x MnO ₂ battery. SEM images of MnO ₂ (a-b) before and (c-d) after 50000 cycles and (g) XRD patterns of pristine MnO ₂ (green) and after 50,000 cycles (yellow).....	163
Figure S5.40 Characterization of ZnMn ₂ O ₄ . (a) the XRD pattern and (b) the SEM image.....	163
Figure S5.41 Electrochemical performance of PI-1/CNT//ZnMn ₂ O ₄ and Zn//ZnMn ₂ O ₄ batteries. (a-b) Charge-discharge curves of (a) PI-1/CNT//ZnMn ₂ O ₄ cell and (b) Zn//ZnMn ₂ O ₄ cell. (c) Rate performance at different current densities and (d) cycling performance at 0.5 A g ⁻¹	164
Figure S5.42 Electrochemical performance of PI-1/CNT//ZnMn ₂ O ₄ full cell using high-loading, free-standing, current-collector-free, and binder-free electrodes. (a) Charge-discharge profiles, (b) rate performance, and (d) cycling performance at 0.5 A g ⁻¹ . The capacity is based on ZnMn ₂ O ₄ ..	165
Figure S5.43 CV curves of PI-1/CNT//AC capacitor in the first five cycles with a scan rate of 0.5 mV s ⁻¹	166
Figure S5.44 Charge-discharge profiles of (a) PI-1/CNT//AC and (b) Zn//AC capacitors under different current densities.....	166
Figure S5.45 Digital photographs of disassembled ZICs after long cycles. (a-b) PI-1/CNT//AC capacitor after 500,000 cycles and (c-d) Zn//AC capacitor after 107,000 cycles.....	167
Figure S5.46 Structural characterization of after-500k-cycle PI-1/CNT electrode in the PI-1/CNT//AC capacitor. (a-d) SEM images and (e) XRD patterns.....	167
Figure S5.47 Structural characterization of after-cycling Zn anode in the Zn//AC capacitor. (a-d) SEM images of Zn anode.....	168

Figure S5.48 Structural characterization of pristine and after-500k-cycle AC cathode in the PI-1/CNT//AC capacitor. SEM images of AC (a-b) before and (c-d) after half million cycles. (e) XRD patterns of AC before (yellow line) and after half million cycles (green line).....168

Figure 6.1 Structural characterization of anode materials. (a) XRD patterns of fresh, spent, and regenerated anode materials as well as standard cards. SEM images and EDX elemental mappings of fresh, spent, and regenerated anode materials. (b-d) fresh anode, (e-g) spent anode, and (h-j) regenerated anode.....180

Figure 6.2 Cathode Regeneration and Structural Characterization. XRD patterns of (a) fresh, spent, and regenerated cathodes, and (b, c) regenerated cathode materials at different temperature and standard JCPDS cards. SEM images of (d) fresh cathode, (e) spent cathode, (f) Reg400, (g) Reg300, and (h) Reg500. (i) EDX elemental mappings of Reg400.....182

Figure 6.3 Electrochemical performance of regenerated Zn and commercial Zn anodes. (a) symmetric cells based on regenerated Zn powder (10 mg) and commercial Zn foils (28.5 mg) tested at different current rates and capacity, corresponding (b) voltage hysteresis, and (c) depth of discharge values. (d) Symmetric cells based on regenerated Zn powder (5 mg) and commercial Zn foils (95 mg) tested at 2 mA cm⁻² and 2 mAh cm⁻². (e) the plot of current density against overpotential. SEM images of after-cycle electrodes in symmetric cells: (f) regenerated Zn (after 100 h), and (g) commercial Zn (after 39 h)184

Figure 6.4 Electrochemical performance of regenerated cathodes. (a) 3D profiles of current densities-capacity-samples. (b) Charge-discharge profiles of Reg400. (c) Cycling performance of Reg400 and Reg300, and (d) CV profiles of Reg400 at diverse scan rates and derived (e) linear fitting of log (current) against log (scan rate) at redox peaks. (f) Capacitive contributions at different scan rates. (g) rate and cycling performance of Reg400 electrode under high loading and lean electrolyte. (h) Profiles of areal capacity against mass loading.....187

Figure 6.5 Full cells based on regenerated anodes and cathodes. (a) CV curves of regenerated Zn cell and commercial Zn cell at a scan rate of 0.2 mV s⁻¹. (b) CV profiles of regenerated electrodes-based cell at different rates from 0.2 to 1.5 mV s⁻¹. (c) Voltage gaps between O and R1 peaks in two cells at different rates. (d) Rate performance of regenerated and commercial cells with high-loading cathodes and different N/P ratios. (e) Discharge profiles of regenerated Zn cell based on

total mass of regenerated anode and cathode materials. (f) Ragone plots of our regenerated Zn cell and previously reported ZMBs and ZIBs.....	191
Figure S6.1 Digital photos of fresh, spent, and regenerated electrode materials. (a) fresh electrodes, (b) spent electrodes, (c) regenerated Zn powder in ethanol and coated on Cu foil....	192
Figure S6.2 SEM images of (a, b) fresh anode, (c) spent anode, and (d) regenerated anode. (b) shows the side product of fresh Zn anode due to the formation of ZnO during self-discharge.....	193
Figure S6.3 EDX point analysis of fresh, cycled, and regenerated anode materials.....	193
Figure S6.4 ATR-FTIR spectrum of regenerated Zn powder.....	194
Figure S6.5 TEM images of regenerated Zn powder. (a-b) TEM images and (c) HRTEM image.....	194
Figure S6.6 STEM elemental mapping of regenerated Zn. (a, e) STEM image and corresponding mapping of (b, f) Zn, (c, g) C, and (d, h) O elements.....	195
Figure S6.7 SEM images of (a) fresh, (b) spent, and (c-e) regenerated cathode materials, (c) Reg300, (d) Reg400, and (e) Reg500.....	195
Figure S6.8 TGA curve of the regenerated cathode materials (Reg400).....	196
Figure S6.9 The first cycle of the symmetric cells in Figure 6.3a.....	196
Figure S6.10 The first cycle of the symmetric cells in Figure 6.3d.....	197
Figure S6.11 Symmetric cells based on fresh Zn powders (7.2 mg). (a) Voltage-time curves in 50 h and (b) first cycle profile. The DOD of the fresh Zn anode is 9.6%.....	197
Figure S6.12 SEM images of regenerated Zn anode after symmetric-cell tests (100h) in Figure 6.3a.....	198
Figure S6.13 SEM images of commercial Zn anode after symmetric-cell tests (~40h) in Figure 6.3a.....	198
Figure S6.14 SEM images of the fresh Zn anode after being plated with 1.0 mAh cm ⁻² of Zn after several cycles.....	198
Figure S6.15 Rate performance of fresh and regenerated cathodes. (a) Fresh, (b) Fresh400, (c) Reg300, (d) Reg400, and (e) Reg500.....	199
Figure S6.16 Charge-discharge curves of (a) Fresh400 cathode, (b) Reg300, and (c) Reg500...	199

Figure S6.17 Cycling performance of Reg400. (a) Cycling profile at 0.1 Ag^{-1} , (b) Charge/discharge curves at different cycle showing change in the discharge platforms including both proton and Zn^{2+} insertion.....200

Figure S6.18 Electrochemical performance of commercial anode (84 mg cm^{-2}) and regenerated cathode (4.6 mg cm^{-2}) with a N/P of 74 for rechargeable full cells. (a, d) charge-discharge curves, (b, e) rate performance, and (c, f) cycling performance. The capacity is based on (a-c) mass (gravimetric capacity) and (d-f) area (areal capacity).....201

Figure S6.19 Electrochemical performance of commercial anode (84 mg cm^{-2}) and cathode (9.3 mg cm^{-2}) with a N/P of 37 for rechargeable full cells. (a, d) charge-discharge curves, (b, e) rate performance, and (c, f) cycling performance. The capacity is based on (a-c) mass (gravimetric capacity) and (d-f) area (areal capacity).....201

Figure S6.20 Electrochemical performance of regenerated anode (10.8 mg cm^{-2}) and cathode (5.4 mg cm^{-2}) with a N/P of 8.2 for rechargeable full cells. (a, d) charge-discharge curves, (b, e) rate performance, and (c, f) cycling performance. The capacity is based on (a-c) mass (gravimetric capacity) and (d-f) area (areal capacity).....202

Figure S6.21 Electrochemical performance of regenerated anode (8.7 mg cm^{-2}) and cathode (9.3 mg cm^{-2}) with a N/P of 3.8 for rechargeable full cells. (a, d) charge-discharge curves, (b, e) rate performance, and (c, f) cycling performance. The capacity is based on (a-c) mass (gravimetric capacity) and (d-f) area (areal capacity).....202

Figure S6.22 Characterization of anodes after cycling. (a) XRD patterns and (b-f) SEM images of (b, c) commercial Zn and (d-f) regenerated Zn anode.....203

Figure S6.23 Characterization of high-loading cathode in the regenerated full cell after cycling. (a) XRD patterns and (b-d) SEM images.....203

Figure 7.1 Summary of research projects about electrode and electrolyte engineering towards practical zinc batteries and capacitors.....208

Chapter 1 Introduction

1.1 Research Background

The increasing energy demand and environmental issues have pushed forward the replacement of fossil fuels with renewable energy resources including solar and wind energy as well as their conversion and storage systems such as solar cells and nanogenerators for energy conversion, batteries and supercapacitors for energy storage.¹⁻³ Supercapacitors work through the charge accumulation at interfaces between electrodes and electrolyte in which rapid surface charge(ions) adsorption/desorption leads to high power density while batteries rely on redox reactions and diffusion-controlled ion transport, often possessing high energy densities but low power densities due to slow kinetics.¹ In general, supercapacitors can be categorized into electrical double layer capacitors (EDLCs) and pseudocapacitors whereas commercial batteries can be categorized into primary batteries including alkaline batteries, lithium metal batteries, and Zn-air batteries, as well as rechargeable batteries, such as lead-acid, nickel–metal hydride, and lithium ion batteries (LIBs).

Among above-mentioned energy storage systems, LIBs have dominated the world battery market thanks to high energy density ($>240 \text{ Wh kg}^{-1}$), long shelf life, and light weight, and thus been widely used in portable electronics, electric vehicles, and communication systems.⁴ However, LIBs are not suitable for large-scale and stationary energy storage, particularly smart grids, because of their high cost, low power density, safety problems and environmental issues. These demerits are caused by the high price of electrode materials (e.g., Li salt in electrolyte, cobalt in cathode) and manufacturing conditions (moisture-free and O_2 -free environment), and also by the use of toxic and flammable organic electrolytes with low ionic conductivity.⁴ Despite efforts on developing solid-state electrolytes and cobalt-free cathodes to mitigate LIB disadvantages, increasing attention has been

paid to the exploration of other promising energy storage systems, such as redox flow batteries, rechargeable metal-air batteries, and aqueous metal ion batteries (such as Na/K/Ca/Zn/Mg/Al ions). Recently, aqueous zinc-based energy storage devices have garnered tremendous attention as promising candidate for smart grids and other stationary applications owing to merits from zinc metal.^{5, 6} First, Zn is earth abundant, low-cost, chemically stable in O₂- and moisture-containing environment, and highly safe to be used in atmospheric condition. Second, Zn has a suitable electrochemical potential (-0.763 V vs. standard hydrogen electrode, SHE) as well as air/water compatibility. Third, Zn possesses a high theoretical capacity (820 mAh/g and 5855 mAh/cm³), promising for high-energy devices. However, the reversibility of zinc metal electrodes is challenged with dendritic growth, low Coulombic efficiency, hydrogen evolution, and metal corrosion in both acidic and alkaline electrolyte. On the other hand, there is still lack of suitable cathode materials that can achieve high working potential, large capacity, and long life for zinc batteries or capacitors mainly due to materials dissolution and structural destruction during operation. Overall, aqueous zinc batteries/capacitors need to meet following prerequisites for practical applications: limited zinc metal, high-loading cathodes, low negative-to-positive (N/P) ratios, lean electrolyte, and wide-temperature operation.^{7, 8} Unfortunately, most reports do not meet these prerequisites and hence aqueous zinc batteries/capacitors are far from broad applications.

1.2 Research Objectives

Despite the research progress on rechargeable zinc ion batteries and capacitors, there remains research gaps and challenges that await to be addressed, especially with respect to cell-level energy densities and cycle life. For example, few reports test their cells under practical conditions as mentioned earlier. The use of excessive amount of zinc, low-loading cathodes, and flooded electrolyte will dramatically decrease cell-level energy/power densities. The first goal of my work is to develop high-loading

cathode materials for zinc batteries/capacitors using low-cost and earth-abundant materials. High-loading cathodes are difficult to maintain high performance as low-loading electrodes due to poor ionic/electronic conductivity and mechanical instability at high thickness. The second and most important goal of my work is to develop highly reversible anodes that work at limited amount and low N/P ratios. There are mainly four routes to obtain limited anode materials, including deposited zinc on host/substrate, zinc-free anodes, zinc powders, ultrathin zinc foils. However, it is still challenging to achieve high reversibility in all these cases.

1.3 Thesis Structure

The structure of this thesis is organized as follows:

Chapter 1 introduces the research background of aqueous energy storage devices and Zn-based batteries/capacitors.

Chapter 2 comprehensively reviews recent research progress on electrode engineering (Zn metal anode, Zn-free anode, Mn-based cathode, capacitive cathode), storage mechanism, and electrolyte engineering in zinc batteries/capacitors to improve device performance and understand underlying mechanism.

Chapter 3 starts from a commercial activated carbon cathode and systematically studies the impact of binder and electrolyte on the performance of zinc metal capacitors. The optimized capacitor achieves high-loading cathode, high-rate, long-life, and wide-temperature performance under the condition of excessive Zn metal and high N/P ratios. This work lays the foundation for following works.

Chapter 4 demonstrates one way of making reversible Zn anode——construction of 3D microflower-shaped carbon for efficiently hosting Zn plating/stripping to achieve limited use of Zn metal and low N/P ratio in both zinc metal batteries (Zn-MnO₂, Zn-iodine) and capacitors. However, cycle life of these devices needs to be further improved.

Chapter 5 presents an ultrafast, ultra-stable and ultrahigh-loading Zn-free polymer anode that enables 100 Ag⁻¹ rate, 1 million cycles, and 50 mg cm⁻² loading in half cells as well as unprecedented cycle life and power densities in full cells including both zinc ion batteries and capacitors.

Chapter 6 shows the making of a reversible zinc powder anode from upcycling of spent alkaline battery electrodes. Meanwhile, cathode has also been regenerated to couple with limited Zn powder to achieve high-loading cathodes and low N/P ratios in upcycled full cells.

Chapter 7 summarizes main results and findings achieved in thesis projects and gives perspectives on future research that could further improve the cell-level performance of Zn batteries and capacitors.

Chapter 2 Literature Review

Aqueous zinc-based energy storage devices including zinc-based batteries and supercapacitors will be firstly summarized, as well as the discussion on their working mechanisms and existing problems. Next, the research progress on anode, cathode, and electrolyte in these energy devices will be discussed in detail with focus on strategies to suppress Zn dendrites and develop Zn-metal-free anodes, Mn-based cathodes with different Zn^{2+} storage mechanism, hierarchical porous carbons fabrication as well as electrolyte engineering to enhanced performance.

2.1 Zinc-based Energy Storage Devices

Zn-based energy storage devices can be dated back to late 19th century when the first battery, voltaic pile was invented.⁹ Since then, a great many Zn-based energy devices have been developed including alkaline primary batteries (e.g., alkaline Zn-MnO₂, Zn-Ni, Zn-Ag, and Zn-air), Zn-based redox flow batteries (e.g., Zn-Br/I, Zn-V, and Zn-Ce), rechargeable Zn-ion batteries (e.g., Zn-MnO₂, Zn-V₂O₅, and Zn-Organics), and Zn ion hybrid supercapacitors (e.g., Zn-AC) in which the milestone for the development of these energy devices are shown in **Figure 2.1A**. Here, focus will be paid on rechargeable zinc batteries and capacitors in this report.

Zinc Metal Batteries and Zinc Ion Batteries. Strictly speaking, most of reported Zn batteries should be called as Zn metal batteries (ZMBs) due to the use of Zn metal as anode while those batteries based on Zn-metal-free anode will be called as Zn ion batteries (ZIBs) in this thesis.^{6, 10} This difference is just like that between lithium metal batteries (LMBs) and LIBs. Device structures for ZMBs and ZIBs are illustrated in **Figure 2.1B** and **Figure 2.1C**, respectively. They both are composed of anode (Zn metal for ZMBs, Zn-metal-free anodes for ZIBs), cathode (e.g. MnO₂), electrolyte (e.g. ZnSO₄ in water), separator (e.g., glassy fiber membrane), and current collectors (e.g., carbon paper, stainless steel mesh, and Ti foil). The working mechanism of ZMBs is similar to that of LMBs whereas ZIBs

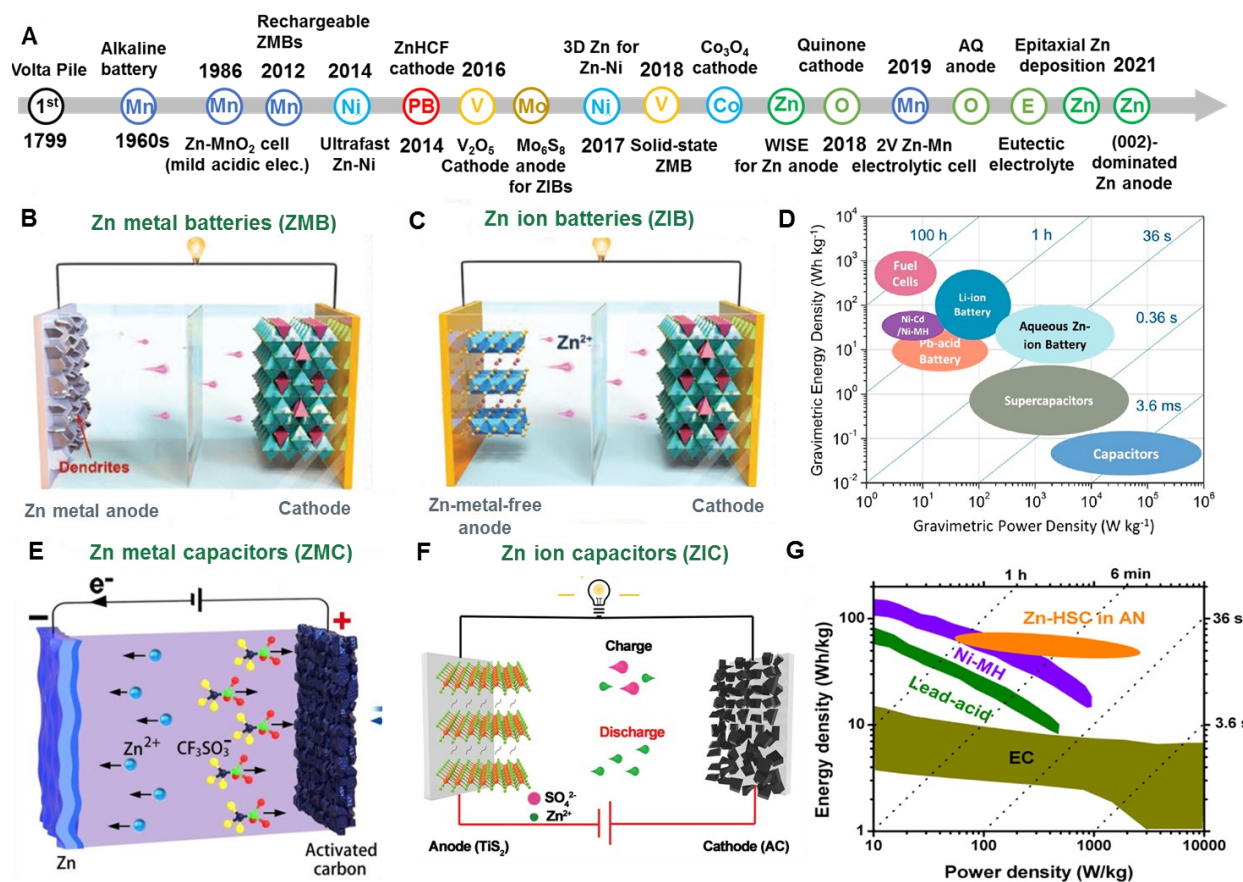


Figure 2.1 Zinc-based Energy Storage Devices. (A) Milestones for Zn-based energy storage devices, Schemes illustrating (B) ZMB with Zn metal anode and intercalative cathode, (C) ZIB with intercalative anode and cathode, (E) ZMC with Zn metal anode and intercalative cathode, and (F) ZIC with intercalative anode and cathode, Ragone plots of (D) Zn batteries and (G) Zn capacitors. Reprinted with permission from Ref. [6, 13, 14, 262]. Copyright © 2020, John Wiley and Sons. Copyright © 2020, American Chemical Society. Copyright © 2018, Elsevier.

is similar to that of LIBs. During ZMBs discharging (or charging) process, Zn²⁺ will strip from (or plate onto) the Zn metal and interact with the cathode material. As regards ZIBs, Zn²⁺ will shuttle back and forth between anodes and cathodes, which is why they are also called as rocking-chair type ZIBs. Of note, these are general mechanisms, but the real mechanism can be very complicated, which will be elaborated in [Section 2.3.2](#). Ragone plot (plot of specific energy versus specific power) in

Figure 2.1D compares the energy and power densities of Zn batteries with existing energy storage systems.⁶ In contrast to LIBs with low power and supercapacitors with low energy, ZIBs combine high gravimetric energy and power densities thanks to fast reaction kinetics and open frameworks of cathode materials, particularly vanadium-based oxides.⁶ Noteworthy is that energy and power densities data are collected from research papers mostly based on cathode materials with excessive Zn anodes while in actual commercial devices, lower values may be obtained.

Zn Metal Capacitors and Zinc Ion Capacitors. Based on the use of Zn metal or Zn-metal-free anode, Zn ion hybrid supercapacitors can be divided into Zn metal capacitors (ZMCs) and Zn ion capacitors (ZICs).^{11, 12} Device structures for Zn-based capacitors are illustrated in **Figure 2.1E** for ZMCs and **Figure 2.1F** for ZICs. The components of Zn-based capacitors are similar to that of Zn-based batteries except that Zn capacitors have capacitive-type cathode materials, typically porous carbon with high surface area.¹² Different from Zn batteries, the working mechanism for Zn capacitors relies on the simultaneous anion adsorption/desorption on the cathode and Zn²⁺ insertion/desertion onto the anode for ZICs or Zn metal plating/stripping for ZMCs.¹³ Overall, Zn capacitors are located at the Ragone plot (**Figure 2.1G**) with higher energy than EDLCs and higher power than aqueous lead-acid and Ni-MH batteries.

Despite promising performances, Zn-based batteries and capacitors are generally faced with several challenges.^{6, 10, 13, 14} First for anode, Zn metal corrosion and dendrite growth can take place in commonly used mild acidic medium accompanied by side reactions from water reduction producing hydrogen gas, shortening battery lifespan, which necessities the development of Zn-metal-free anode. Meanwhile, currently developed Zn-metal-free anodes exhibit low specific capacity which jeopardize the energy density of corresponding batteries or capacitors. Second for cathode in batteries, active materials dissolution can cause fast capacity decay and limit cycle life while for cathode in capacitors,

very limited capacity is achieved and thus lower energy density in Zn capacitors than their batteries cousin; Third for electrolyte, narrow voltage window of water decomposition in aqueous Zn energy devices limit the energy density compared with organic counterparts. Developing concentrated electrolyte can alleviate the issue but increase the cost.

2.2 Anode Materials

2.2.1 Zinc metal and its electrochemistry

In contrast to the reactive Li and Na metals, Zn is quite compatible with water. Combined with advantages of high capacity, suitable potential, low cost, and rich abundance, Zn is a promising anode for aqueous batteries. However, the further application of Zn metal anode in rechargeable aqueous batteries is challenged with the dendrite growth, low CE, hydrogen evolution, and metal corrosion, as a result of the intrinsic electrochemistry of Zn in different pH environment.^{15, 16} Under discharge, the first step for Zn metal is oxidization to Zn^{2+} and electrons are moved to the cathode. In alkaline media, Zn^{2+} coordinate with hydroxide ions forming $Zn(OH)_4^{2-}$ which once reaches solubility limit will decompose into ZnO, resulting in loss of active Zn parts, formation of dendrites and/or passivation. In mildly acidic electrolyte (pH 4–6), these side reactions can be suppressed, and the reversible Zn dissolution/deposition reaction ($Zn \rightleftharpoons Zn^{2+} + 2e^-$) take places to some extent. That is why mildly acidic electrolyte are used in most of rechargeable Zn batteries. However, lower pH also means that water is easier to be reduced to hydrogen, according to Pourbaix diagram (**Figure 2.2A**). Because of the thermodynamic favorability of hydrogen evolution reaction (HER) and its large kinetic overpotentials on Zn surface, HER and Zn deposition competes during battery discharge, which depends on the applied current. Besides side reaction, acidic electrolyte is also corrosive to Zn metal, leading to nonuniform Zn deposition layers and dendritic growth.

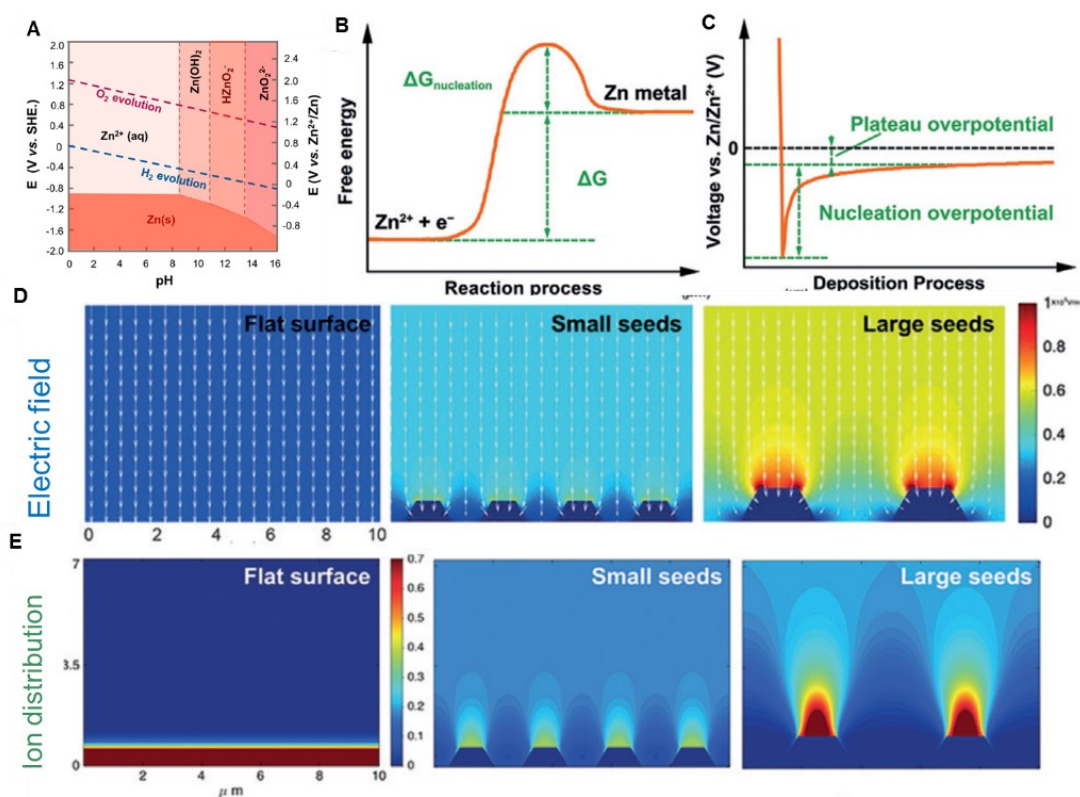


Figure 2.2 Zinc metal and its electrochemistry. (A) Pourbaix diagram of a Zn/H₂O system when taking HER overpotential into consideration. (B) The free energy diagram of the zinc nucleation process. (C) A typical voltage profile for zinc deposition. Simulation of (D) electric field and (E) ion distribution under different nucleation conditions. Reprinted with permission from Ref. [6, 16, 17]. Copyright © 2020, American Chemical Society. Copyright © 2019, 2020, John Wiley and Sons.

To solve these issues of Zn metal anodes, it is necessary to comprehend the Zn deposition process. The deposition starts with nucleation followed by the Zn^{2+} transport to these nucleation sites driven by electric field in which the free-energy diagram (**Figure 2.2B**) reveals an energy barrier for nucleus formation.¹⁶ **Figure 2.2C** shows the typical voltage profile for Zn deposition process with two obvious overpotentials: nucleation overpotential and plateau overpotential in which the former one is defined as the difference between lowest potential and following stable potential while the latter one is the absolute value of stable potential. The smaller these overpotentials, the lower resistance for Zn

nucleation and growth, meaning a higher-quality Zn deposition process with less energy loss. The Zn nucleation process is crucial for subsequent growth. As more Zn^{2+} ions reduce to Zn and deposit onto nucleation sites, Zn grows into different forms under different conditions which is controlled by the diffusion process and affected by the electric field and ion distribution. As shown in the finite element simulation (**Figure 2.2D, E**), protuberate sites formed at the initial nucleation could significantly alter the electric field and ion distribution in the system.¹⁷ As electric field and ion concentration tend to accumulate at these protuberances, Zn seeds could easily grow into dendrites. On the contrary, a flat surface with homogenous nucleation sites benefits uniform zinc growth. The simulation results indicate that construction of structures that can achieve uniform distribution of ion transport and electric field is crucial to develop dendrite-free Zn electrode.

2.2.2 Dendrite-free Zn metal construction

Homogenizing the interfacial electric field and ion distribution are crucial to achieve reversible Zn plating/stripping. Accordingly, various approaches have been developed to realize dendrite-free Zn anode including surface modification, host construction, and structural design.

Surface modification. Cui et al applied a polyamide (PA) coating layer to modify the Zn-electrolyte interface and increase the nucleation barrier.¹⁸ As shown in **Figure 2.3A**, it is difficult for pristine Zn to retain thermodynamic stability in neutral or mildly acidic electrolyte because of the corrosion triggered by O_2 and H_2O , side reaction byproducts from water decomposition and later dendritic growth under continuous plating/stripping (**Figure 2.3B**). These potential problems can be solved by engineering the functional PA interphase with unique H-bonding network and strong coordination interaction, harmonizing the migration of Zn^{2+} to render uniform nucleation and suppress water-related byproducts (**Figure 2.3C**). Besides polymer coating, carbon materials including graphene,¹⁹ graphene oxide,²⁰ carbon nanotube,²¹ and porous carbons as well as carbon-based hybrids²² are also

promising candidates to efficiently modify the Zn-electrolyte interface.^{23, 24} With high conductivity and rapid ion transport pathways, these materials can homogenize electric field and enable smooth Zn deposition. Apart from conductive materials, insulating materials with porous channels, such as

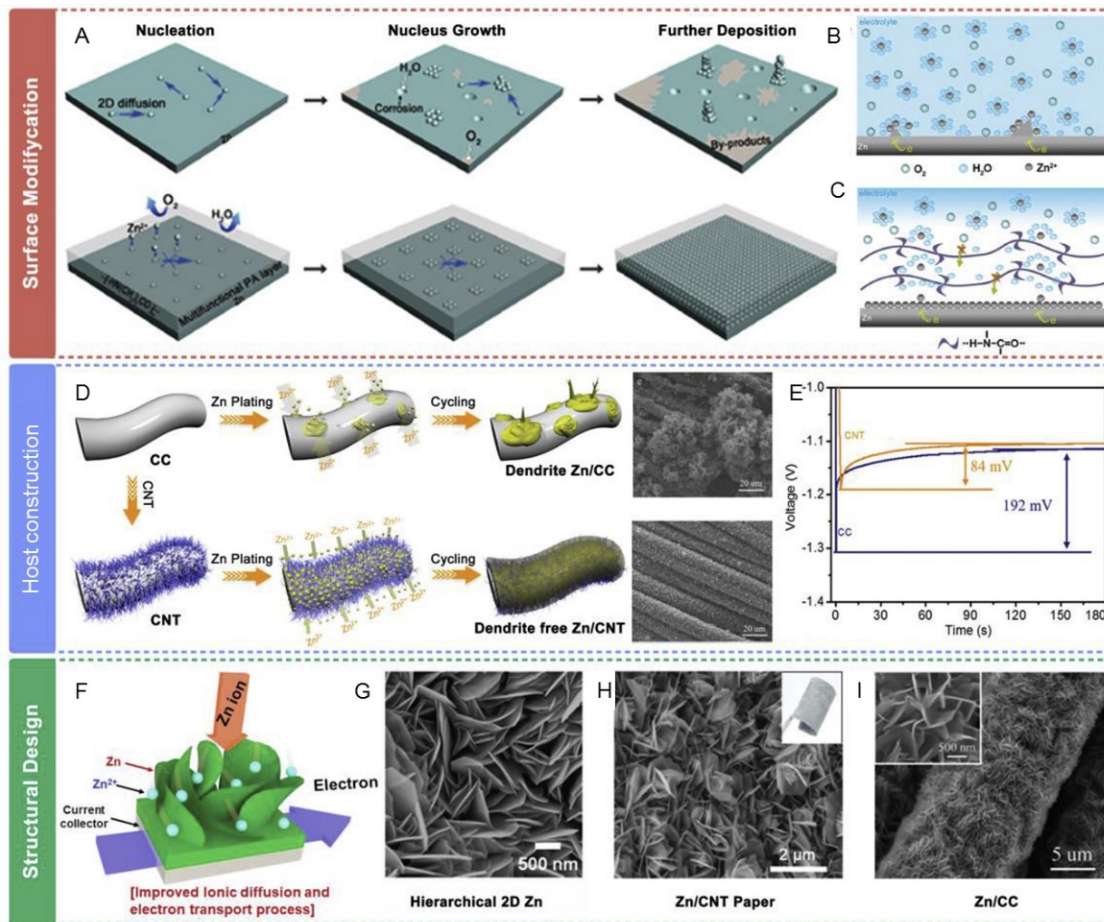


Figure 2.3 Construction of Dendrite-free Zn Anodes. (A-C) Surface modification. (A) Scheme showing Zn deposition on (B) bare Zn electrode and (C) PA coated Zn. (D-E) Host construction. (D) Zn plating/stripping on carbon cloth (CC) or carbon nanotube (CNT)/CC electrode and (E) corresponding nucleation overpotential on bare CC or CNT/CC. (F-I) Structural design. (F) Illustration and (G) morphology of hierarchical Zn. SEM images for (H) Zn/CNT paper and (I) Zn/CC. Reprinted with permission from Ref. [12]. Copyright © 2020, Elsevier.

calcium carbonate²⁵ and MOF materials²⁶ are also able to inhibit dendrite growth through oriented ions transport.

Host construction. Zheng *et al.* reported the hetero-epitaxial mechanism of Zn on graphene to inhibit Zn dendrites.²⁷ The graphene is coated on stainless steel to realize the reversible Zn plating/stripping through a crystallographic matching relation due to the low degrees of lattice mismatch within graphene and Zn. The resulting Zn anode manifests outstanding reversibility under long-life cycling even at a high current density of 40 mA cm⁻². Additionally, the construction of conductive substrate with enhanced surface area can reduce local current density and unify electric field distribution. For example, Lu *et al.* developed a CNT protected carbon cloth (CC) substrate as Zn host to achieve reversible metal plating/stripping (**Figure 2.3D**),²⁸ in which the 3D CNT substrate enriches active sites and reduces Zn nuclei size with smaller nucleation overpotential to enable dendrite-free Zn anodes (**Figure 2.3E**). This approach opens the avenue towards the rational design of 3D host materials.²⁹

Structural design. Aside from the interfacial regulation and host construction, designing suitable Zn electrode structure also enables dendrite-free plating. For example, Rolison *et al.* reported the 3D Zn sponge electrode capable of passivation-free and dendrite-suppressing cycling for long periods.³⁰ Following this work, it becomes a hot research topic to the construction of hierarchical Zn structure.¹⁶ Among different methods for hierarchical structure construction, electrodeposition is the most used due to its simple and facile feature. As a typical hierarchical structure, nanoarrays (**Figure 2.3F**) assembled by 2D nanosheets can simultaneously shorten ions diffusion pathways and expose electroactive surface area,³¹ leading to increased energy density and power density in Zn-based energy devices. Furthermore, by simply using various substrates and solutions with different concentration and compositions, a series of dendrite-free Zn anodes can be fabricated (**Figure 2.3G-I**), such as

Zn/CNT paper,³² Zn/CC,³³ and Zn/Cu,^{34, 35} to name a few. Alternatively, electrolyte modification is also an effective approach to suppress Zn dendrites, which will be discussed in Section 2.4 in detail.

2.2.3 Zn-metal-free anodes (chalcogenides, oxides, and organics)

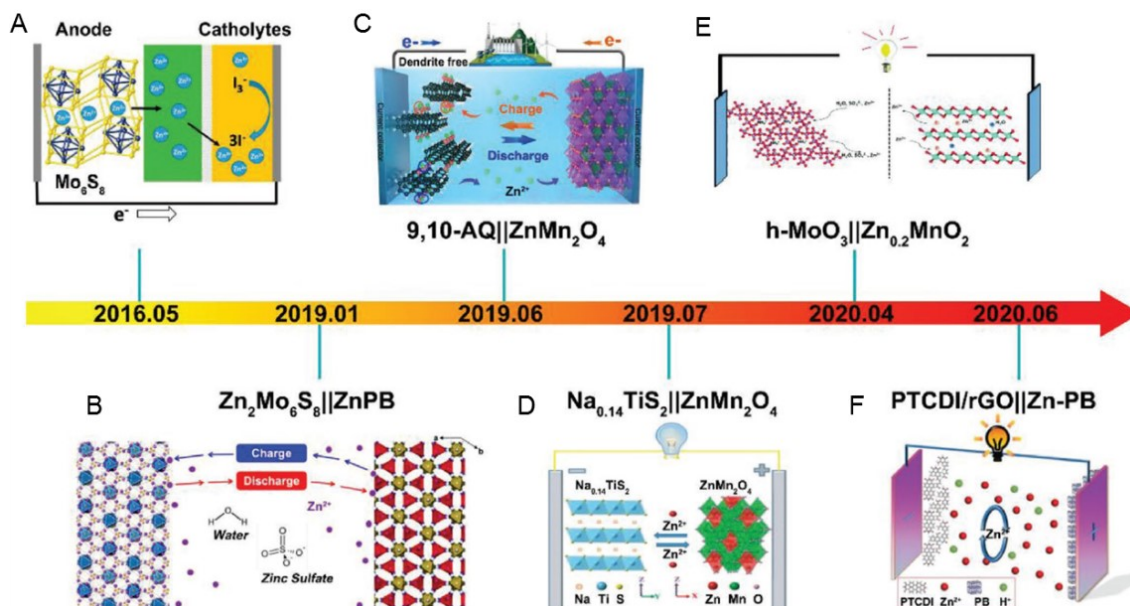


Figure 2.4 Zn-metal-free Anodes for ZIBs. The timeline showing the development of metal sulfides (Mo_6S_8 , $\text{Zn}_2\text{Mo}_6\text{S}_8$ and $\text{Na}_{0.14}\text{TiS}_2$), metal oxides (h-MoO_3), and organics (9,10-AQ and PTCDI/rGO) as Zn-free anodes for rocking-chair type ZIBs. Reprinted with permission from Ref. [14]. Copyright © 2020, John Wiley and Sons.

Aside from the construction of dendrite-free Zn metal anodes for ZMBs, an alternative strategy is the development of Zn-metal-free anodes for rocking-chair type ZIBs.¹⁴ Ideal Zn-metal-free anodes should have following characteristics: low discharge plateau relative to Zn^{2+}/Zn , high theoretical capacity, good electronic conductivity, robust structure, and electrochemical stability.¹⁴

Metal Chalcogenides. Gocke *et al.*³⁶ firstly discovered that Zn^{2+} could intercalate into Chevrel-type Mo_6S_8 under galvanostatic discharge in 2 m $\text{Zn}(\text{ClO}_4)_2/\text{CH}_3\text{CN}$ electrolyte with two potential plateau located at ~ 0.47 V and ~ 0.3 V, corresponding to the transformation into $\text{Zn}_x\text{Mo}_6\text{S}_8$ with $0 \leq x \leq 1$ and

$1 \leq x \leq 2$, respectively. These low discharge voltages of Mo_6S_8 render it promising Zn-free anodes for ZIBs. Later, Hong *et al.*³⁷ further studied structural changes and electrochemical features of Mo_6S_8 electrode in 0.1 M aqueous ZnSO_4 electrolyte in a three-electrode system. Two plateaus at 0.45~1.0 V and ~0.35 were detected in CV curves, indicating two-step (de)intercalation of Zn^{2+} into Mo_6S_8 , corresponding to the structural evolution from Mo_6S_8 to ZnMo_6S_8 and $\text{Zn}_2\text{Mo}_6\text{S}_8$, respectively, as revealed by the ex situ XRD. Galvanostatic charge/discharge (GCD) curves show that Mo_6S_8 electrode delivered an 88 mAh g^{-1} capacity at a low current density of 0.05C ($C=128 \text{ mA g}^{-1}$). Liu *et al.*³⁸ for the first time applied Mo_6S_8 as the anode in ZIB by coupling with polyiodide catholytes containing 1.5 M ZnI_2 and 0.2 M I_2 in which the I^-/I_3^- cathode couple displayed a redox potential around 1.299 V versus Zn^{2+}/Zn (**Figure 2.4A**). The full cell could achieve a 90% capacity retention after 350 cycles tested at 0.6 A g^{-1} . Likewise, another full cell was constructed based on $\text{Zn}_2\text{Mo}_6\text{S}_8$ anode and rhombohedral zinc Prussian blue analogue cathode in 0.1 M ZnSO_4 (**Figure 2.4B**),³⁹ which could deliver a working voltage as high as ~1.4 V and an energy density around 47 Wh kg^{-1} (based on both electrode active materials, N/P=1.2/1).

$\text{Na}_{0.14}\text{TiS}_2$ was also reported as a promising Zn-metal-free anode for aqueous “rocking-chair” ZIBs (**Figure 2.4D**).⁴⁰ In 2 M $\text{Zn}(\text{OTf})_2$ electrolyte, pristine TiS_2 presented a discharge potential around 0.3 V vs Zn^{2+}/Zn , a high capacity about 123 mAh g^{-1} along with a 20% capacity retention after 50 cycles due mainly to irreversible structural change and strong electrostatic repulsion from inserted Zn^{2+} in the host. Through discharging/charging in a sodium ion battery, Na^+ was inserted to TiS_2 to stabilize the structure and enhance the performance. The resulting $\text{Na}_{0.14}\text{TiS}_2$ delivered much longer cycle life with a high capacity retention (98% after 700 cycles at 0.2 A g^{-1} and 77% after 5000 cycles at 0.5 A g^{-1}), which can be attributed to the improved electronic conductivity, reduced overpotential, and decreased ion migration barriers compared with TiS_2 . Encouraged by this, a full cell based on

$\text{Na}_{0.14}\text{TiS}_2$ anode and ZnMn_2O_4 cathode was constructed, delivering 0.95 V output voltage, 105 mAh g^{-1} capacity, and 26% capacity loss after 100 cycles at 0.2 A g^{-1} , exceeding Zn-metal-based counterpart with low capacity and fast decay.

Wang *et al.*⁴¹ investigated the Zn^{2+} storage capability of VS_2 electrode and detected reversible redox voltages at 0.37/0.65 and 0.87/0.9 V along with stable cycle performance over 500 cycles, which renders VS_2 a potential Zn-metal free anode for “rocking-chair” ZIBs.

Metal Oxides. Kang *et al.*⁴² studied the Zn^{2+} storage behavior of $\alpha\text{-MoO}_3$ electrode and found three pairs of redox peaks ($\sim 0.4\text{--}0.95$ V) in the first cycle which disappeared in subsequent cycles. The low redox voltages endow $\alpha\text{-MoO}_3$ with potential for “rocking-chair” ZIBs anode but its fast decay indicates the irreversible phase transition in $\alpha\text{-MoO}_3$ during Zn^{2+} (de)intercalation, which awaits further improvement before it can be used as anode in full cells. Alternatively, Xue *et al.*⁴³ reported h- MoO_3 as an promising Zn-metal-free anode for “rocking-chair” ZIBs. According to half-cell tests in 1 M ZnSO_4 , h- MoO_3 electrode exhibits a low working voltage around 0.36 V relative to Zn^{2+}/Zn couple, a high capacity around 120 mAh g^{-1} , and long life over 100 cycles. The storage mechanism of h- MoO_3 was revealed to be very complicated, which involved the insertion/extraction of Zn^{2+} , H_2O , and SO_4^{2-} , as well as the reversible NH_4^+ exchange. Coupling h- MoO_3 anode with Zn^{2+} -intercalated MnO_2 ($\text{Zn}_{0.2}\text{MnO}_2$) cathode and 1 M ZnSO_4 electrolyte, a “rocking-chair” ZIB was assembled (**Figure 2.4E**) that can operate in the 0.2–1.9 V voltage window, showing high working voltages at 1.0/1.23 and 1.46/1.8 V, large energy density of 61 Wh kg^{-1} and negligible capacity loss over 1000 cycles. Besides MoO_3 , complex oxides such as molybdenum–vanadium oxide ($\text{Mo}_{2.5+y}\text{VO}_{9+z}$)^{44, 45} and Ti-substituted tungsten molybdenum oxide (Mo/Ti:WO_3 , MTWO)⁴⁶ may also be prospective candidates for ZIBs.

Organics. Organic materials have demonstrated great potential for various rechargeable metal-ion batteries including aqueous ZMBs.⁴⁷⁻⁵¹ With resource sustainability, environmentally friendliness, and molecular-scale structural diversity as well as finely-tunable capacity, working voltage, ionic conductivity, and solubility, organics, particularly, carbonyl-rich organics hold great potential for “rocking-chair” ZIBs.^{48, 52} For example, Yan *et al.*⁵³ investigated quinone (9,10-AQ) as anode and ZnMn₂O₄ as cathode, respectively, and then constructed a 9,10-AQ||ZnMn₂O₄ full cell (**Figure 2.4C**). In half cells, 9,10-AQ showed sharp redox peaks at 0.45/0.64 V with apparent voltage plateaus, a capacity of 146 mAh g⁻¹ with an 84.3% capacity retention after 200 cycles while ZnMn₂O₄ presented one anodic peak (1.61 V) and two cathodic peaks (1.4 and 1.21 V), a high capacity of 145 mAh g⁻¹ with nearly unity CE. Benefiting from suitable redox potentials, large capacity, and long cycle life, the 9,10-AQ||ZnMn₂O₄ ZIB delivered a 189.5 mAh g⁻¹ capacity with 94.4% retention after 500 cycles. Of note, no dendrites were observed in 9,10-AQ anode after cycling.

Liu *et al.*⁵⁴ prepared a carbon-based hybrid containing perylene-3,4,9,10-tetracarboxylic diimide (PTCDI) and reduced graphene oxide (PTCDI/rGO) to function as a Zn-free anode for ZIBs. Firstly, electronic structures, particularly, the lowest unoccupied molecular orbital (LUMO) associated with the discharge potential, of several molecules including chloranil (TCBQ), benzoquinone (PBQ), 9,10-AQ, 3,4,9,10-perylenetetracarboxylic dianhydride (PTCDA), PTCDI-O, and PTCDI were calculated to predict their feasibility as anode in ZIBs. Among them, PTCDI displays the highest LUMO level (-0.2247 eV) and thus is expected to show the lowest discharge potential, rendering it a potential anode for “rocking-chair” ZIBs. According to (dis)charge curves in half-cell tests, PTCDI/rGO electrode exhibited two voltage plateaus (0.38 and ~0.28 V) and reversible Zn²⁺ storage capability over 200 cycles. Coupled with a Zn-PB cathode, a PTCDI/rGO||Zn-PB full cell was constructed (**Figure 2.4F**), delivering a 0.95V output voltage and a 193 mAh g⁻¹ capacity (based on anode).

2.3 Cathode Materials

2.3.1 Cathodes for Zn-based batteries

Cathodes with high redox potentials, large capacity, and long lifespan are desirable to construct high-performance ZIBs and ZMBs. **Figure 2.5A** shows the brief history of cathodes development and different energy storage mechanisms.¹⁰ To date, widely studied cathode materials include manganese dioxides (MnO_2), Prussian blue analogues (PBA), vanadium-based compounds (e.g. VO_x and MVO_x , $\text{M}=\text{Na, Mg, Ca, Zn, Al, Cu, etc.}$), and organic materials.⁵⁵ In general, MnO_2 delivers a high theoretical capacity of 308 mAh g^{-1} and a discharge voltage of $\sim 1.35 \text{ V}$ but fast capacity decay due to Mn^{2+} dissolution.⁵⁶⁻⁶¹ PBAs manifest high voltage ($\sim 1.7\text{V}$) but limited capacity ($< 100 \text{ mAh g}^{-1}$)⁶²⁻⁶⁶ whereas VO_x exhibit high capacity exceeding 300 mAh g^{-1} and up to 500 mAh g^{-1} but low discharge voltage ($\sim 0.8 \text{ V}$).⁶⁷⁻⁷¹ Organics containing active functional groups (such as $\text{C}=\text{O}$ and $\text{C}=\text{N}$) can achieve high capacity (up to $\sim 300 \text{ mAh g}^{-1}$) and moderate discharge voltage ($\sim 1.0 \text{ V}$).^{72, 73} For example, Chen group⁷⁴ reported the ZMB performance of several quinone compounds in which the calix[4]quinone (C4Q) electrode manifested a flat voltage platform at 1 V , a high capacity of 335 mAh g^{-1} , an energy efficiency of 93% , and 87% capacity retention over 1000 cycles. Other cathode materials have also been investigated including molybdenum- or cobalt-containing compounds,⁷⁵⁻⁷⁷ polyanions,^{23, 78} polysulfide,^{79, 80} and graphite.⁸¹ **Figure 2.5B** illustrates typical specific energy density and power density for these cathode materials.

2.3.2 Storage mechanisms

The storage mechanism for different cathodes in Zn batteries is complicated. For MnO_2 cathode, Zn^{2+} ion insertion, proton insertion or conversion reaction, Proton/ Zn^{2+} ion co-insertion, and deposition/dissolution mechanisms have been reported. For V-based compounds, Zn^{2+} ion insertion, proton insertion, proton/ Zn^{2+} ion co-insertion, and anionic redox mechanisms are proposed. For

organics, Zn^{2+} ion insertion, proton insertion, and proton/ Zn^{2+} ion co-storage mechanisms are also presented.¹⁰ Here, taking the MnO_2 cathode as an example, mechanisms will be explained in detail.

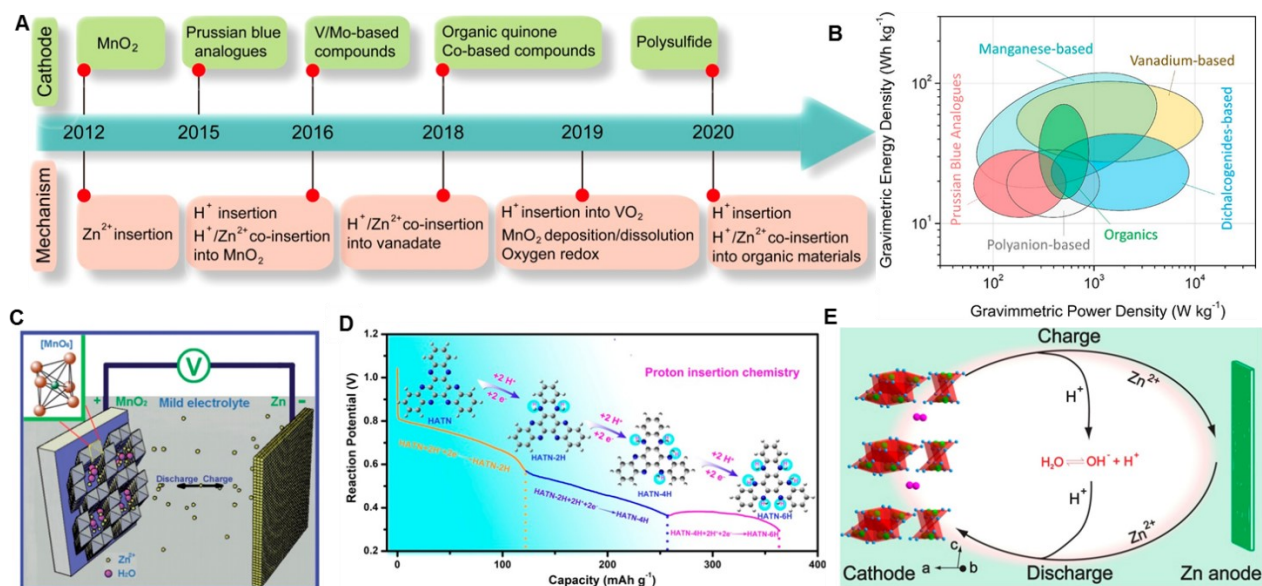


Figure 2.5 Cathode Materials and Storage Mechanisms in Zn Batteries. (A) Brief development history of the cathode materials and energy storage mechanism of aqueous rechargeable ZMBs. (B) Ragone plots based on various Zn battery cathode materials. (C-E) Different energy storage mechanisms for aqueous Zn batteries with different cathode materials. (C) Zn^{2+} insertion/extraction into/from MnO_2 . (D) H^+ insertion chemistry in diquinoxalino [2,3-a:2',3'-c] phenazine (HATN). (E) $\text{H}^+/\text{Zn}^{2+}$ coinsertion/extraction into/from $\text{NaV}_3\text{O}_8 \cdot 1.5\text{H}_2\text{O}$. Reprinted with permission from Ref. [6, 8, 82, 88]. Copyright © 2020, American Chemical Society. Copyright © 2012, 2020, John Wiley and Sons.

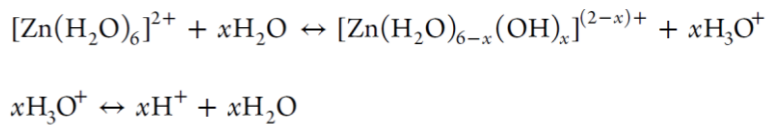
Zn^{2+} ion insertion mechanism. This is the mostly reported reaction mechanism involved in Zn batteries (Figure 2.5C) in which a $\text{Zn}/\alpha\text{-MnO}_2$ cell with aqueous ZnSO_4 electrolyte was firstly proposed to follow the following reaction:⁸²



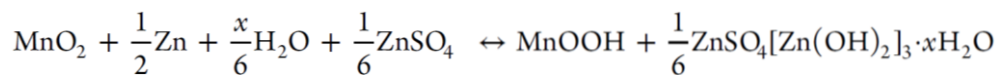
Later, this mechanism was also reported in other MnO_2 with different phases (β -, γ -, T-, δ -, and λ -types).^{57, 83-86} During the Zn^{2+} ion insertion process, complex phase transformation can take place in

MnO₂, e.g., in the Zn- γ -MnO₂ battery.⁸³ At the initial stage of Zn²⁺ intercalation, tunnel-type γ -MnO₂ partially transformed to spinel ZnMn₂O₄, and a subsequent insertion of Zn²⁺ converts residual γ -MnO₂ to tunnel γ -Zn_xMnO₂. Under a further Zn²⁺ intercalation, tunnel γ -Zn_xMnO₂ could be partially altered to layered L-Zn_yMnO₂. As such, three phases coexisted after complete Zn ion insertion, including spinel ZnMn₂O₄, tunnel γ -Zn_xMnO₂, and layered L-Zn_yMnO₂.

Proton insertion or conversion mechanism. Besides Zn²⁺, proton (H⁺ ions) exists in mildly acidic electrolyte, which is donated from Zn²⁺ ions, can also insert into electrode materials. Following reactions describe the proton generation process:



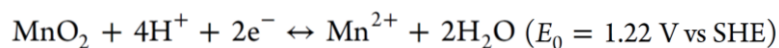
Compared with Zn²⁺ ion, proton is smaller in both size and weight and thus its insertion into host material may precede that of the Zn²⁺ ion. As in an example, the reaction between proton and α -MnO₂ in ZnSO₄ electrolyte has been proposed.⁸⁷ Despite the formation of ZnSO₄[Zn(OH)₂]₃·xH₂O from water decomposition during MnO₂ electrode discharge, the chemical conversion reaction between proton and α -MnO₂ gives rise to MnOOH. The following describes the mechanism:



In contrast to other ion insertion mechanism with cathode facing structural change and phase transition leading to fast capacity decay, chemical conversion mechanism in α -MnO₂ affords long lifespan up to 5000 cycles with a high capacity retention of 92% due to the occurrence of simple reaction from MnO₂ to MnOOH. The proton (de)insertion behavior has also been reported in organics, such as Zn/HATN battery in a ZnSO₄ electrolyte (**Figure 2.5D**).⁸⁸

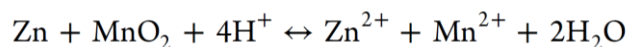
Proton/Zn²⁺ co-insertion mechanism. Apart from Zn²⁺ ion insertion mechanism and proton insertion mechanism, the proton/Zn²⁺ co-insertion mechanism has also been proposed in cathodes materials including MnO₂, V-based compounds (**Figure 2.5E**), and organics in which α -MnO₂ was firstly discovered following the proton/Zn²⁺ co-insertion mechanism in the ZMB using aqueous ZnSO₄/ MnSO₄ electrolyte.⁵⁶ From the battery voltage-capacity curves, two discharge plateaus are detected and it is found that an increase in (dis)charging rates lead to negligible change in the voltage and capacity of the first discharge plateaus but fast decline in those of the second discharge plateaus, apparently demonstrating the faster reaction kinetics of the first plateau than that of the second one. Given that proton has a smaller size than that of Zn²⁺ ion, authors proposed that the first discharge plateau belongs to proton insertion, while the second one associated with Zn²⁺ ion insertion. Control experiments of ZMBs in the MnSO₄ electrolyte show only the first discharge plateau, corresponding to the proton insertion but no sign of Zn²⁺ ion insertion was detected. Above results confirm the co-insertion from proton and Zn²⁺ ions and that proton insertion mechanism happens at the first discharge plateau while Zn²⁺ ion insertion in the second plateau in the Zn/ α -MnO₂ system.

Deposition/dissolution mechanism. In acidic electrolyte, MnO₂ electrode can follow the deposition/dissolution mechanism as described in the following:



Two electron transfers are involved in this redox reaction, giving a two-fold theoretical capacity (616 mAh g⁻¹) compared with that (308 mAh g⁻¹) of the Mn⁴⁺/Mn³⁺ redox process involving one electron transfer commonly found in the MnO₂ cathode. Besides higher capacity, a higher potential around 1.22 V vs SHE can also be presented in MnO₂/Mn²⁺ redox pair, leading to a 1.98 V working voltage when matching with the Zn anode (Zn²⁺/Zn, -0.76 V vs SHE), which is much higher than ~1.35 V voltage in traditional Zn/MnO₂ batteries. This novel electrolytic Zn/MnO₂ system was designed by

Chao *et al.* using H₂SO₄/ZnSO₄/MnSO₄ electrolyte, Zn anode, and CC cathode.⁸⁹ During charge process, Mn²⁺ ions are oxidized into MnO₂ which deposits onto CC cathode while under discharge, MnO₂ is reduced to Mn²⁺ and dissolves into the electrolyte following the reaction below:



The electrolytic Zn/MnO₂ batteries can afford a 570 mAh g⁻¹ capacity and a 1.95 V voltage. Furthermore, the redox pair of MnO₂/Mn²⁺ (1.22 V vs SHE) can also be coupled with Zn(OH)₄²⁻/Zn (-1.2 V vs SHE), amounting to a high output voltage up to 2.4 V. This system was achieved by Zhong *et al.* using two chambers containing alkaline electrolyte (KOH) for the anode and an acidic electrolyte (H₂SO₄/MnSO₄) for the cathode separated by a neutral electrolyte (K₂SO₄) sandwiched between two ion-selective membranes.⁹⁰ During discharge, OH⁻ and H⁺ ions are consumed in the Zn side and MnO₂ side, respectively, and the corresponding counterions (K⁺ and SO₄²⁻ ions) diffuse into the neutral electrolyte through the cation exchange membrane and anion exchange membrane, respectively. Later, Liu *et al.* further constructed Zn-based cells based on redox reactions of MnO₂/Mn²⁺ and Zn(OH)₄²⁻/Zn by using acid-alkaline dual electrolyte and ion-selective membranes.⁹¹ However, cell-level energy densities of these electrolytic cells are still low due to the use of flooded electrolyte and bulky container.

2.3.3 Hierarchical porous carbons for Zn-based capacitors

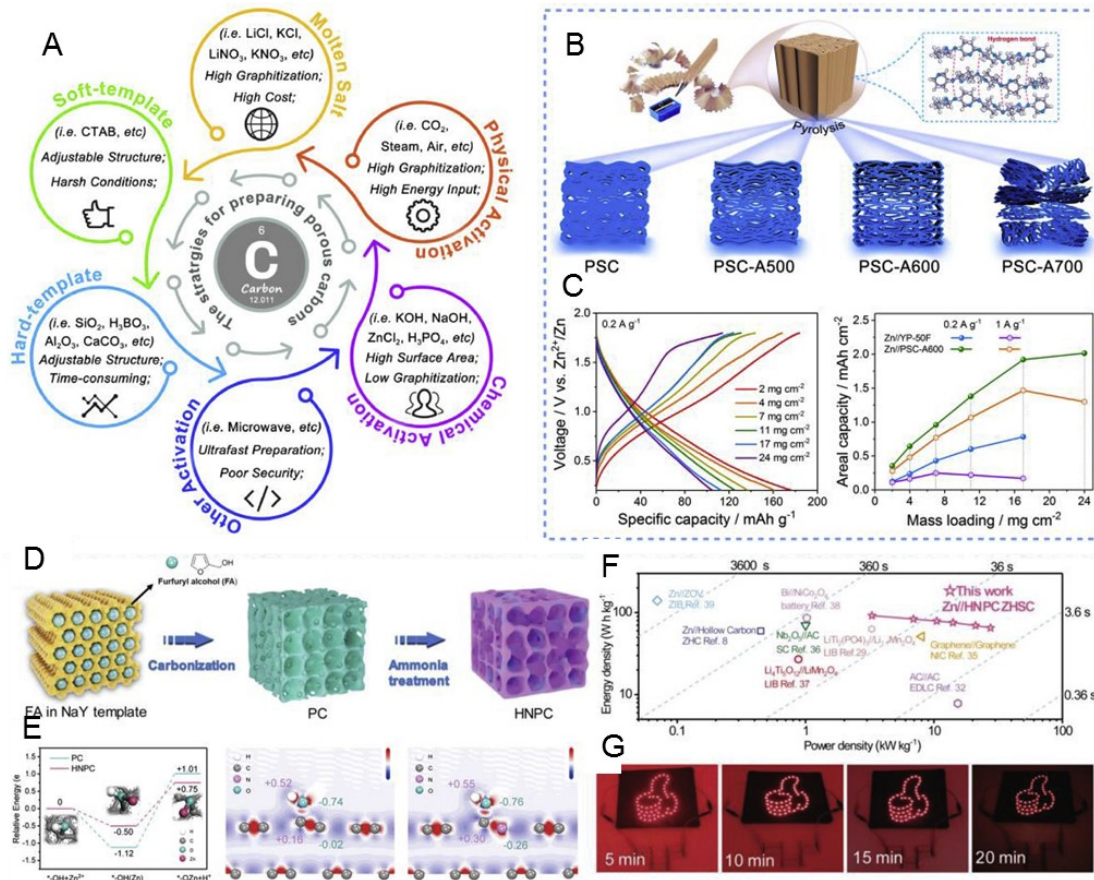


Figure 2.6 Preparation of Hierarchical Porous Carbon Cathodes. (A) Strategies for fabricating HPCs. (B) Schematic illustration for PSC samples preparation and corresponding (C) electrochemical performances at different mass loading. (D) Scheme showing the synthetic process of HNPC. (E) DFT calculation of binding energy between Zn and heteroatoms dopants. (F) Ragone plot and (G) the LED board powered by ZIC. Reprinted with permission from Ref. [12, 92, 97]. Copyright © 2019, John Wiley and Sons. Copyright © 2020, Elsevier.

In most cases, Zn capacitor cathode materials are based on hierarchical porous carbons (HPCs). **Figure 2.6A** illustrates the engineering strategy of hierarchical porous carbon (HPCs) with specific

surface area, porous structure, and morphology through modulating parameters like temperature, time, and chemicals in the synthetic protocol.^{11, 12} HPCs are typically prepared by activation approaches and/or template-assisted synthesis. The former method relies on activation agents (such as water vapor, ammonia gas, CO₂, KOH, and ZnCl₂) whereas the latter one involves the use of hard or soft templates (such as silica, alumina, calcium carbonate, and surfactants). Other emerging approaches including molten salt pyrolysis and microwave-activation have also been developed to make HPCs but with disadvantages that the molten salt pyrolysis requires the use of a large amount of inorganic salts and microwave-activation method arouses safety concerns. As such, the templated and activation methods are commonly used to make HPCs thanks to their tunable architecture and easy operation.

Activated carbon (AC). Kang *et al.*⁹² applied a commercial AC material, YP-50F, into Zn capacitors, delivering a high capacitance and elucidated the working mechanism involving the reversible ion adsorption/desorption on cathode and Zn plating/stripping on anode. Zhang *et al.*⁹³ utilized pencil shaving derived porous carbon (PSC) as the capacitor cathode (**Figure 2.6B**). After activation in KOH at 600 °C, the resultant PSC-A600 shows highly porous structure which could benefit matter/ions kinetics and energy storage. Accordingly, even at a high loading of 24 mg cm⁻², the PSC-A600 electrode could deliver a 100 mAhg⁻¹ capacity at 0.2 Ag⁻¹ (**Figure 2.6C**). Furthermore, an anti-freezing hydrogel electrolyte was employed to enable low-temperature applications of the PSC-A600-based Zn capacitor, which demonstrated a high capacitance retention of 80.7% and 63.9% at 0 °C and -15 °C, respectively, compared with that of 20 °C tested at 1 A g⁻¹. Alternatively, Liu *et al.*⁹⁴ fabricated the HPC through the one-step pyrolysis of chitosan, iron nitrate, and potassium bicarbonate in which chitosan, ferric salt, potassium salt plays the role of carbon source, catalyst, and activation agents, respectively. As-made HPC displayed a micropore-dominated porous structure along with some mesopores as well as rich N-dopants and hierarchical architecture. The corresponding ZMC

device delivered a high capacity (136.8 mAhg^{-1} at 0.1 A g^{-1}) and a long cycle life (over 5000 cycles). Besides exploring high-performance materials for Zn-based capacitors, device architecture including fiber-shaped and in-plane miniaturized structures have received tremendous research interest too. For instance, Zhang *et al.*⁹⁵ demonstrated a Zn-based micro-supercapacitor with AC and electrodeposited Zn as cathode and anode, respectively, realizing a high capacitance of 1297 mF cm^{-2} (259.4 F g^{-1}) at 0.16 mA cm^{-2} (0.05 A g^{-1}), corresponding to a high energy density of $115.4 \text{ } \mu\text{Wh cm}^{-2}$ along with a remarkable cyclability with 100% capacitance retention over 10000 cycles.

Templated carbon. For templated synthesis of HPCs, the structure of templates determines that of porous carbons. H_3BO_3 can be processed into lamellar crystals by recrystallization and its decomposition product, B_2O_3 can be easily recycled in water enabling sustainable and low-cost template for 2D materials preparation. By employing H_3BO_3 as the template, Lu *et al.*⁹⁶ fabricated 2D layered porous carbon (LDC) derived from acrylonitrile copolymer. Compared with commercial AC and rGO, the LDC realized the highest capacity and superb long cycling. The assembled capacitor device with a gel electrolyte can deliver a maximum energy density of 86.8 Wh kg^{-1} and power density of 12.1 kW kg^{-1} along with insignificant self-discharge. Using SiO_2 and tetrapropyl orthosilicate as the template and phenolic resin as the carbon precursor, Yan and coworkers⁹⁷ prepared a mesoporous carbon hollow sphere (MCHS) with highly uniform morphology. Benefitting from vertical porous channels-enabled fast ion diffusion, the MCHS electrode afforded a high (dis)charging capability, a high capacity even at a 20 mg cm^{-2} loading, and exceptional cycling stability with negligible capacity loss over 10,000 cycles. Aside from its use as cathode material, MCHS is also applied as a dendrite-suppressing coating on Zn anode because of its capability to homogenize electric field and orient ions diffusion channels. Combining templated synthesis (NaY as template) and activation treatment (ammonia gas), Zhang *et al.*⁹⁸ synthesized nitrogen-doped porous carbon (HNPC,

Figure 2.6D) and elucidated the effect of N dopants on enhancing electrochemical performance. As shown in **Figure 2.6E**, undoped carbon needs to conquer a relatively high energy barrier (2.13 eV) during the energy storage process ($C-OH + Zn^{2+} + e^- \leftrightarrow C \cdots O \cdots Zn + H^+$) while the HNPC demands smaller values around 1.25 eV, which suggests the N dopant in HNPC benefits the rapid Zn^{2+} adsorption, agreeing well with previous publications.⁹⁹ Additionally, nitrogen atoms could alter the electronic structure of nearby carbon atoms to accelerate the dissociation of the $-OH$ bond cleavage and adsorption of the released H^+ . Combined with experimental results, nitrogen dopants can simultaneously reduce binding energy barrier of C-O-Zn and improve the wettability and conductivity, leading to the quasi-solid-state ZMC with a remarkable energy/power density of 107.3 Wh kg^{-1} /27.6 kW kg^{-1} (**Figure 2.6F**) and the application of three ZMCs connected in series as the power source for 56 red LED bulbs lasting over 20 min (**Figure 2.6G**). Of note, Zn is excessively used in most of ZMCs, meaning the real device energy density and power density is far lower than those reported values when taking the Zn anode mass into account.

2.4 Electrolyte Engineering (Solvent, Salt, Concentration and Additives)

As the bridge between the cathode and anode, the electrolyte is a crucial component in Zn-based energy devices, which offers the pathway for ions transport. As shown in **Figure 2.7A**, the electrolyte structure is complex during operation which involves solvation and de-solvation process, proton co-interaction along with $Zn(OH)_x(H_2O)_y$ formation. Because the electrolyte is strongly associated with the voltage window, ionic conductivity, the Zn plating/stripping process, the Zn corrosion behavior, and the cathode dissolutions, it becomes a hot topic to regulate components and structures of electrolyte (solvent, salt, concentration, etc.) to address existing issues in Zn-based energy devices (**Figure 2.7B**).¹⁰⁰ As shown in Figure 2.7B, regulation of solvent, salt, concentration, and additives in the electrolyte could change the local electric field, concentration polarity, water activity, and

solvation structure of zinc ions, which could further influence the electrochemical window, zinc dendrites, zinc corrosion, cathode dissolution in corresponding energy devices.

Selection of solvents. Solvents for electrolyte preparation can be divided into water and organic solvent. Organic electrolyte has the advantage of widened voltage window and suppressed Zn corrosion and dendrites formation, but there also exists many associated problems including toxicity,

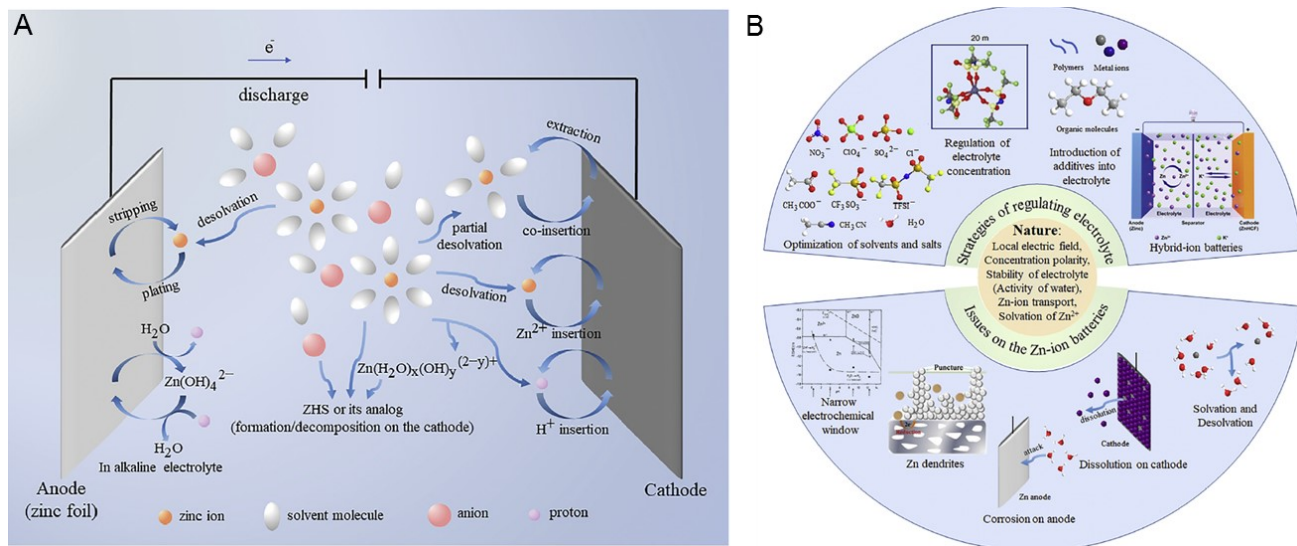


Figure 2.7 Electrolyte Engineering. (A) Schematic illustration of Zn batteries with liquid electrolyte, (B) electrolyte regulation strategies for addressing ZIBs issues. Reprinted with permission from Ref. [100]. Copyright © 2020, Elsevier.

flammability, low conductivity, large desolvation penalty, and sometimes high viscosity.^{101, 102} On the contrary, aqueous electrolyte has superiority over organic counterparts in terms of safety, abundance, conductivity, viscosity, and Zn^{2+} kinetics ascribed to weak interaction between water and Zn^{2+} /anions as well as small energy penalty for Zn^{2+} desolvation.^{103, 104}

Optimization of salts. Theoretically, any dissolvable salt containing zinc ions can be used for electrolyte preparation such as $ZnCl_2$, $Zn(NO_3)_2$, $Zn(ClO_4)_2$, $ZnSO_4$, $Zn(CH_3COO)_2$ (or $Zn(OAc)_2$), $Zn(CF_3SO_3)_2$ (or $Zn(OTf)_2$) and zinc bis(trifluoromethanesulfonyl)imide ($Zn(TFSI)_2$), to name a few.

These salts differ in the anion structure and this difference has a huge influence on battery performance. For example, Cl^- and NO_3^- are instable which will lead to irreversible Zn anode and narrow voltage window, NO_3^- is also a strong oxidant which can oxide Zn metal and cause an increase in local pH,¹⁰⁵ ClO_4^- can cause polarization upon contacting with Zn metal forming ZnO layer and passivating the Zn anode.^{105, 106} Overall, ZnSO_4 , $\text{Zn}(\text{OTf})_2$ and $\text{Zn}(\text{TFSI})_2$ are mostly used for electrolyte preparation due to the appropriate electrochemical window and reversible Zn plating/stripping. Compared with ZnSO_4 , $\text{Zn}(\text{OTf})_2$ and $\text{Zn}(\text{TFSI})_2$ have weaker cation-anion interaction, less water amount in solvation shell, weaker solvation effect, smaller desolvation energy and higher ionic conductivity, leading to better reversibility and faster kinetics for Zn deposition/dissolution.^{107, 108} However, the high cost of $\text{Zn}(\text{OTf})_2$ and $\text{Zn}(\text{TFSI})_2$ is their demerits.

Regulation of concentration. Superconcentrated electrolyte (e.g. water-in-salt electrolyte, WIS) with less water amount in both the solvent and the solvation structure can lower the activity of water and thus reduce side reactions from water dissociation.^{109, 110} Accordingly, WIS electrolyte can widen the potential window, enable reversible Zn deposition/dissolution and inhibit metal dissolution in cathode materials. Unfortunately, a high concentration usually accompanies with high expense and high viscosity, slowing down ionic transport and thus hindering its wide application in battery system.¹⁰⁰

Introduction of additives. Additives in the electrolyte can widen voltage window, inhibit Zn dendrites growth and alleviate cathode materials dissolution. Particularly, some polymers and small molecules as the additive can be adsorbed on the Zn metal surface to decelerate the Zn plating process to the formation of smooth deposition layer instead of dendrites.^{111, 112} Metal ions, either with more positive potentials or less positive potentials than zinc can be used as the additive to suppress Zn

dendrites and prohibit the dissolution of cathode materials containing same metal ions.¹¹³⁻¹¹⁵ Besides, the surfactant as the additive can widen the electrochemical window.¹¹⁶

Besides the research on liquid electrolyte, polymer electrolytes are also under intensive scrutiny due to advantages such as limited water content, suppressed Zn dendrites, minimized cathode dissolution as well as high flexibility promising for wearable and biocompatible applications .¹¹⁷

Chapter 3 Ultrafast, Long-life, High-loading, and Wide-temperature Zinc Ion Supercapacitors

A version of this Chapter has been published in *Energy Storage Materials*:

Zhixiao Xu, Rujiao Ma, Xiaolei Wang*, Ultrafast, long-life, high-loading, and wide-temperature zinc ion supercapacitors. *Energy Storage Materials*, 2022, 46, 233-242.

3.1 Introduction

Low-cost, safe and durable energy storage systems are required for smart grids and other stationary applications.^{118, 119} To that end, aqueous batteries and supercapacitors have garnered tremendous research interest due to high safety.¹²⁰ However, commercial aqueous batteries such as lead-acid and nickel-cadmium batteries could only deliver low energy densities (40~50 Wh kg⁻¹) and short life spans. By contrast, electric double layer capacitors show extended cycle life but decreased energy densities. These demerits of aqueous batteries and capacitors restrict their widespread applications and call for novel aqueous energy storage systems.¹²¹ Among candidates, zinc anode-based energy devices show great promise due to the high theoretical capacity (820 mAh g⁻¹), proper potential (-0.76 V vs standard hydrogen electrode), water compatibility, and high safety of Zn metal.^{6, 122, 123} To pair with Zn anode for making batteries, many cathode materials have been developed including transition metal oxides,^{87, 124} sulfides,⁷⁷ Prussian blue analogs,^{63, 66} and organic materials.^{72, 74} However, most of them show poor kinetics and limited cycle life due to large diffusion barriers and the dissolution of active materials.

Alternatively, zinc ion capacitors (ZICs) based on carbon-based cathodes hold great potentials.^{12, 125} For one, unlimited lifespan and fast charging can be theoretically achieved in porous carbon cathode due to its energy storage mechanism involving surface ion adsorption/desorption. For another, surface redox reactions could be introduced to carbon cathode by heteroatom doping (O, N, B, P, etc.) to increase pseudocapacitance and energy density.^{96, 126, 127} The delicate design of porous structures and heteroatom dopants in carbon cathode is crucial for achieving high-energy, high-power, and long-life ZICs. In general, large surface area and hierarchically porous structures offers potential space for electrode-electrolyte interaction whereas hydrophilic heteroatom dopants enhance electrode-electrolyte wettability and offers extra redox sites.¹²⁵ For instance, Tang et al.¹²⁸ made a 3D hierarchically porous activated carbon possessing high surface area ($3525 \text{ m}^2 \text{ g}^{-1}$) and abundant mesopores, resulting in the carbon-based ZIC with a large capacitance of 462 F g^{-1} and a high energy density of 77.5 Wh kg^{-1} . Zhao et al.¹²⁹ fabricated ZICs based on a nitrogen, oxygen-co-doped carbon cathode with a low surface area of $197.45 \text{ m}^2 \text{ g}^{-1}$ but enriched N (6.52 at%) and O (3.76 at%) dopants, which engendered a large capacitance (311.6 F g^{-1}) in a wide voltage range (0.2-1.8 V). Lu et al.⁹⁸ first demonstrated nitrogen dopants could lower the energy barrier for forming C-O-Zn, facilitating the surface reaction between O dopants and Zn^{2+} ions on carbon electrode, giving rise to a high power density of 24.9 kW kg^{-1} in corresponding ZICs. Despite the progress, it remains challenging to simultaneously attain high energy, high power, and long lifespans in ZICs.

To meet practical applications, high-mass-loading electrodes and harsh environment need to be taken into account when designing energy storage devices. On one hand, high-loading electrodes bring simultaneously the dense packing of active materials in limited space and the reduction of inactive components, leading to lower production cost and higher energy densities at the cell level compared with thin electrodes.¹³⁰⁻¹³² Actually, active mass loadings ought to be no less than 10 mg cm^{-2} for

practical applications and typical values for commercial energy storage devices are 10-20 mg cm⁻².^{130,}
¹³³ However, this is not the case in most research papers with typical loadings of only 1-4 mg cm⁻².
On the other hand, harsh environment such as low and high temperatures will be encountered in not
only extreme regions like North Pole and outer space but also residential areas with ever-changing
climate.^{134, 135} As such, it is critical to develop cells working in a wide-temperature range of -30 °C–
50 °C for most human habitats and a broader range from -50 °C to 70 °C for military uses. Strangely,
those two important factors are often ignored in the development of ZICs with only few exceptions.
For example, Zhang et al.⁹³ developed biowaste-derived carbon and anti-freezing hydrogel for ZICs
working under high mass loading (17 mg cm⁻²) and -15 °C temperature. Chen and coworkers¹³⁶
employed concentrated ZnCl₂-based hydrogel for making high-energy ZICs functioning well under 5
mg cm⁻² and -20 °C. Hydrogel seems to be essential for low-temperature aqueous ZICs but the use of
hydrogel could also jeopardize the ionic conductivity and electrochemical stability of ZICs.¹¹⁷ To our
best knowledge, hydrogel-free aqueous electrolyte for low-temperature ZICs is still absent.
Bearing above points in mind, herein we demonstrate workable ZICs under harsh conditions including
ultrafast and ultralong cycling, ultrahigh loading mass, and low/high temperatures through the
incorporation of activated carbon, aqueous binder and concentrated electrolyte. First, with highly
exposed surface area and enriched oxygen, nitrogen dopants, the activated carbon manifests large
electrical double layer capacitance and Faradic pseudocapacitance. Second, sodium alginate-based
aqueous binder shows better electrolyte wettability than the commonly used polymer binder, resulting
in much improved capacitance. Third, highly concentrated electrolyte enables large zinc
stripping/plating efficiency, long life cycles as well as low freezing temperature due to reduced
hydrogen bonding interaction of water. The combination of three aspects brings a large capacitance
of 436 F g⁻¹ (capacity: 200 mAh g⁻¹), ultrafast kinetics up to 200 A g⁻¹, ultralong cycles (0.3 million),

ultrahigh loadings (10 mg cm^{-2}), and wide-temperature cycling ($-60 \text{ }^{\circ}\text{C} \sim 60 \text{ }^{\circ}\text{C}$), resulting in a maximum energy density of 134.8 Wh kg^{-1} and power density of 118.4 kW kg^{-1} based on AC electrode, which lies among the best performance level for carbon-based ZICs. The working mechanism of AC was explored by ex situ characterizations and electrochemical measurements, which revealed a reversible proton/zinc ion co-interaction at the heteroatom-containing site of AC during capacitor charging/discharging. For practical demonstration, AC-SA based pouch cells with certain flexibility and low self-discharge rate were fabricated to power electronics. Altogether, strategies developed in our ZIC system will open an avenue towards practical supercapacitors.

3.2 Experimental Section

3.2.1 Materials

Commercial activated carbon (AC, TF-B520) was purchased from MTI corporation. Polyvinylidene difluoride (PVDF), sodium alginate (SA), zinc sulfate heptahydrate ($\text{ZnSO}_4 \cdot 7\text{H}_2\text{O}$), zinc chloride (ZnCl_2), acrylamide, N, N'-methylenebisacrylamide, ammonium persulfate and N-methylpyrrolidone (NMP) was purchased from Sigma-Aldrich, zinc trifluoromethanesulfonate ($\text{Zn}(\text{OTf})_2$) was purchased from TCI AMERICA, They are all in the analytical grade and directly used without further purification. Stainless steel mesh (SSM, #304 with a mesh size of 500) was purchased from China.

3.2.2 Characterization

Fourier transform infrared spectra (FTIR) were collected on Nicolet IS50 with the KBr pellet technique or ATR mode. Raman spectra were obtained on a laser confocal Raman spectrometer (Renishaw inVia Qontor) with the laser wavelength of 532 nm. The Rigaku XRD Ultima IV X-ray diffractometer with the Cu target (wavelength: 1.5406 \AA) was used for X-ray diffraction (XRD) analysis. The morphology of samples was observed on the field-emission scanning electron microscope (Zeiss Sigma FESEM) equipped with an EDX analyzer (Oxford AZtecSynergy). N_2 gas

adsorption-desorption isotherms were obtained on the Autosorb iQ-XR with samples degassed at 200 °C for 10 h and specific surface area was calculated according to the BET method while the pore size distribution was obtained by the NLDFT calculation using carbon models. X-ray photoelectron spectroscopy (XPS) experiments were performed on an AXIS Ultra DLD system from Kratos with Al K α radiation as X-ray source for radiation. The wettability of electrolyte (3M ZnSO₄-H₂O) on different substrates (SSM, AC-SA coated SSM, AC-PVDF coated SSM) was tested by the contact angle meter (FTA-200).

3.2.3 Electrochemical measurement

Slurry preparation. The slurry was prepared by mixing 80 wt.% of AC, 10 wt.% Super P, and 10 wt.% of binder, either SA in water or PVDF in NMP under constant stirring for more than two hours.

Electrode making. The slurry was then drop coated onto SSM for low-loading (1-4 mg cm⁻²) samples or Ti mesh for high-loading samples (5-10 mg cm⁻²) using digital pipette and dried immediately under infrared light radiation, resulting in the AC electrode with an area around 1.13 cm². **ZIC assembly.**

The ZIC was assembled into CR2032 type coin cells for all tests in the open atmosphere. While the AC electrode functions as the working electrode, Zn foil (250 μ m or 30 μ m thickness, \sim 1.13 cm²), glassy fiber membrane (Whatman Grade A), Zn-containing salt in water (e.g., 3M ZnSO₄) was adopted as the reference/counter electrode, separator, and electrolyte, respectively. 100 μ L of electrolyte was used unless noted otherwise. Galvanostatic charging/discharging (GCD), rate, and cycling performance was measured by the battery cycler (Neware) whereas the cyclic voltammogram technique was performed on the electrochemical workstation (VMP-3, Biologic) at room temperature (\sim 20 °C). **Low-temperature test.** The assembled coin-cell type ZICs (using 3M ZnSO₄ or 5.5M ZnCl₂ as electrolyte) were put inside the mini freezer (DW-60W28, Ligfreezer Low-Temp Equipment Co., Ltd) and connected by copper wires with the electrochemical workstation in which the GCD was

conducted. After setting the temperature (0 °C, -20 °C, -40 °C and -60 °C), coin cells were put inside and hold for at least one hour and then cycled under 0.1 A g⁻¹ for 5 cycles before collecting data.

High-temperature test. The assembled coin-cell ZICs using 3M ZnSO₄ or 0.5M Zn(OTf)₂ DMF as the electrolyte were put inside the gravity oven (Fisher) set at desired temperature (60 °C and 80 °C) for 30 min, connected with battery channels, and cycled under 0.1 A g⁻¹ for 5 cycles before collecting data. The weight for Zn foil (250 μm thick, ~1.13 cm²) and Zn foil (30 μm thick, 1.13 cm²) is ~210 mg and 28.5 mg, respectively. The weight for 3M ZSO (100 μL), 3M ZSO (70 μL), 5.5M ZnCl₂ (100 μL), and 0.5M Zn(OTF)₂-DMF (100 μL) is 141.1 mg, 98.8 mg, 150.7 mg, and 109.0 mg, separately. Whatman separator (Grade A, 16 mm diameter) has a weight of 11 mg.

Making of Soft-packaged Pouch Cells

Soft-packaged Zn//AC hybrid supercapacitor was assembled by sandwiching hydrogel electrolyte between anode and cathode followed by sealing in Al-plastic package. The hydrogel electrolyte was prepared based on a previous paper.¹³⁷ Firstly, 1.454 g of acrylamide, 0.875 mg of N, N'-methylenebisacrylamide, and 7.15 mg of ammonium persulfate was used as the monomer, crosslinker and initiator, respectively. They were added into 10 mL deionized water under stirring and after the solution become transparent, 0.18 g of sodium alginate was added under vigorous stirring until completely dissolved followed by ultrasonic treatment for 20 min to obtain transparent and light-yellowish solution. Next, the solution was injected into glass petri dish and put in vacuum oven at 70 °C for 30 minutes to undertake polymerization and degassing. At this stage, covalently crosslinked PAM hydrogel network was prepared. To obtain ionically crosslinked Zn-alginate network, the former hydrogel film was soaked in 2M ZnSO₄ solution for 1 hour at room temperature. Finally, the resulting Zn-alginate/PAM hydrogel electrolyte was peeled off from the petri dish and cut into a size of 24 mm × 36 mm to assemble the pouch cell. Ultrathin Zn foil with a thickness around 30 μm was

used as the anode. The loading for the AC-SA electrode is around 16-18 mg with areal loading around 2 mg cm⁻².

3.2.4 Calculation

Calculation of Gravimetric/Areal Capacity and Capacitance

Gravimetric capacity:

$$Q_s = \frac{1000 * I * t}{m}$$

in which I, t, and m represents discharge current (A), discharge time (h), the mass (g) of active materials in the cathode, respectively.

Areal capacity:

$$Q_s = \frac{1000 * I * t}{A}$$

in which I, t, and A represents discharge current (A), discharge time (h), the area (cm²) of active materials in the cathode, respectively. A=1.13 cm²

Capacitance:

$$C_s = \frac{Q_s * 3600}{1000 * V}$$

in which Q_s and V represents discharge capacity (mAh g⁻¹) and voltage window of the capacitor.

Herein, V=1.65V.

Calculation of Gravimetric/Areal Energy and Power Densities

The gravimetric energy density E (Wh kg⁻¹) and power density P (Wkg⁻¹) of ZICs were calculated based on the following equations:

$$E = \frac{1000 * \int IV(t) dt}{m}$$

$$P = \frac{E}{t}$$

in which $V(t)$, I , dt , and m represents discharge voltage (V), current (A), differential time (h), the mass (g) of active materials in the cathode, respectively.

The areal energy density E (Wh cm^{-2}) and power density P (W cm^{-2}) of ZICs were calculated based on the following equations:

$$E = \frac{1000 * \int IV(t) dt}{A}$$

$$P = \frac{E}{t}$$

in which $V(t)$, I , dt , and A represents discharge voltage (V), current (A), differential time (h), and the area (cm^2) of active materials in the cathode, respectively. $A=1.13 \text{ cm}^2$ in our electrodes.

Calculation of Self-discharge rate

For the measurement of self-discharge rate, the pouch cell was charged to 1.8 V at a current density of 0.1 Ag^{-1} (charging time: 6820 s) and rest for 3560 min ($\sim 59.33 \text{ h}$), then discharged to 0.15 V at the same current density (discharge time: 5096 s). The self-discharge rate can be calculated as

$$r_{\text{SD}} = (6820 - 5096) / (6820 * 3560 * 60) = 0.42\% \text{ h}^{-1}$$

On the other, the open-circuit voltage after resting for 3560 min ($\sim 59.33 \text{ h}$) is 1.2258 V, and the corresponding the self-discharge rate is $r_{\text{SD}} = (1.8 - 1.2258) / 59.33 = 9.67 \text{ mV h}^{-1}$.

3.3 Results and Discussion

3.3.1 Structural characterization of activated carbon

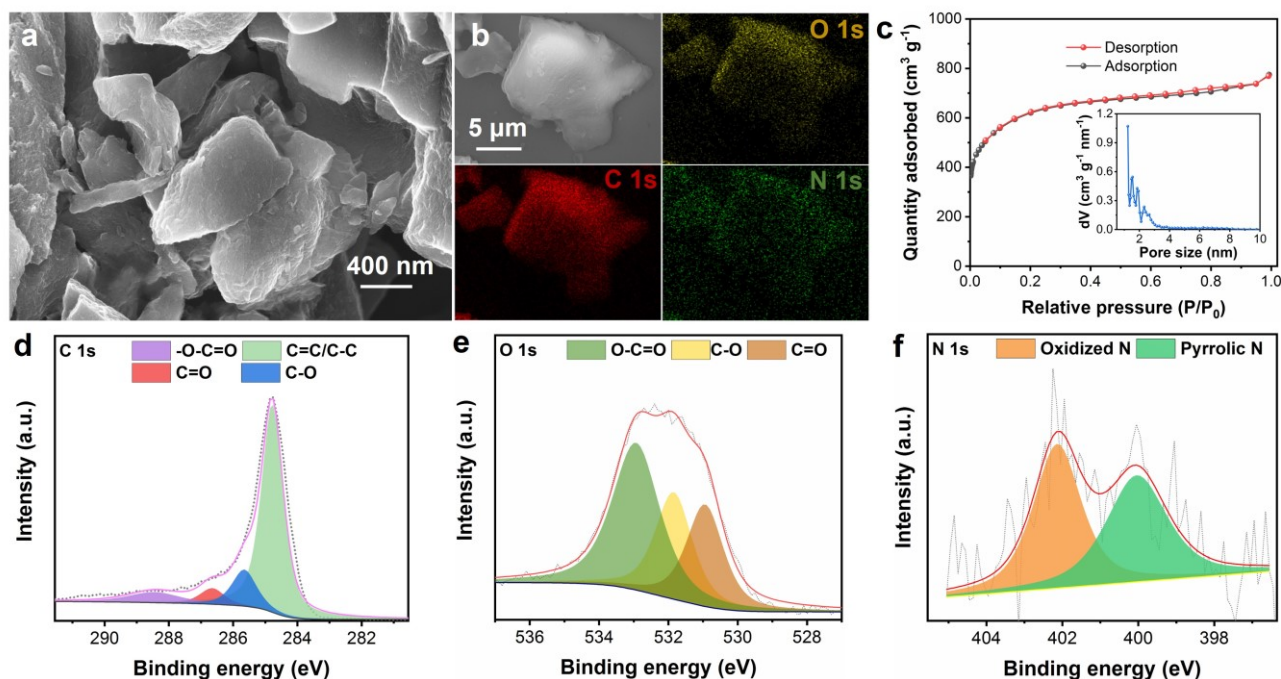


Figure 3.1. Structural characterization of AC. (a) SEM image, (b) EDX mapping, (c) isotherm adsorption/desorption curve and its corresponding pore size distribution, high-resolution XPS (d) C 1s, (e) O 1s, and (f) N 1s spectrum.

The commercial AC was characterized by microscopes and spectroscopes. SEM shows the bulky structure of the material with a wide size range of 1-20 μm (**Figure 3.1a**) while its corresponding elemental mapping indicates the uniform distribution of carbon, nitrogen, and oxygen elements (**Figure 3.1b**). Raman spectrum shows typical D ($\sim 1350\text{ cm}^{-1}$), G ($\sim 1590\text{ cm}^{-1}$), and 2D bands ($\sim 2910\text{ cm}^{-1}$) in which the D band and G band is ascribed to the disordered sp^3 -hybridized carbon and ordered graphitic sp^2 -hybridized carbon, respectively (**Figure S3.1a**, supporting information).¹³⁸ The intensity ratio of D to G (I_D/I_G) is found as 0.847, implying the presence of defects in AC. XRD showcases typical amorphous carbon structure with two broad peaks at around 25° and 42° , matching well with

previously reported activated porous carbon materials (**Figure S3.1b**).^{13, 93} The porous structure was further explored by the gas sorption technique and the isotherm curve displays typical microporous structure (Type I) with high gas sorption at near-zero pressure in which micropores (1.2-2 nm) are dominant accompanied by some mesopores averaged at 2.3 nm (**Figure 3.1c**). The specific surface area and pore volume is calculated to be 2066 m² g⁻¹ and 1.20 cm³ g⁻¹, respectively. The surface structure and chemical valence state was probed by XPS. The survey spectrum indicates the only existence of carbon, oxygen, and nitrogen in the AC and their content is 90.2 at%, 9.1 at%, and 0.7 at% (**Figure S3.1c**). High-resolution XPS C 1s spectra (**Figure 3.1d**) can be deconvoluted into C=C/C-C (284.8 eV), C-O/C-N (285.6 eV), C=O (286.6 eV) and carboxyl (288.5 eV) peaks, with the respective content of 71.1%, 14.0%, 6.2%, and 8.7% in AC.¹²⁷ High-resolution O 1s spectrum in **Figure 3.1e** manifests O-C=O (532.9 eV, 47.5%), C-O/-OH (531.9 eV, 26.9%), and C=O (530.9 eV, 25.6%) groups whereas the high-resolution N 1s spectrum (**Figure 3.1f**) displays pyrrolic N (400.1 eV, 50.8%), and oxidized N (402.1 eV, 49.2%).¹³⁹ The rich heteroatom doping and high surface area with hierarchical pores render the AC electrode promising for supercapacitor application.¹⁴⁰

3.3.2 Optimization of binder and electrolyte

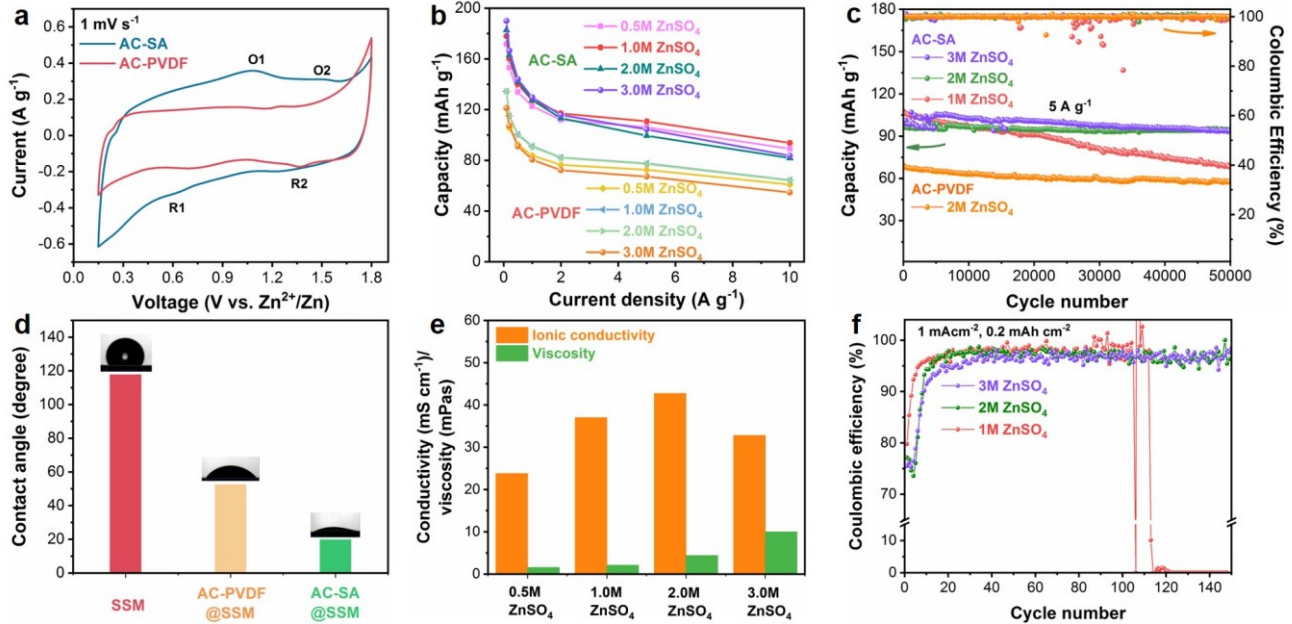


Figure 3.2 Optimization of binder and electrolyte. (a) CV curves of AC-SA and AC-PVDF. (b) Plot of capacity against current density of AC-SA and AC-PVDF in different electrolyte. (c) Cycling performance of AC-SA in 1.0/2.0/3.0M ZnSO₄ at the current density of 5 Ag⁻¹. (d) Contact angles of 3M ZnSO₄ electrolyte on the surface of pristine SSM, AC-PVDF coated SSM, and AC-SA coated SSM. (e) pH values, viscosity, and ionic conductivity of ZnSO₄ electrolyte with different concentration. (f) Coulombic efficiency of Zn metal plating/stripping in different electrolyte (1.0/2.0/3.0M ZnSO₄).

To optimize AC electrode for ZICs with high energy density and power density, we here study the influence of binder and electrolyte on capacity, rate, and cycling performance. For the binder, sodium alginate-based aqueous binder (SA) and polymer-based organic binder (PVDF) were explored. PVDF is the most used binder for battery/capacitor electrode manufacturing but the organic solvent used for dissolving PVDF is toxic, expensive, and hazardous.^{141, 142} On the contrary, aqueous binders like SA are water soluble, cheap, safe, and sustainable, thus receiving increasing attention in recent years.^{143,}

¹⁴⁴ Ding *et al*¹⁴⁵ reported the first use of SA binder for aqueous zinc ion batteries and found that SA could crosslink with zinc ions to form water-insoluble binder. Inspired by this, here we firstly explored the use of SA binder for aqueous ZICs. The electrode using SA or PVDF is denoted as AC-SA and AC-PVDF, respectively. Interestingly, AC-SA electrode is easily dispersible in water but stable in ZnSO₄ electrolyte due to the formation of crosslinking network induced by coordination interaction between zinc ions and carboxylic/hydroxyl groups of SA (Figure S2). The stability of AC-SA electrode in ZnSO₄ electrolyte is further confirmed by no loss of sodium element in the AC-SA electrode and no decay on the mass of cathode after cycling, which makes SA suitable for aqueous ZICs. As shown in the CV curves (**Figure 3.2a**), SA binder enables more apparent redox peaks and larger capacitive areas (around 1.3-fold) compared with PVDF binder, resulting in a significant increase in the pseudocapacitance of corresponding AC. **Figure 3.2b** and **Figure S3.3** shows the rate performance of ACs based on different binders and electrolytes. Apparently, AC-SA shows much higher capacity than AC-PVDF in all current rates and electrolytes, further demonstrating the superiority of SA over PVDF binder. The cycling performance (**Figure 3.2c**) indicates that first, long life up to 50000 cycles at a high rate of 5 Ag⁻¹ with nearly 100% capacity retention and 100% Coulombic efficiency (CE) can be achieved in concentrated electrolytes (2.0 M and 3.0 M ZnSO₄) in stark contrast to the fast capacity decay in the dilute electrolyte (1.0 M ZnSO₄) with only 64% retention and unstable CE; second, AC-SA delivers higher capacity (97 mAh g⁻¹) than AC-PVDF (averaged at 60 mAh g⁻¹) throughout ultralong cycles. The different chemical structure of SA and PVDF could explain the performance difference. While PVDF is composed of hydrophobic groups in the chain, SA is enriched with hydrophilic carboxylic/hydroxyl groups. To confirm this, the electrolyte//electrode interface was studied by the contact angle meter in which electrolyte (3M ZnSO₄) was dropped onto different electrode surface (SSM, AC-SA@SSM, AC-PVDF@SSM) and

the contact angle was measured to be 117.8°, 52.6°, and 19.9° for SSM, AC-PVDF@SSM, and AC-SA@SSM electrode, respectively (**Figure 3.2d**). The lower angle in AC-SA@SSM suggests that SA binder enables better electrolyte wettability and higher hydrophilicity, which could facilitate the interaction between charge carriers and active sites including micro/mesopores and heteroatom dopants in resulting ZICs. Also, carboxylic groups in SA binder could coordinate with cations such as proton and Zn^{2+} , boosting the capacitor kinetics in the AC-SA electrode. The better wettability and coordination effect explain why more apparent redox peaks and larger capacitance can be gained in the AC-SA electrode than AC-PVDF electrode.

As regards the influence of electrolyte on ZIC, electrolyte containing different salt (ZnSO_4 , ZnCl_2 , and $\text{Zn}(\text{OTf})_2$) was firstly compared with each other and it was found that only ZnSO_4 -based electrolyte enables stable cycling in the wide voltage window of 0.15-1.8 V at room temperature (**Figure S3.4-S3.5**). Next, ZnSO_4 electrolyte with different concentrations (0.5M, 1.0M, 2.0M, and 3.0M) was investigated, the rate performance (**Figure 3.2b**) shows that at low current rates (0.1~2.0 Ag^{-1}), higher capacity can be obtained in concentrated electrolytes (2.0M and 3.0M ZnSO_4) whereas dilute electrolytes (0.5M and 1.0M ZnSO_4) favors high capacity at high current rates (5, 10 Ag^{-1}). This could be explained by the difference in ionic conductivity and viscosity of different electrolyte.^{100, 146} As shown in **Figure 3.2e**, with the increase in concentration from 0.5M to 3.0M, the viscosity increases from 1.58 mPas to 10.0 mPas while the ionic conductivity increases from 23.8 mS cm^{-1} in 0.5M ZnSO_4 to the highest value of 42.7 mS cm^{-1} in 2.0M ZnSO_4 but decreases to 32.8 mS cm^{-1} in 3.0M ZnSO_4 . At low current rates, the electrochemical performance is largely determined by ion concentration and ionic conductivity which explains why concentrated electrolyte can achieve higher capacity than dilute electrolyte. At high current rates, however, the high viscosity of concentrated electrolytes could retard the mass transfer and is unfavorable for fast-rate

charging/discharging. On the other hand, electrolytes with different concentration also have an influence on the deposition/dissolution efficiency of zinc metal anode.¹⁴⁷ **Figure 3.2f** shows the CE of Zn metal in three electrolytes (1.0M/2.0M/3.0M ZnSO₄) at 1 mA cm⁻². Although the CE in initial 10 cycles are relatively higher (80%-97%) in 1.0M ZnSO₄ than 2.0M and 3.0M ZnSO₄, it can last for only 100 cycles with dramatic drop to almost 0% at the 106th cycle. On the contrary, the CE in 2.0M and 3.0M ZnSO₄ gradually increases from 75% to 97.5% in initial cycles and stabilizes at around 97.5% in following cycles. This difference on CE in different electrolyte results in the long cycle life in concentrated electrolyte and short lifespan in dilute electrolyte as displayed in **Figure 3.2c**. Besides, Zn foil shows relatively slow corrosion in ZnSO₄ electrolyte (**Figure S3.6**). Above results suggest that the optimal ZICs can be achieved by the combination of aqueous SA binder and concentrated electrolytes (particularly 2.0M ZnSO₄).

3.3.3 Ultrahigh rates, ultralong cycles, and kinetics analysis

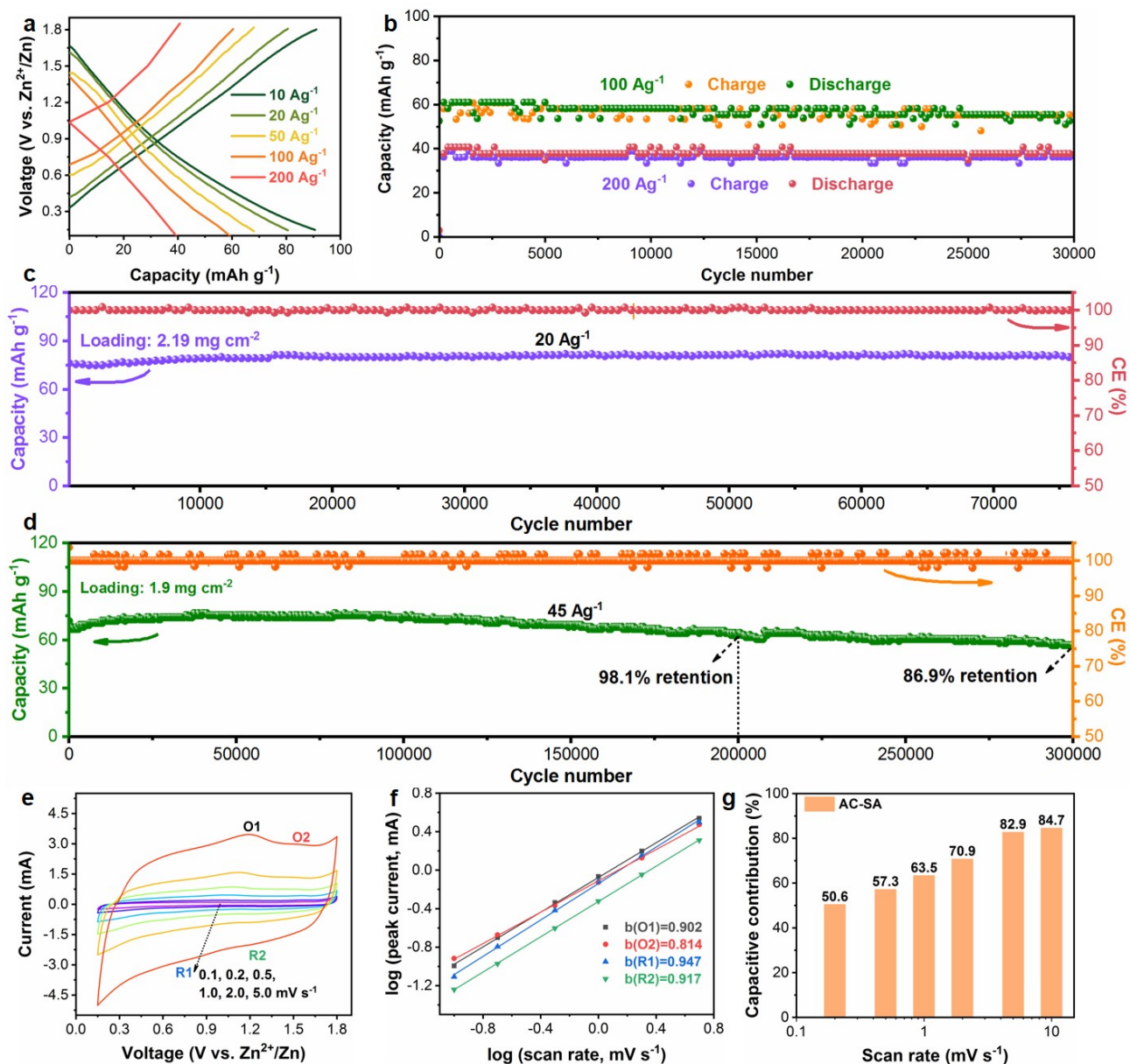


Figure 3.3. High-rate performance and kinetics. (a) Charge-discharge curves of the AC-SA electrode at high current densities from 10 to 200 Ag^{-1} . (b-d) Long cycling performance of AC-SA electrodes at (b) 100 and 200 Ag^{-1} , (c) 20 Ag^{-1} , and (d) 45 Ag^{-1} . (e) CV profiles of AC-SA electrode at scan rates from 0.1 mVs^{-1} to 5.0 mVs^{-1} . (f) The linear fitting between $\log(\text{current})$ and $\log(\text{scan rate})$ at redox peaks. (g) capacitive contributions at different scan rates.

The combination of SA binder and concentrated electrolyte (2.0 M ZnSO₄) was further applied for ultrafast charge/discharge tests. **Figure 3.3a** shows that at current densities of 10, 20, 50, and 100 A g⁻¹, the specific capacity is 90, 80, 69, and 60 mAh g⁻¹, respectively. Even at an ultrahigh rate of 200 A g⁻¹, corresponding to 0.72 s charging time, the capacity can still be maintained at 40 mAh g⁻¹. Aside from the remarkable rate performance, the stability is also exceptional, negligible capacity loss was observed over 30000 cycles at 100 A g⁻¹ (**Figure 3.3b**), no decay was found over 75000 cycles at 20 A g⁻¹ (**Figure 3.3c**), and 98.1% (86.8%) capacity was retained after 0.2 (0.3) million cycles at 45 A g⁻¹ (**Figure 3.3d**), demonstrating one of the longest cycle life in aqueous ZICs, comparable to the state-of-the-art supercapacitors. Besides, high Coulombic efficiency approaching 100% is well maintained in all long-cycling tests. This simultaneous achievement of ultrafast and ultralong cycling in AC-SA electrode lies among best of reported Zn-based supercapacitors and batteries (**Table S3.1** and **Table S3.2**). Compared with AC-SA electrode with long life at high current densities, AC-PVDF electrode, however, shows rapid capacity decay under high rate (**Figure S3.7**). Of note, despite these high rates and long cycles in ZICs, Zn anode experienced dendritic growth (**Figure S3.8**) and low depth of discharge (~0.1% for 250 μm-thick Zn and ~0.45% for 30 μm-thick Zn, **Figure S3.9**). As such, ZICs are not yet applicable for high energy density storage until solving the dendritic growth and low depth of discharge issue of Zn anode.

To understand the simultaneous achievement of fast charging and long cycling, the kinetics of AC-SA electrode was analyzed by the CV technique. As shown in the **Figure 3.3e**, CV curves of AC electrodes were tested at scan rates from 0.1 to 5.0 mV s⁻¹ in which there appears two couples of redox peaks located at 1.1V/0.8V and 1.5V/1.2V, denoted as O1/R1 and O2/R2 peaks, respectively, indicating the presence of Faradic surface reactions, which should be ascribed to the heteroatom dopants. According to the $i=av^b$ equation,^{148, 149} the logarithmic relationship between peak currents

and scan rates was calculated as b value (**Figure S3.10**). The b value of 0.5 corresponds to a diffusion-controlled redox reaction while the b value of 1.0 is associated with capacitive reactions.¹⁴⁹ The b values for the O1, O2, R1, R2 peaks of AC were calculated to be 0.902, 0.814, 0.947, and 0.917, respectively, implying the pseudocapacitive reactions plays the major part (**Figure 3.3f**). The quantitative distribution from pseudocapacitive reactions and diffusion-controlled processes in the AC-SA electrode was further calculated according to the Dunn method (**Figure S3.11**).^{148, 149} With the increase of scan rate from 0.2 mV s⁻¹, to 0.5, 1.0, 2.0, 5.0, and 10 mV s⁻¹, the capacitive contribution increases from 50.6% to 57.3%, 63.5%, 70.9%, 82.9%, and 84.7% (**Figure 3.3g**). This result suggests the fast kinetics mainly result from rapid surface Faradic reactions, which is in line with b values. The analysis on kinetics and capacitive contribution were also conducted on the AC-PVDF (**Figure S3.12-S3.13**). Compared with AC-PVDF, AC-SA shows relatively higher contribution from the capacitive process, suggesting the SA binder facilitates the surface Faradic reactions due to better electrolyte wettability and coordination effect.

3.3.4 Storage mechanism analysis

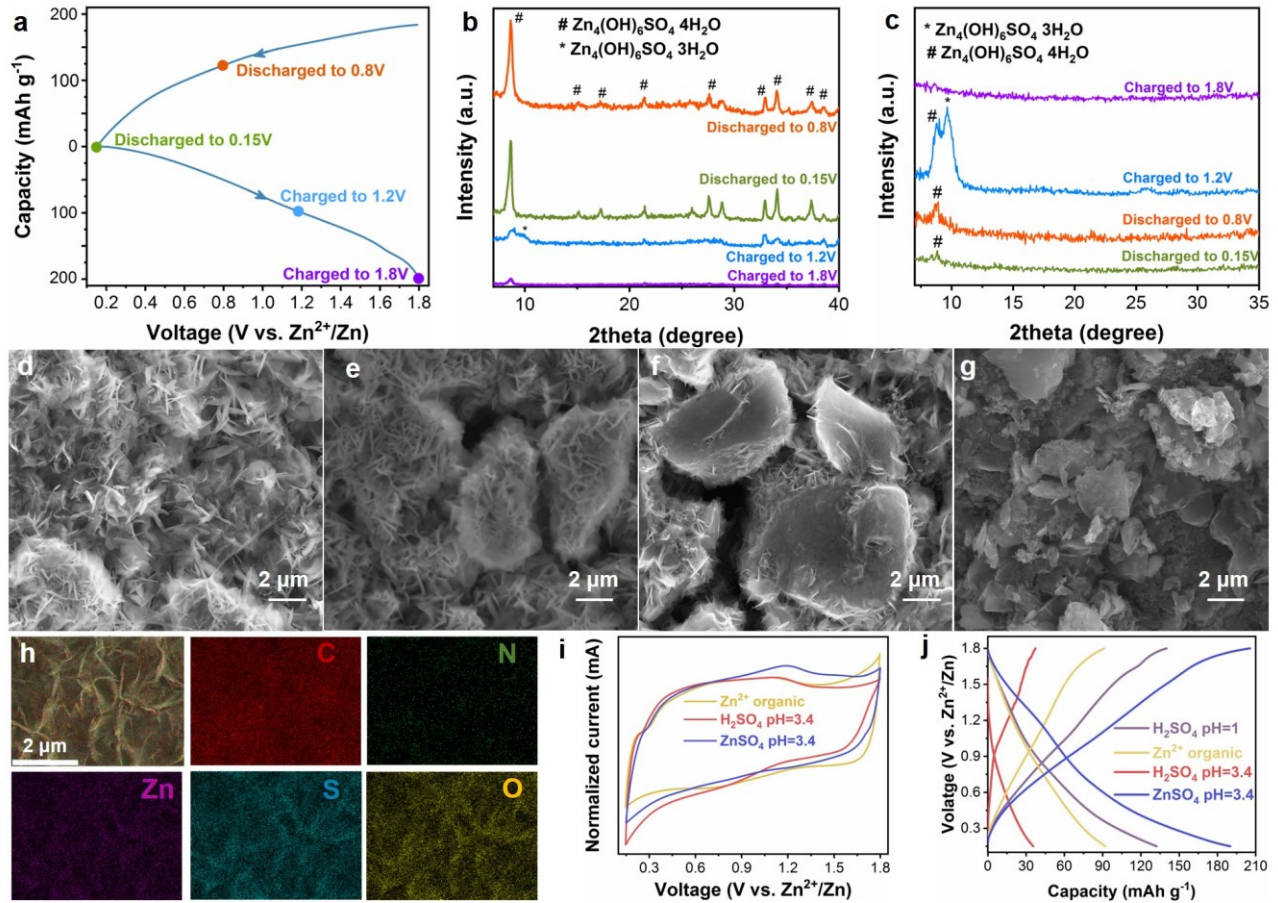


Figure 3.4 Storage mechanism of AC-SA for ZICs. (a) Charge-discharge profiles containing different colored points indicating electrodes under different states. (Yellow: discharged to 0.8V, green: discharged to 0.15V, blue: charged to 1.2V, purple: charged to 1.8V). (b-c) XRD patterns of (b) AC and (c) Zn electrode under different charge/discharge states. (d-g) SEM images of AC-SA electrode at different states: (d) discharged to 0.8V, (e) discharged to 0.15V, (f) charged to 1.2V, (g) charged to 1.8V. (h) SEM EDX elemental mapping of zinc sulfate hydroxide covered AC electrode. (i) normalized CV curves and (j) voltage-capacity profiles of AC-SA electrode in different electrolyte.

To comprehend the storage mechanism, ex situ XRD, SEM, and elemental mapping analysis were conducted on AC-SA electrode at different status. XRD patterns (**Figure 3.4b**) of the discharged AC-SA electrodes only show diffraction peaks of Zn₄SO₄(OH)₆·4H₂O (JCPDS card #044-0673) and

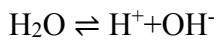
$\text{Zn}_4\text{SO}_4(\text{OH})_6 \cdot 3\text{H}_2\text{O}$ (JCPDS card #039-0689). Since zinc sulfate hydroxide precipitates in solutions with $\text{pH} > 5.5$, its formation in ZnSO_4 electrolyte with a pH of 3.4 should be due to proton insertion into AC cathode leaving OH^- behind and causing local pH increase.¹⁵⁰ And these $\text{Zn}_4\text{SO}_4(\text{OH})_6 \cdot x\text{H}_2\text{O}$ peaks disappear after charging back to 1.8V in the AC-SA electrode, implying the reversible insertion/de-insertion of proton at the cathode during the electrochemical processes. The appearance and disappearance of zinc sulfate hydroxide was also observed in the XRD patterns of Zn anode during discharge and charge process, as a result of the faster mobility of hydroxide anions than sulfate anions. The reversible proton (de)insertion process is further verified by SEM images (**Figure 3.4d-g**) in which zinc sulfate hydroxide nanoflakes gradually appear and disappear on the bulky AC particles during the discharge and charge process. The elemental mappings verify that the nanoflakes formed at the discharged state are composed of Zn, O, and S elements (**Figure 3.4h**), matching well with XRD patterns. Above results suggest that protons take part in the energy storage during ZIC charging and discharging.

To gain insight into the ions storage mechanism and see if Zn^{2+} ions are also (de)inserted into the AC-SA electrode, electrochemical measurements were conducted in a series of electrolytes including Zn^{2+} -only organic electrolyte, H^+ -only acidic electrolyte (H_2SO_4 with $\text{pH}=1$ and $\text{pH}=3.4$), and ZnSO_4 electrolyte ($\text{pH}=3.4$) with AC-SA as the cathode and Zn as the anode. Firstly, CV profiles in different electrolyte was normalized to compare the position of redox potentials. As presented in **Figure 3.4i**, the profile of ZnSO_4 ($\text{pH}=3.4$) does not overlap with that of either H_2SO_4 ($\text{pH}=3.4$) or Zn^{2+} -only organic electrolyte but locates between that of these two electrolytes, implying the mechanism involving both proton and zinc ion storage. Next, voltage-capacity curves show that low capacities of only 35.6, 92.1, and 132 mAh g^{-1} can be delivered in H_2SO_4 ($\text{pH}=3.4$), Zn^{2+} -only organic electrolyte, and H_2SO_4 ($\text{pH}=1$), respectively, which is much lower than 185 mAhg^{-1} in ZnSO_4 ($\text{pH}=3.4$). The

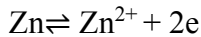
large capacity achieved in ZnSO₄ results from the synergistic interaction between AC-SA electrode and active cations including proton and Zn²⁺. These results confirm that both proton and Zn ions are active cation contributing to the capacity during ZICs operation. Based on above results, we propose five reversible reactions involved during ZIC charge/discharge process including water ionization reaction, Zn stripping/plating process, proton interactions on AC, zinc ion interactions on AC electrode, as well as reversible formation and removal of Zn₄(OH)₆SO₄ xH₂O (please see more information in the Supporting information).

Five major reactions involved in the ZICs:

1. Water ionization reaction:



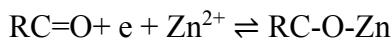
2. Reversible Zn stripping/plating process:



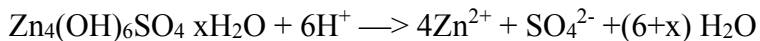
3. Reversible proton interactions on hydroxyl and carbonyl groups of AC-SA electrode:



4. Reversible zinc ion interactions on hydroxyl and carbonyl groups of AC-SA electrode:



5. Reversible formation of Zn₄(OH)₆SO₄ xH₂O :



3.3.5 The influence of mass loadings on capacitor performance

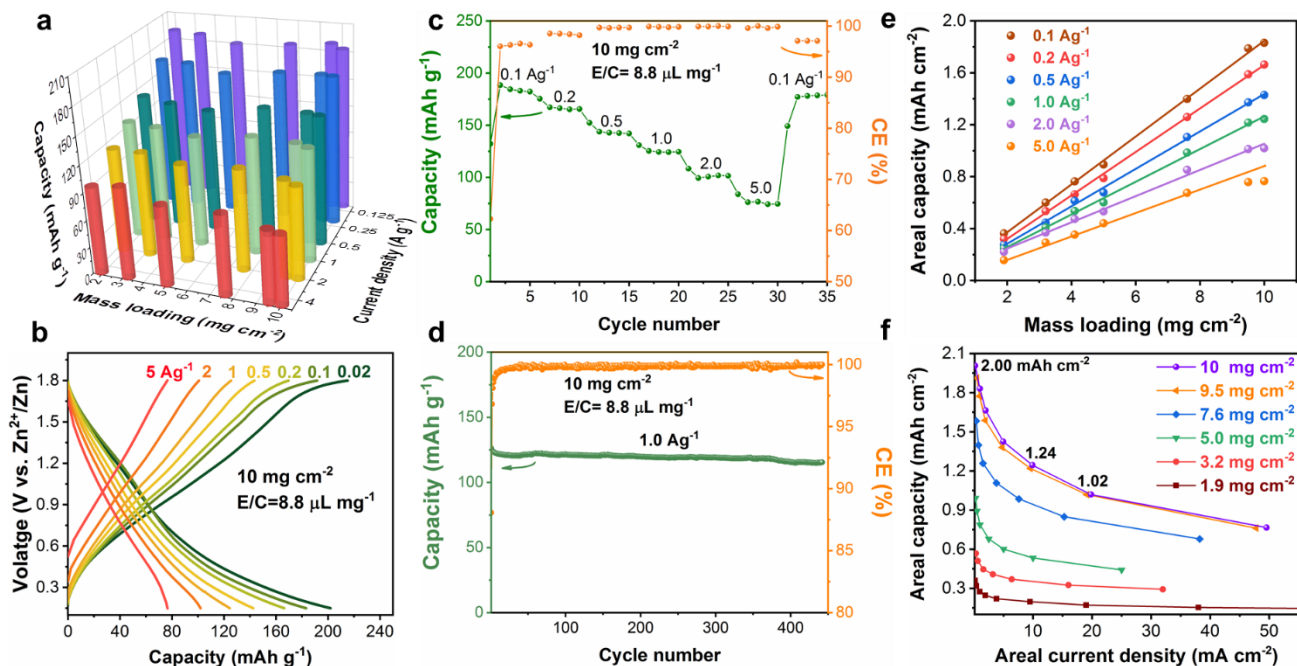


Figure 3.5 High-loading performance. (a) 3D profiles for the capacity-current density-mass loading relationship. (b) Charge-discharge curves, (c) rate performance, and (d) cycling performance (at 1.0 A g⁻¹) of the high-loading AC-SA electrode (10 mg cm⁻²). (e) Plots for the areal capacity vs. the mass loading. (f) Areal capacity versus areal current density of AC-SA electrode with different mass loadings.

Aiming at high-loading AC electrodes, we here investigate three different levels of mass loading, including typical loading amounts for research studies (1.9~3.9 mg cm⁻²), practical applications (9.5, 10 mg cm⁻²) and intermediate values (4~7.6 mg cm⁻²).¹⁵¹ Noteworthy is that the amount of electrolyte is kept constant (100 μL) and thus the electrolyte-to-carbon (E/C) ratio decreases as the mass loading increases. Even under this condition, specific capacities of AC-SA electrodes show insignificant change with the increase of mass loading from 1.9 to 10 mg cm⁻² at current densities from 0.1 to 5.0 A g⁻¹ (**Figure 3.5a**). Specifically, at the low rate of 0.1 A g⁻¹, the capacity of high-loading electrode (10 mg cm⁻²) maintains 96.3% of that obtained by the low-loading electrode (1.9 mg cm⁻²). Even at

a high rate of 2 A g^{-1} , the AC-SA electrode with a high loading of 10 mg cm^{-2} retains a capacity of $\sim 101.9 \text{ mAh g}^{-1}$, a decrease of only 12% from that of the 1.9 mg cm^{-2} electrode (**Figure 3.5a**). In stark contrast, AC-PVDF electrode exhibits obvious capacity decay from 140 mAh g^{-1} to 89.5 mAh g^{-1} and to 62.5 mAh g^{-1} at the rate of 0.1 A g^{-1} as the loading increases from 1.8 mg cm^{-2} to 4.0 mg cm^{-2} and to 10 mg cm^{-2} (**Figure S3.14**). The charge-discharge curves of the AC-SA electrode show small voltage drops and capacity loss with increased mass loading from 1.9 to 10 mg cm^{-2} (**Figure 3.5b** and **Figure S3.15-S3.19**). As such, the AC-SA electrode with the 10 mg cm^{-2} loading shows capacities of 200.5, 183, 166.3, 142.9, 124.4, 101.9, and 76.5 mAh g^{-1} at the rate of 0.02, 0.1, 0.2, 0.5, 1.0, 2.0, and 5.0 A g^{-1} , respectively. The 10 mg cm^{-2} loading electrode manifests stable cycles even at the high rate of 5 A g^{-1} , and when the rate is returned to 0.1 A g^{-1} , the capacity can be recovered to 183 mAh g^{-1} , suggestive of the high rate and reversibility of AC-SA electrode at high loadings (**Figure 3.5c**). Unsurprisingly, the AC-SA electrode fails after high-rate cycles (**Figure S3.20**), mainly due to the harsh testing condition with lean electrolyte (E/C ratio of only $8.8 \mu\text{L mg}^{-1}$) and the dendritic growth of zinc metal (**Figure S3.21**). However, after replenishing the Zn anode and electrolyte (still E/C= $8.8 \mu\text{L mg}^{-1}$), this 10 mg cm^{-2} AC-SA electrode can still deliver remarkable cycling stability with 92.8% capacity retention and $\sim 100\%$ Coulombic efficiency after 450 cycles at 1 A g^{-1} (**Figure 3.5d**).

Increasing areal capacity is crucial for realizing high energy and power densities at the cell level and thus the areal capacity is an important figure of merit for evaluating energy storage systems.¹⁵¹ Accordingly, the curves of areal capacity against mass loading at different rates were plotted. **Figure 3.5e** shows linear increase of areal capacity with the mass loading up until 10 mg cm^{-2} at rates from 0.1 to 2 A g^{-1} , indicating no limitation has been reached in mass loading at rates less than 2 A g^{-1} (which corresponds to a current density of 20 mA cm^{-2} for the 10 mg cm^{-2} electrode). At the high rate of 5

Ag^{-1} , slight deviation from the linearity takes place, which should result from limitation of ion diffusion and concentration effects as commonly seen in thick electrodes and high rates. **Figure 3.5f** shows the influence of mass loading and current rate on the areal capacity of AC-SA electrode. Overall, with the increase of areal current density, areal capacity shows the same decreasing trend with similar curve slopes, suggesting the fast-rate capability at high loadings. The highest areal capacity of 2.0 mAh cm^{-2} (capacitance of 4.36 F cm^{-2}) can be obtained by the high-loading (10 mg cm^{-2}) electrode at 0.2 mA cm^{-2} . The same electrode can reach high areal capacities of 1.24, 1.02, and 0.76 mAh cm^{-2} (areal capacitances of 2.71, 2.23, and 1.66 F cm^{-2}) at high rates of 10, 20, 50 mA cm^{-2} . The curves for gravimetric/areal energy densities against power densities were plotted, and nearly overlapping curves could be found in different mass loadings of AC-SA electrodes, again confirming the SA binder-enabled high-loading capability (**Figure S3.22a**). The highest areal energy density of 1.39 mWh cm^{-2} and maximal power density of 41.7 mW cm^{-2} can be obtained in the 10 mg cm^{-2} electrode. Overall, the large areal capacity (energy density) at high rates (power density) achieved in thick AC-SA electrodes are among the best ZICs (**Table S3.3**). Aforementioned results demonstrate the fast kinetics and good stability of ultrahigh-loading AC-SA electrodes, promising for the development of high-energy and high-power ZICs.

3.3.6 Extremely low- and high-temperature performance

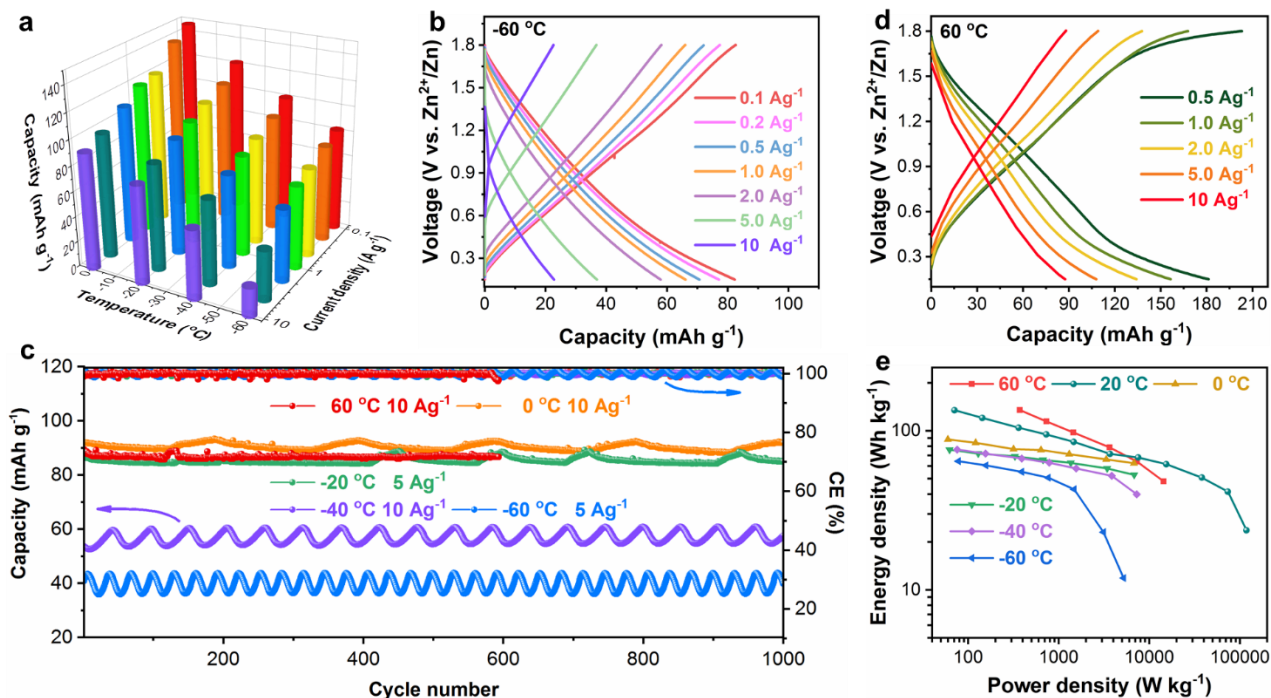


Figure 3.6 Low/high-temperature performance. (a) 3D plot showing the ZIC capacity against temperature and current density. Charge-discharge curves of ZICs under different rates at (b) -60 °C and (d) 60 °C. (c) Long-cycling performance of ZICs at low/high temperatures (60, 0 °C, -20 °C, -40 °C, and -60 °C). (e) energy and power density of AC-SA electrodes at different temperatures.

Developing low(high)-temperature ZICs is important for their use in cold(hot) environment.¹³⁵ Among components for making low-temperature ZICs, the electrolyte plays the critical role.¹⁵² Concentrated ZnSO₄ could function at 0 °C but fail at -20 °C (**Figure S3.23**), as a result of its relatively high freezing temperature (**Figure S3.24a**). Inspired by the low-temperature electrolyte for zinc ion batteries,¹⁵³ the concentrated electrolyte of 5.5 M ZnCl₂ with a freezing temperature <-85 °C was prepared and applied for the AC-SA electrode (**Figure S3.24b**). **Figure 3.6a** shows capacities of AC-SA electrode at different temperatures (0 °C, -20 °C, -40 °C, and -60 °C) and different current densities (0.1-10 A g⁻¹). In general, with the decrease of temperature, the capacity of AC-SA electrode decreases proportionally in all current rates, which could be attributed to the decreased ionic conductivity and

sluggish kinetics at lower temperatures. Of mentioning, this 5.5M ZnCl₂ electrolyte could work in a narrow window of 0.15-1.5 V at 0 °C and -20 °C but a widened voltage window of 0.15-1.8 V at lower temperatures of -40 °C and -60 °C (**Figure S3.25**), which should be due to retarded corrosion reaction from chloride anions at extremely low temperatures. Impressively, the AC-SA electrode could work at an ultralow temperature of -60 °C. At the rate of 0.1 Ag⁻¹, the capacity is 82.3 mAh g⁻¹ which decreases to 57.9 mAh g⁻¹ at 2.0 Ag⁻¹ and 22.8 mAh g⁻¹ at 10 Ag⁻¹ (**Figure 3.6b**). This high-rate capability of AC-SA electrode at extremely low temperature has rarely been reported in ZICs (**Table S3.4**). **Figure 3.6b** displayed charge-discharge curves at -60 °C, small voltage drops appear at low rates of 0.1-2.0 Ag⁻¹ but large voltage drops occur at high rates (5.0, 10 Ag⁻¹), indicating the low capacities at high rates resulting from large internal resistance. Aside from the excellent rate performance, AC-SA electrodes at low temperatures inherit the superior cycling stability at the room temperature, as nearly 100 % capacity and 100% Coulombic efficiency at high rates of 5.0 Ag⁻¹ and 10 Ag⁻¹ can be well preserved after 1000 cycles in the AC-SA electrodes under low temperatures (**Figure 3.6c**). Of mentioning is that the ups and downs in capacity of Figure 6c is caused by ±4 °C temperature changes. The storage mechanism of AC-SA electrode at -60 °C (**Figure S3.26**) again reveals co-interaction from proton and zinc ions during charge/discharge.

Apart from the low-temperature performance, AC-SA electrode could also work at high temperatures. When the temperature is increased from 20 °C to 60 °C, higher capacities can be obtained. As presented in **Figure 3.6d**, at the rate of 0.5, 1, 2, 5, and 10 Ag⁻¹, the respective capacity is 181.3, 156.5, 134.2, 107.8, and 87.5 mAh g⁻¹ at 60 °C, which are higher than those obtained at room temperature. Also, at 60 °C, voltage-capacity curves at high rates of 0.5-2.0 A g⁻¹ still exhibit apparent redox plateaus (0.15-0.3 V and 1.65-1.8V), which are not obvious at same rates under room temperature, suggesting the elevated temperature boosted the surface Faradic reactions, which could

explain the higher capacities obtained at 60 °C. Additionally, the cycling performance is also excellent since no capacity loss was found over 500 cycles at a high rate of 10 Ag⁻¹. With a further increase of temperature to 80 °C, however, the AC-SA electrode fails to provide stable capacities over long cycles, which should be ascribed to the increased pressure of sealed coin cells due to accelerated side reactions from water decomposition and the peeling off of the AC-SA electrode from the current collector due to increased solubility of SA at high temperature (**Figure S3.27**). The use of organic electrolyte based on DMF solvent could solve this problem (**Figure S3.28-S3.30**).

Energy densities and power densities under different temperatures were plotted in **Figure 3.6f**. The highest energy density at 60 °C, 20 °C, 0 °C, -20 °C, -40 °C, and -60 °C is 134.8, 134.6, 88.2, 76.1, 76.1, and 64.4 kWh kg⁻¹, respectively whereas the highest power density achieved is 14.4, 118.4, 6.78, 6.82, 7.27, and 5.2 kW kg⁻¹, respectively. Of mentioning is that only the mass of AC is considered when calculating energy and power densities, the cell-level values are much smaller because of heavy Zn foil and electrolyte. That is why we further tested ZICs using thin Zn foils and lean electrolyte (**Figure S3.31**) but the cell-level energy and power densities remain relatively low. Above results show the wide-temperature workability of the AC-SA electrode for ZICs, promising for their use under harsh conditions.

3.3.7 Soft-packaged ZIC pouch cells

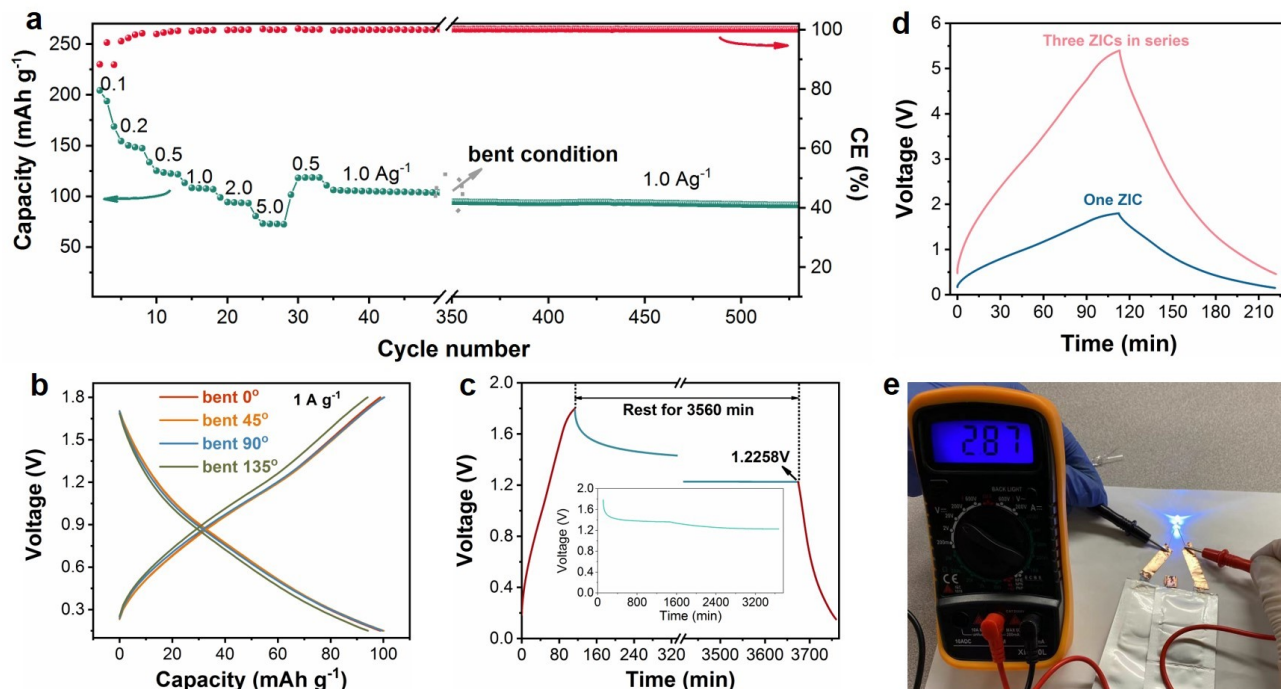


Figure 3.7 Performance of soft-packaged pouch cells. (a) Rate and cycle performance of a Zn-AC pouch cell. (b) Charge/discharge profiles of pouch cells bent at different angles. (c) Self-discharge test and inset shows the open-circuit voltage change with time. (d) Voltage-time profiles of single ZIC and three ZICs connected in series. (e) The digital photo showing two ZICs in series powering one blue LED.

To further demonstrate the potential application of AC-SA electrodes, soft-packaged pouch cells were fabricated through sandwiching hydrogel between AC-SA cathode and thin Zn foil anode followed by sealing inside the Al plastic films.¹³⁷ The specific capacity of the cell at the current density of 0.1, 0.2, 0.5, 1.0, 2.0, and 5.0 A g⁻¹ is 190, 150, 125, 105, 90, and 75 mAh g⁻¹, respectively, based on the AC electrode (**Figure 3.7a**), which is slightly lower than those values in coin cells, as a result of the larger interfacial resistance between electrode and electrolyte due to the use of hydrogel and the lack of compression force during the assembly process. The pouch cell shows certain flexibility. As shown

in **Figure 3.7b**, no capacity loss was observed in the pouch cell bent at 45 ° and 90 ° angles whereas only 5% capacity was lost when bending the pouch cell to an angle of 135 °. After bending tests, the pouch cell can still run for over 500 cycles at 1 Ag⁻¹. A capacity retention of 87% and a Coulombic efficiency of ~100% is obtained, suggesting its excellent cycling performance.

Moreover, the self-discharge behavior was measured by charging the cell to 1.8 V at a current of 0.1Ag⁻¹ followed by resting for 3560 min and discharging to 0.15 V at the same current density (**Figure 3.7c**). The self-discharge rate of the ZIC pouch cell is calculated as 9.67 mV h⁻¹ or 0.42% h⁻¹ based on different methods,^{121, 154} indicative of a low self-discharge rate. When connecting three ZICs in series, the output voltage can be increased two times without jeopardizing the discharge time and capacity (**Figure 3.7d**). As a result, two ZIC pouch cells in series can power blue and color-changing LEDs (**Figure 3.7e** and **Video S3.1**). These results show the potential of AC-SA-based ZICs for wearable and flexible electronics.

3.4 Summary

In summary, we report the making of fast, durable, low-cost, high-loading, and wide-temperature zinc ion hybrid supercapacitors through combining O/N-doped AC, aqueous binder and concentrated electrolyte. Benefiting from large surface area, hierarchically porous structure, and enriched oxygen-nitrogen dopants, the activated carbon manifests large capacitance for charge storage. Aqueous binder based on sodium alginate not only shows much improved capacitance due to enhanced electrode//electrolyte wettability but also enables high-mass-loading electrode. Concentrated electrolyte demonstrates enhanced Zn stripping/plating efficiency extending cycle life and suppressed hydrogen bonding interaction in water lowering freezing temperature. As a result, optimized ZICs function well under extreme conditions including 200 Ag⁻¹ charging rate, 0.3 million cycles, 10 mg

cm⁻² loading, and -60~60 °C temperature range. The strategy employed in the work will be of great significance to the development of cheap, multifunctional and extreme supercapacitors beyond ZICs.

3.5 Supporting Information

Structural Characterizations of AC

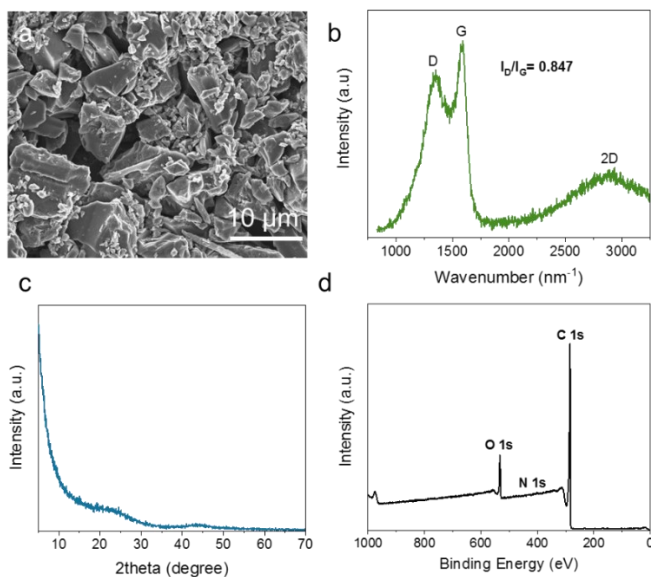


Figure S3.1 Structural characterization of AC. (a) SEM image, (b) Raman spectrum, (c) XRD pattern, and (d) XPS full spectrum.

AC-SA stability in water vs. ZnSO₄ electrolyte

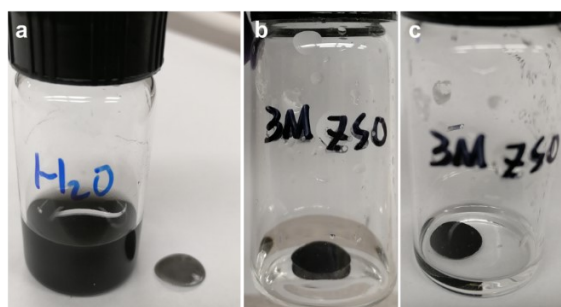


Figure S3.2 Digital photos of AC-SA electrodes in different solution: (a) deionized water, (b) 3M ZnSO₄, and (c) 3M ZnSO₄ for 10 days. AC-SA is easily dispersible in water due to high water solubility of SA. However, in 3M ZnSO₄, AC-SA is pretty stable for more than 10 days due to the formation of crosslinking network between zinc ions and sodium alginate with carboxylic/hydroxyl groups.

AC electrodes in different electrolyte

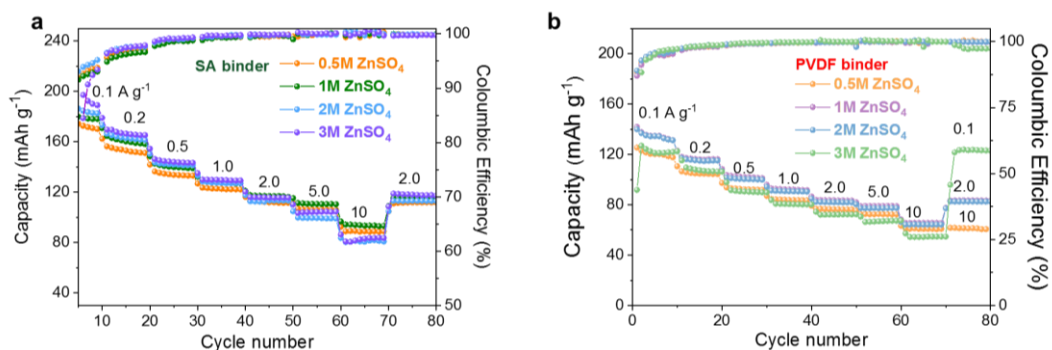


Figure S3.3 Rate performance of AC-SA and AC-PVDF electrodes in different electrolyte (0.5M, 1M, 2M, 3M ZnSO₄).

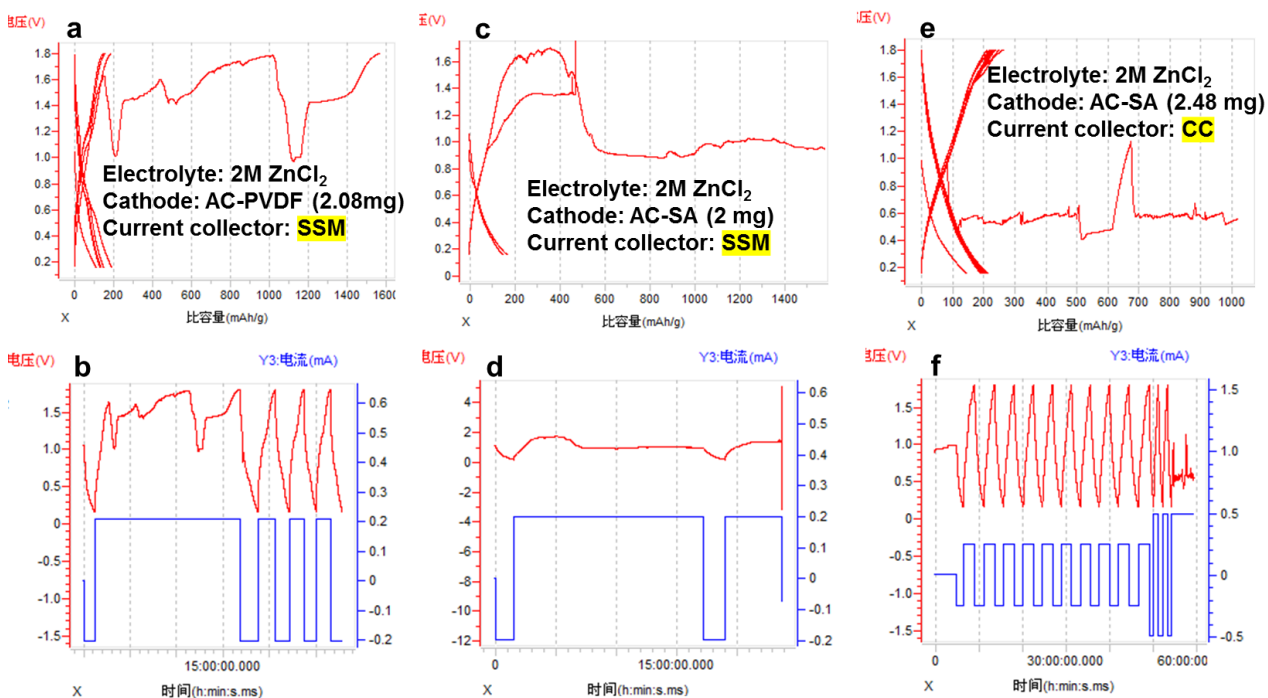


Figure S3.4 Electrochemical performance of AC electrodes in 2M ZnCl₂ electrolyte: (a,b) AC-PVDF electrode using SSM as the current collector, (c, d), AC-SA electrode using SSM as the current collector, (e, f) AC-SA electrode using carbon cloth as the current collector.

The reason for the short cycles of AC electrodes in 2M ZnCl₂ electrolyte may be caused by the chloride corrosion on the stainless-steel current collectors, packaging materials, and Zn foil at room temperature. One possible solution is the use of special cells like Swagelok cell composed of glassy carbon electrodes and PEEK body.

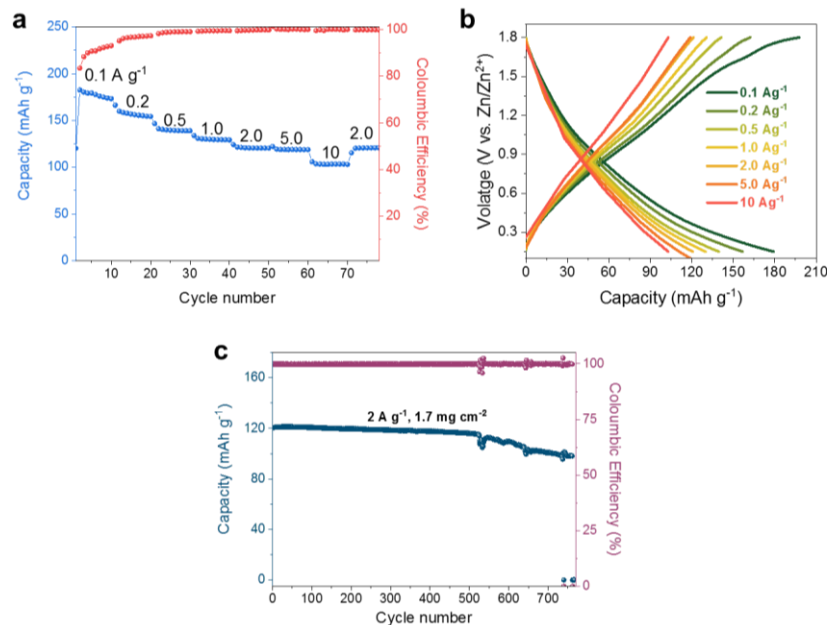


Figure S3.5 Electrochemical performance of AC-SA electrode in 2M Zn(OTf)₂ electrolyte.

Corrosion behavior of Zn metal in ZnSO₄ electrolyte

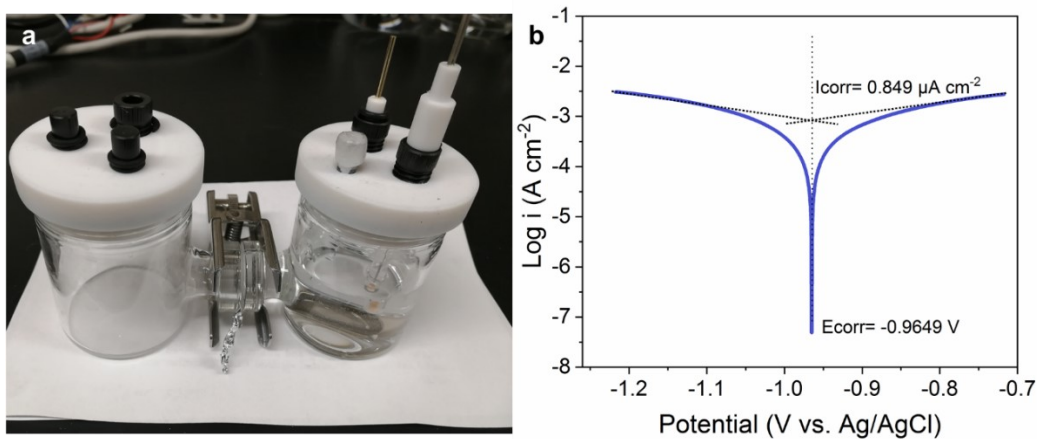


Figure S3.6 (a) H-cell setup for the testing of corrosion behavior of Zn foil in which only one chamber is filled with 3M ZnSO₄ electrolyte and the Zn foil was put in between two chambers so that only one side is exposed to the electrolyte. (b) Tafel polarization curve of Zn electrode tested in a three-electrode system with 3M ZnSO₄ (pH=3.4) as the electrolyte, Zn foil (diameter: 1.6 cm) as the working electrode, and Ag/AgCl (saturated KCl) as the reference electrode. In 3M ZnSO₄, Zn anode displays a high corrosion potential of -0.9649 V vs. Ag/AgCl and a low corrosion current density of 0.849 μA cm⁻².

AC-PVDF electrode for high-rate cycling

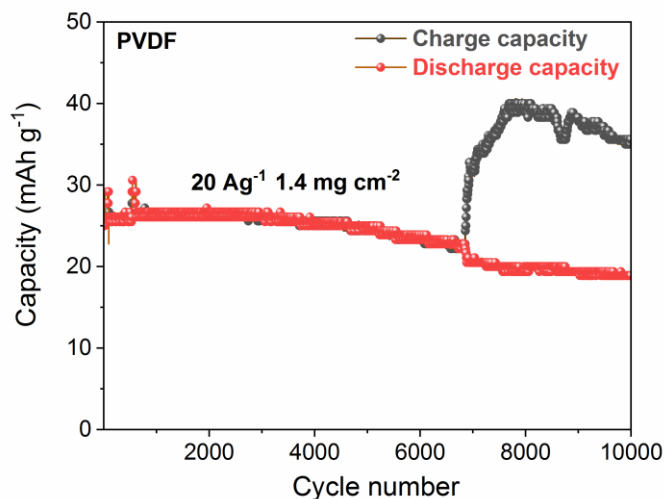


Figure S3.7 Cycling performance of AC-PVDF electrode in 2M ZnSO₄ electrolyte at a high rate of 20 Ag⁻¹.

Zn morphology after ultrahigh-rate cycling

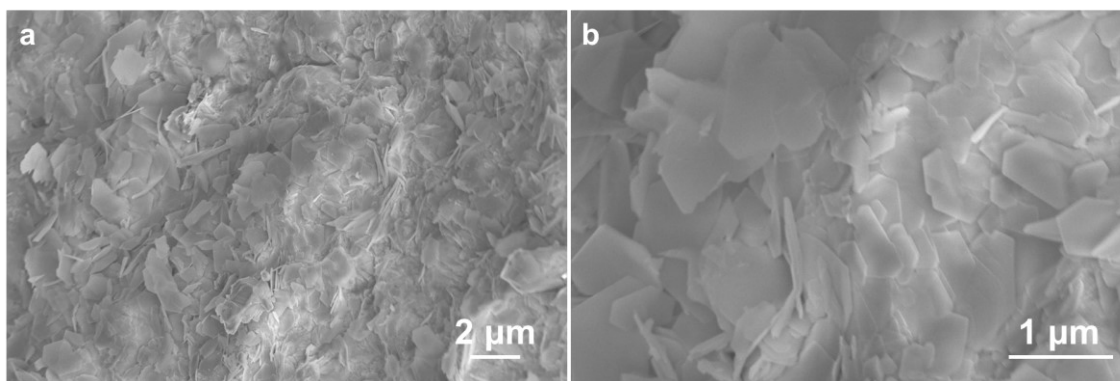


Figure S3.8 SEM images of Zn anode after 80000 cycles at 20 Ag⁻¹. Hexagonal flakes can be found which may be composed of zinc hydroxide sulfate. Zn dendrites may be underneath zinc hydroxide sulfate.

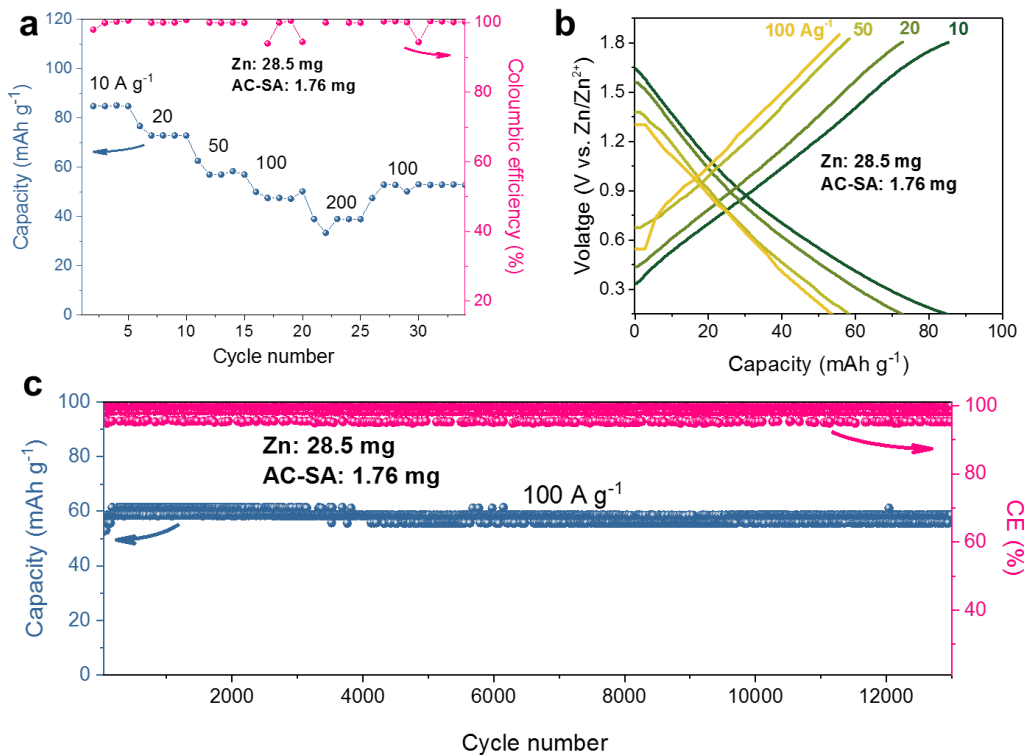


Figure S3.9 Electrochemical performance of AC-SA electrode under ultrahigh-rate cycling using thin Zn foils (30 μm thickness). (a) Rate performance, (b) Charge/discharge profiles, (c) cycling at 100 A g^{-1} .

Kinetic Analysis of AC-SA vs. AC-PVDF electrode

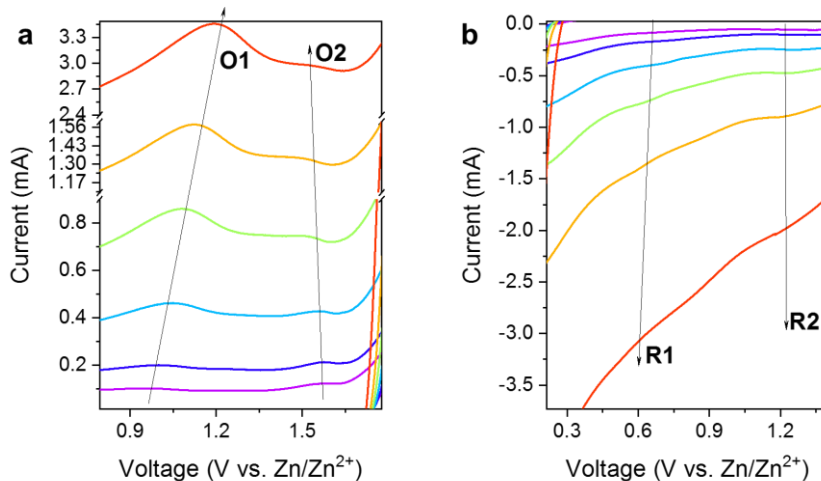


Figure S3.10 Redox peaks for calculating b values in AC-SA electrode.

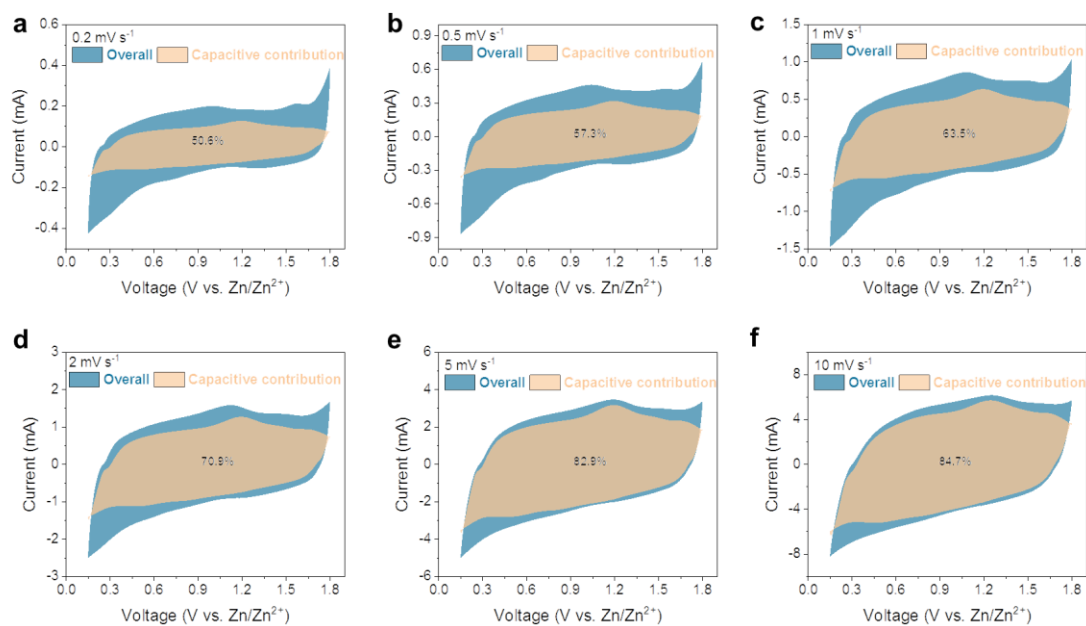


Figure S3.11 Capacitive contributions of AC-SA electrode under different scan rates.

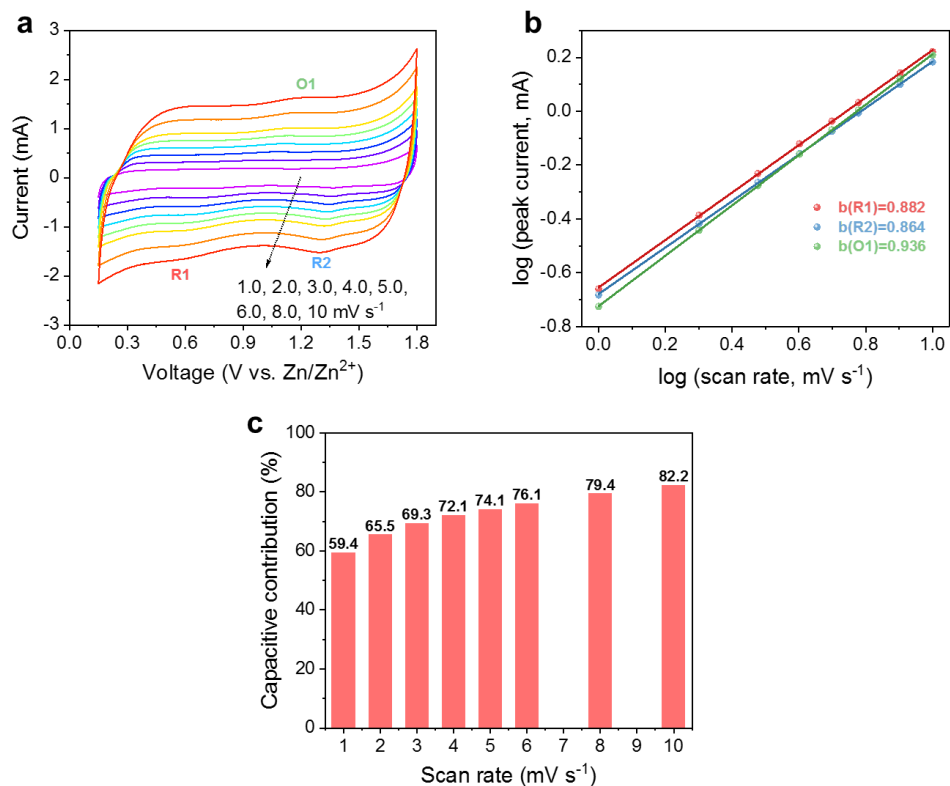


Figure S3.12 The kinetics analysis of AC-PVDF electrode. (a) CV curves, (b) b value plot, and (c) capacitive contributions at different scan rate.

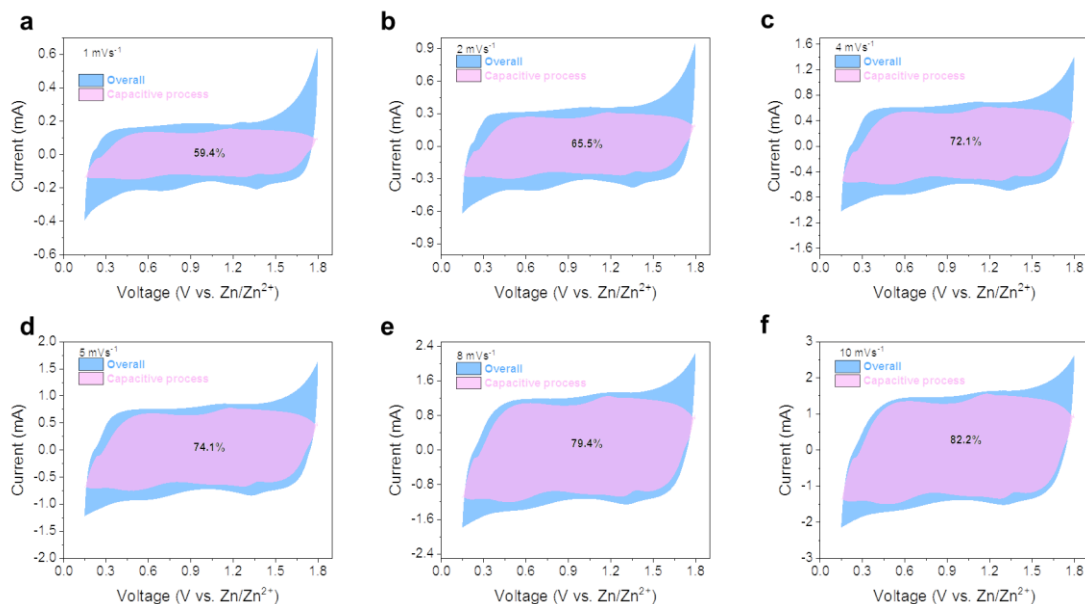
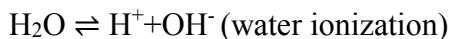


Figure S3.13 Capacitive contributions of AC-PVDF electrode under different scan rates.

Probable electrochemical reactions for the AC electrode:



Discharging:

<p>Anode:</p> $\text{Zn} - 2\text{e} \longrightarrow \text{Zn}^{2+}$ $4\text{Zn}^{2+} + 6\text{OH}^- + \text{SO}_4^{2-} + \text{xH}_2\text{O} \longrightarrow \text{Zn}_4(\text{OH})_6\text{SO}_4 \cdot \text{xH}_2\text{O}$ (small amount)	<p>Cathode:</p> $\text{AC-C=O} + \text{e} + \text{H}^+ \longrightarrow \text{AC-C-OH}$ $\text{AC-C=O} + \text{e} + \text{Zn}^{2+} \longrightarrow \text{AC-C-O-Zn}$ $4\text{Zn}^{2+} + 6\text{OH}^- + \text{SO}_4^{2-} + \text{xH}_2\text{O} \longrightarrow \text{Zn}_4(\text{OH})_6\text{SO}_4 \cdot \text{xH}_2\text{O}$ (large amount)
--	--

Charging:

<p>Anode:</p> $\text{Zn}^{2+} + 2\text{e} \longrightarrow \text{Zn}$ $\text{Zn}_4(\text{OH})_6\text{SO}_4 \cdot \text{xH}_2\text{O} + 6\text{H}^+ \longrightarrow 4\text{Zn}^{2+} + \text{SO}_4^{2-} + (6+\text{x}) \text{H}_2\text{O}$ (small amount)	<p>Cathode:</p> $\text{AC-C-OH} \longrightarrow \text{AC-C=O} + \text{e} + \text{H}^+$ $\text{AC-C-O-Zn} \longrightarrow \text{AC-C=O} + \text{e} + \text{Zn}^{2+}$ $\text{Zn}_4(\text{OH})_6\text{SO}_4 \cdot \text{xH}_2\text{O} + 6\text{H}^+ \longrightarrow 4\text{Zn}^{2+} + \text{SO}_4^{2-} + (6+\text{x}) \text{H}_2\text{O}$ (large amount)
---	---

The contribution of N dopants during ions storage

As reported by a previous report⁹⁸, N dopants could considerably lower the energy barrier for C-O-Zn bonding and hence facilitating the chemical adsorption of Zn ions onto AC electrode, which could further enhance the zinc-ion storage capability with larger capacitance. On the other hand, N doping improve the wettability and electrical conductivity of the AC electrode, further boosting charge/mass transports at the electrode/electrolyte interface.

AC-PVDF electrodes with different mass loading

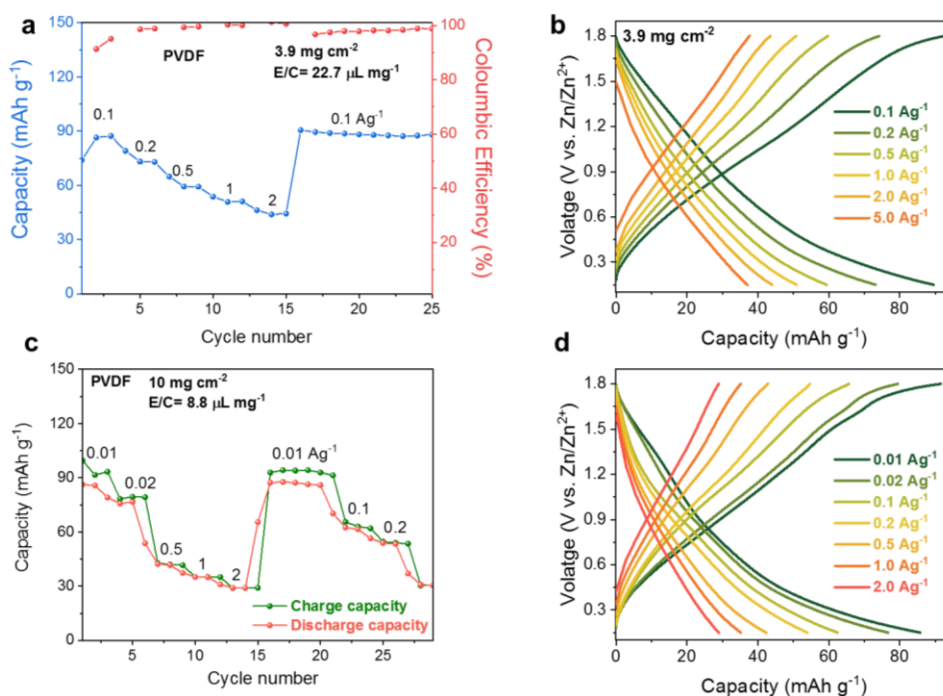


Figure S3.14 Electrochemical performance of AC-PVDF electrodes under different mass loadings. (a) rate performance and corresponding (b) charge-discharge curves of AC-PVDF with a 3.9 mg cm^{-2} loading. (c) rate performance and corresponding (d) charge-discharge curves of AC-PVDF with a 10 mg cm^{-2} loading.

AC-SA electrodes with different mass loading

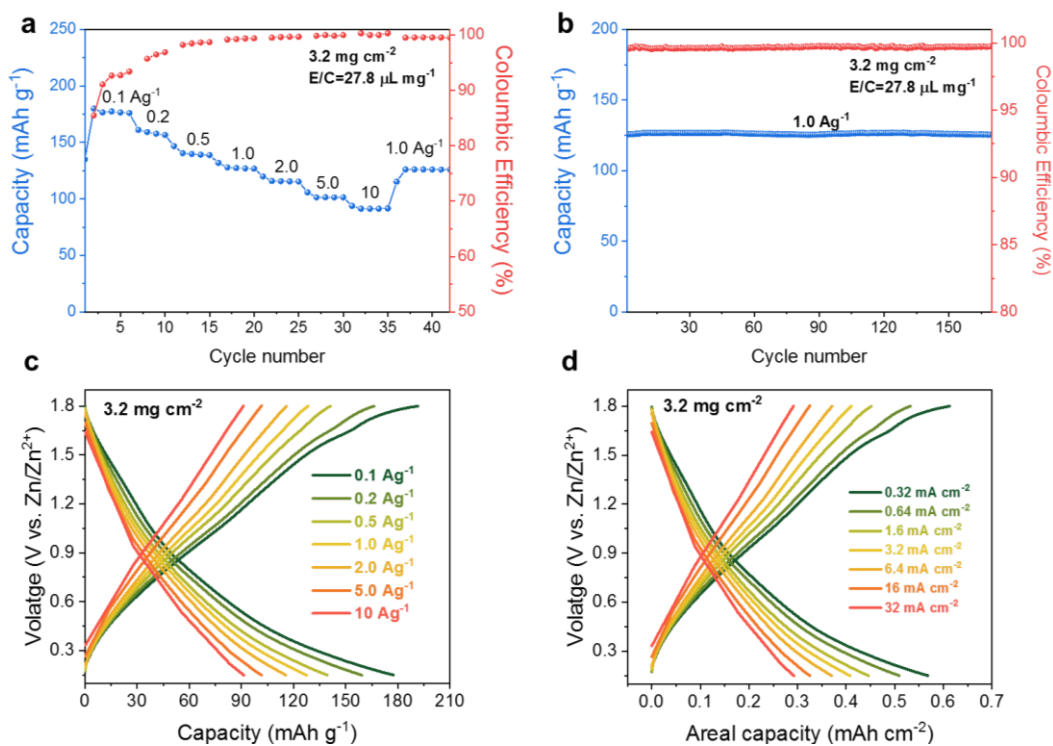


Figure S3.15 Electrochemical performance of low-loading AC-SA electrode (3.2 mg cm⁻²).

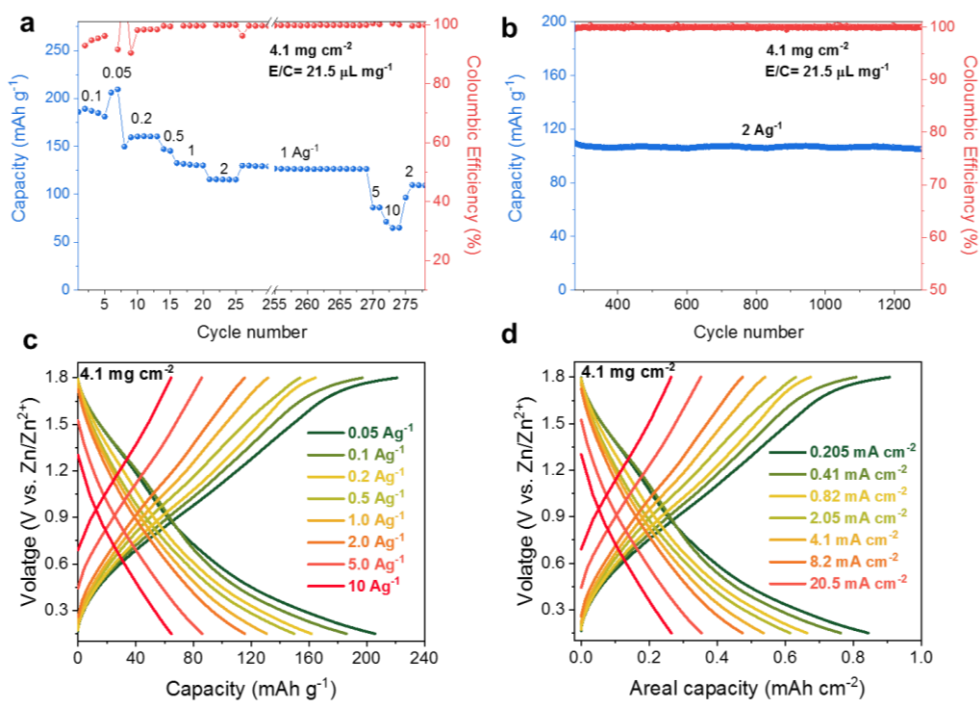


Figure S3.16 Electrochemical performance of low-loading AC-SA electrode (4.1 mg cm⁻²).

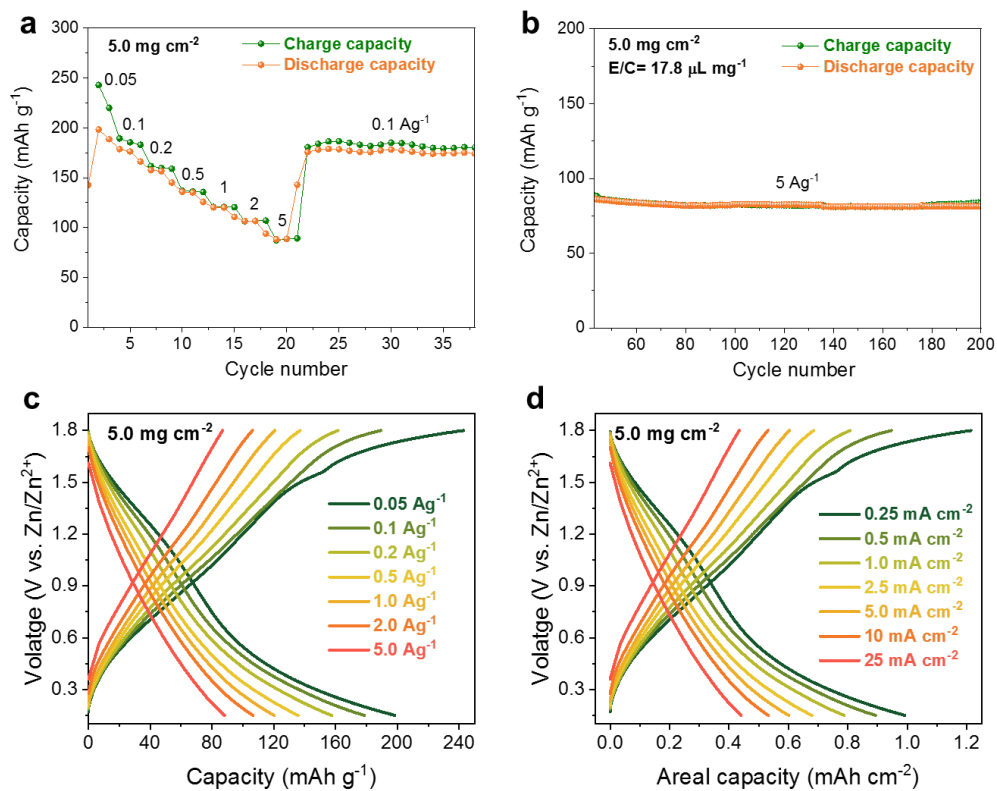


Figure S3.17 Electrochemical performance of medium-loading AC-SA electrode (5.0 mg cm⁻²).

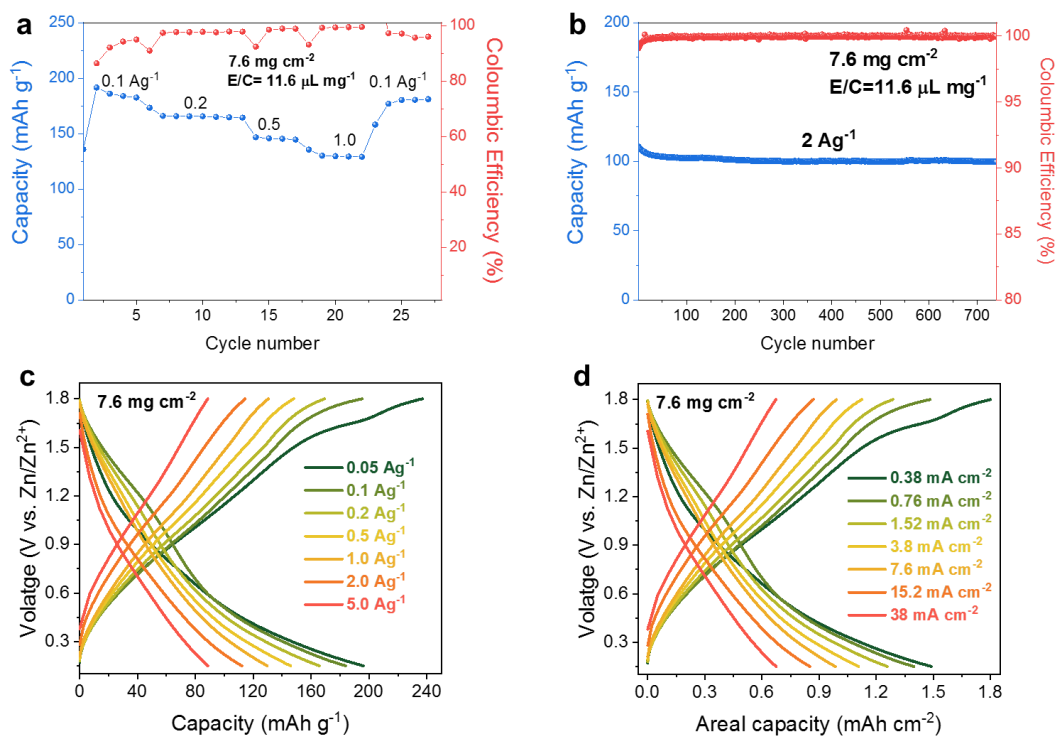


Figure S3.18 Electrochemical performance of medium-loading AC-SA electrode (7.6 mg cm⁻²).

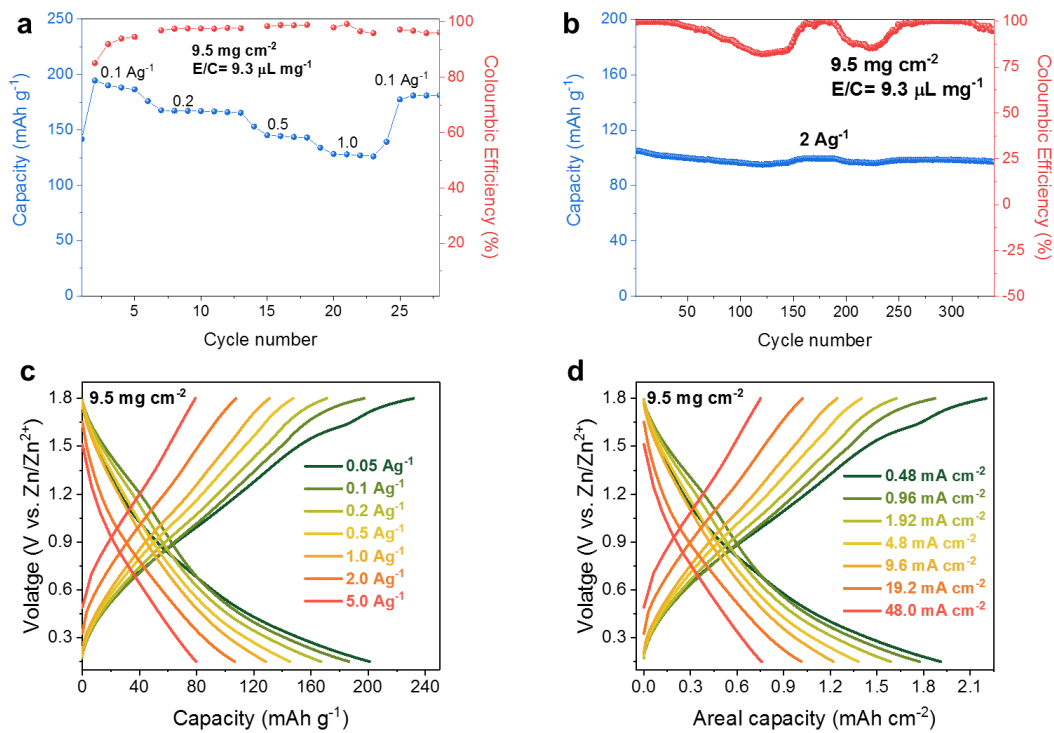


Figure S3.19 Electrochemical performance of high-loading AC-SA electrode (9.5 mg cm⁻²).

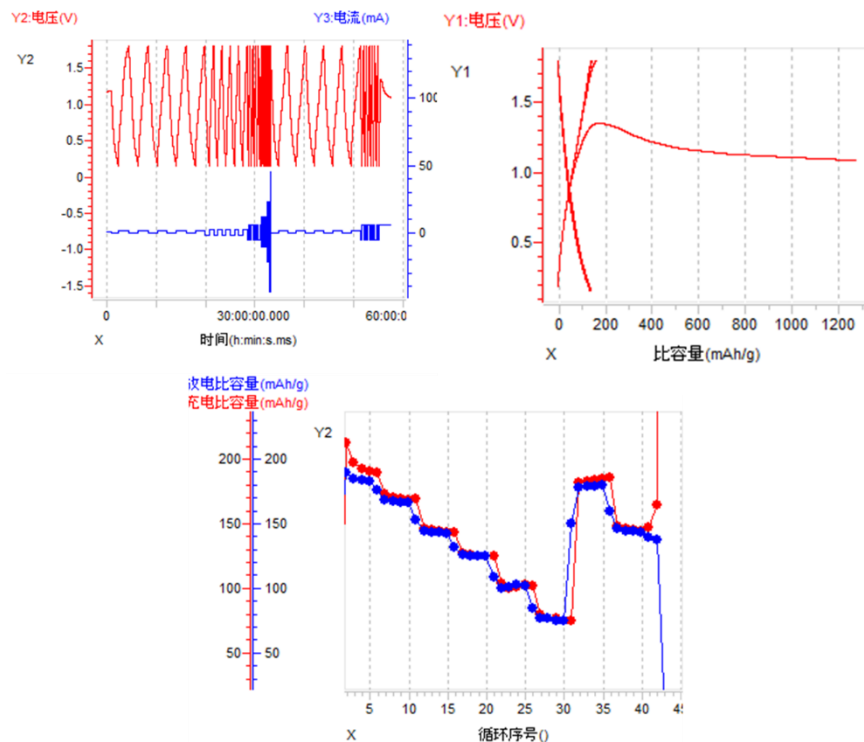


Figure S3.20 Cycling performance of high-loading AC-SA electrode (10 mg cm⁻²) showing the failure of the capacitor after 42 cycles.

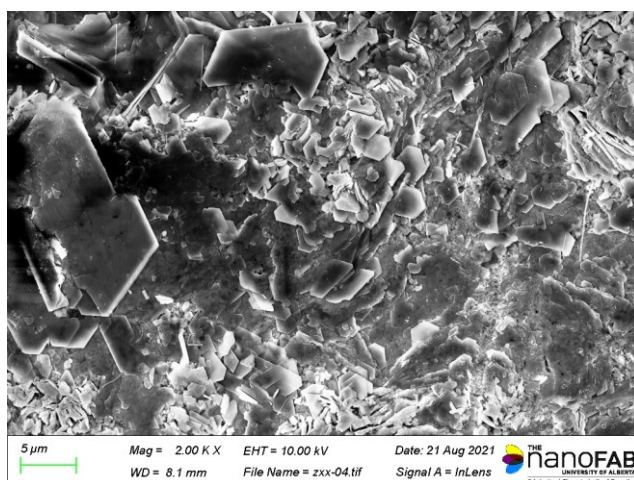


Figure S3.21 Morphology of after-cycling zinc electrode in Figure S3.20 indicating the presence of Zn dendrites.

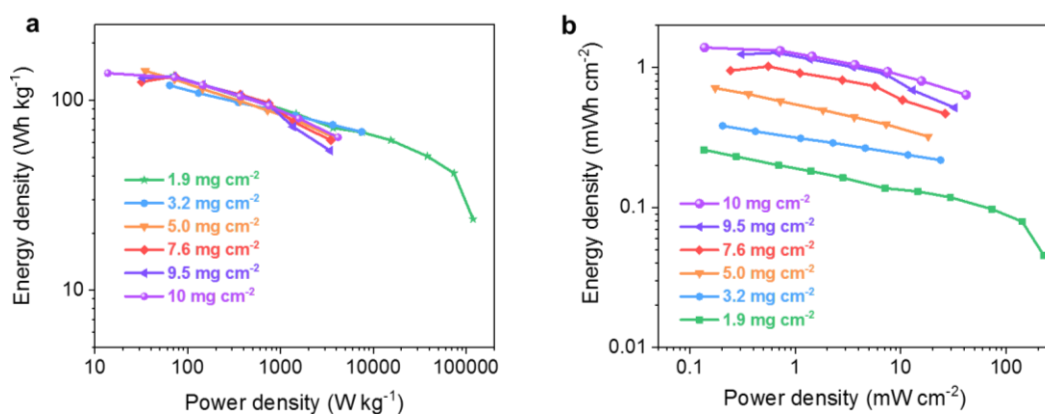


Figure S3.22 Energy density and power density of AC-SA electrodes with different mass loadings. (a) gravimetric energy/power densities and (b) areal energy/power densities. The calculation is based on the active mass of the AC-SA electrode.

AC electrodes for low-temperature ZICs

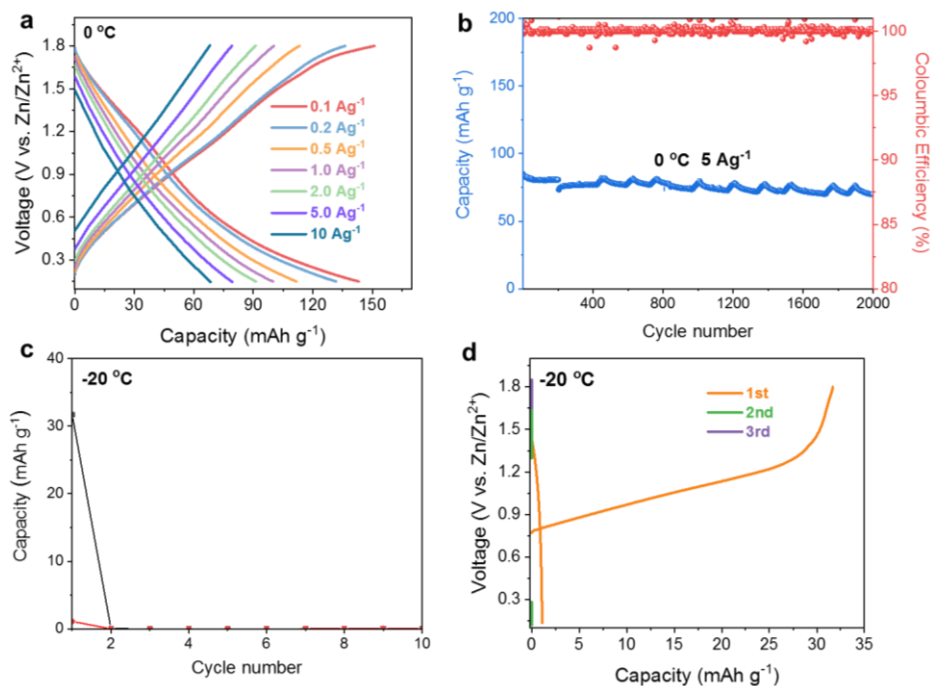


Figure S3.23 Electrochemical performance of AC-SA electrode at low temperatures (0 °C and -20 °C) in 3M ZnSO₄ electrolyte.

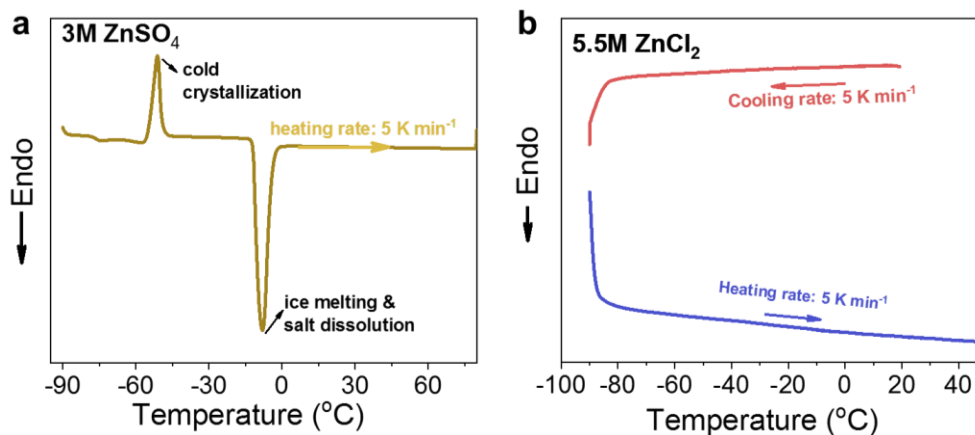


Figure S3.24 DSC curves of electrolyte. (a) 3M ZnSO₄, (b) 5.5M ZnCl₂.

The peaks in the heating process of ZnSO₄ can be ascribed to cold crystallization, ice melting and salt dissolution, respectively. Due to the low ice melting temperature around -10 °C, 3M ZnSO₄ is not suitable for ZICs working at a temperature less than -10 °C. By contrast, 5.5M ZnCl₂ shows a broad peak starting from -85 °C during the heating/cooling process belonging to the glass-liquid transition process, suggesting its ultralow-temperature workability.

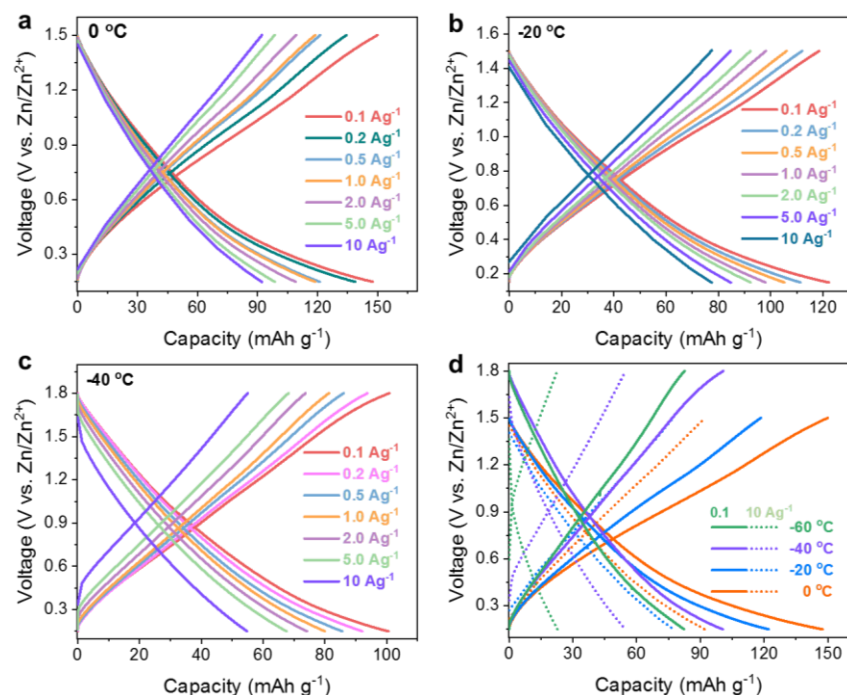


Figure S3.25 Charge-discharge curves of AC-SA electrode at different current densities under low temperatures (0 °C, -20 °C, -40 °C, and -60 °C) in 5.5M ZnCl₂ electrolyte.

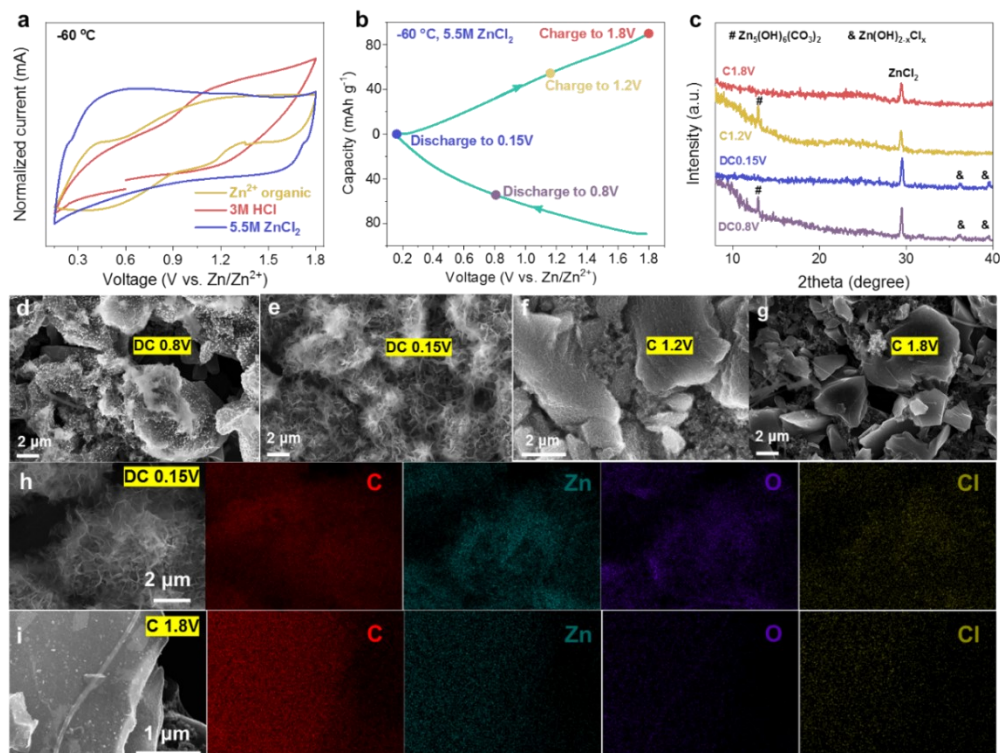


Figure S3.26 Storage mechanism of AC-SA electrode for ZICs in 5.5 M ZnCl₂ at -60 °C. (a) normalized CV curves of AC-SA electrode in different electrolyte. (b) Charge-discharge profiles

indicating electrodes under different states. (purple: discharge to 0.8V, blue: discharge to 0.15V, yellow: charge to 1.2V, red: charge to 1.8V). (c) XRD patterns of AC electrodes under different charge/discharge states. (d-f) SEM images of AC-SA electrode at different states: (d) DC 0.8V, (e) DC 0.15V, (f) C1.2V, (g) C1.8V. (h-i) SEM EDX elemental mapping of AC-SA electrode under (h) DC 0.15V and (i) C 1.8V.

XRD patterns (Figure S3.26c) of DC 0.15V and DC 0.8V electrodes all show diffraction peaks of Zn(OH)_2 (JCPDS card #76-1778) while these peaks are absent in charged electrodes, indicating the reversible (de)insertion of proton during storage process. XRD patterns also suggest the involvement of $\text{Zn}_5(\text{OH})_6(\text{CO}_3)_2$ intermediate (JCPDS card #72-1100) during charge/discharge, which may be derived from interaction between carboxylic group and zinc hydroxide, which needs further study to comprehend the detailed process. The reversible proton (de)insertion process is further verified by SEM images (Figure S3.26d-g) in which zinc hydroxide nanoflakes gradually appear and disappear on the AC particles when the electrode was discharged to 0.15V and charged back to 1.8V. The elemental mappings verify that the nanoflakes formed at the discharged state are composed of Zn and O elements (Figure S3.26h-i), matching well with XRD patterns. The Zn(OH)_2 may also be intercalated with certain Cl^- anions. Above results suggest that protons take part in the energy storage during ZIC charging and discharging. Besides the proton interaction, the zinc ion insertion should also contribute to the storage, as suggested by CV profiles in different electrolyte (Figure S3.26a). The profile of 5.5M ZnCl_2 does not overlap with that of either 3M HCl or Zn^{2+} -only organic electrolyte (1M ZnCl_2 -DMF) but combines characteristics of both electrolytes, implying the mechanism involving both proton and zinc ion storage. These results confirm that both proton and Zn ions are active cation contributing to the capacity during ZICs operation in 5.5M ZnCl_2 at -60°C .

AC electrodes for high-temperature ZICs

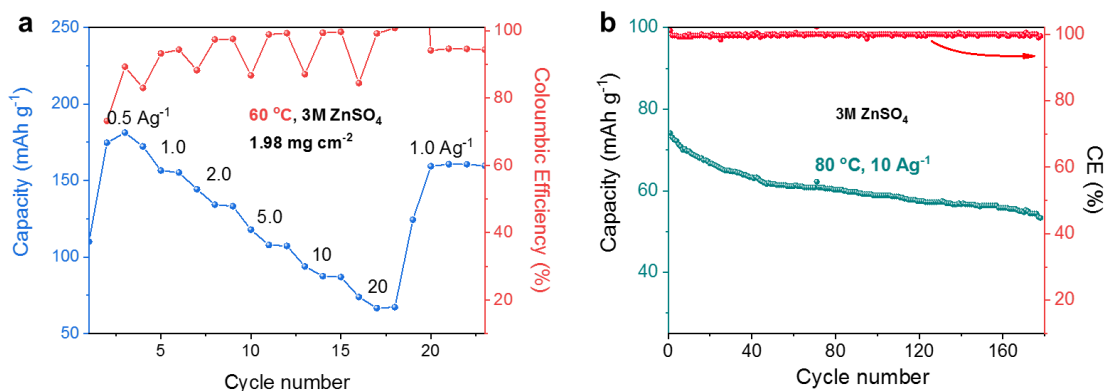


Figure S3.27 Electrochemical performance of AC-SA electrode in 3M ZnSO₄ electrolyte at high temperatures. (a) Rate performance at 60 °C and (b) cycling performance at 10 Ag⁻¹ at 80 °C.

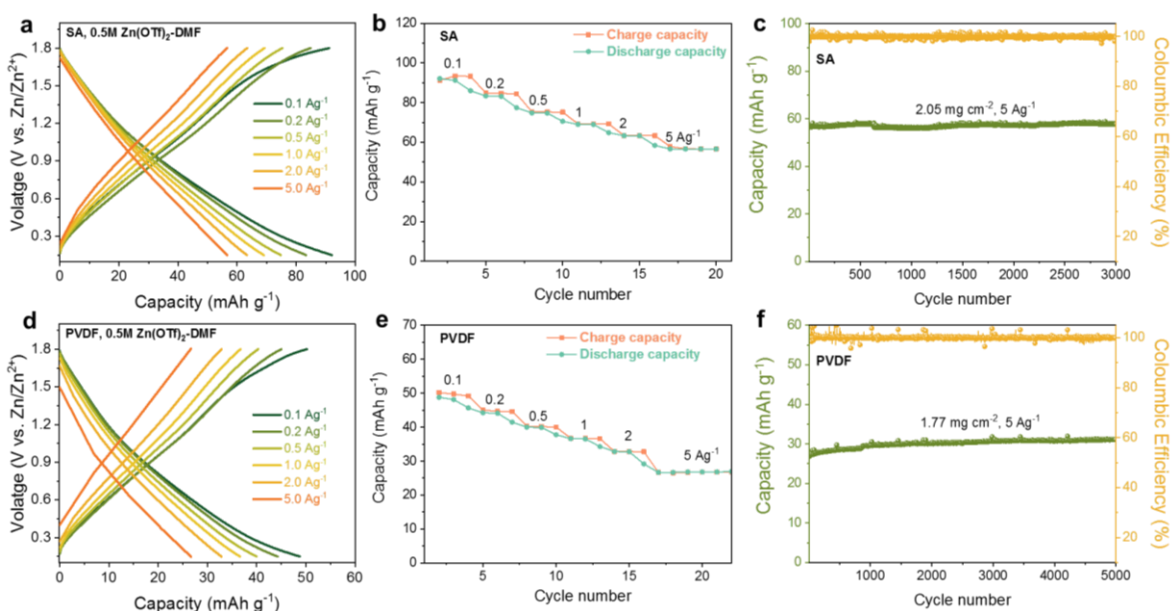


Figure S3.28 Electrochemical performance of AC-SA and AC-PVDF electrode in organic electrolyte (0.5M Zn(OTf)₂-DMF) at room temperature (20 °C). (a, d) charge-discharge curves, (b, e) rate performance, (c, f) cycling performance of (a-c) AC-SA and (d-f) AC-PVDF electrodes.

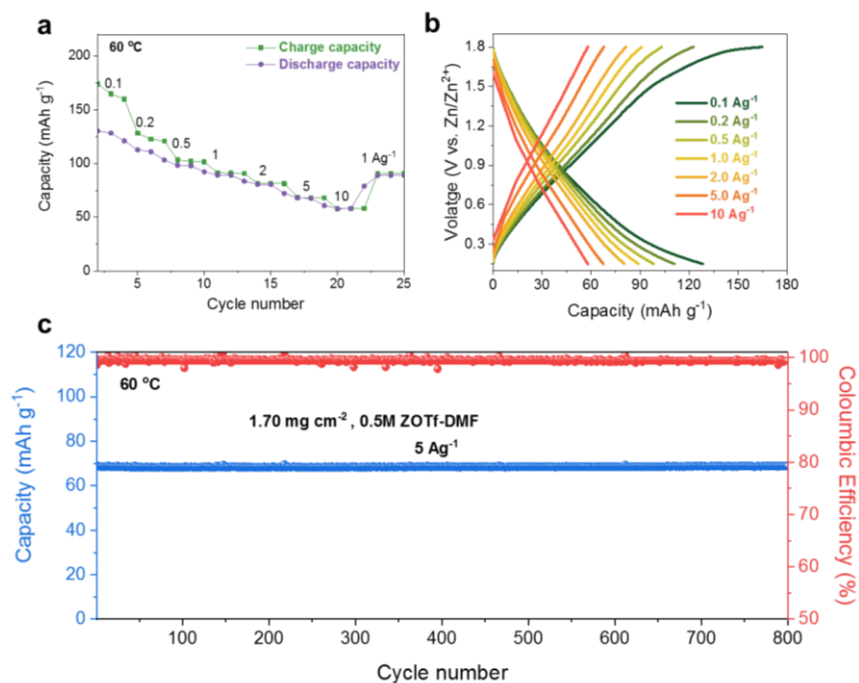


Figure S3.29 Electrochemical performance of AC-SA electrode in organic electrolyte (0.5M Zn(OTf)₂-DMF) at 60 °C. (a) rate performance, (b) charge-discharge curves, (c) cycling performance at 5 Ag⁻¹.

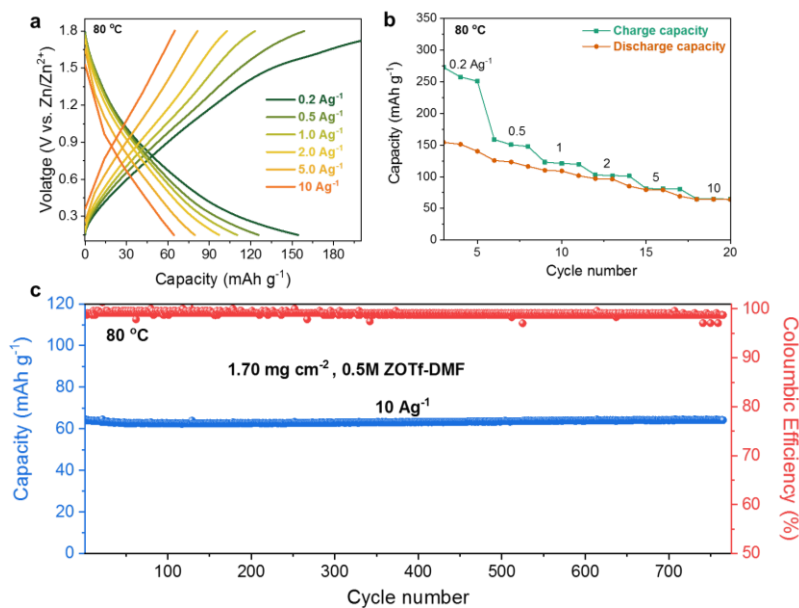


Figure S3.30 Electrochemical performance of AC-SA electrode in organic electrolyte (0.5M Zn(OTf)₂-DMF) at 80 °C. (a) rate performance, (b) charge-discharge curves, (c) cycling performance at 10 Ag⁻¹.

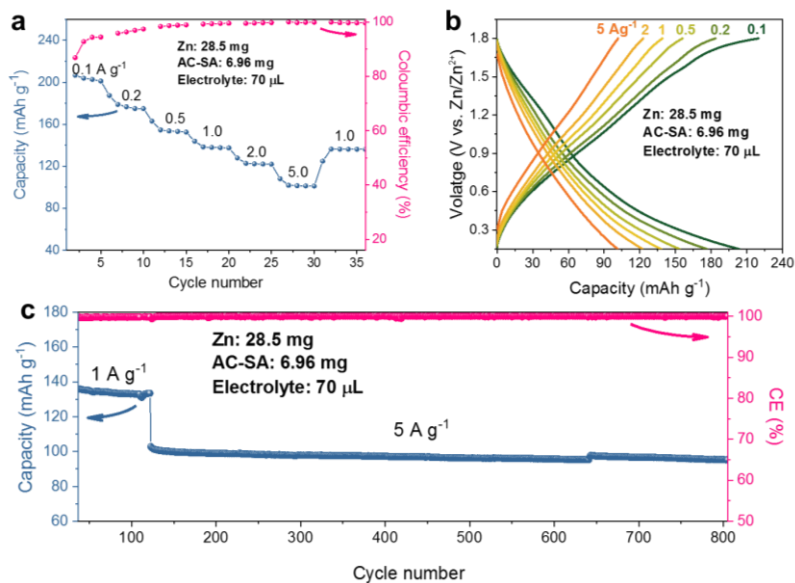


Figure S3.31 Electrochemical performance of high-loading AC-SA electrode (6.96 mg) tested under harsh conditions including thin Zn foil (30 μm thick, 1.13 cm², 28.5 mg) and lean electrolyte (70 μL 3M ZSO, 98.8 mg). Unexpectedly, the use of thin Zn foil and lean electrolyte enables slightly higher capacity in AC-SA electrode compared with thick Zn foil and flooded electrolyte. The capacity is around 205 mAh g⁻¹ at 0.1 A g⁻¹ and 100 mAh g⁻¹ at 5 A g⁻¹. It can be cycled stably for over 800 cycles with negligible capacity loss and ~100% Coulombic efficiency.

Table S3.1 Comparison of high-rate electrode materials for zinc ion capacitors

Cathode	Loading (mg cm ⁻²)	Electrolyte	Rate performance (@ Ag ⁻¹)	Cycle performance (% , cycles, Ag ⁻¹)	Reference
AC-SA	1.9-10	2M ZnSO ₄	90 mAh g ⁻¹ (196 Fg ⁻¹) @10 69 mAh g ⁻¹ (150.5 Fg ⁻¹) @50	100%, 70000, 20 98.1%, 200000, 45	This work
AC	0.7–0.8	2M ZnSO ₄	41 mAh g ⁻¹ @ 20	100%, 10000, 10	<i>Energy Storage Mater.</i> , 2018, 13, 96 ⁹²
AC	N.A.	2M ZnSO ₄	45 mAh g ⁻¹ @ 0.6	100%, 10000, 0.3	<i>Adv. Mater.</i> , 2018, 31, 1806005 ⁹⁵
AC	N.A.	1M Zn(OTf) ₂ /AN	72 mAh g ⁻¹ @ 2	91%, 20000, 2	<i>Energy Storage Mater.</i> , 2018, 13, 1 ¹³
AC	6	2M ZnSO ₄	29 mAh g ⁻¹ @ 10	72%, 20000, 4	<i>Joule</i> , 2019, 3, 1289 ¹⁵⁵
BNC	2	1M ZnSO ₄	42.8 mAh g ⁻¹ @20	81.3%, 6500, 5	<i>Nano Energy</i> , 2019, 66, 104132 ⁹⁶
HNPC	1–1.2	1M ZnSO ₄	108.2 mAh g ⁻¹ @ 33.3	73.6%, 100000, 16.7	<i>Adv. Mater.</i> , 2019, 31, 1904948 ⁹⁸
N-HPC	1.0	2M ZnSO ₄	66.7 mAh g ⁻¹ @ 10	90.9%, 5000, 1	<i>Nano Res.</i> 2019, 12, 2935 ⁹⁴
aMEGO	N.A.	3M Zn(OTf) ₂	100 F g ⁻¹ @20	93%, 80000, 8	<i>Adv. Energy Mater.</i> 2019, 9, 1902915 ¹⁴⁷
AC	N.A.	2M ZnSO ₄	150 F g ⁻¹ @20	99%, 10000, 10	<i>Adv. Energy Mater.</i> 2020, 10, 1902981 ³¹
Diamond	N.A.	1M ZnSO ₄	56.8 F g ⁻¹ @1	89.9%, 10000, 1	<i>Adv. Energy Mater.</i> 2020, 10, 2002202 ¹⁵⁶
PSC-A600	2	1M Zn(OTf) ₂	81.8 mAh g ⁻¹ @20	92.2%, 10000, 10	<i>Energy Storage Mater.</i> 2020, 28, 307 ⁹³
PC800	1.4–2.0	3M Zn(ClO ₄) ₂	78.4 mAh g ⁻¹ @20	99.2%, 30000, 20	<i>Adv. Energy Mater.</i> 2020, 10, 2001705 ¹²¹
HPAC	0.6	3M Zn(OTf) ₂	119 mAh g ⁻¹ @20	70%, 18000, 10	<i>Small</i> 2020, 16, 2003174 ¹²⁸
AC	0.8	2M ZnCl ₂	159.7 F g ⁻¹ @20	95.1 %, 100000, 5	<i>Angew. Chem. Int. Ed.</i> 2021, 60, 990 ¹³⁶
HHT-rGO	1.7–3.2	1M ZnSO ₄	159 F g ⁻¹ @100 mVs ⁻¹	97.8%, 20000, 2.5	<i>Adv. Funct. Mater.</i> 2020, 2007843 ¹²⁷
MCHS	1-20	2M ZnSO ₄	96.9 mAh g ⁻¹ @10	100%, 10000, 1	<i>Energy Storage Mater.</i> 2020, 25, 858. ⁹⁷
OPCNF-20	~1	1M ZnSO ₄	38.8 mAh g ⁻¹ @ 20	81%, 50000, 5	<i>Chem. Eng. J.</i> 2021, 421, 129786. ¹⁵⁷
Ti ₃ C ₂ T _x -rGO	~1	2M ZnSO ₄	40.3 F g ⁻¹ @6	95%, 75000, 5	<i>Adv. Electron. Mater.</i> 2019, 5, 1900537 ¹⁵⁸
Ti ₃ C ₂	N.A.	2M ZnSO ₄	121 F g ⁻¹ @3	82.5%, 1000, 3	<i>ACS Nano</i> 2019, 13, 7, 8275 ¹⁵⁴

Table S3.2 Comparison of high-rate electrode materials for zinc ion batteries

Materials	Loading (mg cm ⁻²)	Electrolyte	Rate performance (mAhg ⁻¹ @ Ag ⁻¹)	Cycling performance (%, cycles, Ag ⁻¹)
AC-SA (This work)	1.9-10	2M ZnSO ₄	90@10 69@50	100%, 30000, 20(100) Ag ⁻¹ 98.1%, 200000, 45 Ag ⁻¹
Organics				
PTCDA ¹⁵⁹	2.5	2 M ZnCl ₂	76.9 @ 32	68.2%, 1000, 8 Ag ⁻¹
PANI ¹⁶⁰	1.5	1 M Zn(OTf) ₂	95 @ 5	92%, 3000, 5 Ag ⁻¹
PPy ¹⁶¹	N.A	Zn(Ac) ₂ - KCl-PVA	37 @ 44.7	38%, 200, 4.4 Ag ⁻¹
PTO ¹⁶²	4-6	2M ZnSO ₄	113 @ 20	70%, 1000, 3Ag ⁻¹
poly(1,5-NAPD) ¹⁶³	2.7	2M ZnSO ₄	145 @ 14.8	91%, 10000, 10 Ag ⁻¹
Mn-based				
β-MnO₂ ⁵⁷	~2.0	3M Zn(OTf) ₂ + 0.1M Mn(OTf) ₂	100 @10	94%, 2000, 2Ag ⁻¹
δ-MnO₂ ¹⁶⁴	N. A.	2M ZnSO ₄ + 0.1M MnSO ₄	124 @ 3	74%, 2000, 3Ag ⁻¹
γ-MnO₂ ¹⁶⁵	2.0-3.0	3M ZnSO ₄ + 0.2 M MnSO ₄	80 @ 5	95%, 1000, 2Ag ⁻¹
O-deficient σ-MnO₂ ⁹⁹	1.0	1 M ZnSO ₄ + 0.2 M MnSO ₄	100 @ 10	80%, 2000, 5 A g ⁻¹
V-based				
V₂O₅ ¹⁶⁶	1.5	saturated ZnSO ₄	108@10	82%, 6200, 10Ag ⁻¹
V₂O₅·1.6H₂O ¹⁶⁷	2-3	3M Zn(OTf) ₂	251@20	95%, 5000, 10Ag ⁻¹
V₆O₁₃ ¹⁶⁸	1.0-1.5	3M Zn(OTf) ₂	144@24	90%, 2000, 4Ag ⁻¹
VN_{0.9}O_{0.15} ¹⁶⁹	N. A.	3M Zn(OTf) ₂	124@102.4	95%, 1800, 4.5 Ag ⁻¹
Na₂V₆O₁₆·3H₂O ¹⁷⁰	~3	1 M ZnSO ₄	112 @20	80%, 1000, 14.44 A g ⁻¹
Cu_{0.1}V₂O₅·0.08H₂O ¹⁷¹	N. A.	2 M ZnSO ₄	122 @ 20	88%, 10000, 10Ag ⁻¹
Zn_{0.3}V₂O₅·1.5H₂O ⁷⁰	2.0	3M Zn(OTf) ₂	265.2 @ 10	96%, 20000, 10Ag ⁻¹
Na₃V₂(PO₄)₂F₃ ²³	10	2M Zn(OTf) ₂	33 @ 3	95%, 4000, 1 A g ⁻¹
Li₃V(PO₄)₃ ⁷⁸	8-10	4M Zn(OTf) ₂	121.9 @ 9	78.8%, 4000, 1.5 A g ⁻¹
PBA				
ZnHCF ¹⁷²	8.0	3M ZnSO ₄	29.3 @ 1.2	80%, 200, 0.3 Ag ⁻¹
CoFe(CN)₆ ⁶⁵	N. A	4M Zn(OTf) ₂	109 @ 6	100%, 2200, 3 Ag ⁻¹

Table S3.3 Comparison of high-mass-loading electrode materials for zinc ion capacitors

Cathode	Loading (mg cm ⁻²)	Electrolyte	Rate performance (F cm ⁻² @ Ag ⁻¹)	Cycling performance (%, cycles, Ag ⁻¹)	Reference
AC-SA	4	3M ZnSO ₄	1.66 @ 0.05, 1.03 @ 1.0, 0.58 @ 5.0	100%, 1000, 2	This work
	7.6		3.44 @ 0.05, 2.15 @ 1.0, 1.48 @ 5.0	91%, 700, 2	
	10		4.36 @ 0.02, 2.71 @ 1.0, 1.67 @ 5.0	92.8%, 450, 1	
AC	3	7.5M ZnCl ₂ /PAM	0.84 @ 0.5	N. A.	<i>Angew. Chem. Int. Ed.</i> 2021, 60, 990. ¹³⁶
	5		1.22 @ 0.5	N. A.	
	10		1.60 @ 0.5	N. A.	
MCHS	5	2M ZnSO ₄	1.60 @ 0.1, 0.60 @ 1.0	N. A.	<i>Energy Storage Mater.</i> 2020, 25, 858. ⁹⁷
	10		1.65 @ 0.1, 1.15 @ 1.0	N. A.	
	20		3.24 @ 0.1, 2.20 @ 1.0	N. A.	
PSC-A600	4	1M Zn(OTf) ₂	1.44 @ 0.2, 0.56 @ 1.0	N. A.	<i>Energy Storage Mater.</i> 2020, 28, 307. ⁹³
	7		2.14 @ 0.2, 1.12 @ 1.0	N. A.	
	11		3.08 @ 0.2, 1.31 @ 1.0	N. A.	
OPCNF-20	4.4	1M ZnSO ₄	0.72 @ 0.5	54%, 50, 0.5	<i>Chem. Eng. J.</i> 2021, 421, 129786. ¹⁵⁷
	8.75		1.31 @ 0.5	55%, 50, 0.5	
	12.76		1.79 @ 0.5	56%, 50, 0.5	

Table S3.4 Comparison of low-temperature zinc ion capacitors

Cathode	Temperature	Electrolyte	Rate performance (Fg ⁻¹ @ Ag ⁻¹)	Cycle performance (%, cycles, Ag ⁻¹)	Reference
AC-SA	0 °C	5.5M ZnCl ₂	259.2 @ 1, 215.1 @ 5, 201.2 @ 10	100%, 1000, 10	This work
AC-SA	-20 °C	5.5M ZnCl ₂	213.8 @1 184.8 @5 169.1 @10	100%, 1000, 5	
AC-SA	-40 °C	5.5M ZnCl ₂	174.5 @1 147.5 @5 119.6 @10	100%, 1000, 10	
AC-SA	-60 °C	5.5M ZnCl ₂	144.2 @1 86.8 @5 49.5 @10	100%, 1000, 5	
AC	0 °C	7.5M ZnCl ₂ /PAM	190 @ 1, 160 @ 5, 140 @ 10,	N.A.	
AC	-20 °C	7.5M ZnCl ₂ /PAM	162 @ 1, 144.4 @ 5, 144.4 @ 10,	92.9%, 40000, 5	
PSC-A600	0 °C	1M Zn(OTf) ₂ / PVA	256.6 @ 1	100%, 80, 1	<i>Energy Storage Mater.</i> 2020, 28, 307 ⁹³
PSC-A600	-15 °C	1M Zn(OTf) ₂ /PVA	203.2 @ 1	86%, 80, 1	

Chapter 4 Efficient Zn Metal Anode Enabled by O, N-Codoped Carbon Microflowers

A version of this Chapter has been published in Nano Letters:

Zhixiao Xu, Song Jin, Nianji Zhang, Wenjing Deng, Min Ho Seo, Xiaolei Wang*, Efficient Zn Metal Anode Enabled by O, N-Codoped Carbon Microflowers. *Nano Letters*, 2022, 22, 1350-1357.

4.1 Introduction

Large-scale energy storage requires the development of safe, low-cost, and environmental-friendly systems, which cannot be met by the current market-dominated lithium ion batteries with limited lithium reserve and flammable organic electrolyte.^{120, 173} Alternatively, aqueous zinc metal-based energy devices show great promise for large-scale energy storage due to the advantage of Zn metals including high theoretical capacity (gravimetric: 820 mAh g⁻¹), suitable redox potential (-0.764 V vs. standard hydrogen electrode), high stability in air/water, cost effectiveness, and eco-friendliness.⁶ Accordingly, many Zn-based energy storage systems have been developed in past decades such as alkaline batteries,^{174, 175} flow batteries,^{176, 177} Zn-air batteries,^{178, 179} Zn-ion batteries,^{6, 137} and Zn-ion capacitors.¹² However, commercial Zn batteries are mostly primary ones that cannot be recharged for secondary uses due to the poor reversibility of Zn deposition/dissolution.^{15, 16} This poor reversibility is mainly caused by the low Coulombic efficiency (CE) and dendritic growth of Zn metal during cycling accompanied by side reactions from metal corrosion and hydrogen evolution due to water decomposition, significantly shortening device lifespan and reducing energy efficiency.^{10, 180} As such, it is of great significance to develop dendrite-free Zn metal anodes with high CE for rechargeable

batteries or capacitors, which unfortunately is still challenging as with other metal anodes (e.g. Li, Na, K and Al).¹⁸¹⁻¹⁸³

Accordingly, several strategies have been proposed, such as Zn host construction,^{22, 28} interfacial protection,^{25, 184, 185} and electrolyte engineering.^{41, 110} Despite the progress, most of reported Zn anode only experienced low depth of discharge (DOD, <1%),^{41, 186, 187} which will considerably lower cell-level energy densities. As such, construction of Zn hosts, e.g., carbon-rich nanomaterials, to regulate the plating/stripping of Zn metal anode under high DOD is of great significance to achieve large energy densities in full cells. For example, taking advantage of the small lattice mismatch between graphene and zinc, Zheng et al²⁷ reported the heteroepitaxial plating/stripping of Zn metal at ultrahigh current densities and capacities while Xia et al¹⁵⁵ reported the metal organic framework derived Zn atom-decorated carbon host with dendrite-suppressing capability and high efficiency. Qian *et al* reported MOF-derived N, O-codoped carbon array on Cu foam could serve as efficient host for Zn metal plating/stripping.¹⁸⁸ Through in/ex situ spectroscopy and experiments, Qiao *et al* revealed that zinc ions could bond with pyridine sites to generate Zn-N bonds which facilitates the Zn nucleation on carbon hosts and homogenous Zn deposition without dendrites.¹⁸⁹ Other carbon-based host materials include carbon nanotube (CNT) arrays,²⁸ graphene oxide,¹⁹ and graphite fiber,¹⁹⁰ to mention a few. As potential carbon hosts, 3D carbon superstructures with highly exposed surface area and hierarchically oriented building blocks could homogenize ionic flux, decrease local current densities, and guide Zn deposition in a unique way.^{138, 188, 191} Given that 3D carbon can be derived from different precursors including polymers and covalent/metal organic frameworks along with their wide tunability on micro-/nanostructures, heteroatom dopants, and vacancies,¹²³ there is still plenty of room to optimize 3D carbon-rich materials for Zn metal anode yet relevant studies are strangely rare.

Taking polymer-derived carbon as an example, we here firstly regulate heteroatom-doped 3D carbon host for high-DOD Zn metal chemistry, including Coulombic efficiency, deposition morphology, and full cell applications. Density functional theory (DFT) calculations reveal that among oxygen/nitrogen dopants the ether (C-O), carboxylic (-O-C=O-) and pyrrolic N groups show strong binding with Zn, making them favorable heterogeneous nucleation sites for zinc growth. Accordingly, monomers enriched with those O/N groups were rationally selected and corresponding polymers were prepared via controlled self-assembly and converted to carbon with different morphologies and sizes. Among carbon hosts, carbon flowers (C_{flower}), with microscale hierarchical structure, abundant meso/macro-porosity, and zincophilic oxygen/nitrogen dopants, enable horizontal Zn deposition following a heteroepitaxial mode and deliver superb electrochemical performance with high CE values of 97~99% at current densities of 0.5~10 mA cm⁻², surpassing other structured hosts. As a proof of concept, under high DOD (4.1-41.3%), the C_{flower} hosted Zn-based batteries and supercapacitors deliver better performance than those using hostless Zn.

4.2 Experimental Section

4.2.1 Samples preparation

Materials. Pyromellitic dianhydride (PMDA), dimethylformamide (DMF), polyvinylidene difluoride (PVDF), zinc sulfate heptahydrate ($ZnSO_4 \cdot 7H_2O$), manganese sulfate monohydrate ($MnSO_4 \cdot H_2O$) was purchased from Sigma-Aldrich, N-methylpyrrolidone (NMP), 4,4'-oxydianiline (ODA) and Zinc trifluoromethanesulfonate ($Zn(OTf)_2$) was purchased from TCI AMERICA, commercial activated carbon (AC) was purchased from MTI corporation. They are all in the analytical grade and directly used without further purification.

Synthesis of carbon flowers, disks, and spheres. Carbon is derived from corresponding polymer by carbonization. First, equal molar amount of monomers (ODA, 1.927 g and PMDA, 2.121 g) was

added sequentially into DMF (60 mL) and the solution was stirred at room temperature for 3 h. To make polyimides with flower-like morphology, part of the above solution (30 mL) was poured into Teflon-lined autoclave (40 mL capacity) and the polycondensation reaction was conducted at 160 °C for 6 h in the isotherm oven. The precipitate was collected after cooling, filtration, and drying, which was denoted as PI_{flower}. To make disk-like polyimides, another part of precursor solution (20 mL) was heated to the boiling point under strong stirring. Then it was filtrated, and the precipitate was collected after drying under 80 °C overnight. The sample was named as PI_{disk}. To make spherical polyimide, the above remaining precursor solution was directly poured into large amount of ethanol (80 mL) in a beaker under strong stirring. After filtration, drying and thermal imidization in tubular furnace (300 °C, 4h), the polymer powder was collected and denoted as PI_{sphere}. To make carbon materials, powdery polyimides (PI_{flower}, PI_{disk}, and PI_{sphere}) were thermally treated in the tubular furnace at 900 °C for 2h under flowing Ar gas, giving rise to their corresponding carbon products, including flower-like carbon (C_{flower}), disk-like carbon (C_{disk}), and spherical carbon (C_{sphere}).

4.2.2 Characterization

Fourier transform infrared spectra (FTIR) were collected on Nicolet 8700 with the KBr pellet technique. Raman spectra were obtained on a laser confocal Raman spectrometer (Renishaw inVia Qontor) with the laser wavelength of 532 nm. The thermal property of polymers was measured by the thermogravimetric analyzer (TGA Q50). The Rigaku XRD Ultima IV X-ray diffractometer with the Cu target (wavelength: 1.5406 Å) was used for X-ray diffraction (XRD) analysis. The morphology of samples was observed on the field-emission scanning electron microscope (Zeiss Sigma FESEM or Zeiss EVO M10 SEM) equipped with an EDX analyzer (Oxford AZtecSynergy). The Zn deposition morphology on different substrates was obtained after electrodeposition at a current density of 10 mA cm⁻² for one hour to generate a 10 mAh cm⁻² capacity in a two-electrode beaker cell with the target

substrate as the working electrode, Zn foil as the counter electrode and 2M ZnSO₄ as the electrolyte. Transmission electron microscopy (TEM) imaging was conducted on a JEM-2100 under 200 kV voltage in which the sample was prepared by drop coating powder dispersion in ethanol onto carbon-coated Cu grid. N₂ gas adsorption-desorption isotherms were obtained on the Autosorb Quantachrome 1MP with samples degassed at 200 °C for 10 h. X-ray photoelectron spectroscopy (XPS) experiments were performed on an AXIS Ultra DLD system from Kratos with Al K α radiation as X-ray source for radiation.

4.2.3 Electrochemical measurement

The electrochemical performance was tested using CR2032-type coin cells assembled in the open atmosphere. The slurry was prepared by mixing 90 wt.% of carbon powder (e.g. C_{flower}) and 10 wt.% of PVDF binder in NMP or 10 wt. % sodium alginate binder in water under stirring for at least 2h. The slurry was then coated onto Cu foil using doctor blade or drop coating technique. After being dried under vacuum overnight, Cu foils with/without carbon coating were punched into the circle disc (~1.13 cm²) as the working electrode. Zn foil (250 μ m thickness), glassy fiber membrane (Whatman Grade A), 3M ZnSO₄ was adopted as the reference/counter electrode, separator, and electrolyte respectively. Galvanostatic charge-discharge tests of half cells, symmetric cells, and full cells were carried out on the Neware battery testing system.

For Coulombic efficiency tests, batteries were first cycled in a potential range of 0.1–1 V vs. Zn/Zn²⁺ at a current of 0.1 mA for five cycles to stabilize the electrode and remove contaminations. Subsequently, certain amount (0.25-2.5 mAh cm⁻²) of Zn was plated onto the working electrodes (Cu foil, C_{flower}/Cu, C_{disk}/Cu and C_{sphere}/Cu) and then stripped to a cutoff voltage of 0.5 V at a certain current density (0.5-20 mA cm⁻²). The Coulombic efficiency was calculated based on the stripping capacity to plating capacity.

For symmetric-cell tests, same amount of carbon ($C_{\text{flower}}/C_{\text{disk}}/C_{\text{sphere}}$, 1-2 mg cm⁻²) was coated onto Zn foils to serve as electrodes for the symmetric cell and then Zn was plated and stripped at different current densities (0.5-20 mA cm⁻²) between two electrodes for certain time (7.5-30 min) for every cycle.

For Zn//MnO₂ batteries, Cu/Zn or Cu/ C_{flower} /Zn with a deposited capacity of 1, 2, and 10 mAh was used as the anode while MnO₂ was employed as the cathode which was synthesized according to the paper.⁵⁷ Cathodes were made by casting slurries containing MnO₂ (active material, 70 wt%), Super P (conductive carbon, 20wt%) and polyvinylidene difluoride (binder, 10 wt%) in NMP onto SSM disk (~1.13 cm²) by drop coating and dried under vacuum overnight. The areal mass loading of MnO₂ active materials was controlled at around 1.5 mg cm⁻². The electrolyte used in full cells was composed of 1 M Zn(OTf)₂ and 0.1M MnSO₄. Depth of discharge (DOD) of the Zn anode is calculated as the total theoretical capacity of the Zn anode divided by the cycled capacity.

For Zn//AC capacitors, Cu/Zn or C_{flower} /Zn with an electrodeposited Zn capacity of 2 or 5 mAh was used as the anode while commercial AC and 3 M ZnSO₄ was employed as the cathode and electrolyte, respectively. Cathodes were made by casting slurries containing AC (active material, 80 wt%), Super P (conductive carbon, 10wt%) and sodium alginate (binder, 10 wt%) in water onto SSM disc (~1.13 cm²) by drop coating and dried immediately under infrared light. The areal mass loading of AC was controlled at around 2~3 mg cm⁻².

For Zn//I₂-AC full cells, C_{flower} /Zn with an electrodeposited Zn capacity of 5 mAh was used as the anode while iodine/AC composite and 3 M ZnSO₄ was employed as the cathode and electrolyte, respectively. Iodine was melt diffused into AC at 150 °C for 12h and the final composite is composed of 30 wt% of I₂ and 70 wt% of AC. The I₂/AC composite was mixed under magnetic stirring with Super P and sodium alginate in a weight ratio of 8:1:1 to make the slurry. The slurry was drop coated

onto SSM and dried under infrared light. Of note is that the electrode should be kept a distance from the infrared light to mitigate the sublimation of iodine. Typically, the areal mass loading of I₂/AC was around 1.5~2 mg cm⁻². The theoretical capacity of reversible iodine electrode (I₂/I⁻) is 211 mA g⁻¹.

4.2.4 Theoretical calculation

To elucidate the mechanism of suppressing uncontrollable dendrite growth by introducing N- and O-doping into carbon micro-flowers with zincophilic modification, the density functional theory (DFT) calculation was carried out using the Vienna ab initio simulation package (VASP). The projector augmented wave method (PAW) was used to calculate efficiently with the replacement of core electron interactions in ab-initio electronic structure calculation.¹⁹² The generalized gradient approximation (GGA) was applied to describe the electron exchange-correlation energy¹⁹³ and Revised Perdew-Burke-Ernzerhof (RPBE) functional was used to confine the over-binding with adsorbates on prepared slab models.¹⁹⁴ A plane-wave basis set with an energy cut-off of 520 eV was employed to expand the Kohn-Sham wave functions of valence electrons. The total energy was adjusted below 10⁻⁴ eV for the full ionic relaxation step and the maximum atomic forces were used to be smaller than 0.05 eV Å⁻¹. We used the Methfessel-Paxton smearing method for better ionic optimization and geometry.¹⁹⁵ A vacuum gap of 30 Å was employed to prevent interactions between the top and bottom in the unit cell box. The total energies of designed structures were calculated with the k-points mesh of (6 x 1 x 6). To additionally consider van der Waals interactions, the DFT-D2 approach developed by Grimme et al. was applied.¹⁹⁶ The density of state (DOS) was investigated to comprehend the electronic structure modification using the tetrahedron method with Blöchl's corrections. **Model design.** DFT calculations were suggested to verify the prevention effect of Zn dendrite formation by O- and N-doping into carbon micro-flowers for sustainable Zn-ion batteries. First, it is important to define the most stable pristine graphene nanosheet (GNS) model to generate

O- and N-doped GNS. After geometry relaxation of pristine GNS, 10 species are modeled with incorporating O and N dopants into GNS slab model, including ether₁ oxygen (e₁O), ether₂ oxygen (e₂O), ketone group (kO), carboxylic group (aO), hydroxyl group (hO), pyridinic nitrogen (pN), pyrrolic nitrogen (pyN), oxidized nitrogen (oN), graphitic nitrogen in the bulk (g_nN), and graphitic nitrogen on the edge (gN). On these optimized model structures, the binding energies with Zn atoms were calculated by investigating the most stable site among the possible adsorption sites as below shown in the following equation:¹⁹⁷

$$E_{BE} = E_{Zn\ atom/sl\ ab} - E_{sl\ ab} - E_{Zn\ atom}$$

where E_{BE} described the binding energy of Zn atom with each slab model, and $E_{Li\ atom/sl\ ab}$, $E_{sl\ ab}$, and $E_{Li\ atom}$ are the total energies of Zn atom on the slab, each slab (pristine, O-doped, or N-doped GNS), and Zn atom, respectively.

4.3 Results and Discussion

To unveil the O- and N-doping effect on zincophilicity chemistry, DFT calculation was firstly performed on binding energies between Zn atom and O/N-doped graphene nanosheet (GNS). O- and N-doped GNS were modeled with all possible doping sites as described in **Figure 4.1a**. The calculated oxygen dopants include ether₁ group (e₁O), ether₂ group (e₂O), ketone group (kO), carboxylic group (cO), and hydroxyl group (hO). Among these species, Zn tends to bind with ether₁ oxygen (e₁O) and carboxylic oxygen (cO) site with strong Zn adsorption energy of -3.42 eV and -0.20 eV, respectively (**Figure 4.1b, d and Table S4.1**). Nitrogen-containing groups were also investigated including pyridinic nitrogen (pN), pyrrolic nitrogen (pyN), oxidized nitrogen (oN), graphitic nitrogen in the bulk (g_nN), and graphitic nitrogen on the edge (gN) by searching the most stable site among the

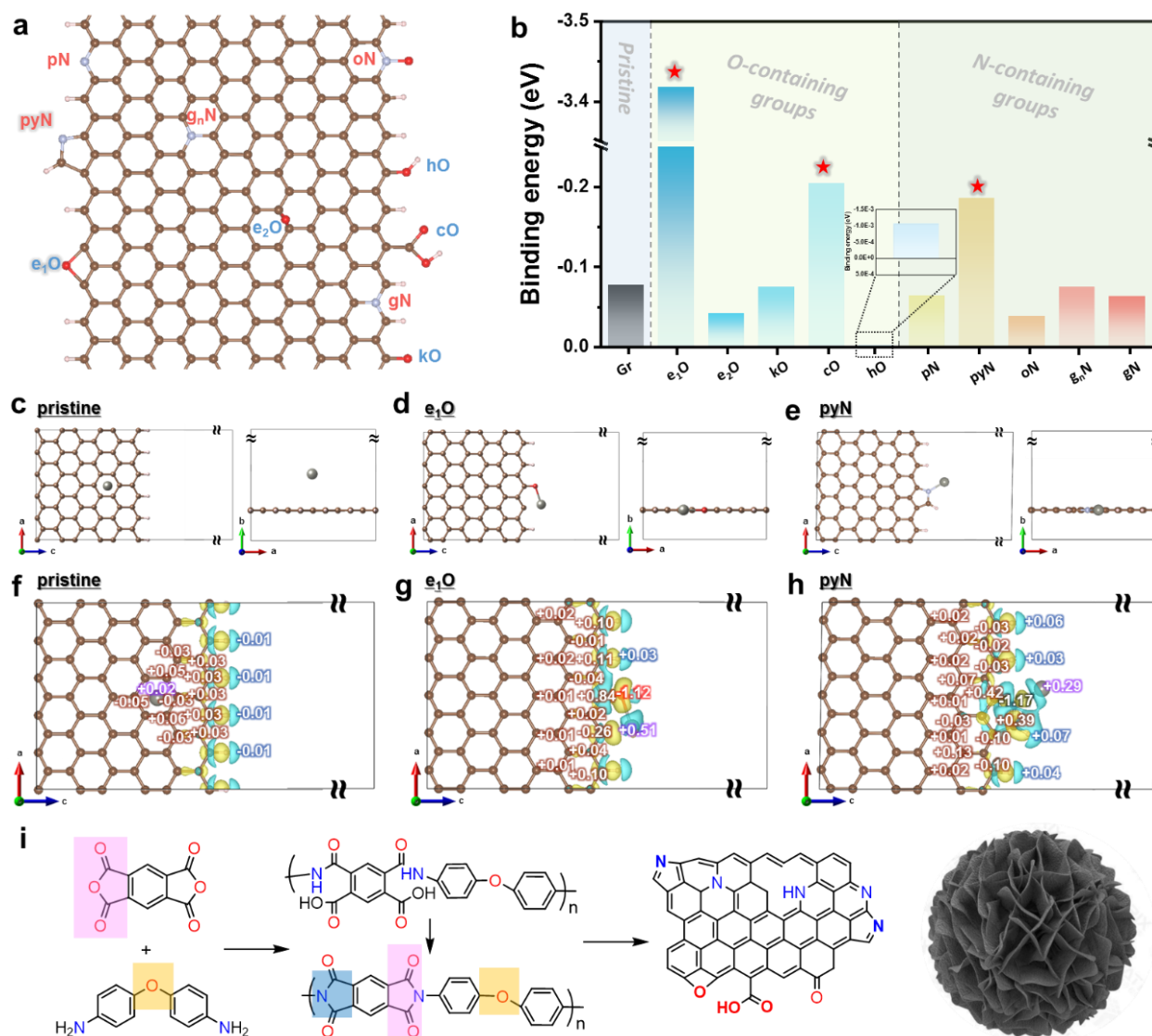


Figure 4.1 (a) Modeling of oxygen/nitrogen-doped graphene. (b) Summary of the calculated binding energies of Zn atoms with all possible configurations of pristine, O- and N-doped graphene. (c-e) model structure for the most stable adsorption sites of Zn atoms and (f-h) charge density differences of (c, f) pristine, (d, g) O-doped and (e, h) N-doped graphene, respectively. (i) Scheme showing the ideal transition from monomers to polyimide precursor, polyimide, and derived O/N-codoped carbon.

possible adsorption sites as shown in **Figure S4.1-S4.2**. Among them, pyrrolic N site (pyN) in GNS matrix has the strongest adsorption (-0.19 eV, **Figure 4.1e** and **Table S4.1**). Moreover, charge

difference with deposited Zn atom indicates that O- and N-doping into GNS could modify the electronic structure of GNS with electrons transferring from Zn to O and N dopants (**Figure 4.1f-h**). This was further confirmed by the change on degree of empty state from high degree in pristine GNS to medium and low degree in pyN-GNS and e₁O-GNS, respectively, as shown in projected-density of state (**Figure S4.3**). Moreover, the strongest binding energy between e₁O and Zn could be explained by its empty anti-bonding state with strongest adsorption energy (**Figure S4.4**).

Based on DFT results, we rationally selected molecules as monomers for making polymer that possesses ether₁ oxygen, carboxylic oxygen, and pyrrolic nitrogen groups, as shown in **Figure 4.1i**. And the polymer (polyimide, PI)-derived carbon is expected to act as favorable host for heterogeneous

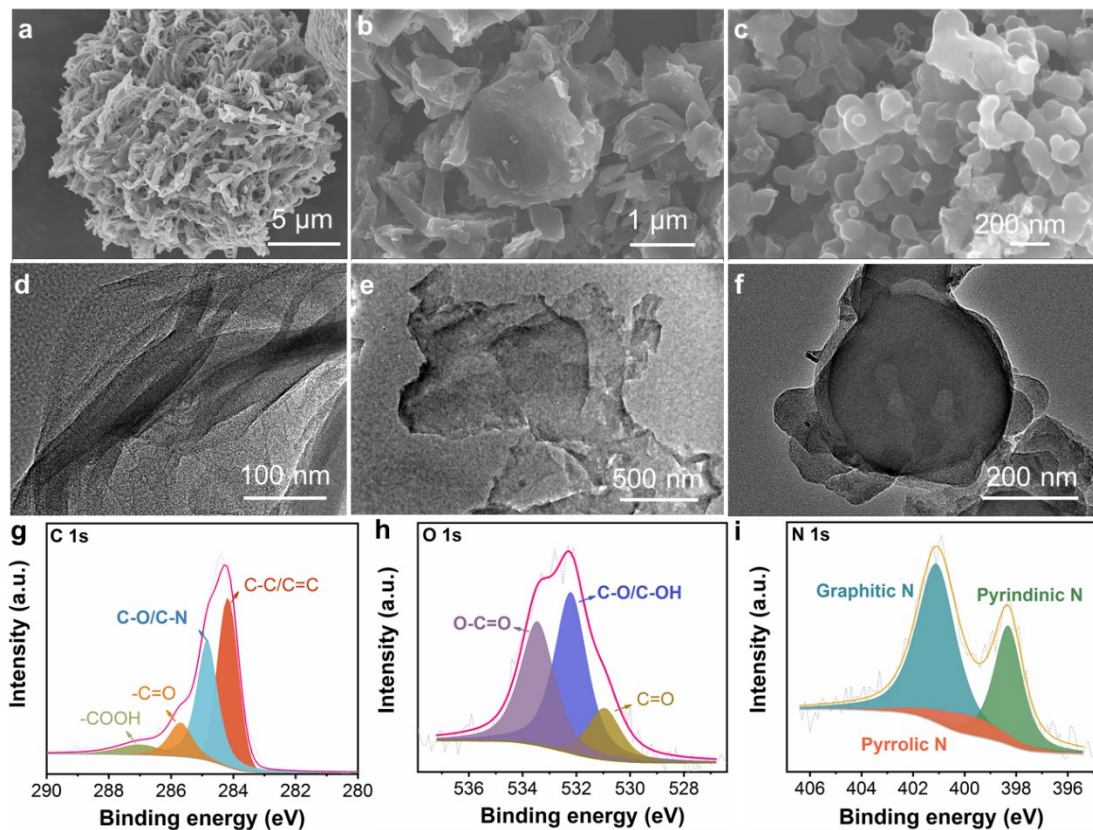


Figure 4.2 SEM images of (a) C_{flower}, (b) C_{disk}, (c) C_{sphere} and TEM images of (d) C_{flower}, (e) C_{disk}, (f) C_{sphere}. High-resolution XPS spectra of (g) C 1s, (h) O 1s, and (i) N 1s.

nucleation of Zn metal. Besides desired heteroatom dopants, micro-/nanostructures of PI-derived carbon were tuned to evaluate their impact on hosting Zn plating/stripping by controlling polymer self-assembly during polymerization (**Figure S4.5-S4.8**), giving rise to carbon flowers (C_{flower}), carbon disks (C_{disk}), and carbon spheres (C_{sphere}). SEM images show that C_{flower} with a lateral size of 5–20 μm is constructed by numerous nanobelts radically orienting outside (**Figure 4.2a**), C_{disk} with a size around 1–2 μm is assembled by few layers of nanosheets (**Figure 4.2b**), and C_{sphere} shows irregular nanosphere particles with a size around 100-200 nm (**Figure 4.2c**). TEM images show ultrathin layers as building blocks in C_{flower} (**Figure 4.2d**), two-dimensional structure in C_{disk} (**Figure 4.2e**) as well as solid nanoparticles in C_{sphere} (**Figure 4.2f**), in agreement with SEM results. The elemental distribution measurement shows the uniform distribution of C, N, and O signals in all samples (**Figure S4.9**). XRD patterns (**Figure S4.10a**) present two broad peaks around 20-30 ° and 45 °, suggesting the presence of microcrystalline graphite domains in the carbon structures while Raman spectra (**Figure S4.10b**) display D, G, and 2D band and the intensity ratio of G to D group ($I_{\text{G}}/I_{\text{D}}$) is found as 1-1.1 for three samples,^{198, 199} indicating the presence of both topological defects and graphitic structures, which are favorable for the horizontal deposition of Zn metal.^{21, 27} N_2 sorption measurements were conducted to gain insight into the porous structure of C_{flower} , C_{disk} , and C_{sphere} , in which three carbon manifests similar surface areas around 240 $\text{cm}^2 \text{g}^{-1}$ (**Figure S4.10c**) but slightly different pore size distributions dominated with mesopores (**Figure S4.10d**). XPS was characterized to probe into bonding condition, taking the C_{flower} as an example. The survey spectra show the only existence of C, N, and O elements (**Figure S4.11**). High-resolution XPS $C 1s$ spectrum can be deconvoluted into 284.8 eV, 285.4 eV, 286.3 eV and 287.7 eV peaks, corresponding to C=C/C-C, C-O/C-N, C=O, and carboxyl groups with the respective content of 37.35%, 33.25%, 16.46%, and 12.94% (**Figure 4.2g**). The high-resolution $O 1s$ spectrum was deconvoluted into three groups:

carboxylic (O-C=O, ~533.0 eV), ether/hydroxyl (C-O/C-OH, ~532.0 eV), and carbonyl (C=O, ~530.8 eV) groups (**Figure 4.2h**). Among them, carboxylic and ether/hydroxyl groups accounted for 85.72% of all oxygen atoms. High-resolution *N 1s* spectrum in **Figure 4.2i** manifests graphitic N (401.3 eV), pyrrolic N (400.3 eV) and pyridinic N (398.5 eV) groups. XPS results verify the successful making of carbon materials with desired heteroatom dopants through the rational selection of monomers and controlled polymerization. Overall, these carbon structures with graphitic structures and heteroatom dopants could function as prospective zincophilic host while their only difference on the micro-/nanostructures could provide the platform to investigate the influence of carbon microstructure on Zn deposition behavior, electrochemical efficiency, and cycle life.

The feasibility of three carbon materials as Zn metal host was firstly investigated in Zn/Cu half cells in which carbon-coated Cu foil ($C_{\text{flower}}/\text{Cu}$, $C_{\text{disk}}/\text{Cu}$, and $C_{\text{sphere}}/\text{Cu}$) was applied as the working electrode. **Figure 4.3a** shows the CE (the ratio of stripped capacity to plated capacity) and cycling stability of Zn plating/stripping at 0.5 mA cm^{-2} on different substrates. Among them, $C_{\text{flower}}/\text{Cu}$ and $C_{\text{disk}}/\text{Cu}$ electrodes display high CE (ca. 99.3%) for 400 cycles while $C_{\text{sphere}}/\text{Cu}$ and pure Cu electrodes present unstable CE values and short life less than 100 cycles (**Figure 4.3a**). Compared with $C_{\text{disk}}/\text{Cu}$, $C_{\text{flower}}/\text{Cu}$ exhibits higher initial CE and higher stability (**Figure S4.12**), suggesting the best performance can be achieved in the C_{flower} host. This $C_{\text{flower}}/\text{Cu}$ electrode was further plated/stripped with Zn metal at current densities from 0.5 to 10 mA cm^{-2} and capacities from 0.25 to 5 mAh cm^{-2} . As presented in **Figure 4.3b**, average CE values of 98.5%, 98.4%, 97.9%, and 96.9% can be obtained at high rates of 2, 3, 5, 10 mA cm^{-2} , separately, with low voltage hysteresis in the range of 110~137 mV (**Figure 4.3c** and **Figure S4.13**). The high CE values and long life realized by the C_{flower} host is

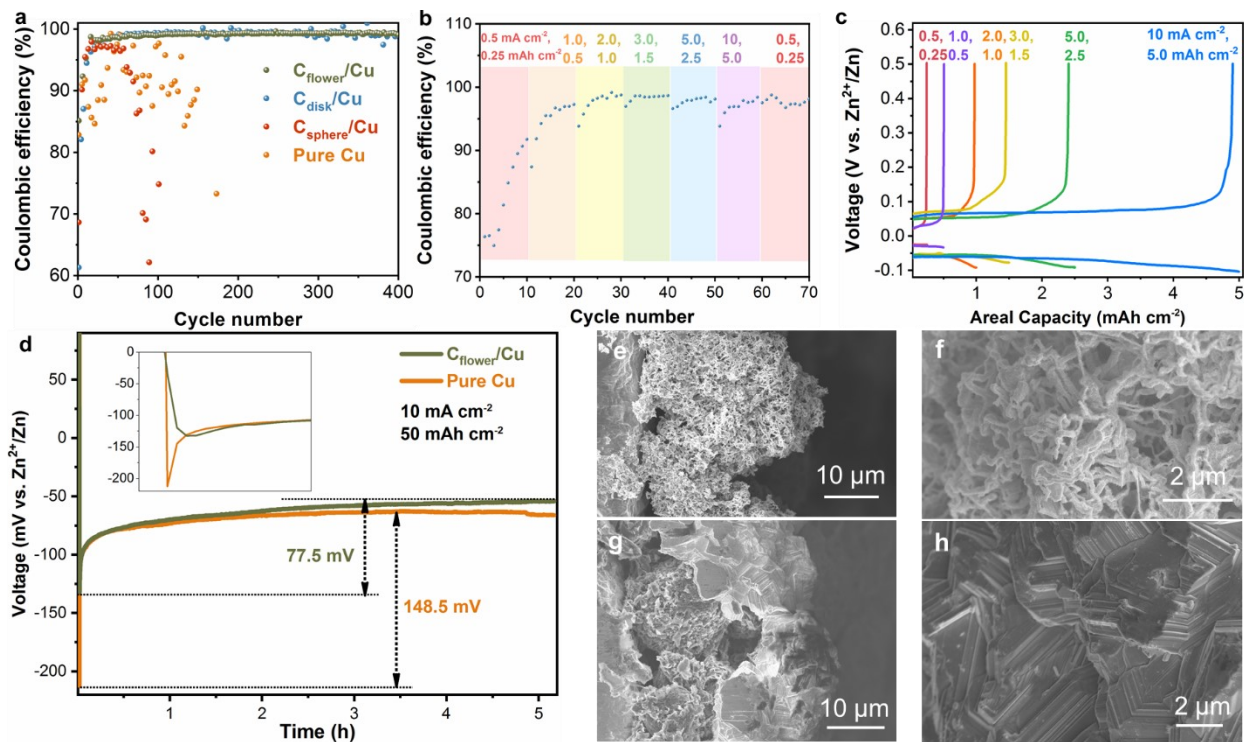


Figure 4.3 Zn/Cu half-cell tests. (a) Coulombic efficiency of Zn stripping/plating onto different substrates (pure Cu, $C_{\text{flower}}/\text{Cu}$, $C_{\text{disk}}/\text{Cu}$, and $C_{\text{sphere}}/\text{Cu}$) at 0.5 mA cm^{-2} and 0.25 mAh cm^{-2} . (b) CE of the $C_{\text{flower}}/\text{Cu}$ electrode at different current rates and capacities and (c) corresponding discharge/charge profiles. (d) Zn plating profiles of $C_{\text{flower}}/\text{Cu}$ and pure Cu at 10 mA cm^{-2} and 50 mAh cm^{-2} . (e-h) SEM images of deposited Zn morphology onto (e, f) pure Cu and (g, h) $C_{\text{flower}}/\text{Cu}$.

comparable and even better than previously reported Zn hosts, such as CNT array,²⁸ polymer coating,¹⁸ $\text{Ti}_3\text{C}_2\text{T}_x$ Mxene,²⁰⁰ and ZIF-8 derived carbon¹⁵⁵ (**Table S4.2**, Supporting Information). Above results reveal that the C_{flower} host enables the high-rate plating/stripping of Zn metal anode with high CE.

To probe into the nucleation process of Zn deposition onto $C_{\text{flower}}/\text{Cu}$ vs. pure Cu, Zn was plated onto $C_{\text{flower}}/\text{Cu}$ and pure Cu. As shown in Zn plating profiles at 10 mA cm^{-2} (**Figure 4.3d**) of $C_{\text{flower}}/\text{Cu}$ and pristine Cu electrodes, at the early stage of nucleation, bare Cu electrode experiences abrupt potential drop to the lowest value of ca. 212.3 mV whereas the $C_{\text{flower}}/\text{Cu}$ electrode shows gradually decreased

potential to the point of 132.3 mV, indicating different Zn nucleation behavior on two substrates. The nucleation overpotential was calculated to be 148.5 mV and 77.5 mV for pure Cu and C_{flower}/Cu electrode, respectively, evidencing reduced energy barrier for Zn nucleation and improved Zn affinity enabled by the C_{flower} host. This was further confirmed by the plating profiles of C_{flower}/Cu and pristine Cu electrodes at a low rate of 0.2 mA cm⁻² (**Figure S4.14**).

To study the Zn deposition morphology on C_{flower}/Cu vs. pure Cu, cross-sectional and top-view SEM images were captured (**Figure 4.3e-h**). The electrodeposition was conducted at 10 mA cm⁻² for 1 h in a two-electrode open cell. **Figure 4.3e** shows that Zn deposit on pure Cu is highly porous and spherical and the spherical deposit is composed of numerous nanofilaments with random arrangement, indicating the formation of Zn dendrites (**Figure 4.3f**). On the contrary, in the presence of C_{flower}, Zn deposition can be guided in a controlled manner. According to **Figure 4.3g**, it is proposed that Zn firstly deposited onto C_{flower}, then grew inside gaps between these C_{flower}, and ultimately grew into compact layers on the top of C_{flower} host. These compact layers of Zn deposit is composed of horizontal hexagonal plates stacking in a layer-by-layer mode (**Figure 4.3h**), similar to the heteroepitaxial growth mode of Zn plating onto graphene sheets due to small lattice mismatch.²⁷ The high Zn plating/stripping reversibility and dendrite-free features enabled by the C_{flower} host should result from its hierarchical oriented nanobelts, microcrystalline graphitic layers, numerous meso-/macroporous channels and zincophilic O/N co-dopants. And the uniform distribution of these structural features throughout the C_{flower} electrode ensures the homogenous nucleation and growth of Zn metal into horizontal layers without dendrites.

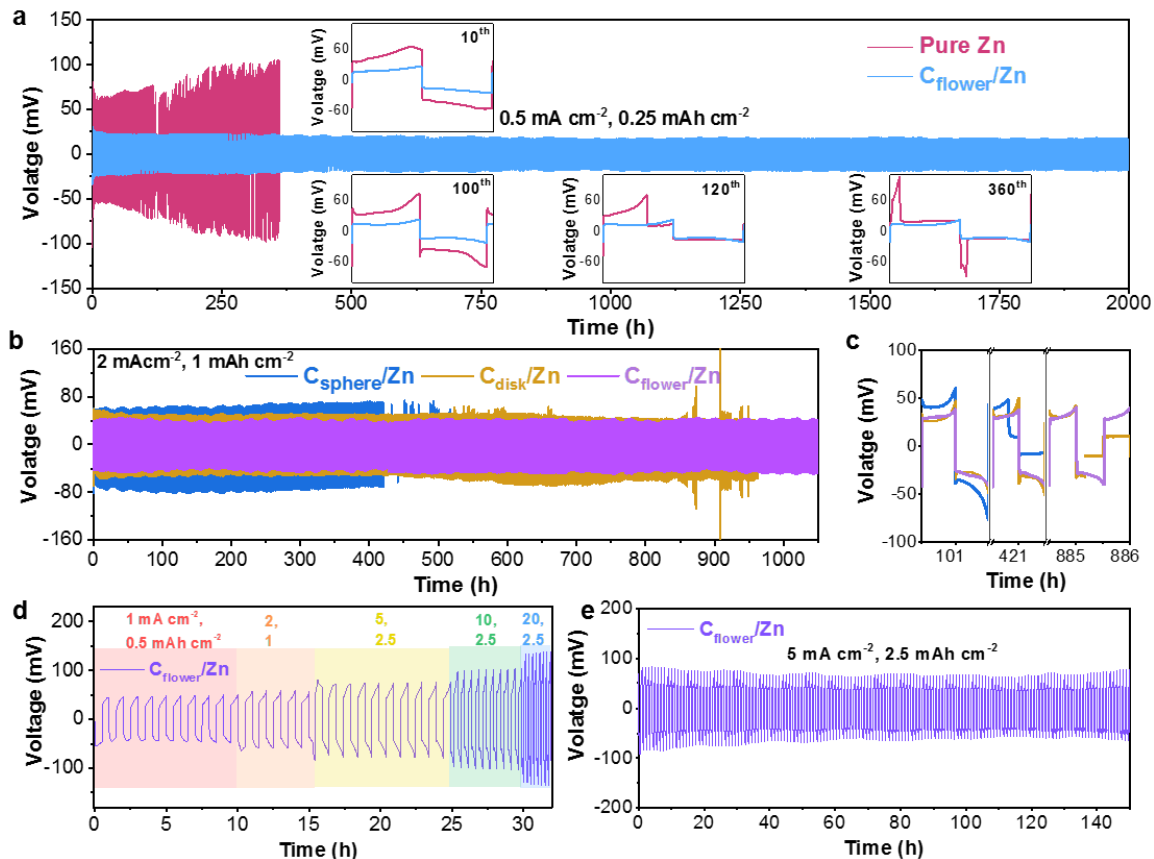


Figure 4.4 Symmetric cells based on Zn metal anodes with or without carbon coating. a) Voltage profiles of symmetric cells using $C_{\text{flower}}/\text{Zn}$ and pure Zn electrodes at 0.5 mA cm^{-2} . b) Comparison of voltage profiles of symmetric cells based on $C_{\text{flower}}/\text{Zn}$, $C_{\text{disk}}/\text{Zn}$, and $C_{\text{sphere}}/\text{Zn}$ at 2 mA cm^{-2} . d) Rate performance of symmetric cells based on $C_{\text{flower}}/\text{Zn}$ electrodes at current densities from 1.0 to 20 mA cm^{-2} with plating capacities from 0.5 mAh cm^{-2} to 2.5 mAh cm^{-2} . e) Long-term cycling performance of $C_{\text{flower}}/\text{Zn}$ electrodes-based cell at a high rate of 5 mA cm^{-2} .

Symmetric Zn//Zn cells were further fabricated to evaluate the cycling stability of different Zn metal anodes including pure Zn foil, $C_{\text{flower}}/\text{Zn}$, $C_{\text{disk}}/\text{Zn}$, and $C_{\text{sphere}}/\text{Zn}$ working electrodes. **Figure 4.4a** shows the voltage profiles of the pure Zn and $C_{\text{flower}}/\text{Zn}$ -based cells at a current density of 0.5 mA cm^{-2} and a capacity of 0.25 mAh cm^{-2} . The pure Zn-based cell shows gradually increased voltage hysteresis more than 100 mV for 100 h and sudden failure after only 120 h in contrast to the stable

voltage hysteresis values of ca. 30 mV in the $C_{\text{flower}}/\text{Zn}$ -based cell for over 2000 h, meaning 165-fold improvement on cycle life of Zn electrodes under the protection of C_{flower} coating. **Figure 4.4b** compares voltage curves of symmetric cells based on different carbon coated Zn electrodes at 2.0 mA cm^{-2} and 1.0 mAh cm^{-2} . Results show that $C_{\text{sphere}}/\text{Zn}$ -based cell experiences sudden voltage drop after cycling for only 421 h and the voltage of $C_{\text{disk}}/\text{Zn}$ -based cell starts to fluctuate after 885 h, both of which results from the formation of Zn dendrites. By stark contrast, $C_{\text{flower}}/\text{Zn}$ -based cell maintains stable voltage hysteresis over 1000 h, implying the best dendrite-suppressing capability of carbon micro-flower among three carbon structures (**Figure 4.4c**). Also, during the stable cycling of three cells, voltage hysteresis values are 87 mV, 62 mV, and 60 mV for $C_{\text{sphere}}/\text{Zn}$, $C_{\text{disk}}/\text{Zn}$, and $C_{\text{flower}}/\text{Zn}$, separately, further indicating the best reversibility of Zn metal electrode enabled by carbon flowers (**Figure 4.4c**). Aside from that, C_{flower} also enables longer cycling stability in the symmetric cell than commercial carbon materials such as Super P and activated carbon (**Figure S4.15**). The best-performed $C_{\text{flower}}/\text{Zn}$ -based symmetric cell was further measured at high current rates from 1, 2, 5, 10, to 20 mA cm^{-2} . Impressively, the cell maintains stable voltage hysteresis even at an ultrahigh rate of 20 mA cm^{-2} (**Figure 4.4d** and **Figure S4.16**), which is in stark contrast to the short-circuit phenomena of pure Zn-based symmetric cell cycling at a low rate of 3 mA cm^{-2} (**Figure S4.17**). Besides the high-rate capability, its stability is also excellent. As shown in **Figure 4.4e**, the $C_{\text{flower}}/\text{Zn}$ -based cell achieves long cycles over 150 h at 5 mA cm^{-2} . These results demonstrate the high-rate and long-life Zn metal electrodes can be realized by the coating of carbon microflowers, which is comparable to many reported Zn anodes (**Table S4.3**).

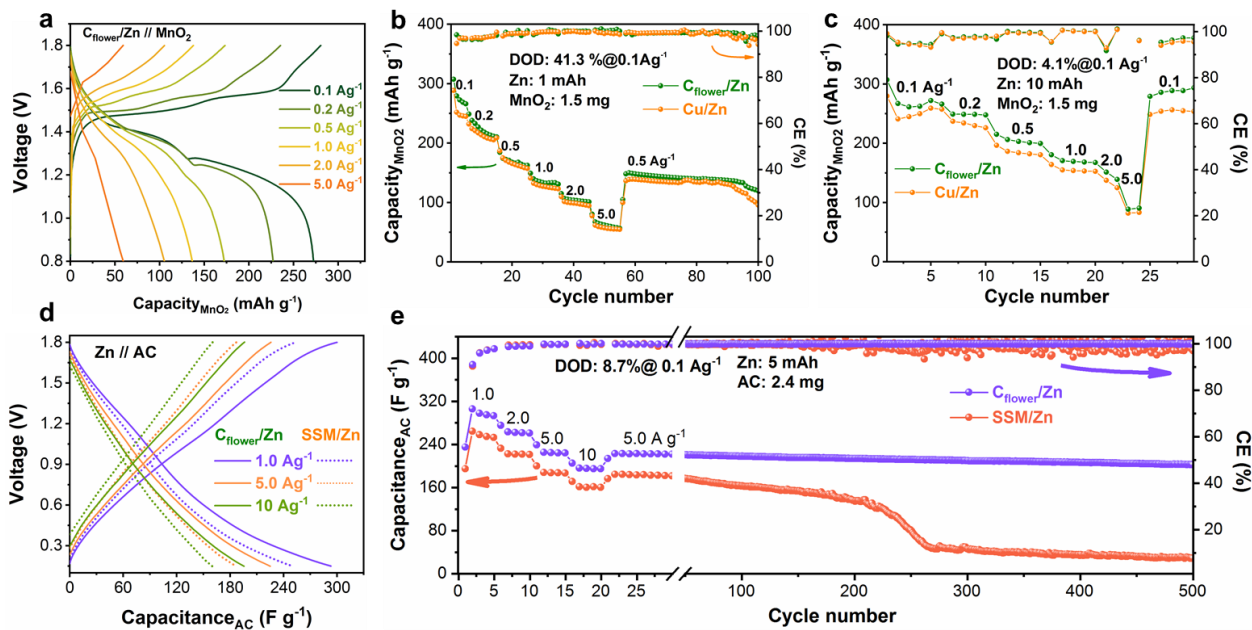


Figure 4.5 Zn metal-based full cells. a) charge/discharge profiles of $C_{\text{flower}}/\text{Zn}/\text{MnO}_2$ batteries at different current densities ($0.1\sim 5\text{ Ag}^{-1}$). Rate performance comparison between $C_{\text{flower}}/\text{Zn}$ -based cells and pure Zn-based cells with limited Zn: (b) 1 mAh and (c) 2 mAh. d) charge/discharge profiles of $C_{\text{flower}}/\text{Zn}/\text{AC}$ capacitor vs. Zn//AC capacitor at different current densities (1, 5, and 10 Ag^{-1}). e) Rate and cycling performance of $C_{\text{flower}}/\text{Zn}$ -based and pure Zn-based capacitor with limited Zn (5 mAh).

To demonstrate practical applications, $C_{\text{flower}}/\text{Zn}$ anode was paired with three cathode materials for full-cell tests under high DOD (Figure S4.18). For comparison, Zn electrodeposited on Cu (Cu/Zn) as the hostless anode was also employed. Firstly, $C_{\text{flower}}/\text{Zn}$ and Cu/Zn anodes with limited Zn capacities (1, 2, 10 mAh) were applied for Zn// MnO_2 batteries. The charge/discharge profiles of these batteries show typical voltage platforms of Zn// MnO_2 cells involving both proton and zinc ion storage (**Figure 4.5a**). Under high DOD of 41.3% at 0.1 Ag^{-1} (11.3% at 5 Ag^{-1}), $C_{\text{flower}}/\text{Zn}$ -based battery shows higher capacities (275 mA h g^{-1} at 0.1 Ag^{-1} , 75 mA h g^{-1} at 5 Ag^{-1}) than Cu/Zn-based battery as well as longer cycle life, suggesting the superiority of the $C_{\text{flower}}/\text{Zn}$ over Cu/Zn anode (**Figure 4.5b**). However, due to the harsh condition of high DOD, batteries show short cycle life. When the

DOD is lowered to 4%~19.8%, cycle life can be extended to more than 250 cycles (**Figure S4.19**). Much higher capacities can be also obtained in the $C_{\text{flower}}/\text{Zn}$ - than Cu/Zn -based cell at a DOD of 4.1% at 0.1 Ag^{-1} and faster rates indicating enhanced kinetics enabled by carbon flower host (**Figure 4.5c**, **Figure S4.20**). Next, activated carbon (AC) was coupled with Zn anodes to make zinc ion hybrid supercapacitors.²⁰¹ The electrodeposited Zn is limited to be 2 mAh and 5 mAh. Here, stainless steel mesh (SSM) was used as the current collector and the Zn anode was denoted as SSM/Zn (**Figure S4.21**). Under a high DOD of ~18% at 0.1 A g^{-1} (**Figure S4.22**), SSM/Zn-based capacitor can operate at a low rate of $0.1\text{-}0.2 \text{ Ag}^{-1}$ but suddenly fail after only ca. 80 cycles while $C_{\text{flower}}/\text{Zn}$ -based capacitor shows stable capacitance at all rates from 0.1 to 5 Ag^{-1} and its lifespan is more than 100 cycles. Cycle life and rate capability can be further enhanced under a DOD of 8.7% (at 0.1 Ag^{-1}) as shown in **Figure 4.5d-e**. The capacitance is 293, 225, and 196 F g^{-1} for $C_{\text{flower}}/\text{Zn}$ -based capacitor at the rate of 1.0, 5.0, and 10 A g^{-1} , respectively (**Figure 4.5d**), surpassing that of SSM/Zn-based capacitor (250, 187, and 160 F g^{-1}). Besides, $C_{\text{flower}}/\text{Zn}$ -based capacitor could stably run for over 500 cycles with 91% of capacitance retention and 100% CE in stark contrast to the SSM/Zn-based capacitor with only 15% capacitance retention and fluctuated CE after 500 cycles. Above results demonstrate faster rates and longer life of Zn metal batteries and supercapacitors can be enabled by the C_{flower} host compared with hostless Zn even under high DOD. The $C_{\text{flower}}/\text{Zn}$ as the reversible anode was further demonstrated by its application in Zn-iodine supercapattery, which displays obvious discharge/charge platforms at ~1.2 V and capacitive-controlled sloping curves in the wide voltage window of 0.2-1.8V (**Figure S4.23**) along with large capacity (175 mAh g^{-1} at 0.1 Ag^{-1}), fast-charging capability (115 mAh g^{-1} at 5.0 A g^{-1}), and long life (80.8% retention after 800 cycles). Of mentioning is that the DOD values of 4.1-41.3% in our Zn anode is much higher than most reported papers in full cells (**Table S4.4**).^{184, 187, 202-204} Due to the use of high-DOD Zn anode, the energy and power density at the cell level could be

enhanced, and the highest energy density achieved in MnO₂, AC, I₂/AC-based full cell is 195.3, 52.58, 30.73 Wh kg⁻¹, respectively (**Figure S4.24**).

4.4 Summary

In summary, guided by DFT calculations, we have rationally prepared three heteroatom-doped carbon micro-/nanostructures (C_{flower}, C_{disk}, and C_{sphere}) through rational monomer selection, controlled polyimide assembly followed by pyrolysis and explored their feasibility as the host material for Zn metal batteries and supercapacitors. DFT calculations revealed among O/N dopants, ether (C-O), carboxylic (-O-C=O-), pyrrolic N groups are favorable for heterogeneous nucleation of Zn. Among carbon hosts, C_{flower} shows enriched active O/N dopants as well as micrometer scale hierarchical structures which guide Zn deposition into horizontal layers, leading to highest Coulombic efficiency (97~99%) at 0.5~10 mA cm⁻² in half cells as well as long life (2000 h) and fast-rate cycling (20 mA cm⁻²) in symmetric cells. As a proof of concept, the C_{flower} hosted Zn anode was coupled with three cathode materials for Zn-based energy devices, delivering better kinetics and longer lifespan than corresponding devices based on hostless Zn anode under high depth of discharge. This work opens the door towards the construction of 3D hierarchical carbon-rich micro-/nanohosts for practical metal anodes beyond Zn.

4.5 Supporting Information

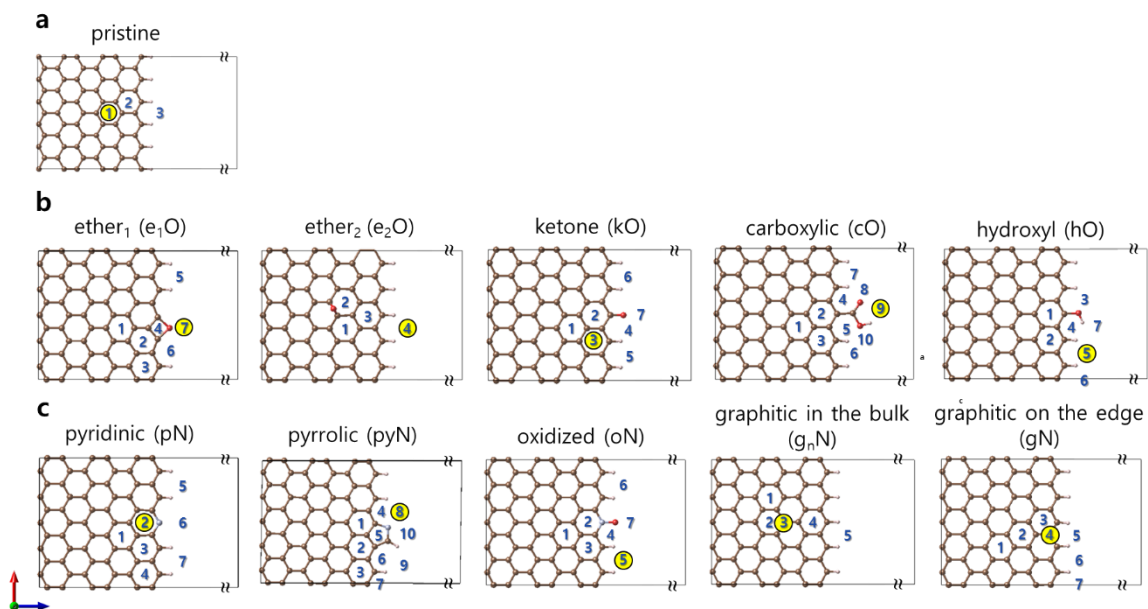


Figure S4.1 Possible configurations of Zn atom adsorption on (a) pristine, (b) O-doped, and (c) N-doped GNS for searching the most stable adsorption site (described as yellow round).

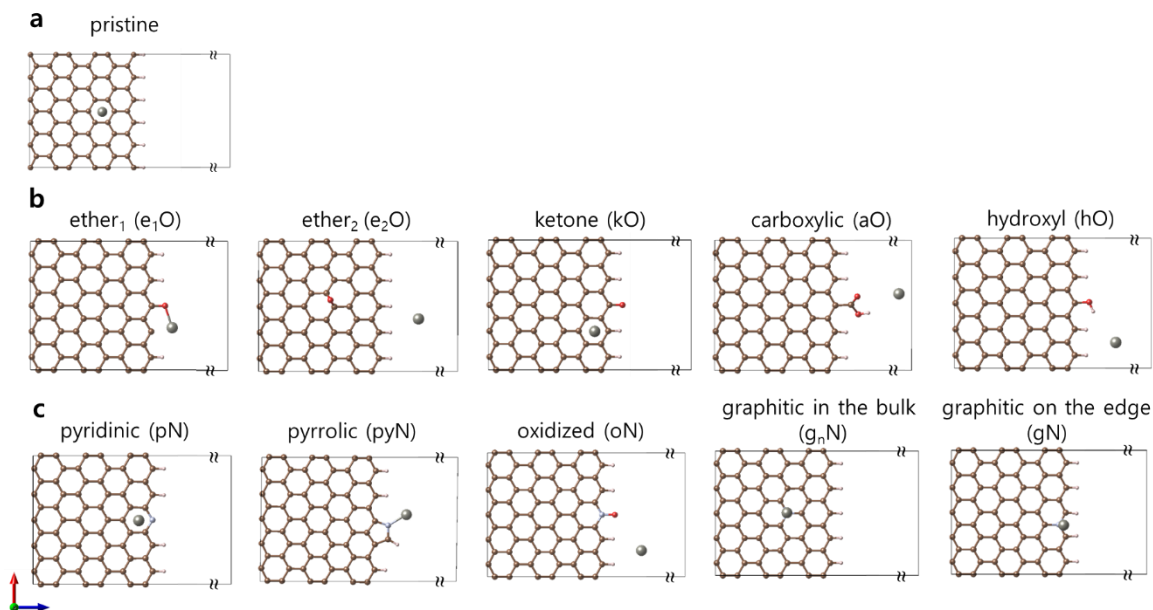


Figure S4.2 Defined configurations of (a) pristine, (b) O-doped, and (c) N-doped GNS which shows the most stable adsorption with Zn atom among the possible adsorption sites.

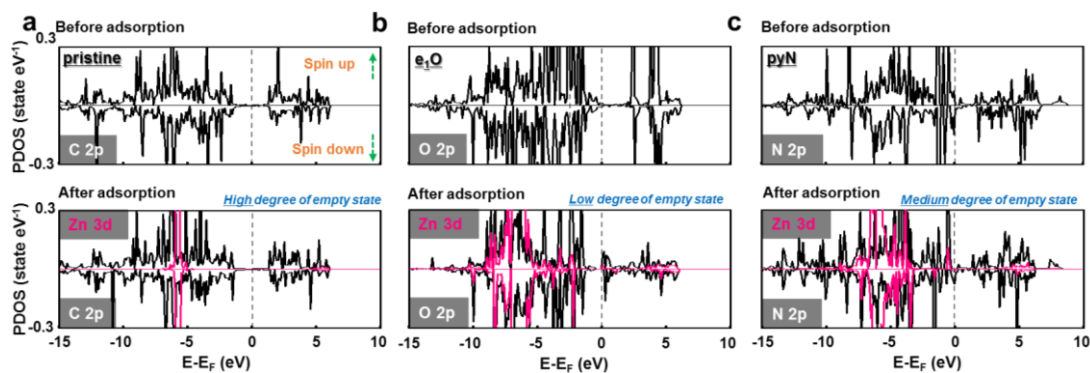


Figure S4.3 Density of state of (a) pristine, (b) O-containing and (c) N-containing graphene, respectively.

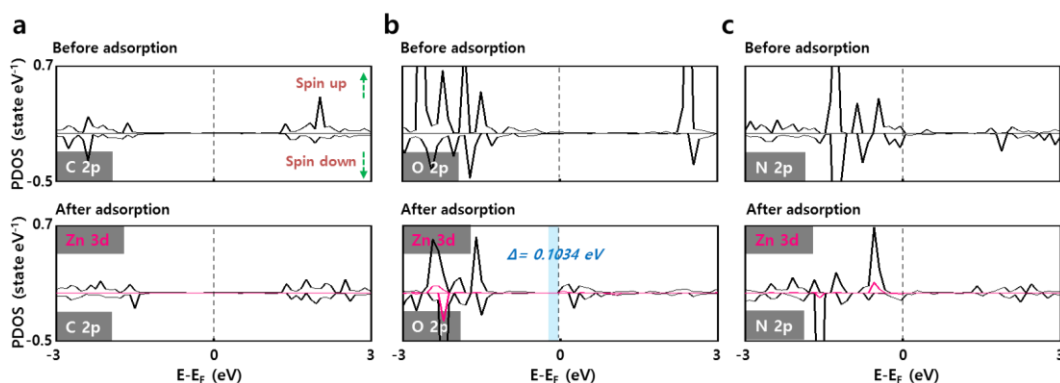


Figure S4.4 The projected-density of state of (a) pristine, (b) O-doped, and (c) N-doped GNS, respectively.

The projected-density of state was further investigated to theoretically understand the electronic structure modification which is closely associated with the Zn affinity through the quantitative amounts of orbital overlapping, additionally, bond splitting near Fermi level between bonding and anti-bonding state of Zn 3d with C 2p, O 2p, and N 2p orbitals of pristine, O-doped, and N-doped GNS, respectively. After Zn adsorption on prepared model slabs, the overlapping of Zn 3d with O 2p and N 2p orbitals in the projected-density of states for ether₁ oxygen (e₁O) site into O-doped GNS and pyrrolic N site (pyN) into N-doped GNS have the low and medium degree of empty state, respectively, whereas the overlapping of Zn 3d with C 2p for pristine GNS has a high degree of empty

state as shown in **Figure S4.3**. This means that O-doped and N-doped GNS have higher zincophilicity because it gives rise to the stronger interaction by sufficient charge transfer compared to pristine GNS. Furthermore, ether₁ oxygen (e₁O) site, which has the strongest binding energy than others, described the splitting of bonding and anti-bonding orbitals at around 0.1034 eV of splitting distance near Fermi level (**Figure S4.4**). It can be interpreted to have relatively stronger adsorption energy with adsorbates because of being empty anti-bonding state.

Based on above-mentioned discussion, the higher interaction of O and N with Zn, that is analogous to the so-called “Zn bond”, can be reasonably explained by Lewis acid-base theory^{205, 206} due to the higher electronegativity of O (3.44) and N (3.04) than that of C (2.55), leading to reduced Zn nucleation overpotential. The surface modification through O- and N-doping into carbon micro-flower matrix has clearly been demonstrated as an effective strategy for higher Zn affinity.

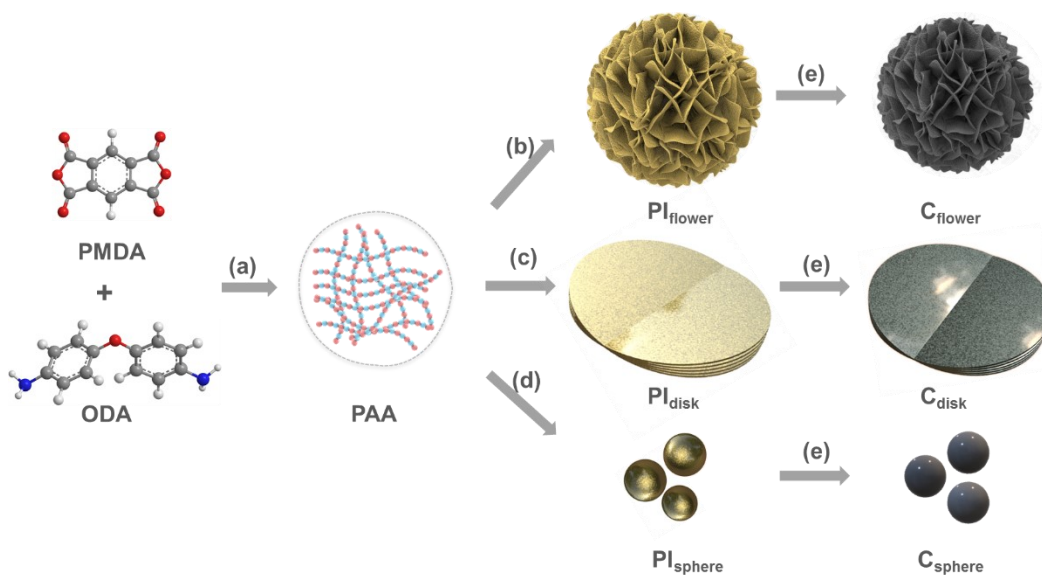


Figure S4.5 Schematic illustration of the synthetic process of different polymer and carbon micro-/nanostructure. (a) pre-polymerization reaction, (b) solvothermal polymerization under high pressure, (c) wet polymerization under stirring and atmospheric pressure, (d) precipitation polymerization, (e) carbonization.

Solvothermal polymerization leads to the formation of flower-shaped PI (PI_{flower}) with a lateral size of 5-20 μm assembled by nanobelts (**Figure S4.6a, b**), stirring polymerization results in disk-like PI (PI_{disk}) assembled by nanosheets (**Figure S4.6c, d**), and precipitation polymerization forms PI nanospheres (PI_{sphere}) with a size of 100-200 nm (**Figure S4.6e, f**). The formation of flower-like polymer in PI_{flower} should be attributed to the hierarchical self-assembly induced by polymerization-crystallization under high pressure while the generation of disk-like polymer in PI_{disk} under atmospheric pressure could be explained by its less order of self-assembly due to lower crystallization degree compared with PI_{flower} , and the spherical polymer in PI_{sphere} is caused by the thermodynamically stable droplet in the form of spheres in the “bad” solvent. These polymer structures of PIs were characterized by FTIR spectra in which peaks appear at 1720, 1780, and 1340 cm^{-1} , assignable to imide carbonyl (C=O) and imide ring (C-N-C) groups, indicating the successful synthesis of PI (**Figure S4.7**).¹⁴⁰ Their crystal structures tested by XRD manifest different degree of crystallization. While PI_{sphere} shows poorly crystalline structure with only broad peaks, PI_{flower} and PI_{disk} shows high crystallinity with strong and sharp peaks in which higher signal-to-noise ratio was observed in PI_{flower} indicating its higher degree of crystallization. These results match well with our proposed formation mechanism of different microstructures. PIs are commonly known as thermally stable polymers that can be used in extreme conditions and thermogravimetric analysis of PIs indeed showcases their excellent thermo-resistant property as negligible weight loss was observed before 400 °C and high carbon yield of 40-50 % can be achieved (**Figure S4.8**).

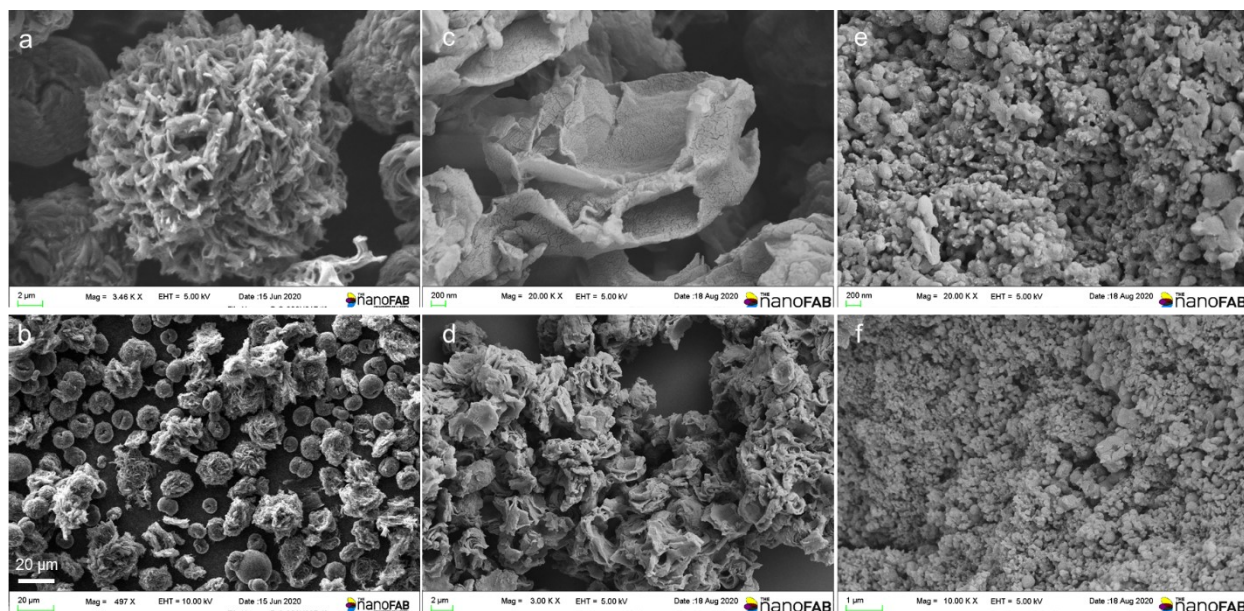


Figure S4.6. SEM images of (a, b) PI_{flower} , (c, d) PI_{disk} , and (e, f) PI_{sphere} .

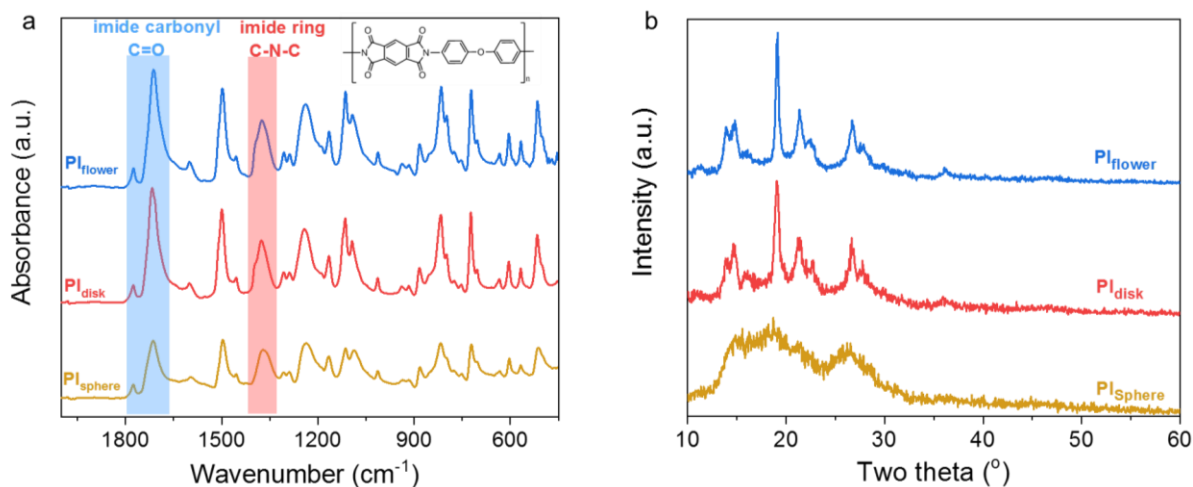


Figure S4.7 FTIR spectra and XRD patterns of PI_{flower} , PI_{disk} , and PI_{sphere} .

As shown in the FTIR spectra, peaks appear at 1720, 1780, and 1340 cm^{-1} , assignable to imide carbonyl (C=O) and imide ring (C-N-C) groups, indicating the successful synthesis of PI. XRD patterns show the different degree of crystallization in three PIs. While PI_{sphere} shows poorly crystalline structure with only broad peaks, PI_{flower} and PI_{disk} shows high crystallinity with strong and sharp peaks.

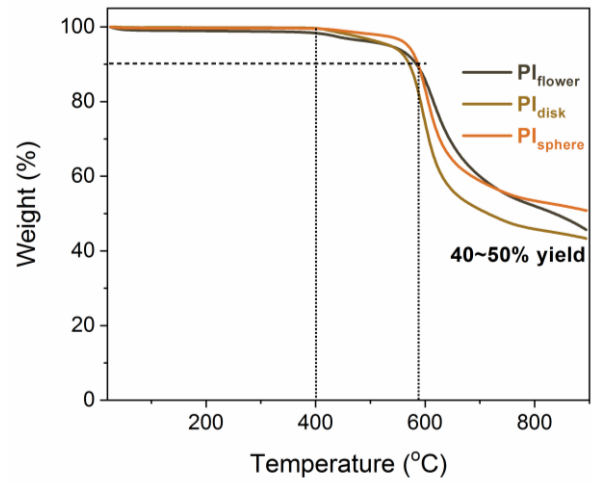


Figure S4.8 TGA curves of PI_{flower}, PI_{disk}, and PI_{sphere} tested at a ramp rate of 10 °C min⁻¹ in the N₂ atmosphere. Results show negligible weight loss before 400 °C, less than 10% weight loss before 580 °C, and high carbon yield around 40-50%, suggesting the excellent thermal stability of PIs.

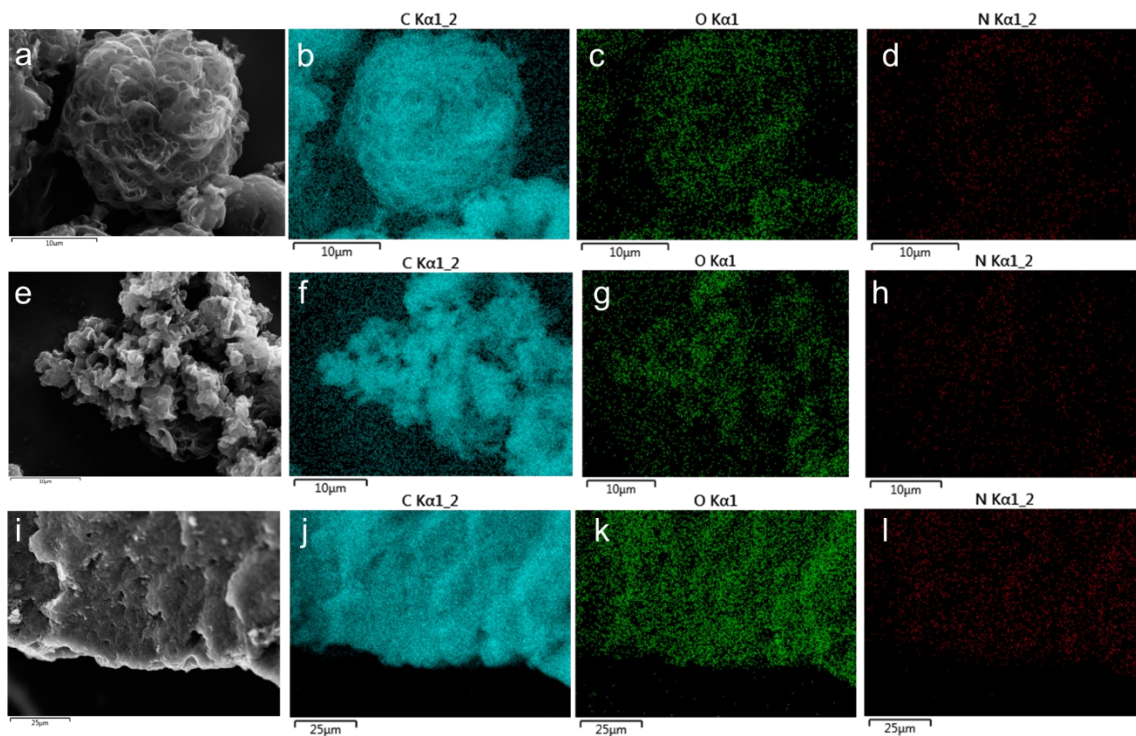


Figure S4.9 SEM image and EDX mapping of (a-d) C_{flower}, (e-h) C_{disk}, and (i-l) C_{sphere}.

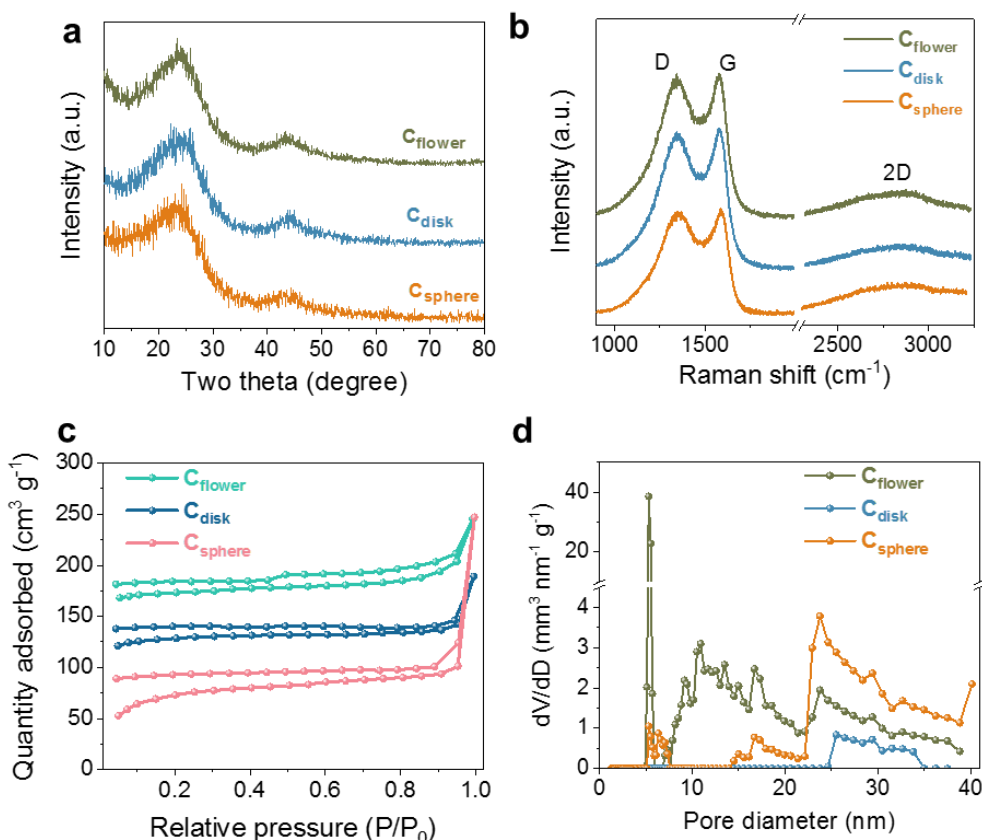


Figure S4.10 Structural characterization of C_{flower} , C_{disk} , and C_{sphere} . (a) XRD patterns, (b) Raman spectra of different carbon materials (C_{flower} , C_{disk} , and C_{sphere}). (c) Nitrogen adsorption/desorption curves of C_{flower} , C_{disk} , and C_{sphere} . For clear comparison, the curve for C_{flower} and C_{disk} is shifted positively along the y axis with a value of 100 and 50 $\text{cm}^3 \text{g}^{-1}$, respectively. (d) corresponding pore size distribution curves of different carbons.

Raman spectra (Figure S4.10b) display two sharp peaks at 1345 cm^{-1} and 1580 cm^{-1} along with one broad peak ($2320\sim 3220 \text{ cm}^{-1}$), assignable to typical D, G, and 2D band, respectively of carbon materials in which D band associates with disorder-induced phonon whereas G band relates to graphitic structure.^{198, 199}

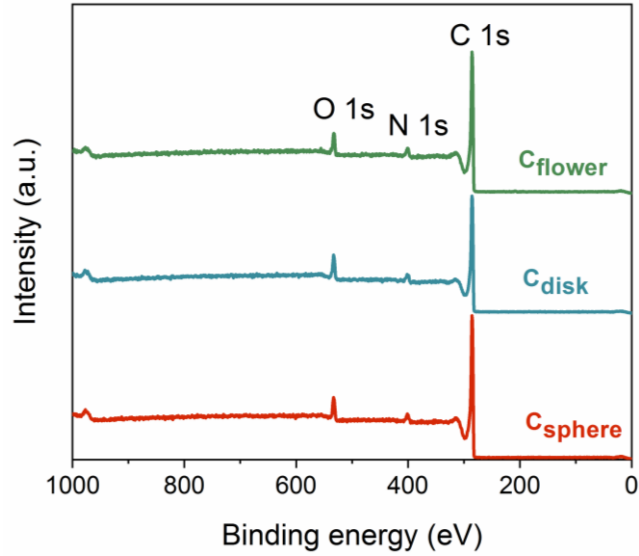


Figure S4.11 XPS survey spectra of different carbon materials. Only C, N, and O elements can be detected in all samples.

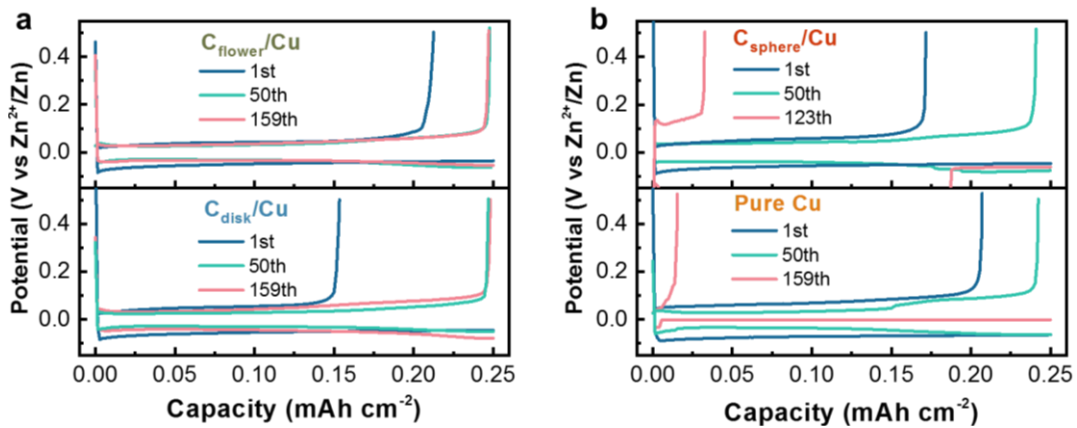


Figure S4.12 Discharge/charge profiles of b) $C_{\text{flower}}/\text{Cu}$, $C_{\text{disk}}/\text{Cu}$ and c) $C_{\text{sphere}}/\text{Cu}$, pure Cu at different cycles, corresponding to Figure 4.3a.

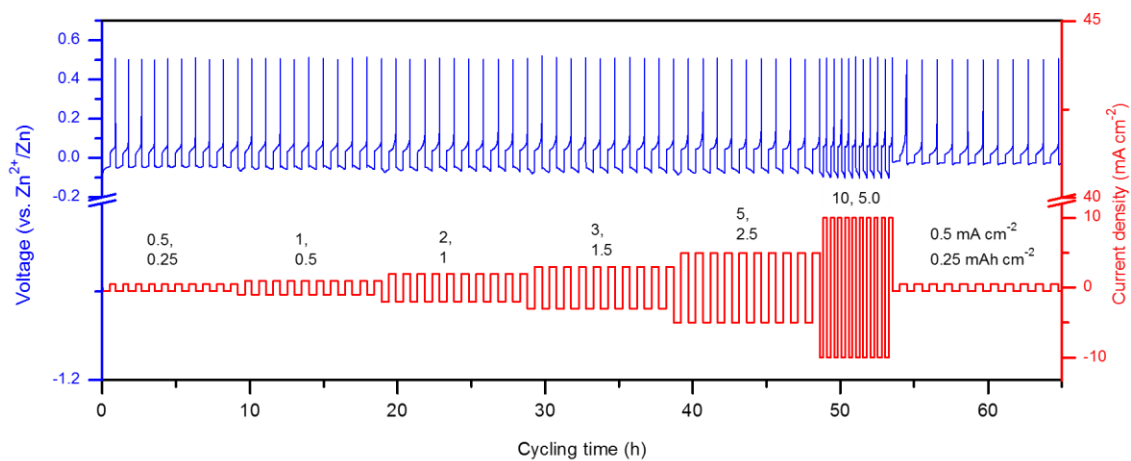


Figure S4.13 Plot for voltage and current density versus cycling time.

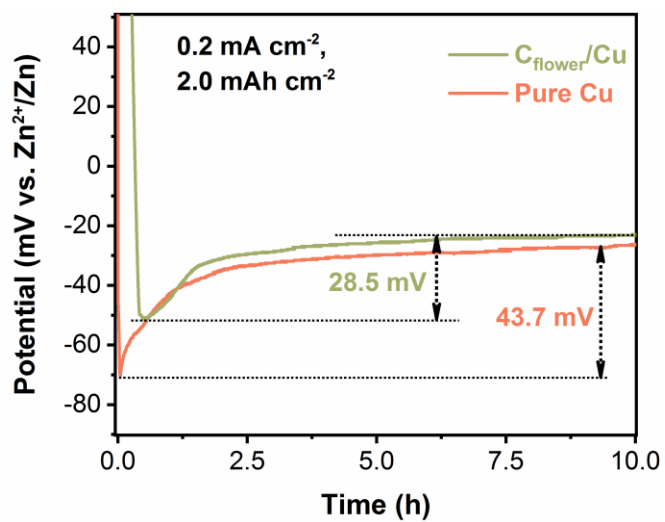


Figure S4.14 Plating profiles of Zn onto $C_{\text{flower}}/\text{Cu}$ vs. pure Cu substrate at a current density of 0.2 mA cm^{-2} and a capacity of 2.0 mAh cm^{-2} .

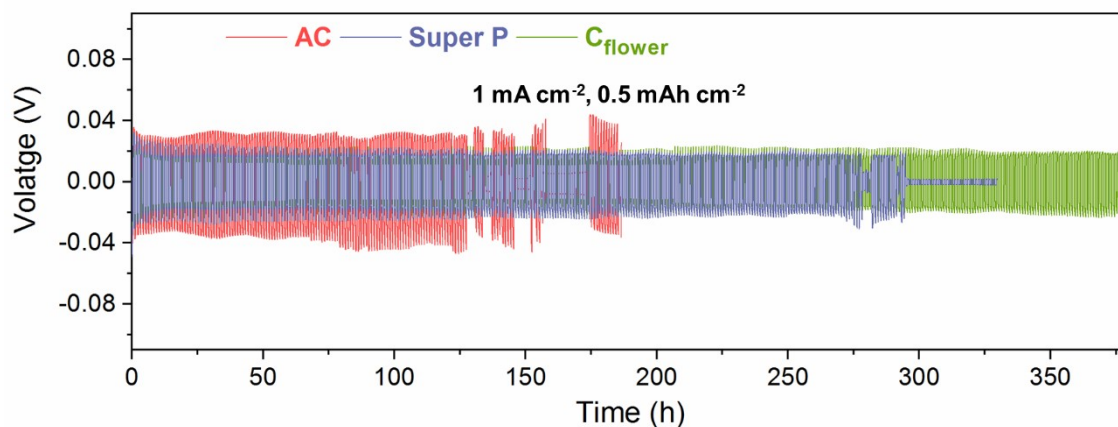


Figure S4.15 Cycling performance of symmetric cells using Zn foils coated with different carbon materials (activated carbon, Super P, and C_{flower}). Test condition: 1 mA cm^{-2} , 0.5 mAh cm^{-2} .

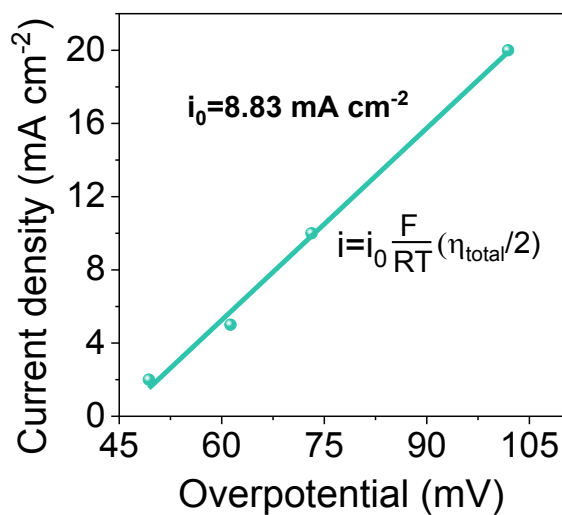


Figure S4.16 Plots of current density against overpotential in symmetric cells.

To evaluate the kinetics of $C_{\text{flower}}/\text{Zn}$ deposition, the exchange current density related to the Zn plating/stripping process is calculated. As shown in the Figure S4.16, $C_{\text{flower}}/\text{Zn}$ showcases an exchange current density of 8.83 mA cm^{-2} , indicating a fast deposition kinetics.²⁰⁷

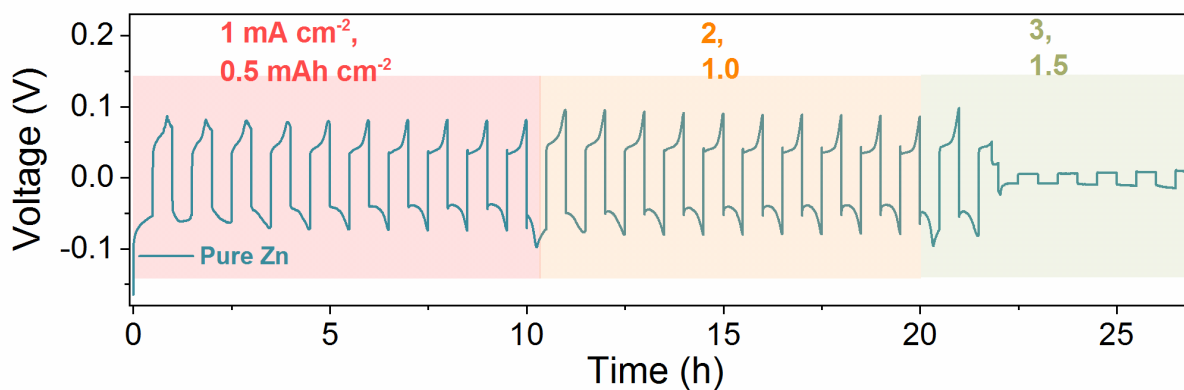


Figure S4.17 Rate performance of symmetric cells based on pure Zn electrodes at current densities from 1.0 to 3 mA cm⁻² with plating capacities from 0.5 mAh cm⁻² to 1.5 mAh cm⁻².

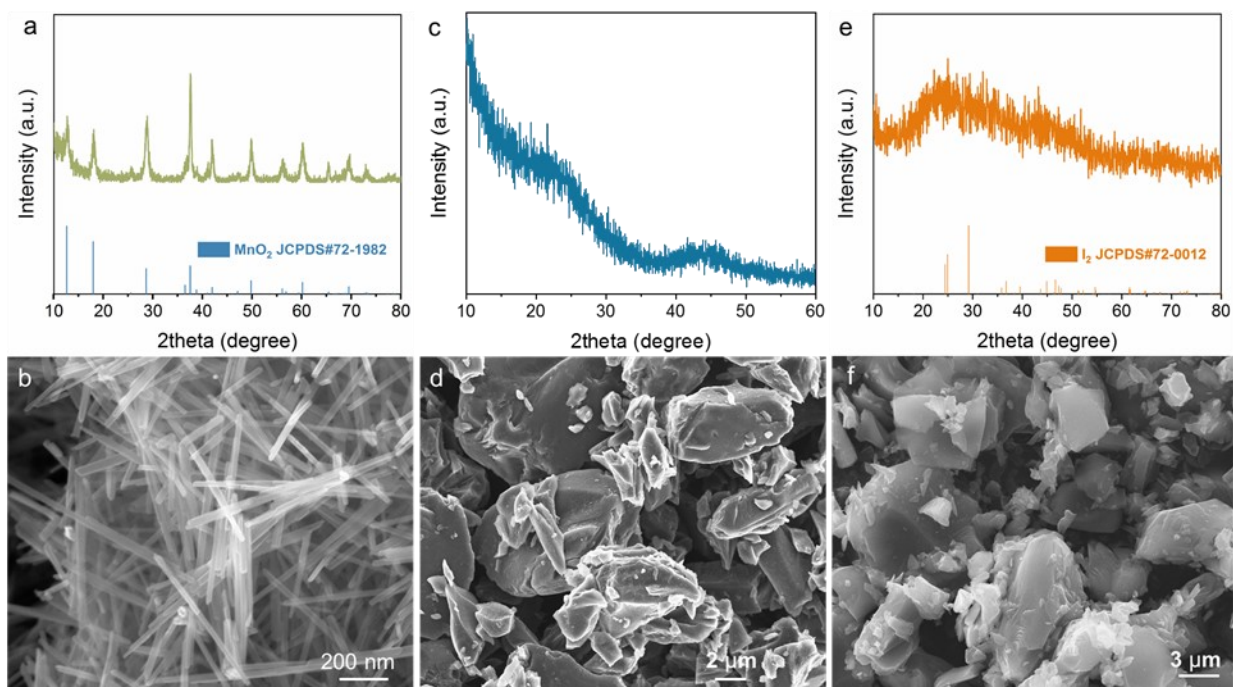


Figure S4.18 Structural characterization of cathode materials. (a, c, e) XRD patterns of (a) MnO₂, (c) AC, and (e) I₂/AC and (b, d, f) SEM images of (b) MnO₂, (d) AC, and (f) I₂/AC.

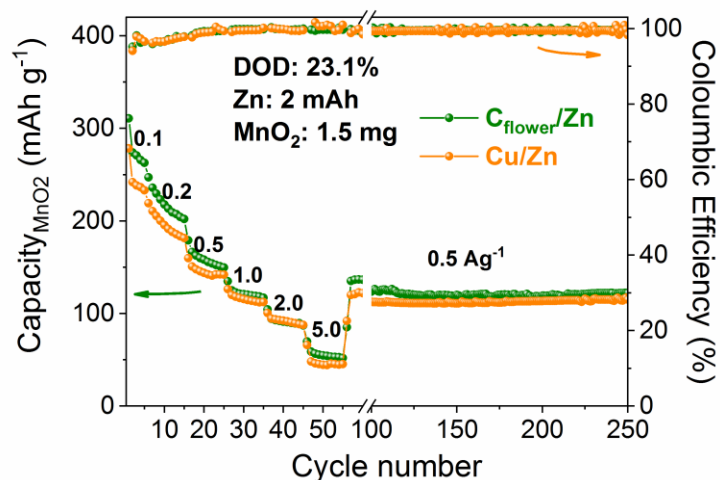


Figure S4.19 Cycling performance of Zn//MnO₂ batteries based on 2 mAh of Zn and 1.5 mg of MnO₂. The green line respernt C_{flower}/Zn-based battery while yellow line is Cu/Zn-based battery.

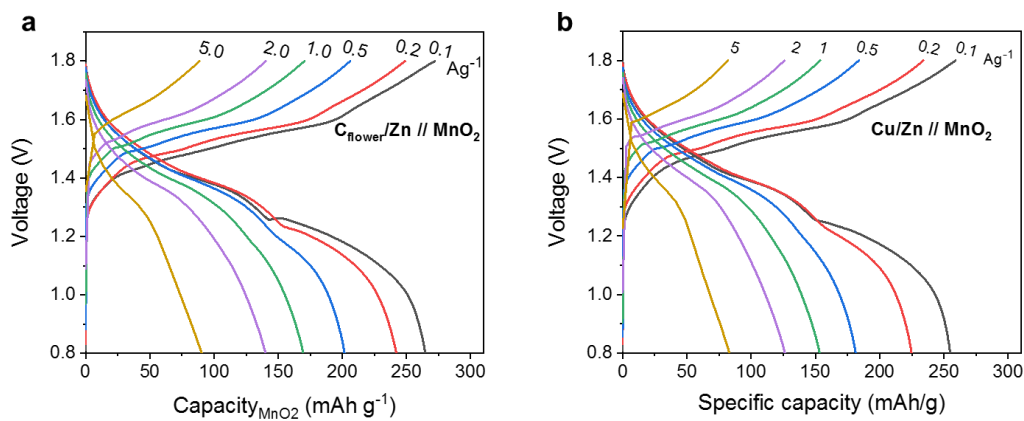


Figure S4.20 Zn//MnO₂ batteries using 10 mAh (ca. 12.2 mg) of Zn and 1.5 mg of MnO₂. Charge/discharge profiles of b) C_{flower}/Zn//MnO₂ battery and c) Cu/Zn//MnO₂ battery at different current densities.

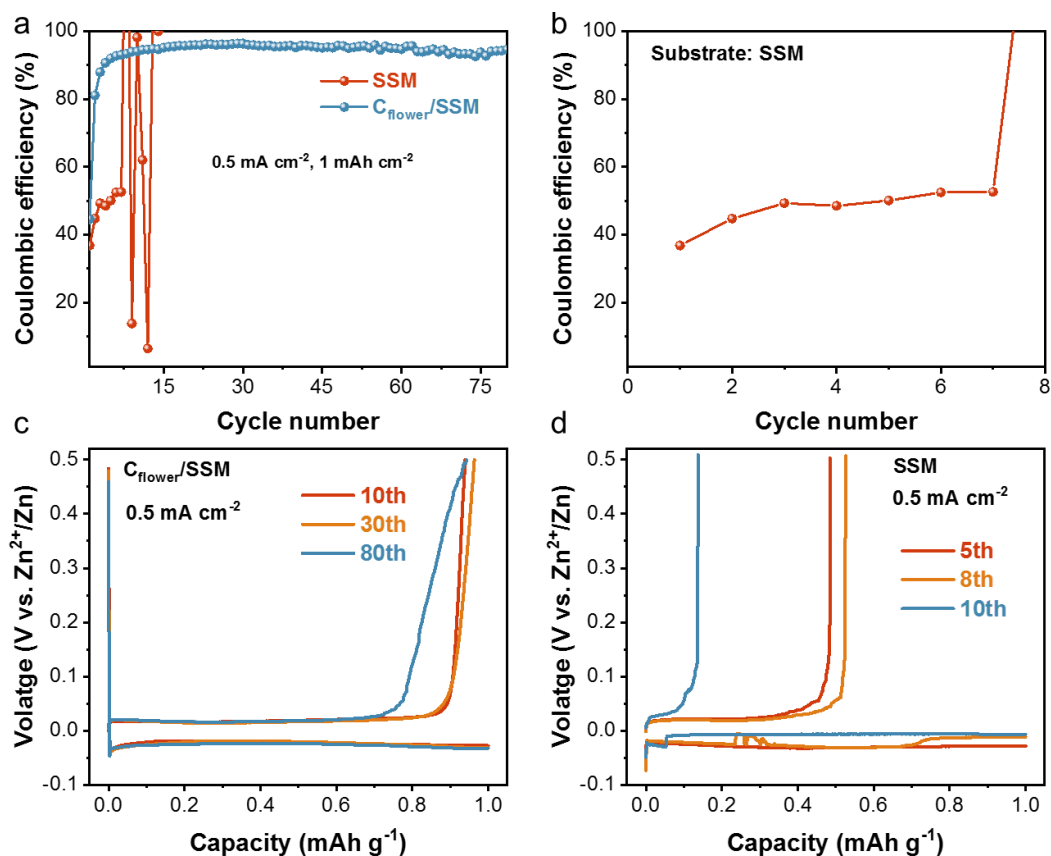


Figure S4.21 Electrochemical performance of Zn/SSM half cells. (a, b) Coulombic efficiency of Zn plating/stripping onto SSM-based substrates (C_{flower} /SSM vs. pristine SSM) at a current density of 0.5 mA cm^{-2} and a capacity of 1.0 mAh cm^{-2} . Charge/discharge curves of Zn plating/stripping on (c) C_{flower} /SSM and (d) pristine SSM at different cycles.

To demonstrate the general applicability of C_{flower} host on different substrates, SSM was used here for the Zn/SSM half-cell tests. At a current density of 0.5 mA cm^{-2} and a capacity of 1.0 mAh cm^{-2} , Figure S4.21a shows that the pristine SSM exhibits low CE values of only 40~50 % and short life of less than 10 cycles for Zn stripping/plating. By stark contrast, after applying C_{flower} host onto SSM substrate, the efficiency could be enhanced to ~95%, suggesting C_{flower} host enabling highly efficient Zn metal anode.

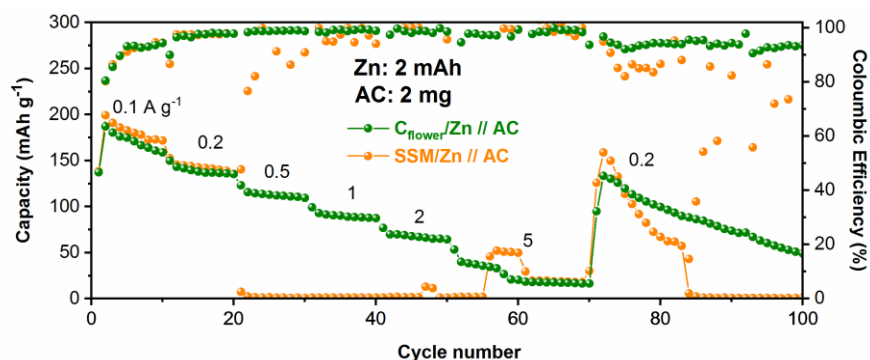


Figure S4.22 Rate performance of $C_{\text{flower}}/\text{Zn}//\text{AC}$ and $\text{SSM}/\text{Zn}//\text{AC}$ capacitors based on 2 mAh (ca. 2.44 mg) of Zn anode and 2 mg of AC cathode.

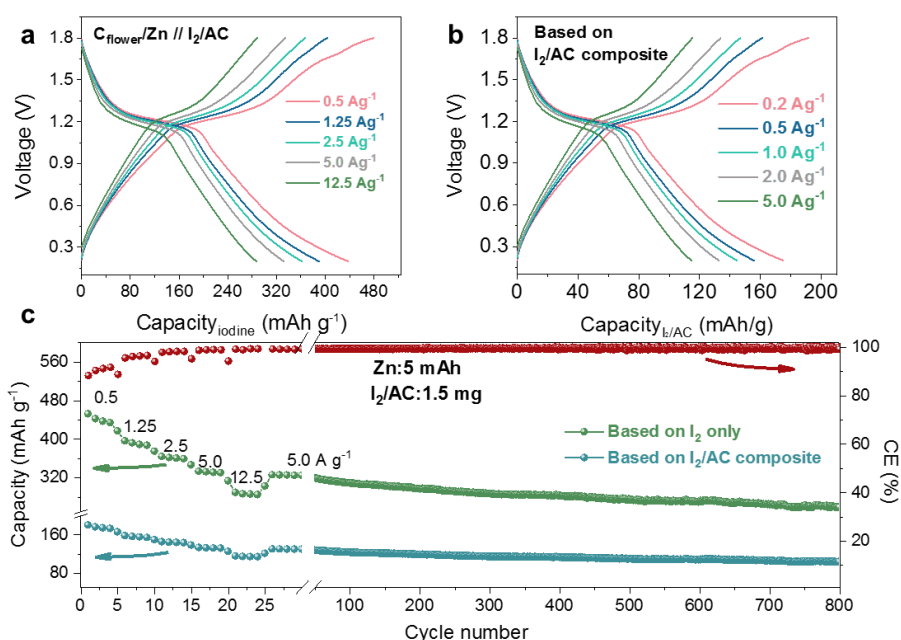


Figure S4.23 $C_{\text{flower}}/\text{Zn}//\text{I}_2/\text{AC}$ full cell constructed by 5 mAh (~ 6.1 mg) of Zn, 1.5 mg of I_2/AC composite, and 100 μL of 3M ZnSO_4 electrolyte. (a) Charge/discharge profiles based on iodine only and (b) iodine/AC composite. (c) Rate and cycling performance.

When calculating the capacity based only on I_2 mass, large capacities of 440 mAh g^{-1} at 0.5 A g^{-1} and 287 mAh g^{-1} at 12.5 A g^{-1} can be obtained. These values are higher than theoretical capacities of I_2/I^- electrodes which is caused by extra capacity from the AC. As such, the capacity was further calculated based on the active I_2/AC composite and high capacities of 175, 156, 145, 133, and 115 mAh g^{-1} can still be gained at 0.2, 0.5, 1.0, 2.0, and 5.0 A g^{-1} , respectively.

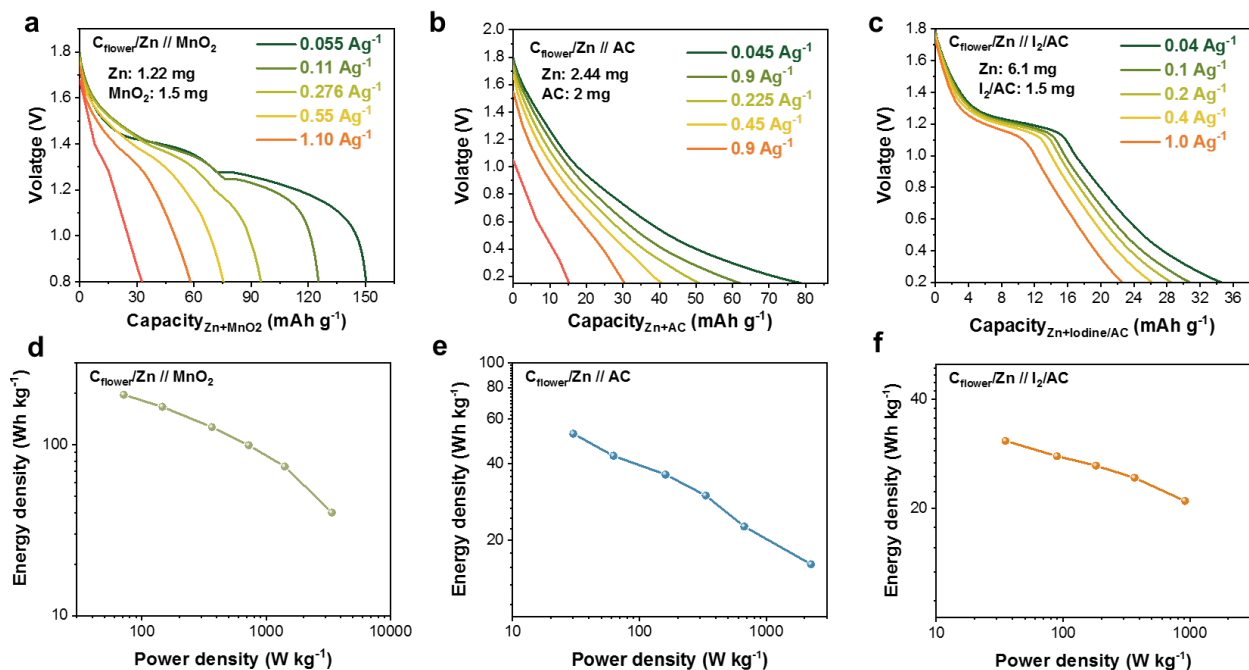


Figure S4.24 Full cell performance. (a-c) Charge/discharge curves of C_{flower}/Zn-based full cells, capacity and current rate is based on the total mass of Zn metal and cathode materials. And corresponding (d-f) Ragone plot of these devices.

For C_{flower}/Zn//MnO₂ battery, the energy density is 195.3, 166.2, 126.4, 99.09, 74.47, and 40.07 Wh kg⁻¹ at the power density of 71.71, 146.4, 366.8, 725.3, 1413, and 3379 W kg⁻¹, respectively. For C_{flower}/Zn//AC capacitor, the energy density is 52.58, 43.01, 36.28, 30, 22.64, and 16.06 Wh kg⁻¹ at the power density of 30.07, 62.41, 160.7, 332.7, 669.4, and 2250 W kg⁻¹, respectively. For C_{flower}/Zn//I₂/AC supercapattery, the energy density is 30.73, 27.89, 26.25, 24.29, and 20.97 Wh kg⁻¹ at the power density of 35.11, 89.48, 181.7, 366, and 914.1 W kg⁻¹, respectively.

Table S4.1 Binding energies of Zn atom on pristine, O-doped, and N-doped GNS.

	Gr	e ₁ O	e ₂ O	kO	cO	hO	pN	pyN	oN	g _n N	gN
E _{BE} (eV)	-0.08	-3.42	-0.04	-0.07	-0.20	0.00	-0.06	-0.19	-0.04	-0.07	-0.06

Table S4.2 Modified Zn anode and corresponding electrochemical performance in Zn/Cu half cells

Sample	Half cell			Reference
	Rate (mA cm ⁻²), Capacity (mAh cm ⁻²)	CE (%)	Cycle number	
C_{flower}	0.5, 0.25	99.3	500	This work
	5, 2.5	98.6	10	
	20, 2.5	98	10	
Zn@ZnO-3D	2, 0.5	99.55	300	<i>Energy Environ. Sci.</i> , 2020,13, 503 ²⁰⁷
CNT@CC	2, 2	97	30	<i>Adv. Mater.</i> 2019, 31, 1903675 ²⁸
	5, 2	97.9	30	
Ti₃C₂T_x MXene	1, 1	94.13	400	<i>ACS Nano</i> 2019, 13, 10, 11676 ²⁰⁰
	5, 1	90	400	
ZIF-8-C-500	2, 1	98.6	200	<i>Joule</i> 3, 2019, 1289 ¹⁵⁵
	20, 1	98.4	200	
	20, 2	99.3	200	
	20, 3	99.5	200	
	20, 5	98.8	200	
	20, 10	97.6	200	
PA-coating	0.4, 0.4	95.12	300	<i>Energy Environ. Sci.</i> , 2019,12, 1938 ¹⁸
Cu-Zn alloy	5, 0.5	91.8	100	<i>Energy Storage Materials</i> , 2020, 27, 205 ²⁰⁴
TiO₂-PVDF coating	1.77, 0.885	99.4	1000	<i>Adv. Funct. Mater.</i> 2020, 2001867 ¹⁸⁷
N-Hollow Carbon Sphere	4, 1	95	200	<i>Adv. Energy Mater.</i> 2021, 11, 2003419 ¹⁸⁹
MXene@Sb-300	1, 0.1	97.2	1500	<i>Energy Storage Mater.</i> 2021, 41, 343 ²⁰⁸
N, O-CNF	1, 1	>99	60	<i>Chem. Eng. J.</i> 2021, 425, 131862 ²⁰⁹
N-Graphdiyne	1, 0.5	>99	300	<i>Angew. Chem. Int. Ed.</i> , 2021 ²¹⁰
N-Zn/CC	1, 1	99.1	300	<i>Adv. Sci.</i> , 2021, 2103952 ²¹¹
Al-ZnO@Cu	1, 0.5	99.5	100	<i>Small</i> , 2021, 2106441 ²¹²
Graphene	16, 0.8	99.9	10000	<i>Science</i> , 2019, 366, 645 ²⁷
	40, 0.8	99.9	10000	

Table S4.3 A survey of modified Zn anodes and corresponding electrochemical properties in Zn||Zn symmetric cells.

Sample	Symmetric cells			Reference
	Rate, Capacity	Voltage hysteresis	Cycle life	
C _{flower}	0.5, 0.25	35 mV	2000 h	This work
	2, 1	80 mV	1100 h	This work
	5, 2.5	134 mV	150 h	This work
PAN	1, 1	90 mV	1145 h	<i>Adv. Sci.</i> 2021, 8, 2100309 ¹⁸⁴
MXene @Sb-300	5, 5	~100 mV	550 h	<i>Energy Storage Mater.</i> 2021, 41, 343 ²⁰⁸
NOCA@CF	2, 1	80 mV	200 h	<i>Chem. Eng. J.</i> 2020, 400, 125843 ¹⁸⁸
ZrO ₂	5, 1	64 mV	2100 h	<i>Adv. Funct. Mater.</i> 2020, 30, 1908528 ¹⁸⁶
MOF	0.5, 0.5	90 mV	3000 h	<i>Angew. Chem. Int. Ed.</i> 2020, 59, 9377. ²⁶
MnO ₂ @CC	0.5, 0.25	50 mV	550 h	<i>Adv. Mater. Interfaces</i> 2020, 7, 2000510 ²¹³
	1, 1	40 mV	150 h	
CNT film	0.1, 0.5	50 mV	1800 h	<i>Chemical Engineering Journal</i> 2020, 384, 123355 ²¹
	1, 1	80 mV	400 h	
CNT@CC	2, 2	50 mV	200 h	<i>Adv. Mater.</i> 2019, 31, 1903675 ²⁸
	5, 2.5	120 mV	110 h	
TiO ₂ -PVDF	0.885, 0.885	100 mV	2000 h	<i>Adv. Funct. Mater.</i> 2020, 2001867. ¹⁸⁷
	8.85, 8.85	200 mV	250 h	
ZIF-8 derived carbon	2, 2	40 mV	400 h	<i>Adv. Energy Mater.</i> 2020, 10, 1904215 ²⁰³
	5, 5	50 mV	400 h	
In-Zn	0.2, 0.2	54 mV	1500 h	<i>Small</i> 2020, 16, 2001736 ²¹⁴
	1, 1	200 mV	500 h	

Table S4.4 Comparison of DOD values of reported Zn metal in full cells

Anode	Cathode	Rate (A g ⁻¹)	DOD of Zn (%)	Life cycle	Reference
C_{flower}/Zn	MnO ₂	0.1~5.0	11.3-41.3	100	This work
	MnO ₂	0.1~5.0	4~19.8	250	
	AC	1.0~10	5.8~8.7	500	
N-Zn	MnO ₂	1.0	0.079	2000	<i>Adv. Sci.</i> , 2021, 2103952 ²¹¹
C-750/Zn	MnO ₂	0.3	0.328	5000	<i>Adv. Energy Mater.</i> 2020, 10, 1904215 ²⁰³
NGO-Zn	LiMn ₂ O ₄	0.14	1.88	600	<i>ACS Appl. Energy Mater.</i> 2021, 4, 6, 6364 ²⁰²
AEC-Zn	MnO ₂	0.62	0.53	300	<i>Adv. Funct. Mater.</i> 2021, 31, 2001867 ¹⁸⁷
MOF/Zn	MnO ₂	0.5	6.8	180	<i>Angew. Chem. Int. Ed.</i> 2020, 59 9377 ²⁶
Zn In	AC	2.0	0.24	5000	<i>Small</i> 2020, 16, 2001736 ²¹⁴
Cu-Zn alloy/Zn	MnO ₂	3.08	0.18	500	<i>Energy Storage Mater.</i> 2020, 27, 205 ²⁰⁴
Zn@GF	PB	0.1	3.33	150	<i>Electrochim. Acta</i> 2017, 244, 172 ¹⁹⁰
Zn with CNF interlayer	MnO ₂	1	1.58	400	<i>Chem. Eng. J.</i> 2021, 425, 131862 ²⁰⁹
Zn (electrolyte)	V ₂ O ₅	1.0	22.26	800	<i>Nat. Sustain.</i> 2021, ²¹⁵
PAN@Zn	MnO ₂	0.5	10	400	<i>Adv. Sci.</i> 2021, 8, 2100309 ¹⁸⁴
Zn@ZIF-8-500	AC	4.0	3.6	20000	<i>Joule</i> 3, 2019, 1289 ¹⁵⁵
	I ₂ /C	2.0	6.0	1600	
Zn/CNT/CC	CNT/MnO _x @PEDOT	20 mA cm ⁻²	12	1000	<i>Adv. Mater.</i> 2019, 31,1903675 ²⁸

Chapter 5 An Ultrafast, Durable, and High-loading Polymer Anode for Aqueous Zinc-Ion Batteries and Supercapacitors

A version of this Chapter has been published in *Advanced Materials*:

Zhixiao Xu, Matthew Li, Wenyuan Sun, Tian Tang, Jun Lu,* and Xiaolei Wang*, An Ultrafast, Durable, and High-loading Polymer Anode for Aqueous Zinc-Ion Batteries and Supercapacitors. *Advanced Materials*, 2022, 34, 2200077.

5.1 Introduction

With high theoretical capacities (820 mAh g^{-1} and 5855 mAh cm^{-3}), suitable electrochemical potential ($-0.763 \text{ V vs. standard hydrogen electrode, SHE}$), low cost, and rich abundance of component materials, aqueous zinc-ion batteries (ZIBs) and capacitors (ZICs) have exhibited great promise for grid-level energy storage and other stationary applications.^{6, 10, 12} The past years have witnessed rapid progress in the development of cathode materials, including Mn- and V-based oxides, Prussian blue analogs, and organic materials for ZIBs and activated carbon for ZICs with seemingly high energy densities (based on the cathodes).^{5, 6, 12} However, in most of these cases, excessive Zn anodes were used to compensate for the uncontrollable dendritic growth, corrosion behavior, and low coulombic efficiency (CE) of the Zn metal.^{5, 10, 122, 216} As such, most of the ZIBs and ZICs developed using these electrode materials exhibited actual device energy and power densities that were significantly lower than the corresponding theoretical values.^{217, 218} Another key performance metric that needs to be improved in ZIBs is their high-rate charge and discharge. Furthermore, in addition to the dendrite-derived problems commonly experienced in other metal anode batteries, ZIBs are

disadvantaged by high rates of hydrogen gas evolution from water decomposition, leading to poor cycle lives.^{5, 10, 122, 216}

Based on the history of lithium-ion batteries,²¹⁹ it is of great value to develop Zn-metal-free anodes for rocking-chair ZIBs, which, however, remains a challenging objective.¹⁴ An ideal Zn-free anode should possess a low potential vs. Zn^{2+}/Zn , high theoretical capacity, good electronic conductivity, robust structure, and electrochemical stability.¹⁴ One material that was explored for its possible use as an anode for ZIBs is Chevrel-phase Mo_6S_8 , which has demonstrated a discharge voltage of 0.36 V vs. Zn^{2+}/Zn ; however, its low capacity and short life have limited its application.^{37, 38} Since then, better ZIB anode materials, such as copper selenide (Cu_{2-x}Se),²²⁰ sodium-intercalated TiS_2 ($\text{Na}_{0.14}\text{TiS}_2$),⁴⁰ and hexagonal molybdenum oxide (h-MoO_3),⁴³ with either lower discharge voltages (*e.g.* 0.3 V vs. Zn^{2+}/Zn) or longer cycle lives (*e.g.* 30000 cycles), have been discovered. Possible anode materials are also not limited to inorganic substances and composites; organic materials, particularly carbonyl-rich molecules and polymers, have also demonstrated great potential as anodes^{47, 51} because of their low water solubility, high electrochemical stability, oxygen-elimination capability,²²¹ passivation toward hydrogen evolution reactions,²²² and low redox potentials relative to the Zn redox potential.^{48, 51, 52, 223} For example, Lu *et al.* devised a carbonyl-rich dianhydride molecule with fast kinetics by enhancing its π - π stacking interaction; however, the molecule exhibited poor cycling stability.¹⁵⁹ On the other hand, Feng *et al.* constructed a 2D-imide-based covalent organic framework as a rapid Zn^{2+} storage anode and revealed a two-step Zn^{2+} storage mechanism involving a reversible carbonyl-enolate group transition.²²⁴ However, although using a Zn-free anode is helpful at raising the potential, there remains a large gap in achieving fast and stable charge/discharge in Zn-based energy storage systems.

In this study, we searched for an anode/electrolyte configuration tailored specifically toward achieving fast and stable charging in ZIBs and ZICs. With the guidance of theoretical calculations, a series of molecules and polymers with and without carbon nanotubes (CNTs) were synthesized and used as ZIB anodes. Among these materials, a polymer/CNT hybrid based on perylene 3,4,9,10-tetracarboxylic dianhydride demonstrated the best performance. Electrolytes containing different zinc salts in a variety of concentrations were then studied experimentally and via simulation, revealing that the incorporation of triflate anions, mild acidity, high ionic conductivity, and low viscosity can produce sufficiently high transport properties that enable fast and stable ions storage. The optimized combination will enable the polymer anode to have a low discharge voltage (0.2–0.4 V vs. Zn²⁺/Zn), approaching-theoretical capacity (128 mAh g⁻¹ at 50 mA g⁻¹), high CE (~100%), ultrahigh loading (~50 mg cm⁻²), fast charging capability (100 A g⁻¹), and extraordinary stability for up to one million cycles. The storage mechanism was uncovered via electrochemical measurements and *in/ex situ* characterizations, revealing a mechanism involving reversible Zn²⁺ (de-)coordination and proton co-interaction at the carbonyl group in the polymer. To demonstrate its practical use, the polymer/CNT anode was coupled not only with battery cathodes for ZIBs, which manifested high power densities (9.1 kW kg⁻¹) and long lives (50000 cycles), but also with supercapacitor cathodes for ZICs, resulting in record-high stabilities for over sub-million cycles at 10 and 200 A g⁻¹, which are far better than those of corresponding devices based on Zn metal anodes, even in excessive amounts.

5.2 Experimental Section

5.2.1 Chemicals and materials preparation

Chemicals. pyromellitic dianhydride (PMDA), 1,4,5,8-naphthalenetetracarboxylic dianhydride (NTCDA), perylene 3,4,9,10-tetracarboxylic dianhydride (PTCDA), ethylene diamine (EDA), sodium alginate, and MWCNT was purchased from Sigma-Aldrich. DMF, NMP, ammonia, ZnSO₄,

Zn(OTf)₂, PVDF, H₂SO₄, HNO₃, HCl, and NaOH were obtained from Thermo Fisher Scientific. Commercial MnO₂ and activated carbon was obtained from Duracell and MTI, respectively.

Synthesis of PTCDI. PTCDA was mixed with dilute ammonia solution in DMF under stirring for 30 min, which was then poured into Teflon-lined autoclave for solvothermal treatment at 180 °C for 12h. The product was collected after filtration, washing, and drying.

Synthesis of polymers. Equal molar amount (2 mmol) of dianhydride (PMDA or NTCDA or PTCDA) and diamine (EDA) was added into NMP (15 mL). The polycondensation reaction was conducted in a capped bottle (30 mL) at 180 °C for 12 h. The product was collected after filtration, drying and thermal annealing in flowing N₂ at 300 °C for 4h. The polyimide (PI) based on PTCDA-EDA, NTCDA-EDA, and PMDA-EDA combinations was denoted as PI-1, PI-2, and PI-3, respectively.

Synthesis of polymer/CNT. The synthetic procedure is similar to the above-mentioned polymerization process except that a small amount of CNT (600 μL of ~70 mg mL⁻¹ CNT/NMP suspension) was added into the polymer precursor solution before the polycondensation reaction.

5.2.2 Characterization

The chemical structure of organic materials was studied by Fourier Transform Infrared Spectroscopy (FTIR, Nicolet 8700). *In situ* FTIR was conducted in the Nicolet 8700 microscope mode. X-ray Diffraction (XRD) measurements were conducted on an Ultima IV (Rigaku) diffractometer equipped with a Cu K α X-ray source. The thermal property was characterized by Thermogravimetric Analyzer (TGA Q50) in the air atmosphere with a heating rate of 10 °C min⁻¹. Material micro/nano-structures were characterized by scanning electron microscope (SEM, Zeiss EVO M10) field-emission scanning electron microscope (FESEM, Zeiss Sigma) equipped with energy dispersive x-ray analysis (EDX, Oxford) and sphere-aberrated transmission electron microscope (TEM, JEOL JEM-ARM200CF) equipped with Atomic Resolution S/TEM. X-ray photoelectron spectrometer (XPS, Kratos AXIS

Ultra) was used to gain insight into the chemical binding environment of elements. The pH, viscosity, and ionic conductivity of electrolytes were measured by pH meter, rheometer, and conductivity meter, respectively.

5.2.3 Electrochemical measurements.

Coin cells (CR-2032) were assembled for both half-cell and full-cell electrochemical measurements. For half cells of organic materials, the working electrode was prepared by thoroughly mixing active materials (e.g. PI-1/CNT), conductive carbon (Super P), and binder (PVDF) in a mass ratio of 6:3:1 in NMP. The slurry was drop coated onto a stainless-steel mesh (SSM, 316L, 325 mesh size), and dried immediately under infrared light. In this way, PI-1/CNT electrode could be made in minutes in stark contrast to the traditional electrode-preparation method under vacuum drying for hours. The loading mass of active materials was controlled around 1~2 mg cm⁻² for low-loading tests and increased to 4~5 mg cm⁻² for high-loading tests. To study the influence of electrolyte, ZnSO₄ or Zn(OTf)₂ was dissolved in water with different concentration and 100 μL of electrolyte was used for all cells. Glassy fiber (Whatman grade A) was used as the separator in all cells. For half cells, Zn foil (default: 250 μm, 100 or 30 μm in some cases) was used as the counter/reference electrode while for full cells Zn_xMnO₂ or AC was used as the counter electrode (cathode). In some cases, cells fail due to the growth of zinc dendrites (e.g. Figure 2E, Figure S11d) and thus they were disassembled and re-assembled by using a new Zn anode and electrolyte. Cyclic voltammetry (CV) and electrochemical impedance spectra (EIS) were conducted by using an electrochemical workstation (VMP3, Biologic). The galvanostatic (dis)charging (GCD) experiments were performed on Neware battery test systems (CT-4008T-5V20mA-164, CT-4008T-5V50mA-164, CT-4008T-5V6A-S1, Shenzhen, China). All electrochemical tests were conducted at ~20 °C.

For making ultrahigh-loading free-standing electrodes ($10\text{-}50\text{ mg cm}^{-2}$), PI-1/CNT (or PI-1) powder was hand mixed with Super P powder in a weight ratio of 7:3 in the mortar for more than 20 min. And the mixture was pressed into disk-like tablets under high pressure (~ 10 Ton) using die mold (diameter: 12.7 mm). Without binder and current collector, tablets could be directly applied as the working electrode for battery fabrication in which the electrolyte amount is kept constant ($100\text{ }\mu\text{L}$).

For studying the storage mechanism, custom-made T-type Swagelok cell was used to conduct two-electrode tests in which PI-1/CNT was coated onto the glassy carbon as the working electrode, Zn foil was applied as the counter/reference electrode, and glassy fiber membrane as the separator. Different electrolyte was prepared including $0.5\text{M Zn(OTf)}_2\text{-H}_2\text{O}$, $1\text{M Na(OTf)}_2\text{-H}_2\text{O}$, $0.5\text{M Zn(OTf)}_2\text{-DMF}$, $1\text{M Na(OTf)}_2\text{-DMF}$, ZnSO_4 and H_2SO_4 with different pH values. CV tests were scanned at a rate of 5 mV s^{-1} .

For making rocking-chair type ZIBs, the PI-1/CNT, Zn_xMnO_2 and $1\text{M Zn(OTf)}_2 + 0.1\text{M MnSO}_4$ aqueous solution were used as the anode, cathode, and electrolyte, respectively and the N/P mass ratio is kept around 1 ($\sim 1.2\text{ mg cm}^{-2}$). Zn_xMnO_2 electrode was prepared in a Zn-MnO₂ battery with commercial $\beta\text{-MnO}_2$ as cathode (MnO_2 : Super P: PVDF=7:2:1) and $1\text{M Zn(OTf)}_2 + 0.1\text{M MnSO}_4$ as the electrolyte in which cells were cycled between 0.8-1.8 V at 0.1 A g^{-1} for 20 cycles and finally discharged to 0.8 V followed by cell disassembly. Besides, The ZnMn_2O_4 cathode was also prepared based on a previous paper.¹⁰⁸ In a typical synthesis, 10 mL 0.2 M $\text{Zn(NO}_3)_2$ (378.6 mg), 20 mL 0.2 M $\text{Mn(NO}_3)_2$ (715.8 mg) and 320 mg commercial carbon (Super P) were loaded in a 100 mL flask. Next, 18 mL aqueous ammonia (25 wt %) was dropped into the mixture under constant stirring for 1 h. Then, the mixture was evaporated and heated at $180\text{ }^\circ\text{C}$ for 3 h, generating $\text{ZnMn}_2\text{O}_4/\text{C}$ composite with $\sim 60\text{ wt \% ZnMn}_2\text{O}_4$ and 40 wt \% carbon . The slurry was prepared by mixing $\text{ZnMn}_2\text{O}_4/\text{C}$ with

Super P and PVDF in a ratio of 7:2:1 in NMP. The electrolyte is 100 μ L of 1.5M Zn(OTf)₂ or 1M Zn(OTf)₂ + 0.1M MnSO₄ for fabricating PI-1/CNT//ZnMn₂O₄ full cells with low N/P ratios.

For making ZICs, PI-1/CNT was firstly discharged to 0.1V in a half cell and then extracted as the anode while the AC cathode was made of 80% AC, 10% Super P and 10% PVDF (for Figure 5E) or sodium alginate (for Figure 5 G), and the N/P mass ratio is kept around 1:1.5 (for Figure 5E) or 1.15:1 (for Figure 5G). The electrolyte is 1M ZnSO₄ (for Figure 5E) or 3M ZnSO₄ (for Figure 5 G) due to the unstable cycling performance of this AC electrode in Zn(OTf)₂.²⁰¹ For comparison, Zn metal anode with controlled amount of capacity was also applied as anode for both ZIBs and ZICs, which was prepared by galvanostatic electrodeposition (5 mA cm⁻²) in a two-electrode system with Cu foil as working electrode, Zn foil as counter electrode and 2M ZnSO₄ as the electrolyte. Of note, for making ultrafast PI-1/CNT//AC capacitor that works at 200 A g⁻¹ (in Figure 5G), the PI-1/CNT slurry was prepared by using the sodium alginate binder with the ratio of 6:3:1.

5.2.4 Calculation of gravimetric energy and power densities

The gravimetric energy density E (Wh kg⁻¹) and power density P (Wkg⁻¹) of ZIBs were calculated based on the following equations:

$$E = \frac{C * V * 1000}{m}$$

$$P = \frac{I * V * 1000}{m}$$

in which C, V, I, m represents the discharge capacity (Ah), mid-capacity discharge voltage (V), discharge current (A), and the total mass (g) of active materials in both the anode and the cathode, respectively.

5.2.5 Molecular dynamics simulation and DFT calculation

The MD simulations were performed through the GROMACS package^{225, 226} in NVT ensemble for 5 ns, and the data from the last 2 ns was extracted to conduct the analysis. Systems were minimized by the steepest descent method to limit the maximum force within 1000.0 kJ/(mol·nm), followed by equilibration in NVE ensemble for 250 ps. The temperature was controlled as 300 K by the Nose-Hoover thermostat^{227, 228}. Motion equations were integrated by the Leap-frog algorithm²²⁹ with a time step of 1 fs and constraints were applied to all bonds by the LINC algorithm.²³⁰ Cut-off distances for van der Waals and electrostatic interactions were 1.0 nm. PME method was used to calculate the long-range electrostatic interactions.²³¹ The force fields for zinc,²³² sulfate,²³³ triflate ion,²³⁴ and electrodes²³⁵ were referred to previous works, which were compatible with the OPLSAA force field.²³⁵ The tip3p water model was adopted. The potential difference was controlled by the fixed charge method (FCM) (assigning atomic charge on the inner layer of electrodes). As the potential difference was less than 2 V, the interface at the electrode has been proved to be almost identical with the one simulated by constant potential method (CPM).²³⁶

DFT calculations were performed in Gaussian 16 to energetically optimize the polymers. The structural optimization of molecules was accomplished at B3LYP/6-31+G (d,p) level.

5.3 Results and Discussion

5.3.1 Anode material design and selection

The electronic structures of organic materials are associated with their electrochemical behaviors in batteries. As such, density functional theory (DFT) calculations were first conducted to investigate the highest occupied molecular orbital (HOMO) and lowest unoccupied molecular orbital (LUMO) levels and bandgaps of several carbonyl-rich molecules (perylene-tetracarboxylic dianhydride or

PTCDA, and perylenetetracarboxylic diimide or PTCDI) and polymers (polyimides: PI-1, PI-2, and PI-3), which are either commercially available or easy to manufacture. As shown in **Figure 5.1A**, the LUMO levels and bandgaps for PTCDA, PTCDI, PI-1, PI-2, and PI-3 are (−4.29 eV, 2.51 eV), (−3.97 eV, 2.49 eV), (−3.88 eV, 2.48 eV), (−3.86, 3.57 eV), and (−3.58 eV, 4.43 eV), respectively. In general, a higher LUMO level leads to a lower discharge potential, whereas a narrower bandgap favors higher electronic conductivity. Thus, according to this principle, the discharge potentials for these organic materials should follow this order: PI-3 < PI-2 < PI-1 < PTCDI < PTCDA. Meanwhile, their conductivities should obey this order: PI-1 > PTCDI > PTCDA > PI-2 > PI-3. Although PI-3 has the lowest discharge potential, its very wide bandgap and low conductivity make it unsuitable for Zn-ion storage. Therefore, among these substances, PI-1 and PI-2 exhibit the greatest promise as anode materials for ZIBs.

To verify the DFT results, the aforementioned organic materials were synthesized and characterized. To increase the electrical conductivity, CNTs were added during the polymerization process to produce PI-1/CNT, PI-2/CNT, and PI-3/CNT. The successful preparation of these organic materials was confirmed by FTIR, in which peaks corresponding to carbonyl and imide groups were clearly detected (**Figure 5.1C** and **Figure S5.1**). XRD patterns reveal highly crystalline structures with negligible changes after compositing with CNTs (**Figure 5.1D** and **Figures S5.2**) due to the ultralow content of the CNTs (2 wt%). This was further confirmed by TGA curves (Figure 1E), which also revealed the excellent thermal stability of the PI, as evidenced by negligible weight loss at temperatures lower than 500 °C in air. SEM and TEM images show the different morphologies of these organic materials. Whereas the molecules exhibit nanorod-like microstructures, the polymers are clearly composed of nanosheets (Figure S5.3). For example, PI-1 exists in the form of ultrathin nanosheets, and when CNTs are introduced to create PI-1/CNT, the combination generates 3D

architectures characterized by tiny nanosheets wrapped around the CNTs (Figure 5.1F–H). By contrast, in PI-2 and PI-3, the nanosheets are assembled in flower-like structures (Figure S5.3). These nanostructures benefit from the exposure of redox-active sites and the transport of electrons and ions during battery charge/discharge.¹²³ The polymer/CNT hybrid (herein, PI-1/CNT is used as an example) was further observed via high-resolution TEM (HRTEM), which revealed that the interface between the PI-1 and CNTs is characterized by crystalline CNT cores coated by PI-1 shells with thicknesses of 20–100 nm (Figure S5.4). Furthermore, high-angle annular dark-field (HAADF) scanning TEM (STEM) and the corresponding elemental mapping showed a homogenous distribution of C, N, and O elements throughout the PI-1/CNT hybrid (Figure 5.1I).

Subsequently, these organic materials were used as electrodes for ZIB tests, with Zn as the counter/reference electrode and 2.0 M ZnSO₄ as the electrolyte. As shown in Figure 5.1B, although the molecules demonstrated high initial capacities (155 mAh g⁻¹ for PTCDA and 122 mAh g⁻¹ for PTCDI), these capacities decayed rapidly to 30 mAh g⁻¹ for PTCDA and 60 mAh g⁻¹ for PTCDI after 40 cycles. By contrast, the PTCDA-derived polymer, PI-1, exhibited a much higher stability (>90 mAh g⁻¹ for over 100 cycles), which can be explained by the lower solubility of the polymer than those of the molecules (Figure S5.5–S5.7). A comparison between the different polymers clearly showed that the performance trend follows PI-1 > PI-2 > PI-3, indicating that a larger π -conjugation structure benefits the stability of the ZIB. Furthermore, although PI-2 and PI-3 have lower discharge voltages, their wider bandgaps and lower π -conjugations suggest lower electrical conductivities, leading to fast capacity decay and large voltage hysteresis (Figure S5.8–S5.9). Evidently, among these

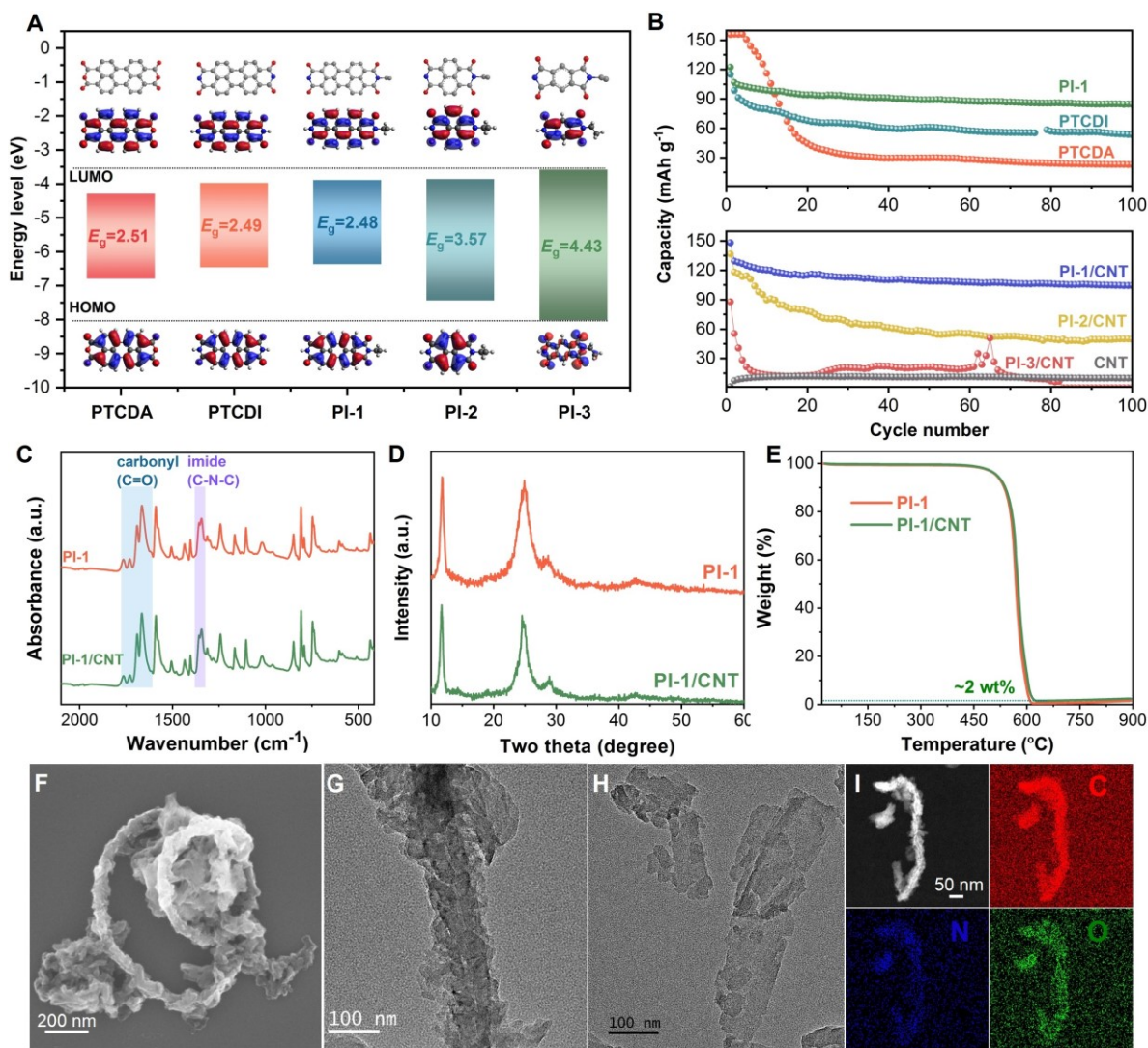


Figure 5.1 Electrode Engineering and Structural Characterization of PI-1 and PI-1/CNT. (A) Electronic structure of different molecules and polymers, (B) Cycling performance of different organic electrodes at 0.1 A g^{-1} , (C) FTIR spectra, (D) XRD patterns, and (E) TGA profiles of PI-1/CNT and PI-1. (F) SEM image, (G-H) TEM images, and (I) HAADF image and elemental mapping images of PI-1/CNT.

molecules and polymers, PI-1 demonstrated the highest intrinsic redox activity, which also matched well with the DFT results. Moreover, the performance of PI-1 could be further enhanced after CNT coupling into PI-1/CNT; by comparison, the pristine CNT exhibited negligible capacity and poor

reversibility (Figure 5.1B and Figure S5.10). Therefore, the resultant PI-1/CNT composite material is an excellent candidate as an anode for fast-charging Zn-ion batteries.

5.3.2 Electrolyte engineering and molecular dynamics simulation

The electrolyte composition has a crucial impact on Zn-based energy storage devices.¹⁰⁰ Of critical importance is the specific pairing between the anode and electrolyte. Here, we aimed to optimize the PI-1/CNT-based ZIB by investigating the influence of zinc salt and concentration on the battery performance. For this experiment, we formulated 0.5 M ZnSO₄, 1.0 M ZnSO₄, 2.0 M ZnSO₄, 1.0 M Zn(OTf)₂, 1.5 M Zn(OTf)₂, and 2.0 M Zn(OTf)₂ in water.

First, the rate performance of PI-1/CNT in different electrolytes was examined. As shown in Figure 2A, as the current density was increased from 0.2 A g⁻¹ to 5 A g⁻¹, the capacity in aqueous Zn(OTf)₂ decreased more slowly compared with that in ZnSO₄, suggesting the superiority of Zn(OTf)₂ over ZnSO₄ as an electrolyte salt for fast charging (Figure S5.11a–c). To demonstrate this better, a 1.0 M electrolyte is used for the following example (Figure 5.2B). At the low rate, i.e., 0.2 A g⁻¹, the PI-1/CNTs in the two electrolytes exhibited comparable capacities (115 mAh g⁻¹ for ZnSO₄ and 112 mAh g⁻¹ for Zn(OTf)₂). By contrast, at the high rate, i.e., 5.0 A g⁻¹, a high capacity of 100 mAh g⁻¹ was attained using Zn(OTf)₂, surpassing that attained using ZnSO₄ (91 mAh g⁻¹). Furthermore, Figure 5.2B shows that the voltage drops for Zn(OTf)₂ were smaller than those for the ZnSO₄ electrolyte, suggesting that the ionic conductivity of Zn(OTf)₂ is higher. This inference was further supported by the lower charge transfer resistance of Zn(OTf)₂ (50 Ω) than that of ZnSO₄ (160 Ω), as revealed by the electrochemical impedance spectra (Figure 5.2C).

Afterward, the cycling performance of PI-1/CNT in different electrolytes was evaluated. As shown in Figure 5.2D and Figure S5.10, aqueous Zn(OTf)₂ electrolytes enabled high capacity retentions of more than 80% after 50000 cycles at 5.0 A g⁻¹, exceeding that produced using aqueous ZnSO₄, which

enabled retentions of approximately only 53–58% in the same conditions, again demonstrating that $\text{Zn}(\text{OTf})_2$ is the better electrolyte salt. Figure 5.2E shows that the resulting capacities for 1.0 M $\text{Zn}(\text{OTf})_2$ and 1.0 M ZnSO_4 after 50k cycles were 85.5 and 51.7 mAh g^{-1} , respectively. Moreover, when $\text{Zn}(\text{OTf})_2$ was used, a high coulombic efficiency (CE) of approximately 100% was maintained during long cycling, whereas when ZnSO_4 was used, later cycles exhibited unstable CE values, indicating the relatively poor reversibility of the electrolyte (Figure 5.2E). Among all electrolytes examined in this study (Figure 5.2F), 1.5 M $\text{Zn}(\text{OTf})_2$ affords the highest ionic conductivity (68.5 mS cm^{-1}), a low viscosity (2.32 mPa s), and a mild acidity ($\text{pH} = 4.8$). These properties contribute to this electrolyte exhibiting the highest performance, with the fastest rate capability (101 mAh g^{-1} at 5.0 A g^{-1}) and highest stability (88% capacity retention and 89 mAh g^{-1} capacity after 50k cycles), among all electrolytes examined herein.

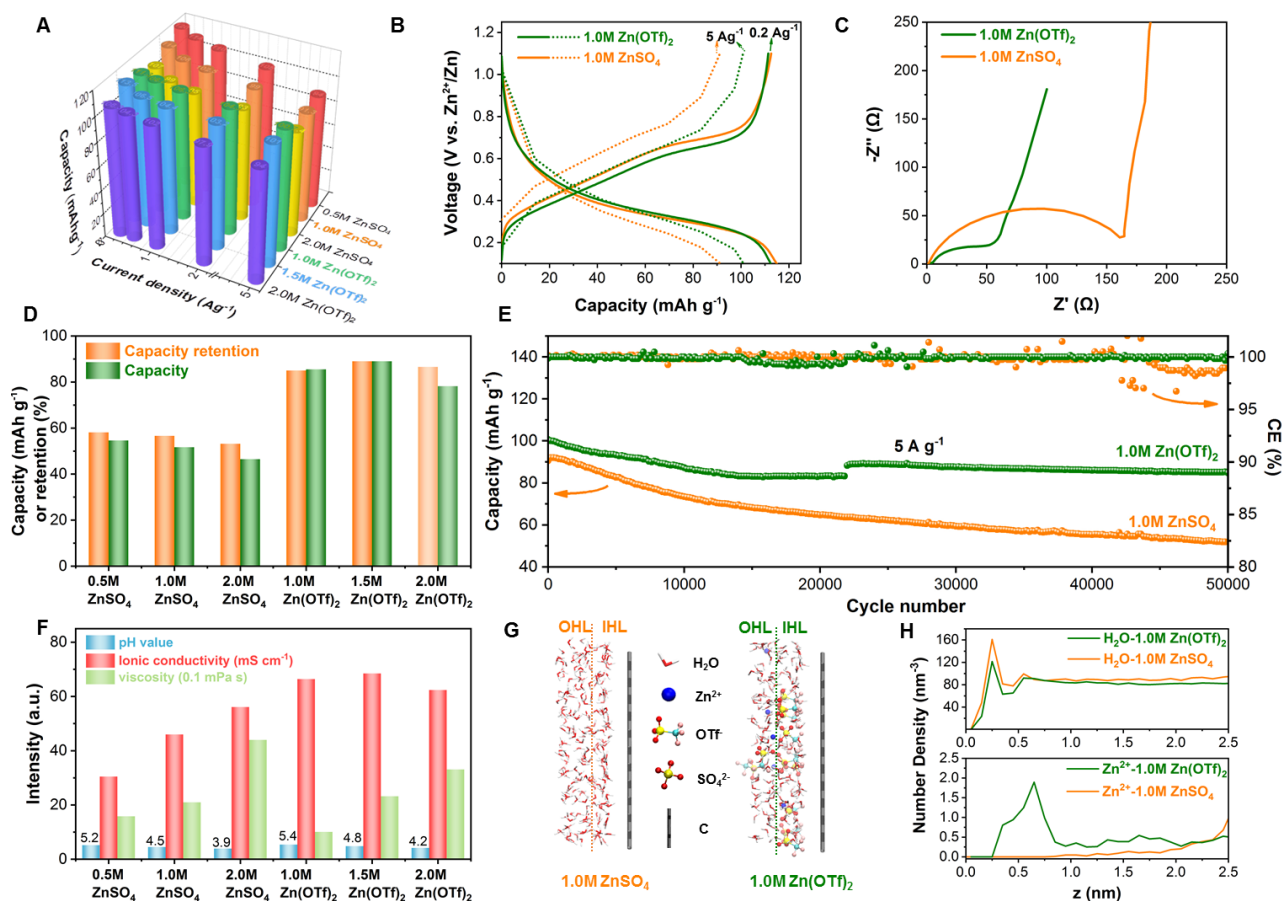


Figure 5.2 Electrolyte Engineering and Molecular Dynamics Simulation. (A) Capacity values of PI-1/CNT in different electrolyte at current densities from 0.2 to 5 A g⁻¹. (B) Voltage–capacity profiles of PI-1/CNT in 1.0 M Zn(OTf)₂ and 1.0 M ZnSO₄ at low (0.2 A g⁻¹) and high (5.0 A g⁻¹) current rates. (C) Electrochemical impedance spectra (EIS) of PI-1/CNT in 1.0 M Zn(OTf)₂ and 1.0 M ZnSO₄. (D) Capacity and Capacity retention of PI-1/CNT in different electrolytes after ultralong cycling. (E) Cycling performance and CE profiles of PI-1/CNT in 1.0 M Zn(OTf)₂ and 1.0 M ZnSO₄ tested at 5.0 A g⁻¹. (F) Ionic conductivities, viscosities, and pH values of different electrolytes. (G) MD-simulated distribution of ions and water near cathode surface. (H) Number density profiles of water and Zn²⁺ along normal direction of cathode surface.

To gain insight into the superiority of triflate (OTf⁻) over sulfate (SO₄²⁻) anions, molecular dynamics simulations were performed. First, an electrical double-layer model was built to simulate the dynamics of ions and water in two electrolytes (1.0 M Zn(OTf)₂ vs. 1.0 M ZnSO₄) and at different

potentials (Figure S5.12).²¹⁹ Because of the presence of the hydrophobic CF_3 group in OTf^- , the hydrophobicity of the triflate anion is exactly opposite to that of the sulfate anion (Figure S5.13). This hydrophobicity disparity between SO_4^{2-} and OTf^- led to distinctly different electrochemical double-layer structures at the electrode surfaces (defined as the layer within 0–0.75 nm to the electrode surface), which determined the distribution of ions and water near the electrode surface (Figure 5.2G). At an applied potential of $U = 0.5$ V, the hydrophobic triflate anions created an H_2O -scarce environment at the inner Helmholtz layer (IHL, defined as the layer within 0–0.25 nm to the electrode surface, as shown in Figure S5.14), in contrast to the H_2O -rich environment generated by the hydrophilic sulfate anions. At an increased potential of $U = 1.1$ V, the triflate anions were further enriched in the IHL of the electrode, which also decreased the amount of H_2O and reduced any water-related reactions (Figure S5.14–S5.15). By contrast, when the ZnSO_4 electrolyte was used, the amount of H_2O in the IHL exhibited only slight changes with respect to the increase in potential. Whereas most of the Zn^{2+} ions were expelled from the double layers in the ZnSO_4 electrolyte, an abundant amount of Zn^{2+} ions remained in the $\text{Zn}(\text{OTf})_2$ electrolyte within a distance of 0.75 nm from the cathode (Figure 5.2H). The density profiles of Zn^{2+} and H_2O indicated that more Zn^{2+} and fewer H_2O molecules accumulated near the electrode surface in the $\text{Zn}(\text{OTf})_2$ electrolyte than in the ZnSO_4 electrolyte (Figure 5.2G–H), leading to easier access to Zn^{2+} for redox reactions and fewer water-related reactions in the $\text{Zn}(\text{OTf})_2$ electrolyte compared to those in ZnSO_4 .

5.3.3 Fast and stable cycling, high loadings, and kinetics analysis

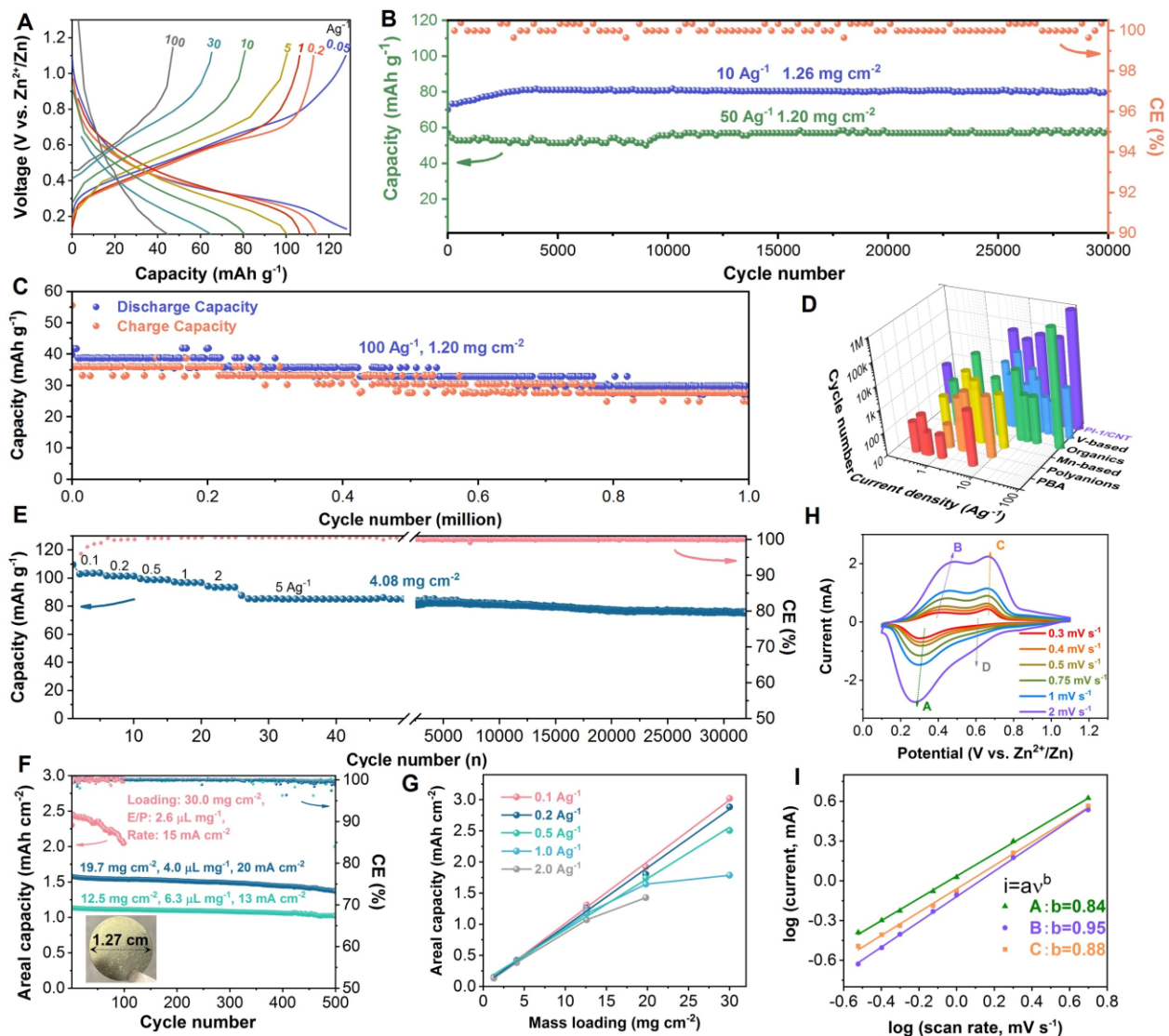


Figure 5.3 Optimized electrochemical performance and kinetics analysis of PI-1/CNT electrode. (A) Voltage–capacity profiles of PI-1/CNT at different current densities from 0.2 to 100 A g⁻¹. (B) Ultralong cycle life of PI-1/CNT at different current densities (10 or 50 A g⁻¹). (C) Million-cycle life of PI-1/CNT at 100 A g⁻¹. (D) Comparison of rate and cycling performance between different ZIB electrode materials. (E–G) High-loading PI-1/CNT electrodes: (E) Rate and cycling performance of PI-1/CNT with high loading of 4.08 mg cm⁻², (F) Cycling performance of ultrahigh-loading PI-1/CNT electrodes, inset of F shows the optical image of the 19.7 mg cm⁻² electrode, (G) Plots of areal capacity against mass loadings. (H) CV curves of PI-1/CNT at different scan rates from 0.3 mV s⁻¹ to 5 mVs⁻¹ and corresponding (I) kinetics profiles of different redox peaks (A, B, C).

Taken together, the results presented thus far indicate that the ideal pairing of anode material and electrolyte composition should employ a PI-1/CNT anode and 1.5 M Zn(OTf)₂ electrolyte. To demonstrate the efficacy of this combination, its rate performance is presented in Figure 3A, showing that at a low current density of 0.05 A g⁻¹, a near-theoretical capacity of 128 mAh g⁻¹ can be delivered. By comparison, when the current density was increased to 0.2, 1.0, 5.0, 10, 30, and 50 A g⁻¹, the specific capacities were 113, 107, 100, 80, 65, and 59 mAh g⁻¹, respectively. Surprisingly, even at an ultrahigh rate of 100 A g⁻¹, corresponding to a charging time of 1.4 s, the capacity could still be maintained at 40 mAh g⁻¹. At all current rates, the average discharge voltages were maintained at approximately 0.35 V vs. Zn²⁺/Zn, which is promising for the application of PI-1/CNT as a Zn-metal-free anode. In addition to this exceptional rate performance, the stability was also extraordinary, with negligible capacity losses of 0.1 A g⁻¹ over 250 cycles (Figure S5.16), of 10 A g⁻¹ over 30000 cycles (Figure 5.3B), and of 50 A g⁻¹ over 60000 cycles (Figure S5.17), whereas a 75% capacity was retained after one million cycles at 100 A g⁻¹ (Figure 5.3C). The performance presented here is one of the longest cycle lives observed in aqueous batteries and is comparable to that of state-of-the-art fast-charging batteries, posing a serious technological contender.²³⁷⁻²⁴⁰ To the best of our knowledge, this simultaneous achievement of ultrafast and ultralong cycling has hardly been reported for Zn-based energy devices and is better than those reported thus far for almost all ZIB electrode materials, including Mn-^{61,99} and V-based oxides,^{70,241} Prussian blue analogs,^{65,66} and organics,^{160,242,243} among others (Figure 5.3D and **Table S5.1**).^{81,124}

High-loading electrodes are of great importance for lowering production costs and increasing energy densities at the cell level.^{132,133,244} Accordingly, we further tested PI-1/CNT electrodes under high loadings (4.08–50 mg cm⁻²) using a constant amount of electrolyte (100 μL). As shown in Figure 5.3E, at a loading of 4.08 mg cm⁻², the specific capacities were 104, 102, 99, 97, 94, and 85 mAh g⁻¹

at current densities of 0.2, 0.5, 1.0, 2.0, 5.0 A g⁻¹, respectively. Furthermore, the capacity at 5.0 A g⁻¹ was maintained at approximately 80 mAh g⁻¹ (94.1% retention) after 30000 cycles, corresponding to a low capacity loss of 0.0167% per cycle. More impressively, without the binder and current collector, free-standing electrodes with loadings of 12.5~50.0 mg cm⁻² can be easily manufactured via direct pressing of PI-1/CNT powders into tablets under high pressure (Figure S5.18-S5.22 and Video S5.1-S5.2). As shown in the inset of Figure 3F and Figure S20, a free-standing PI-1/CNT electrode of 19.7 mg cm⁻² loading has an area around 1.27 cm² and a thickness of 150 μm. As shown in Figure 5.3F and Figure S5.18-S5.19, electrodes of 12.5 mg cm⁻² and 19.7 mg cm⁻² loadings delivered excellent rate and cycling performance with ~90% capacity retention after 500 cycles even under the lean electrolyte condition (6.3 or 4.0 μL of electrolyte per mg of PI-1/CNT, denoted as E/P). More excitingly, under ultrahigh loadings of 30.1 mg cm⁻² and 50.0 mg cm⁻² with lean electrolyte of 2.6 μL mg⁻¹ and 1.6 μL mg⁻¹, respectively, PI-1/CNT-based ZIBs can still run for over 100 cycles with high capacity retentions (Figure S5.21-S5.22). The capacity loss can be attributed to the Zn metal side with dendrite growth rather than to the PI-1/CNT side with an intact structure, as shown in the disassembled cell after long cycling (Figure S5.23-S5.25). The areal capacities against mass loading at different rates were plotted in Figure 5.3G, which shows that, at current densities between 0.1 and 0.5 A g⁻¹, the areal capacity increased linearly with respect to the mass loading up until 30.1 mg cm⁻², indicating that, at these rates, no limitation was reached in the mass loading. Moreover, high areal capacities of 5.0 and 3.0 mAh cm⁻² can be obtained using the 50.0 mg cm⁻² electrode at areal current densities of 1.0 and 25 mA cm⁻², respectively. By contrast, PI-1 electrodes with high loadings cannot achieve high rates and long cycles (Figure S5.26-S5.28), suggesting the essential role of CNT in making high-loading electrodes with application potentials.²⁴⁴ These results demonstrate the fast rate,

long life, and high loading capability of the PI-1/CNT electrode, showing its promise as a future anode for practical use in full power cells.

To comprehend the fast kinetics in the PI-1/CNT electrode, cyclic voltammetry (CV) tests were conducted, with rates ranging from 0.3 to 2.0 mV s⁻¹ (Figure 5.3F). In all the curves, there are two pairs of redox peaks, indicating a two-step ion storage process.²²⁴ As the scan rate was increased, there were no significant changes in the peak shapes and polarization potentials between redox peaks, implying high reversibility in the redox reactions. To quantitatively study the ion storage kinetics, the equation $i = av^b$, in which i and v represent the current density and scan rate, respectively (a and b are constants, where $b=0.5$ indicates a diffusion-controlled process, whereas $b=1.0$ suggests a pseudocapacitive procedure), was employed. To determine the b values, the curves of $\log(i)$ vs. $\log(v)$ were plotted and linearly fitted to the redox peaks. The fitting slopes, which were equal to the b value, for the A, B, and C peaks were 0.84, 0.95, and 0.88, respectively. These approaching-1.0 values indicate that the PI-1/CNT electrode mainly follows a pseudocapacitive process instead of solid-state diffusion for the Zn²⁺ ion storage. To further quantify the contributions from the pseudocapacitive and diffusive processes, the current was divided into two parts in accordance with $i=k_1v+k_2v^{0.5}$. When the k_1 and k_2 values are determined, the percentages of current controlled by pseudo-capacitance and diffusion can be calculated for different scan rates. As shown in Figure S5.29, at rates of 0.3, 0.4, 0.5, 0.75, 1.0, and 2.0 mV s⁻¹, the capacitive contributions were 80, 82, 84, 86, 90, and 94%, respectively, further verifying the dominance of the pseudocapacitive process in the PI-1/CNT electrode, which could explain its exceptional rate and cycling performance.

5.3.4 Storage mechanism analysis

To understand the charge-storage mechanism of PI-1/CNT in the ZIB charge/discharge process, CV tests were performed in different electrolytes. Figure 5.4A shows the CV profiles of the PI-1/CNT

electrode in the separate electrolytes 0.5 M Zn(OTf)₂-DMF, 0.5 M Zn(OTf)₂-H₂O, and 1.0 M NaOTf-H₂O. The CV profiles of 1.0 M NaOTf-H₂O and 0.5 M Zn(OTf)₂-H₂O show apparently different redox peaks, implying the insertion of different cations in the PI-1/CNT electrode (Zn²⁺ or Na⁺). The positive shift in the reduction peak for 0.5 M Zn(OTf)₂-H₂O relative to that for 1.0 M NaOTf-H₂O could be explained by the larger charge density of Zn²⁺ than that of Na⁺.²⁴⁵ By contrast, identical redox peaks at 0.7 V and 0.25 V were detected for the 0.5 M Zn(OTf)₂-DMF and 0.5 M Zn(OTf)₂-H₂O electrolytes, suggesting the insertion of Zn²⁺ ions in the PI-1/CNT electrode. This inference was further confirmed by SEM mapping images, which revealed a uniform distribution of Zn elements in the PI-1/CNT electrode after discharge to 0.1 V in the 0.5 M Zn(OTf)₂-DMF electrolyte (Figure 5.4B). On the other hand, relative to the profile of the 0.5 M Zn(OTf)₂-DMF electrolyte, there exists another oxidation peak at 0.4 V for the 0.5 M Zn(OTf)₂-H₂O electrolyte, which may have resulted from proton insertion. To confirm whether protons do interact with the PI-1/CNT electrode, CV tests were conducted in three electrolytes with controlled pH values: ZnSO₄ (pH=5), H₂SO₄ (pH=5), and H₂SO₄ (pH=1). It was determined that there exists an oxidation platform at approximately 0.45 V for all electrolytes, implying its assignment to proton insertion. Relative to the profile of H₂SO₄ (pH=5), that of H₂SO₄ (pH=1) shows one more oxidation peak at approximately 0.8 V, which can be ascribed to Zn²⁺ insertion due to Zn metal dissolution in the strongly acidic electrolyte (Figure S5.30). The insertion of protons into PI-1/CNT was further confirmed by *ex situ* SEM and XRD characterizations. The SEM images of the discharged electrode show numerous nanoflakes covering the surface of PI-1/CNT (Figure 5.4D). Based on XRD patterns (Figure 5.4E) and SEM mapping images (Figure 5.4F), these nanoflakes were determined to be zinc sulfate hydroxide. Because zinc sulfate hydroxide precipitates in solutions with pH > 5.5, its formation in an electrolyte with a pH of ~5 should be due to proton insertion into the polymer electrode, leaving OH⁻

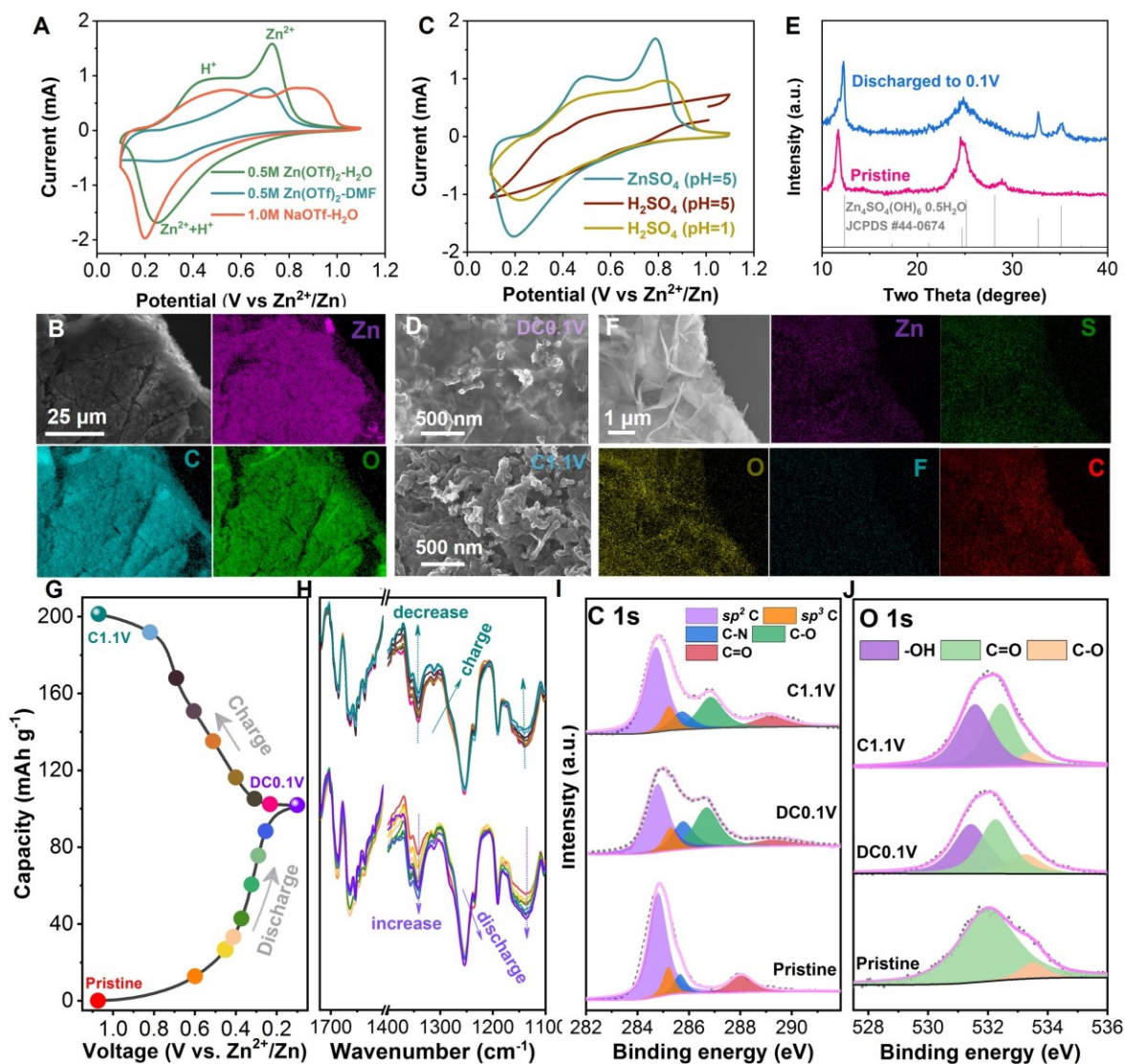


Figure 5.4 Ion storage mechanism of PI-1/CNT Electrode. (A) CV profiles of PI-1/CNT in different Zn/Na-based electrolytes. (B) SEM mapping images of PI-1/CNT electrode discharged to 0.1 V in 0.5 M Zn(OTf)₂-DMF. (C) CV profiles of PI-1/CNT in different aqueous electrolytes with controlled pH values. (D) SEM images of PI-1/CNT electrode discharged to 0.1 V (upper part) and charged back to 1.1 V (downside part). (E) *Ex situ* XRD patterns of PI-1/CNT electrode at pristine and discharged status. (F) SEM image and corresponding elemental mapping images of PI-1/CNT electrode discharged to 0.1 V in 1.5 M Zn(OTf)₂. (G–H) *In situ* ATR-FTIR spectra of PI-1/CNT at different discharge/charge states. *Ex situ* high-resolution (I) C 1s and (J) O 1s XPS spectra of PI-1/CNT electrode at pristine, DC0.1V, and C1.1V statuses.

behind and causing a local pH increase.¹⁵⁰ After the polymer electrode was charged back to 1.1 V, these nanoflakes disappeared, indicating a reversible proton insertion/de-insertion mechanism (Figure 5.4D).²⁴⁶ Overall, these results indicate that both Zn^{2+} and protons act as active cations for energy storage in ZIBs based on PI-1/CNT electrodes.

To further elucidate the active sites for storing Zn^{2+} /protons in the PI-1/CNT electrode, *in situ* FTIR and *ex situ* X-ray photoelectron spectroscopy (XPS) analyses were performed on the PI-1/CNT electrode at different charge/discharge statuses (Figure 5.4G). Holey coin cells and attenuated total reflection (ATR)-FTIR microscopy were employed to investigate the structural changes of PI-1/CNT with the uptake/removal of Zn ions (Figure S5.31). PI-1/CNT was loaded onto a stainless-steel mesh with a 125-mesh size to create an electrode in which infrared light could pass through the hole and enable the IR spectra of PI-1/CNT to be obtained during battery (dis)charging. The characteristic peaks for carbonyl (C=O), imide (C–N–C), and C–O groups were located at 1650–1700, ~1350, and ~1150 cm^{-1} , respectively. For clear comparison, the carbonyl group (C=O) was normalized to 1. During discharge, the intensity ratio of the carbonyl group to the imide group declined, whereas the corresponding ratio of C–O to C=O increased, suggesting a coordination reaction between the Zn ions and carbonyl groups to generate Zn–O–C groups (Figure 5.4H). During charging, the intensities of the aforementioned groups reversed back to their original states, with a decreased C–O/C=O ratio and increased carbonyl-to-imide ratio, indicating the removal of the Zn ion from PI-1 (Figure 5.4H). XPS was also conducted to monitor the bonding changes in PI-1/CNT during the battery (dis)charge. As shown in the *C1s* XPS spectra (Figure 5.4I) for the pristine, DC0.1V, and C1.1V electrodes, five peaks can be deconvoluted at ~284.8, ~285.3, 285.7, 286.9, and 289.3 eV, corresponding to sp^2 C=C, sp^3 C–C, C–N, C–O, and C=O bonds, respectively. Compared with the pristine electrode, DC0.1V exhibited less C=O but more C–O bands, indicating the reduction of the carbonyl group to the C–O–

group and subsequent coordination between $\text{Zn}^{2+}/\text{H}^+$ and $\text{C}=\text{O}$, forming $\text{Zn}^{2+}(\text{C}-\text{O}^-)_2$ or $\text{C}-\text{OH}$ during discharge. On the other hand, after the electrode was charged back to 1.1 V, stronger $\text{C}=\text{O}$ but weaker $\text{C}-\text{O}$ peaks were detected for C1.1V compared with those for DC0.1V, suggesting the de-coordination process from $\text{Zn}^{2+}(\text{C}-\text{O}^-)_2$ ($\text{C}-\text{OH}$) to $\text{Zn}^{2+}/\text{H}^+$ and $\text{C}=\text{O}$. This was further confirmed by the high-resolution O1s XPS spectra (Figure 5.4J), in which the $\text{C}-\text{O}/\text{C}=\text{O}$ bonding increased after discharge but declined after charging. These results imply that the carbonyl group in PI-1 is the active center for the reversible storage of Zn^{2+} ions and protons.

5.3.5 Application of PI-1/CNT as Zn-free anode for ZIBs and ZICs

Now that the exceptional performance of our designed anode system has been confirmed, we further validated its practical use as a Zn-free anode in aqueous Zn-based energy storage devices, including batteries and supercapacitors. To construct a rocking-chair-type ZIB, commercial MnO_2 was first discharged to obtain Zn_xMnO_2 , which was then used as the cathode. Thereafter, this cathode was combined with PI-1/CNT, which was employed as the anode, and the mass ratio of negative to positive electrode (N/P) was maintained at 1 (both 1.32 mg). For comparison, a Zn// MnO_2 battery was also assembled, where an electrodeposited Zn metal with a capacity of 23 mAh (mass of 28 mg) was used as the anode, corresponding to an N/P mass ratio of ~ 23.3 . The voltage windows for discharging/charging were set to 0–1.65 V for the PI-1/CNT// Zn_xMnO_2 battery and to 0.5–1.8 V for the Zn// MnO_2 battery. The voltage vs. capacity profiles of the two batteries at different current densities are shown in Figure 5.5A and Figure S5.32, where the current densities and capacities are based on MnO_2 . At a low current density of 0.1 A g^{-1} , the PI-1/CNT-based battery was able to exhibit a high capacity of 110 mAh g^{-1} and an average discharge potential of 0.91 V (Figure 5.5A). At current rates of 1, 2, 5, 10, and 20 A g^{-1} , capacities of 97.6, 95, 88, 75, and 58 mAh g^{-1} , respectively, were achieved (Figure 5.5A, B). Even when the rate was increased 350 times to 35 A g^{-1} (charging time:

4 s), the PI-1/CNT//Zn_xMnO₂ full cell still delivered a capacity of 39 mAh g⁻¹, corresponding to a 35.5% retention of capacity at 0.1 A g⁻¹, which indicated an excellent rate capability. By contrast, the Zn//MnO₂ battery with the Zn metal anode delivered only 120, 95.6, 64.4, and 39.8 mAh g⁻¹ at rates of 1, 2, 5, and 10 A g⁻¹, respectively (Figure S5.33), suggesting that PI-1/CNT is an efficient anode for achieving high-rate and high-power batteries. The capacity can be further increased by using a N/P mass ratio of ~2.5 (Figure S5.34). To further illustrate the exceptional performance of our material, Ragone curves were plotted in Figure 5.5C based on both anode and cathode materials. According to these data, the PI-1/CNT//Zn_xMnO₂ battery exhibited a high energy density of 50.5 Wh kg⁻¹ at 45.5 W kg⁻¹ and was able to maintain 10.1 Wh kg⁻¹ even at a high power density of 9,100 W kg⁻¹ (Figure 5.5C). The high power and energy densities of the PI-1/CNT//Zn_xMnO₂ battery are among the best documented for rocking-chair-type ZIBs (Figure 5.5C and **Tables S5.2** and **S5.3**).^{40, 54, 220} Figure 5.5D shows the cycling performance and coulombic efficiency of the PI-1/CNT//Zn_xMnO₂ and Zn//MnO₂ cells at a high current density of 2.0 A g⁻¹. Although a large excess of Zn metal was used as the anode, the Zn//MnO₂ battery could deliver only a 58% capacity retention after 6000 cycles, whereas the PI-1/CNT anode enabled a high capacity retention of 83% after 6000 cycles and 43% retention after 50000 cycles with 100% CE (Figure S5.35). This stability is expected to be further enhanced by the use of a better MnO₂ cathode. To comprehend the highly differing levels of performance between the PI-1/CNT//Zn_xMnO₂ and Zn//MnO₂ cells, they were disassembled, and digital photos were obtained to show their contrasting conditions (Figure S5.36). Whereas the photo of the former shows a colorless electrolyte, the photo of the latter shows that it was full of yellow product, likely caused by Mn-ion dissolution. The post-cycling PI-1/CNT anode well maintained its crystal structure and showed no sign of dendrites (Figure S5.37), whereas the Zn anode was full of “dead” and dendritic Zn metal (Figure S5.38). In consideration of practical use, Zn-rich ZnMn₂O₄

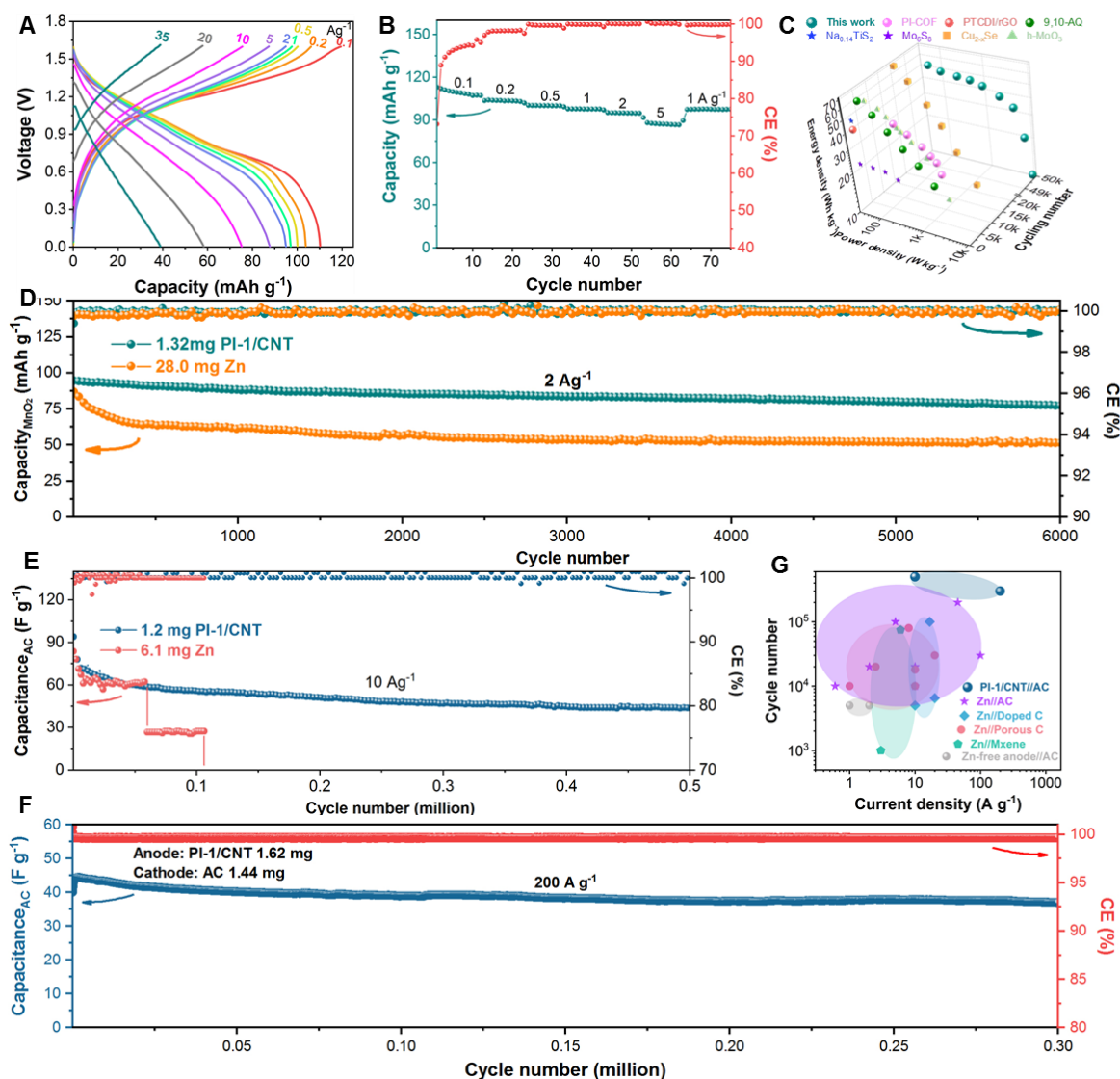


Figure 5.5 Application of PI-1/CNT as Zn-metal-free Anode for ZIBs and ZICs. (A) Galvanostatic charge and discharge potential profiles of PI-1/CNT//Zn_xMnO₂ at different current rates. (B) Rate performance of PI-1/CNT//Zn_xMnO₂ and corresponding CE values. (C) Ragone plots of PI-1/CNT//Zn_xMnO₂ and documented rocking-chair type ZIBs (energy and power densities are based on total active material mass of cathode and anode). (D) Cycling comparison between PI-1/CNT//Zn_xMnO₂ and Zn//MnO₂ with equal MnO₂ mass at current density of 2.0 A g⁻¹. (E) Long cycle performance of PI-1/CNT//AC and Zn//AC at high current density of 10 A g⁻¹. (F) Ultrafast and stable cycling of PI-1/CNT//AC capacitor (N/P mass ratio=1.15). (G) Capacity retention against cycle numbers for different materials in reported papers.

cathode¹⁰⁸ was also prepared (Figure S5.40) and coupled with the PI-1/CNT anode for battery tests in which the PI-1/CNT anode also presents higher rate capability and long cycling stability than Zn anode-based full cells (Figure S5.41). Impressively, a PI-1/CNT//ZnMn₂O₄/C battery using free-standing and high-loading electrodes can stably run for more than 1500 cycles (Figure S5.42). These results clearly demonstrate the immense capability of this anode/electrolyte pairing at enabling high-power and long-life ZIBs.

To further demonstrate its application in zinc-ion hybrid supercapacitors, PI-1/CNT was first discharged to 0.1 V in a half-cell and extracted to serve as an anode and paired with commercial activated carbon (AC) as the cathode,²⁰¹ with an N/P mass ratio of 0.67. For comparison, Zn was also electrodeposited onto a Cu foil to form a Zn anode with a capacity of 5 mAh (~6.1 mg). The galvanostatic charge/discharge was conducted in voltage windows of 0.15–1.8 V for the Zn//AC supercapacitor and 0–1.65 V for the PI-1/CNT//AC supercapacitor at different current densities (Figure S5.43–S5.44), where the current densities and capacitances were based on the mass of the AC electrode. The discharge capacitances of PI-1/CNT//AC were 124.8, 102.4, 97.6, 94.4, and 92.8 F g⁻¹ at current rates of 0.2, 1, 2, 5, and 10 A g⁻¹, respectively, indicating excellent rate performance. These capacitance values were higher than those of Zn//AC at high current densities (Figure S5.44). Figure 5.4E shows the impressive long-cycling performance of the two ZICs; at 10.0 A g⁻¹, the PI-1/CNT//AC capacitor exhibited remarkable stability, with 66% capacitance retention over 100,000 cycles and 50% retention over half million cycles, and ~100% coulombic efficiency. By stark contrast, the Zn//AC capacitor first exhibited a dramatic decrease in capacitance after only 60,000 cycles with a mere 32% retention and failed to work after 107,000 cycles. Furthermore, another PI-1/CNT//AC capacitor was assembled with an N/P ratio of approximately 1.15, which enabled ultrafast charging/discharging (200 A g⁻¹) and ultrahigh stability (93% capacitance retention) over 0.3 million

cycles (Figure 5.5F). Remarkably, the 200 A g⁻¹ charging rate and half-million cycles achieved using PI-1/CNT//AC are some of the fastest and longest life cycles ever reported for Zn-based supercapacitors (Figure 5.5G and **Table S5.4**).^{12, 98, 247} Both capacitors were also disassembled to investigate their different electrochemical behaviors (Figure S5.45). Photographs show the light-yellow colored PI-1/CNT//AC capacitor in contrast to the dark-brown colored Zn//AC capacitor, indicating the occurrence of severe side reactions, which caused the failure of the Zn//AC capacitor. This failure was caused by dendrites formed in the Zn metal anode (Figure S5.46). By contrast, no dendrites were detected in the PI-1/CNT anode even after 0.5 million cycles (Figure S5.47). These results further confirm the advantages of metal-free PI-1/CNT as a practical anode material for ZICs.

5.4 Summary

In summary, we report a polymer anode with an unprecedented high rate and cycling performance for use in aqueous Zn-ion batteries and supercapacitors derived via the careful tailoring of the anode material and its paired electrolyte composition. Because of its low water solubility, high LUMO level, narrow bandgap, and large π -conjugation, the anode material PI-1 exhibits high redox activity and stability towards Zn²⁺ storage. On the other hand, the electrolyte solution 1.5 M Zn(OTf)₂ exhibits high ionic conductivity, mild acidity, low viscosity, and rich Zn²⁺ access. These sets of characteristics of the anode material and electrolyte solution benefit the fast charging and stable cycling of the cell. This combination enables a low discharge voltage, near-theoretical capacity, rapid kinetics of up to 100 A g⁻¹, and long lifespans of up to 1000000 cycles. The study revealed a reversible Zn²⁺/H⁺ co-interaction mechanism at the carbonyl site of PI-1. Furthermore, full cells based on the PI-1/CNT anode delivered the highest power density in rocking-chair-type ZIBs and the longest cycle life in ZICs, surpassing those of corresponding devices based on excessive Zn metal anodes. Given the excellent thermal properties of polyimide, this research will open a new avenue for the preparation of

cheap, sustainable, fast, stable, and high-loading organic anodes for aqueous energy storage devices over a wider range of temperatures.²⁴⁸

5.5 Supporting Information

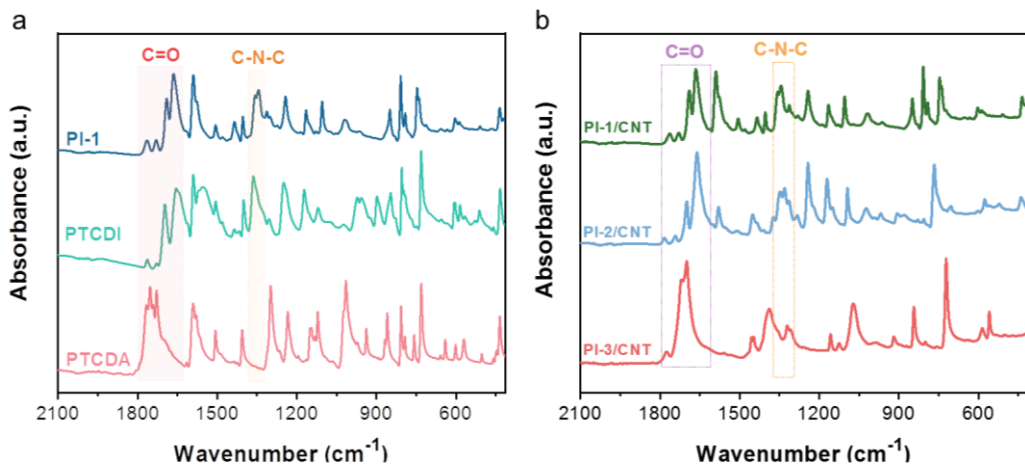


Figure S5.1 FTIR spectra of a) PTCDA, PTCDI, PI-1 and b) PI-1/CNT, PI-2/CNT, PI-3/CNT.

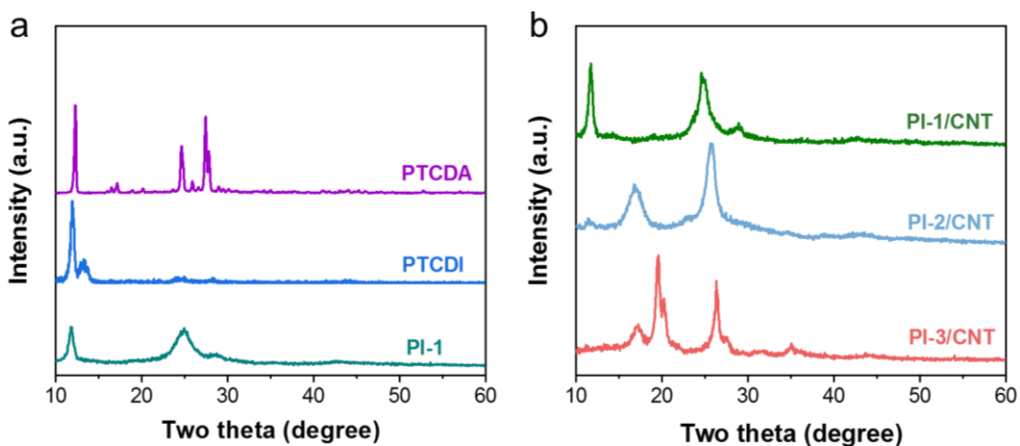


Figure S5.2 XRD patterns of a) PTCDA, PTCDI, PI-1 and b) PI-1/CNT, PI-2/CNT, PI-3/CNT.

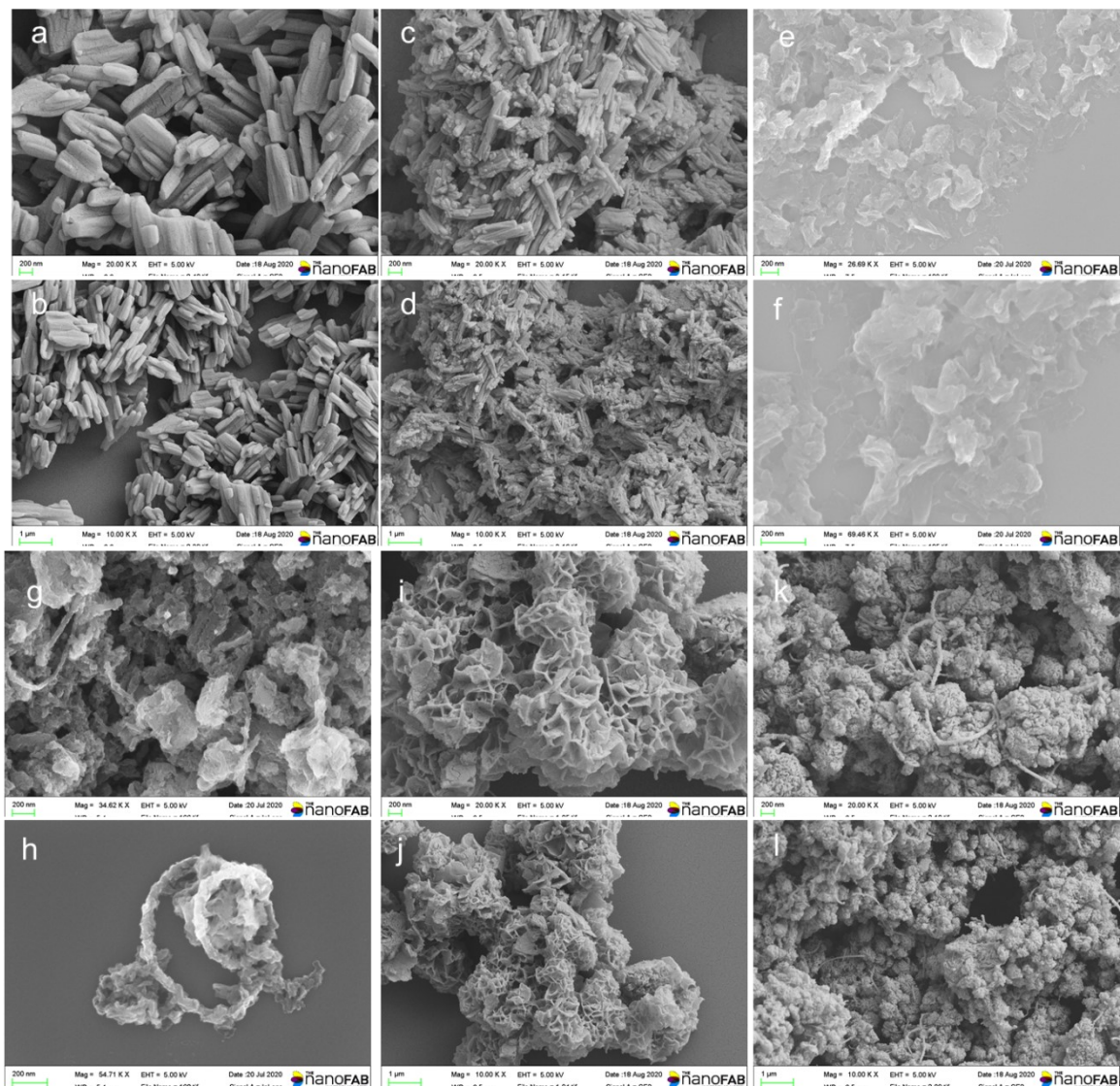


Figure S5.3 SEM images of (a-b) PTCDA, (c-d) PTCDI, (e-f) PI-1, (g-h) PI-1/CNT, (i-j) PI-2/CNT and (k-l) PI-3/CNT.

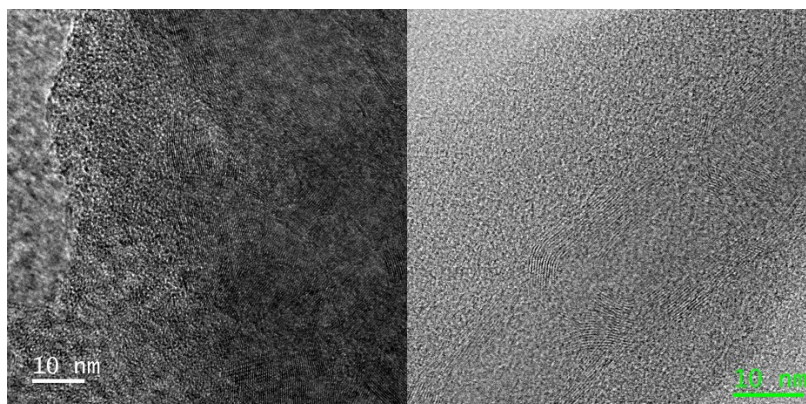


Figure S5.4 HRTEM images of PI-1/CNT. The crystal lattice can be assigned to CNT.

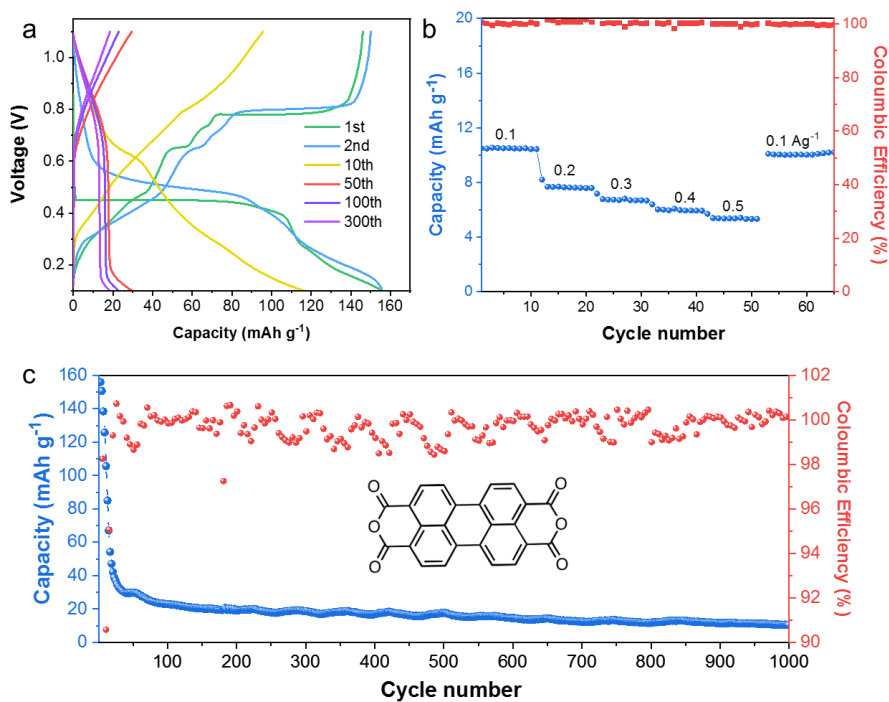


Figure S5.5 ZIB performance of PTCDA. a) Charge-discharge profiles. b) Rate performance. c) cycling performance and Coulombic efficiency at 0.1 Ag⁻¹.

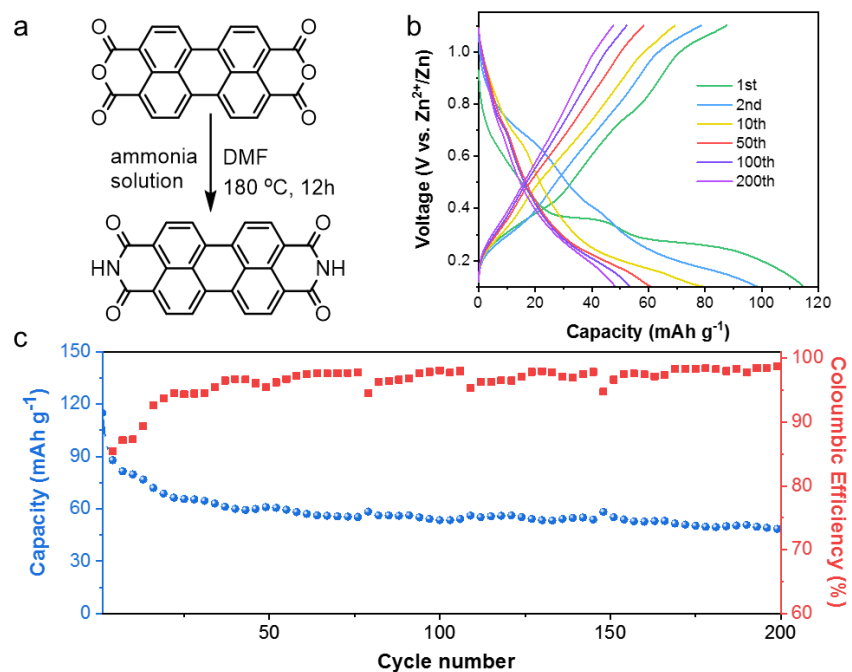


Figure S5.6 ZIB performance of PTCDI. a) Scheme showing the synthesis of PTCDI. b) Charge-discharge profiles. c) cycling performance and Coulombic efficiency at 0.1 Ag⁻¹.

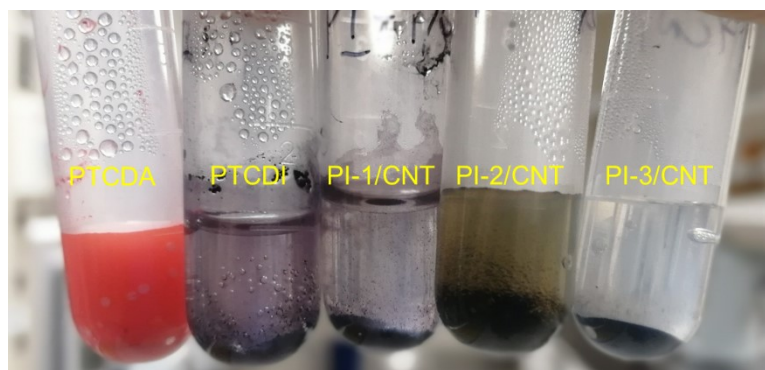


Figure S5.7 The digital photo showing the solubility of different samples in hot water (60 °C) after two days. PTCDA, PTCDI, and PI-2/CNT show certain solubility according to color change of water. All samples are insoluble in water at room temperature after two days.

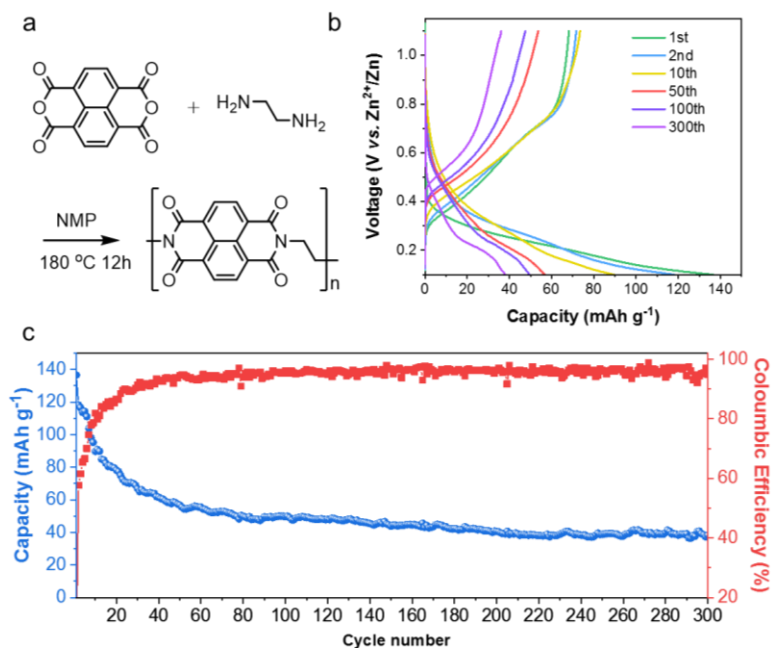


Figure S5.8 ZIB performance of PI-2/CNT. a) Scheme showing the synthesis of PI-2. b) Voltage-capacity profiles. c) cycling performance and Coulombic efficiency at 0.1 Ag^{-1} .

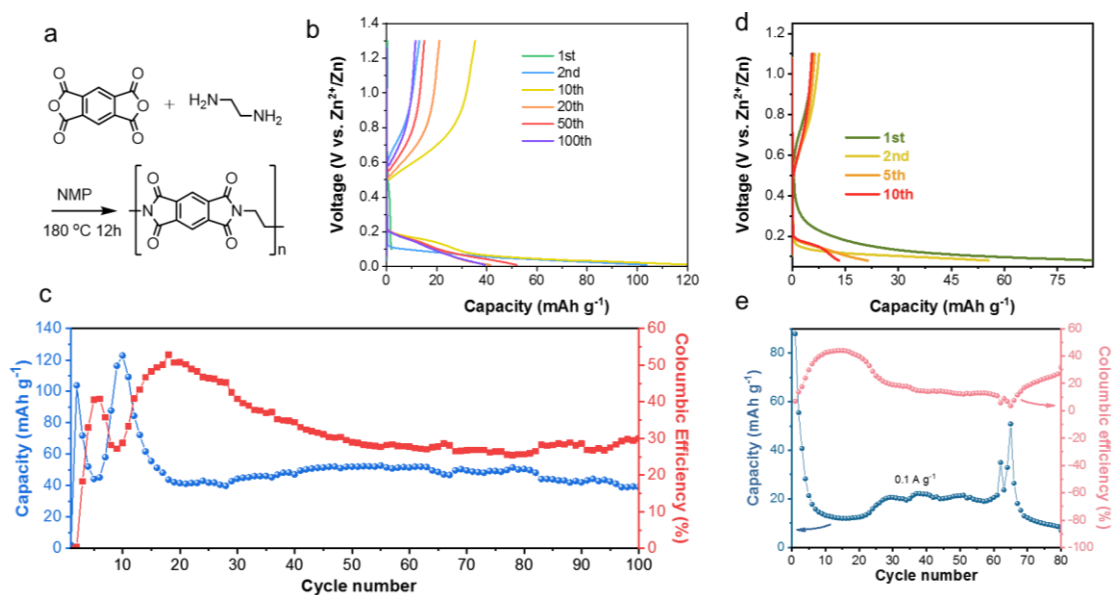


Figure S5.9 ZIB performance of PI-3/CNT. a) Scheme showing the synthesis of PI-3. b, d) Voltage-capacity profiles. c, e) cycling performance and Coulombic efficiency at 0.1 Ag^{-1} . (b-c) is tested in the voltage window of 0.01-1.3 V while (d-e) is tested in 0.08-1.1 V.

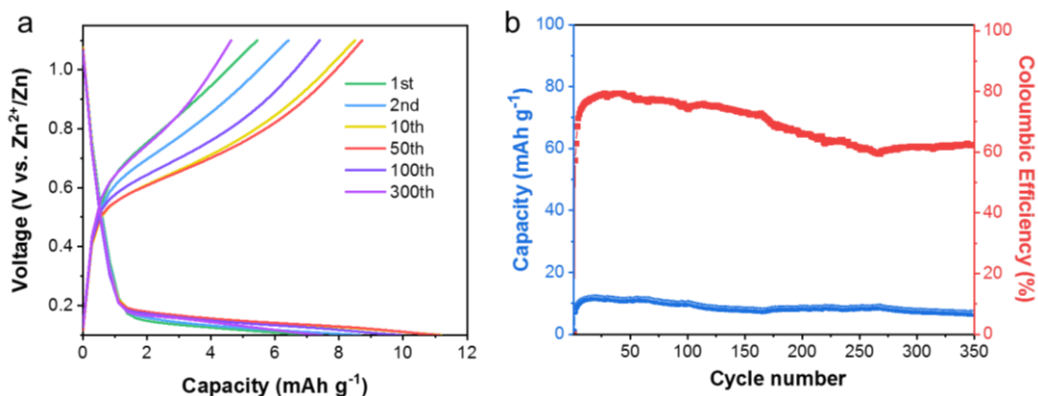


Figure S5.10 ZIB performance of CNT. a) Voltage-capacity profiles. b) cycling performance and Coulombic efficiency at 0.1 Ag^{-1} .

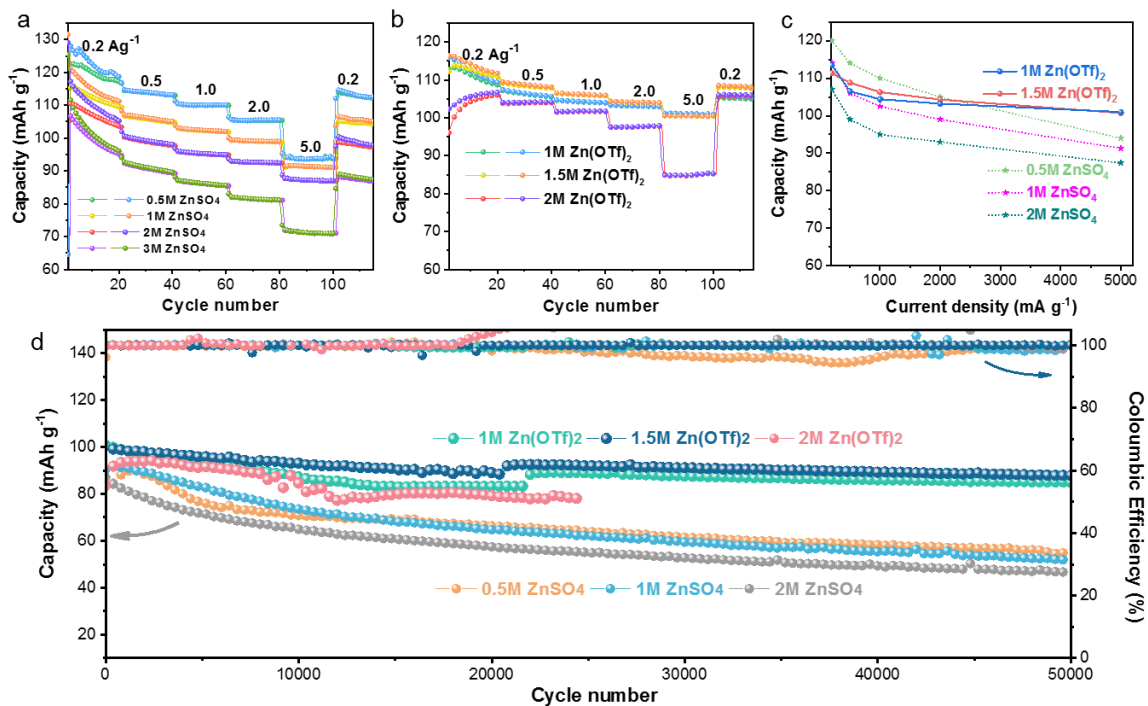


Figure S5.11 ZIB performance of PI-1/CNT in different aqueous electrolyte. Rate performance in a) ZnSO_4 and b) $\text{Zn}(\text{OTf})_2$ electrolyte from 0.2 A g^{-1} to 5 A g^{-1} . c) comparison of different electrolyte at different rates. d) Cycling performance and Coulombic efficiency at 5 A g^{-1} .

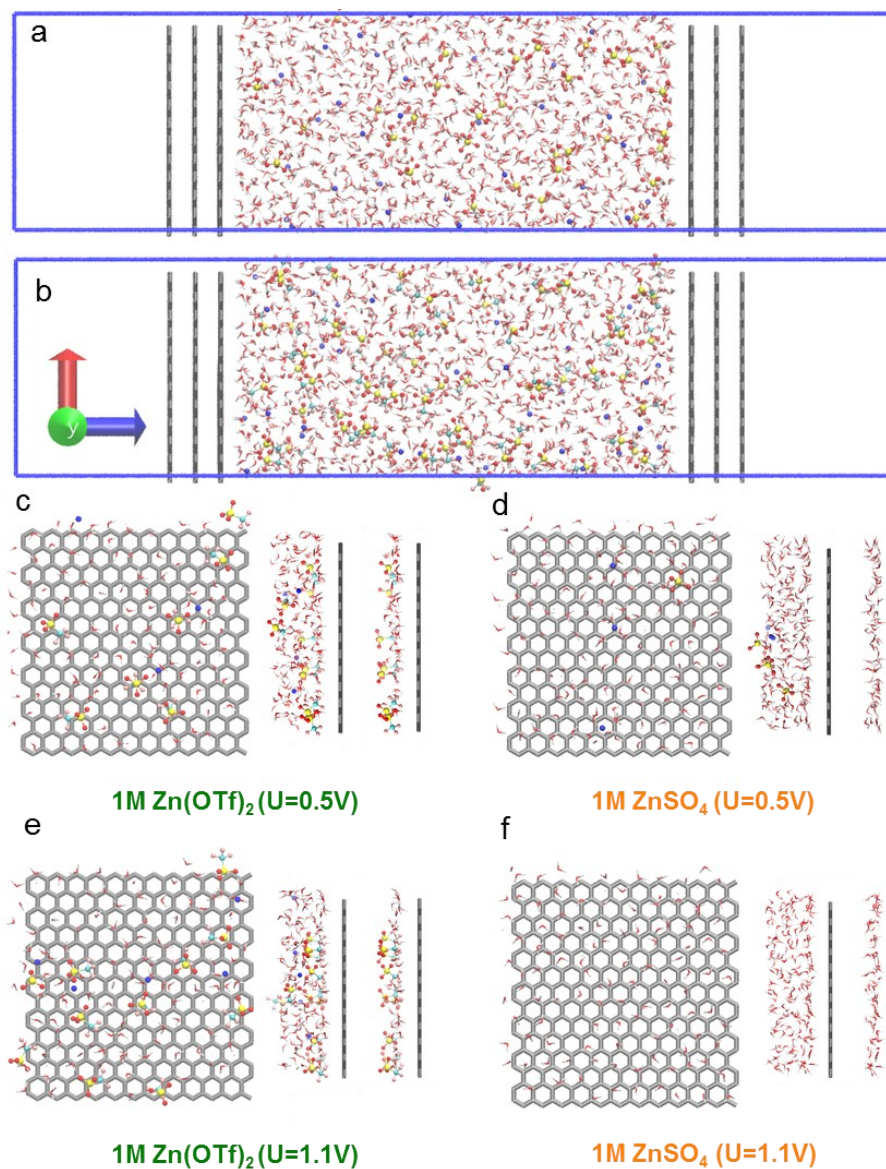


Figure S5.12 MD simulation of ions and water in an electrical double layer model under different electrolytes and potentials. Simulation models for (a) 1M ZnSO₄ electrolyte containing 32 ZnSO₄ and 1598 H₂O molecules and (b) 1M Zn(OTf)₂ electrolyte containing 32 Zn(OTf)₂ and 1390 H₂O molecules. The cell dimension is 2.84×2.97×12 nm³, the interlayer distance of electrodes is 6 nm, and the anode is located at 3 nm while the cathode at 9 nm. Four systems were run in total, including S-0.5, S-1.1, T-0.5, T-1.1, corresponding to the simulation of ZnSO₄ under 0.5 V, ZnSO₄ under 1.1 V, Zn(OTf)₂ under 0.5 V, Zn(OTf)₂ under 1.1 V, respectively. The distribution of ions and water near the cathode surface is shown in (c) T-0.5, (d) T-1.1, (e) S-0.5, and (f) S-1.1.

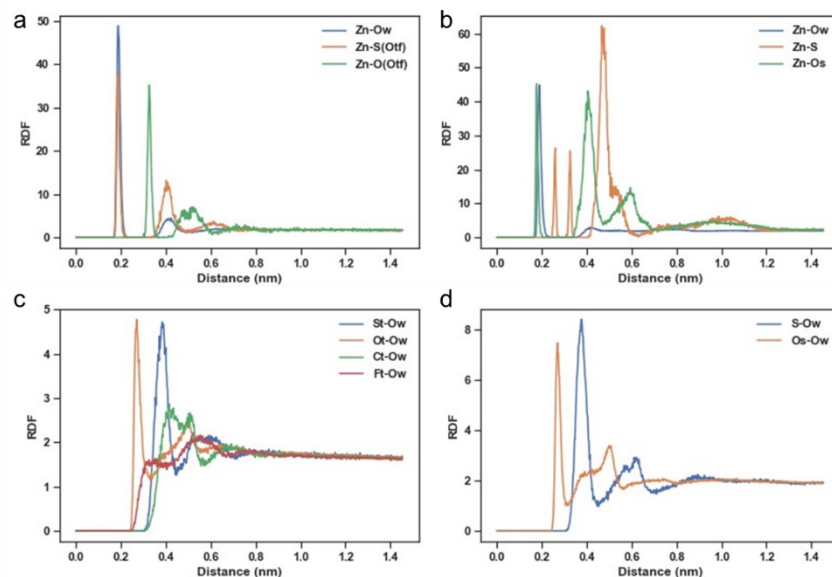


Figure S5.13. Radial distribution function (RDF) of (a) water oxygen around Zn^{2+} (Zn-Ow), S of OTF^- around Zn^{2+} (Zn-S(OTF)), and O of OTF^- around Zn^{2+} (Zn-O(OTf)) in system T-0.5; (b) water oxygen around Zn^{2+} (Zn-Ow), S of SO_4^{2-} around Zn^{2+} (Zn-S), and O of SO_4^{2-} around Zn^{2+} (Zn-Os) in system S-0.5; (c) water oxygen around S of OTF^- (St-Ow), water oxygen around O of OTF^- (Ot-Ow), water oxygen around C of OTF^- (Ct-Ow), and water oxygen around F of OTF^- (Ft-Ow) in system T-0.5; (d) water oxygen around S of SO_4^{2-} (S-Ow), and water oxygen around O of SO_4^{2-} (Os-Ow) in system S-0.5.

The first peak of RDF of Zn-Ow in Figure S13a and S13b indicated that water preferably stayed around Zn^{2+} at a distance of ~ 0.2 nm, which was consistent with the structure of the first solvation shell of Zn^{2+} . The same peak location of the RDF of Zn-Ow suggested a similar solvated structure of Zn^{2+} in systems of T-0.5 and S-0.5. In the system of T-0.5, The RDFs of water oxygens around the S and O atoms of OTF^- displayed a prominent peak at ~ 0.3 nm and ~ 0.4 nm, respectively, implying that water formed stable structures around the SO_3^- group of OTF^- ions, as shown in Figure S13c. In contrast, the lack of obvious peaks of RDFs of water around C and F atoms suggested a poor affinity of water to the CF_3 groups of OTF^- . Similar to the SO_3^- group of OTF^- ions, the prominent peaks in the RDFs of water around S and O in system S-0.5 (Figure S13d) indicated a high affinity of water around the SO_4^{2-} .

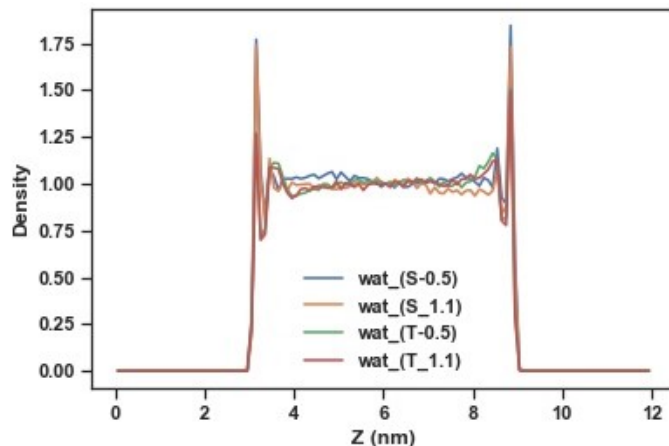


Figure S5.14. Relative number density of water in systems (S-0.5, S-1.1, T-0.5, T-1.1). The densities were normalized with respect to the bulk values at $Z = 6$ nm.

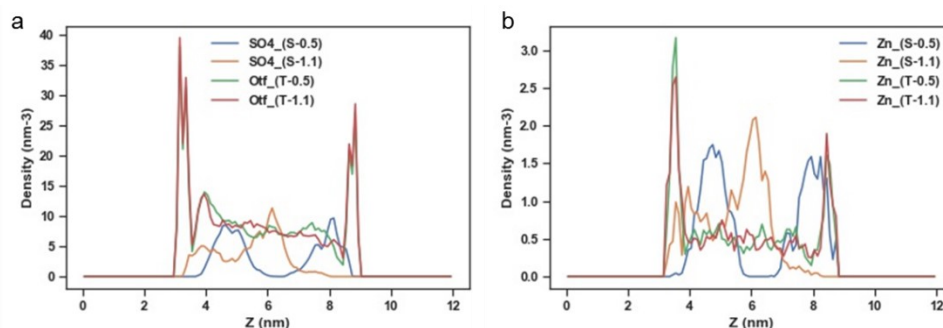


Figure S5.15. Number density of (a) Zn^{2+} and (b) anions in the systems (S-0.5, S-1.1, T-0.5, T-1.1). The inner Helmholtz layer (IHL) was defined by the anions directly adsorbed on the electrode surface.²⁴⁹

As shown in Figure S15b, the cathode surface was at $Z = 9$ nm whereas the first peak of anions (SO_4^{2-} or OTF^-) occurred $Z = 8.75-9$ nm, i.e. the IHL corresponded to 0-0.25 nm from the surface. The outer Helmholtz layer (OHL) was defined by the first peak of Zn^{2+} on the electrode surface, locating at 0.25-0.75 nm from the electrode surface.

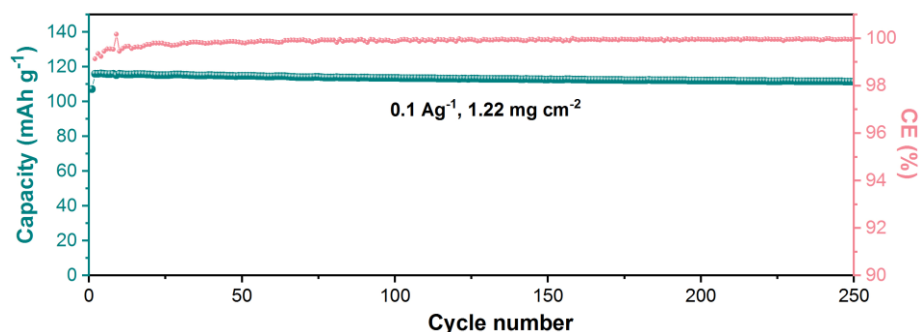


Figure S5.16. Cycling performance of PI-1/CNT in 1.5 M Zn(OTf)₂ at a low rate of 0.1 A g⁻¹.

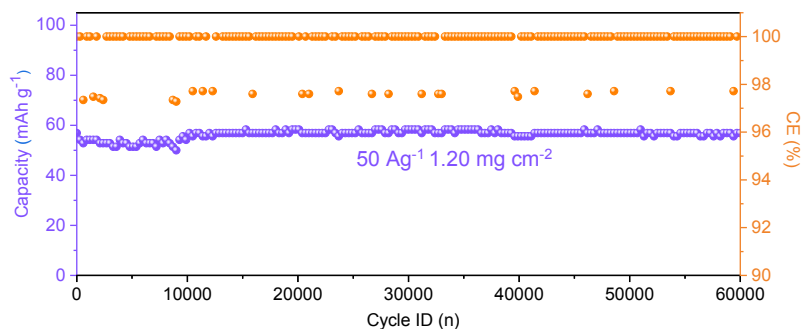


Figure S5.17. High-rate cycling performance of PI-1/CNT at 50 A g⁻¹

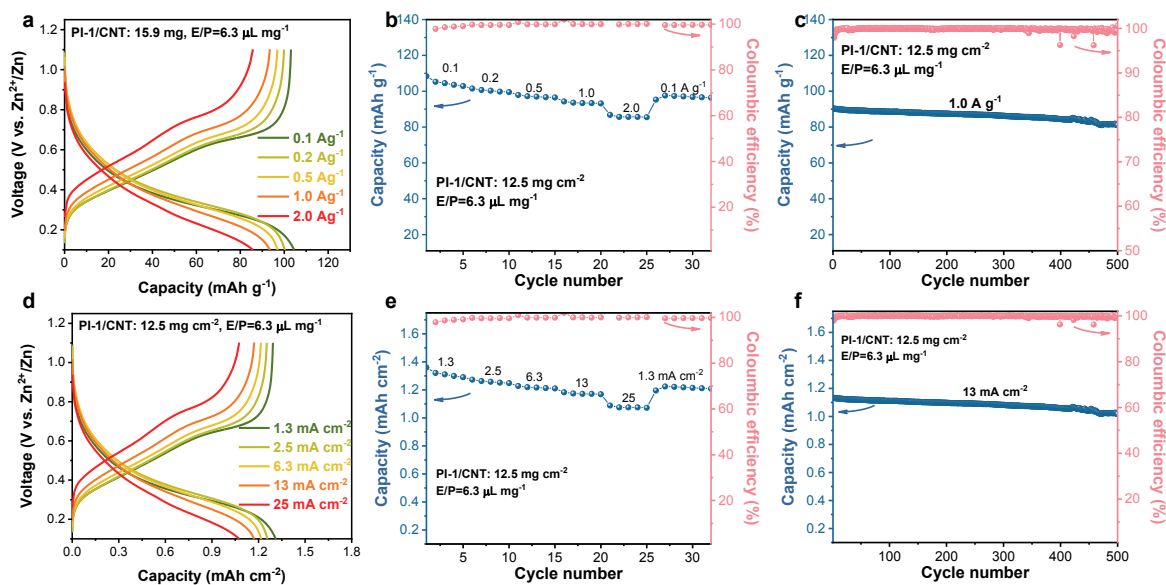


Figure S5.18 Electrochemical performance of free-standing PI-1/CNT electrode with an ultrahigh loading of 12.5 mg cm⁻² under lean electrolyte of 6.3 μL mg⁻¹. (a-c) gravimetric capacities and (d-f) areal capacities. (a, d) charge-discharge profiles at different rates, (b, e) rate performance, (c, f) cycling performance and Coulombic efficiency changes.

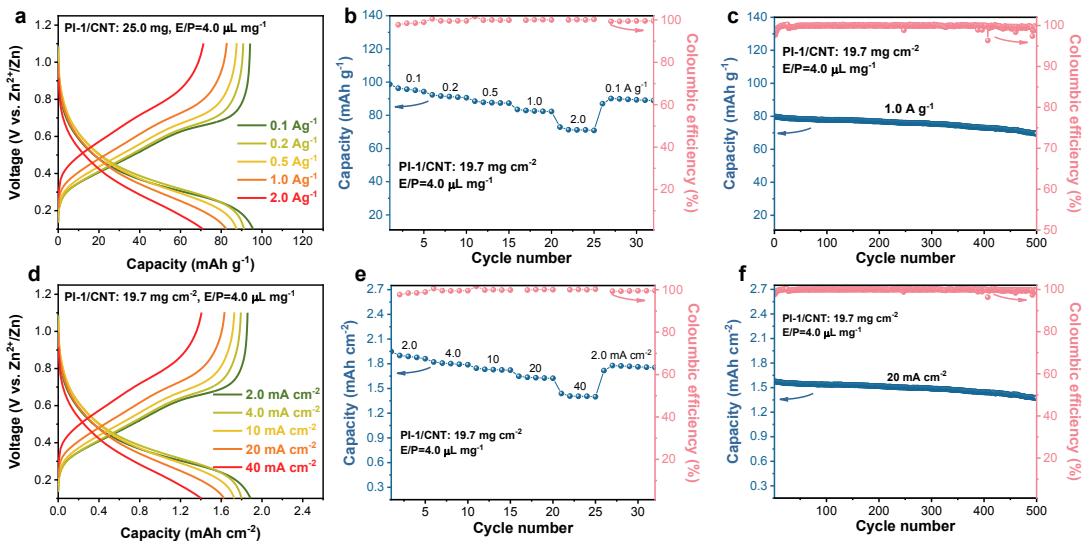


Figure S5.19 Electrochemical performance of free-standing PI-1/CNT electrode with an ultrahigh loading of 19.7 mg cm^{-2} under lean electrolyte of $4.0 \mu\text{L mg}^{-1}$. (a-c) gravimetric capacities and (d-f) areal capacities. (a, d) charge-discharge profiles at different rates, (b, e) rate performance, (c, f) cycling performance and Coulombic efficiency changes.

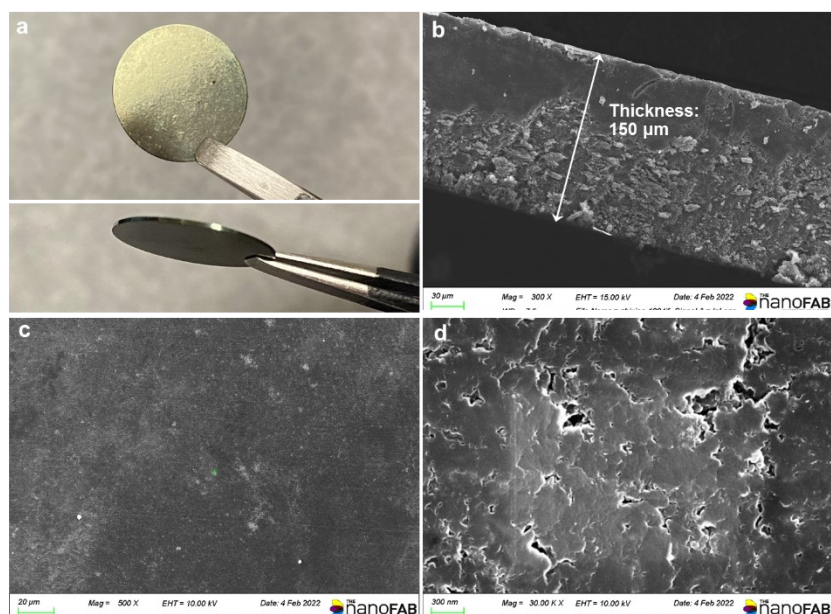


Figure S5.20 Free-standing PI-1/CNT electrode with the loading of 19.7 mg cm^{-2} . (a) Digital photos, (b-d) cross-sectional (b) and top-view SEM images (c-d). Digital photos show the green-shiny color and dense packing of PI-1/CNT powders. The thickness of the high-loading electrode is measured to be $\sim 150 \mu\text{m}$ and the electrode surface is extremely smooth.

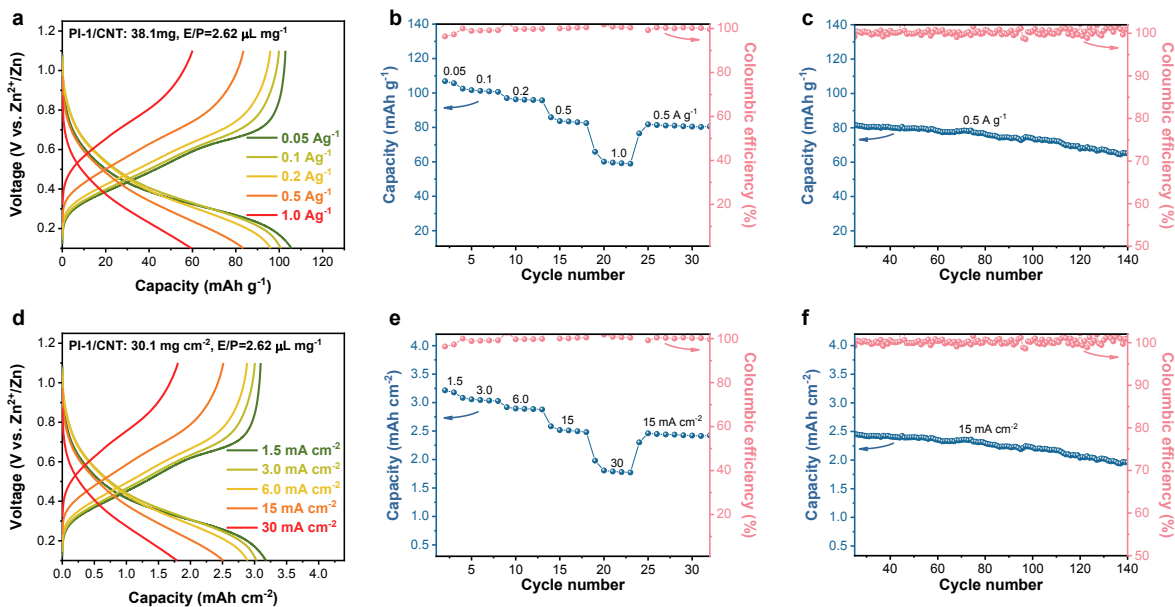


Figure S5.21 Electrochemical performance of free-standing PI-1/CNT electrode with an ultrahigh loading of 30.1 mg cm^{-2} under lean electrolyte of $2.62 \mu\text{L mg}^{-1}$. (a-c) gravimetric capacities and (d-f) areal capacities. (a, d) charge-discharge profiles at different rates, (b, e) rate performance, (c, f) cycling performance and Coulombic efficiency changes. Of note, Zn foil with a thickness of $100 \mu\text{m}$ was used as the anode.

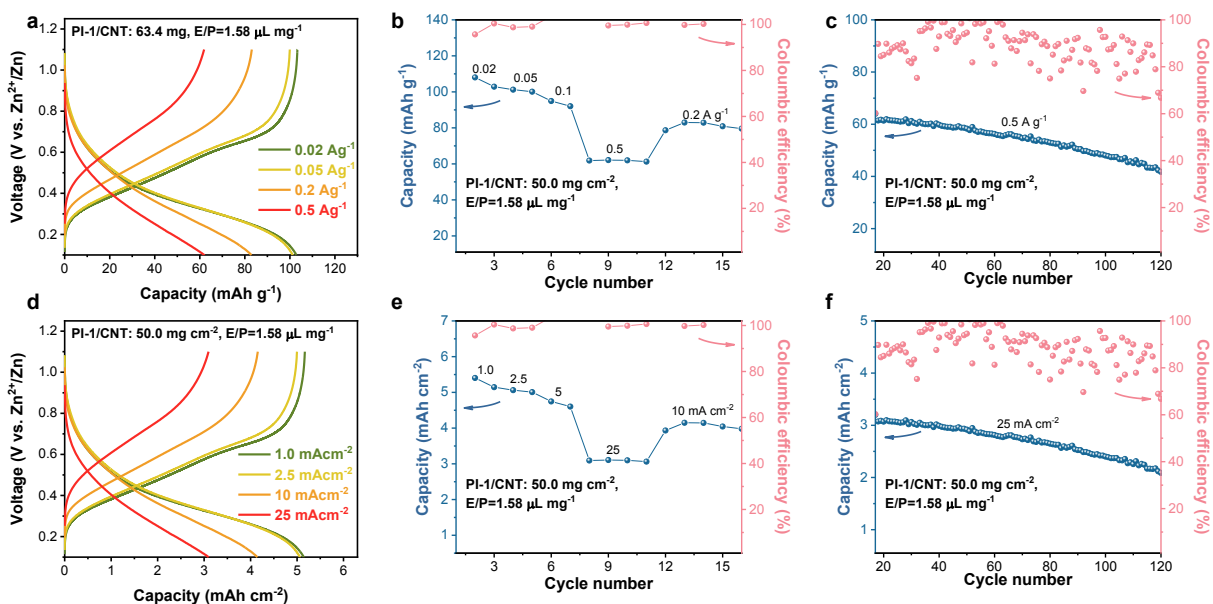


Figure S5.22 Electrochemical performance of free-standing PI-1/CNT electrode with an ultrahigh loading of 50 mg cm^{-2} under lean electrolyte of $1.58 \mu\text{L mg}^{-1}$. (a-c) gravimetric capacities and (d-f)

areal capacities. (a, d) charge-discharge profiles at different rates, (b, e) rate performance, (c, f) cycling performance and Coulombic efficiency changes. Of note, Zn foil with a thickness of 100 μm was used as the anode.

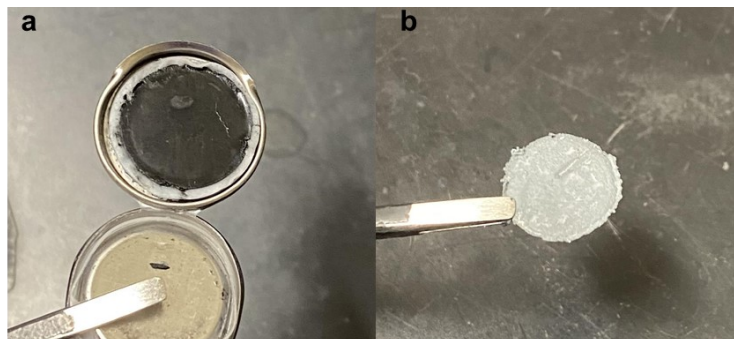


Figure S5.23 Digital photos of disassembled ZIB electrodes after 600 cycles. (a) free-standing PI-1/CNT electrode (19.7 mg cm^{-2}) and (b) Zn metal electrode. Results show the intact feature of the PI-1/CNT electrode but apparent dendrite growth on the Zn metal surface.

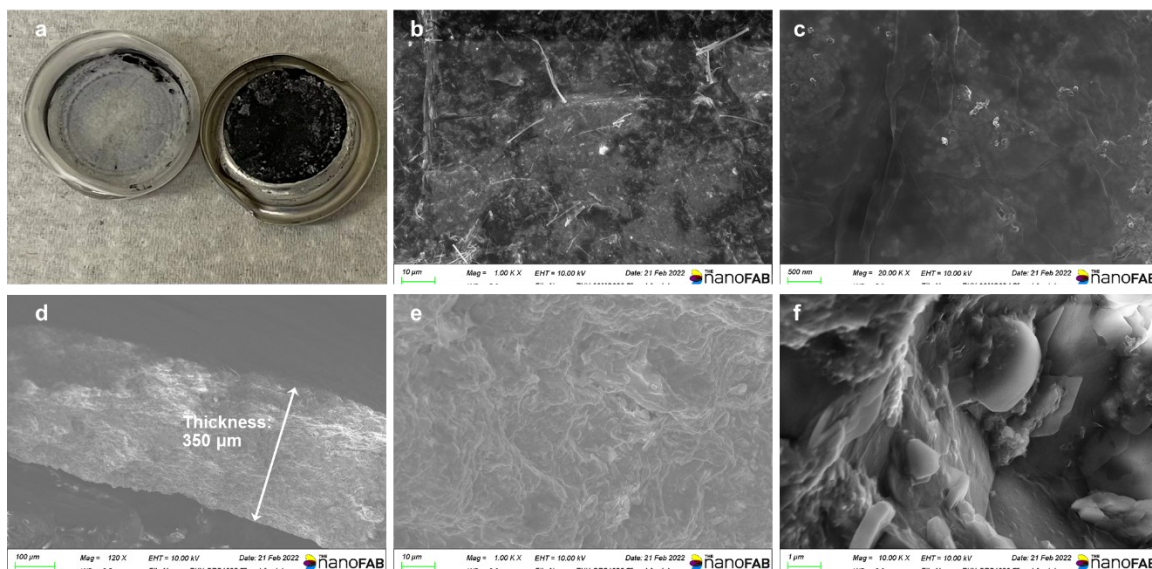


Figure S5.24 Characterization of the 30.1 mg cm^{-2} electrode after cycling. (a) A digital photo of the disassembled PI-1/CNT electrode showing its intact feature. (b, c) Top-view SEM images showing the ultrasmooth surface with layered products covering on the surface without dendrites. (d-f) Cross-sectional SEM images showing the dense packing of PI-1/CNT. The thickness of $350 \mu\text{m}$ indicates a 1.5-fold increase of the electrode volume (the original thickness is $230 \mu\text{m}$) after cycling due probably to the swelling of polymer in the electrolyte and the interaction between Zn ions and PI-1. The battery was disassembled after discharged to 0.1V.

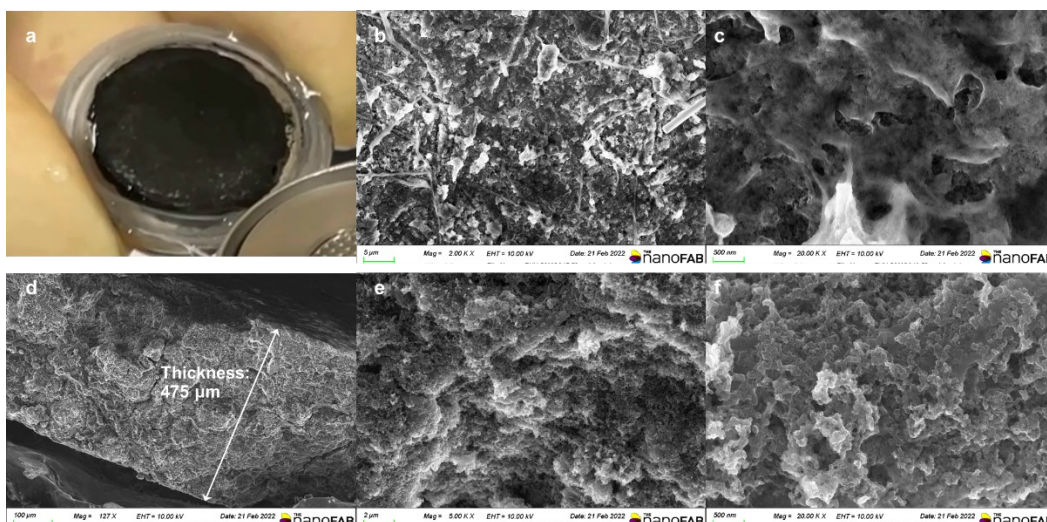


Figure S5.25 Characterization of the 50 mg cm⁻² electrode after cycling. (a) A digital photo showing the intact feature of the disassembled PI-1/CNT electrode after continuous washing by water (Video S2). (b, c) Top-view SEM images showing the nanosheet-like products covering on the surface without dendrites. (d-f) Cross-sectional SEM images showing the dense packing of PI-1/CNT. The thickness of 475 μm indicates a 1.25-fold increase of the electrode volume (the original thickness is 380 μm) after cycling due probably to the swelling of polymer in the electrolyte and the interaction between Zn ions and PI-1. The battery was disassembled after charged to 1.0 V.

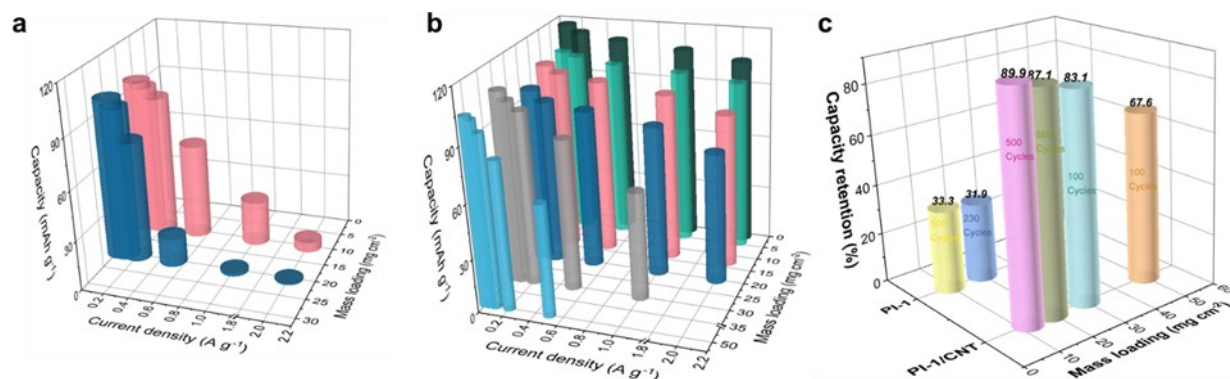


Figure S5.26 Electrochemical performance comparison between high-loading PI-1 and PI-1/CNT electrodes. (a) Capacities of PI-1 electrodes (9.95 and 20 mg cm⁻²) at different rates (0.05-2.0 A g⁻¹). (b) Capacities of PI-1/CNT electrodes (12.5-50 mg cm⁻²) at different rates (0.05-2.0 A g⁻¹). (c) Capacity retentions after hundreds of cycles in PI-1 and PI-1/CNT electrodes under lean electrolyte.

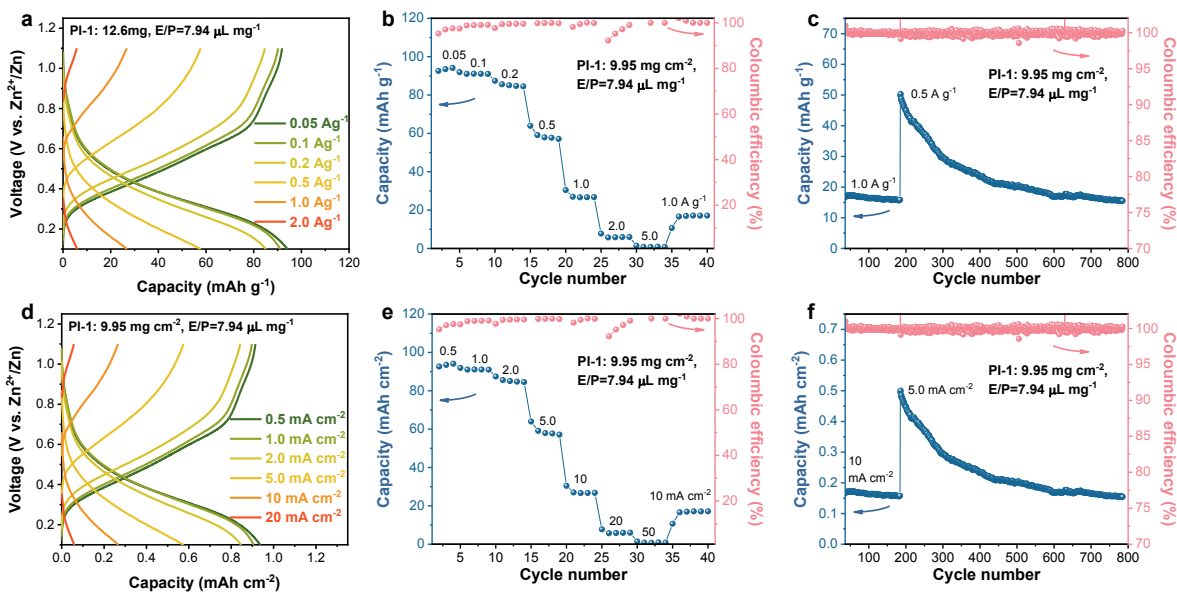


Figure S5.27 Electrochemical performance of free-standing PI-1 electrode with an ultrahigh loading of 9.95 mg cm^{-2} under lean electrolyte of $7.94 \text{ } \mu\text{L mg}^{-1}$. (a-c) gravimetric capacities and (d-f) areal capacities. (a, d) charge-discharge profiles at different rates, (b, e) rate performance, (c, f) cycling performance and Coulombic efficiency changes.

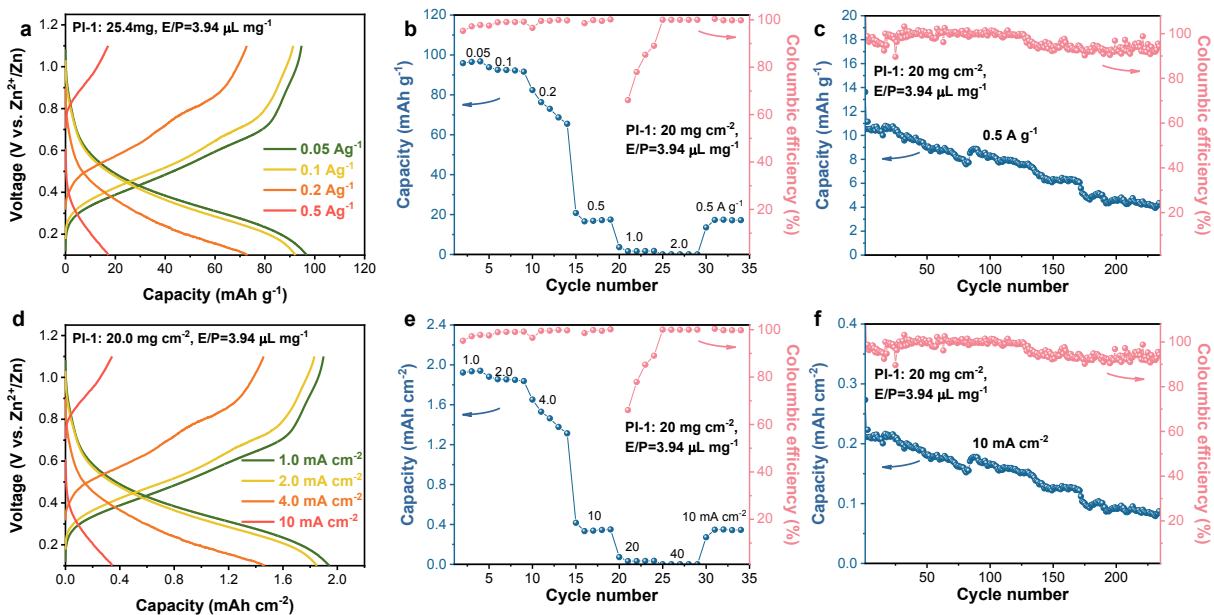


Figure S5.28 Electrochemical performance of free-standing PI-1 electrode with an ultrahigh loading of 20.0 mg cm^{-2} under lean electrolyte of $3.94 \text{ } \mu\text{L mg}^{-1}$. (a-c) gravimetric capacities and (d-f) areal capacities.

capacities. (a, d) charge-discharge profiles at different rates, (b, e) rate performance, (c, f) cycling performance and Coulombic efficiency changes.

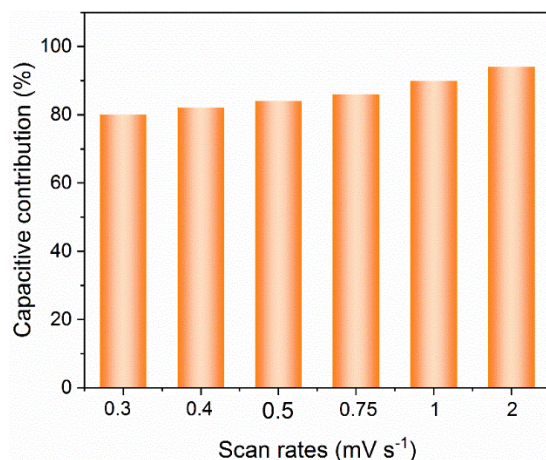


Figure S5.29 Capacitive contribution ratio of PI-1/CNT electrode at different scan rates.

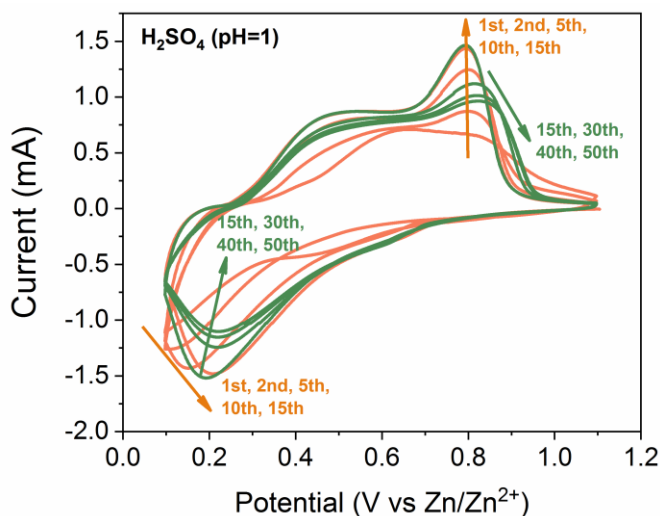


Figure S5.30 Two-electrode CV test in H₂SO₄ (pH=1) electrolyte with the PI-1/CNT as working electrode and Zn metal as counter/reference electrode. Under strongly acidic electrolyte, Zn metal will be dissolved into Zn²⁺ through the reaction: $\text{Zn} + 2\text{H}^+ \longrightarrow \text{Zn}^{2+} + \text{H}_2$. As such, the electrolyte will be composed of gradually increased Zn²⁺ ions but decreased H⁺. That is why the CV profile in this system is continuously changing, corresponding to the competition between proton and Zn²⁺ storage.

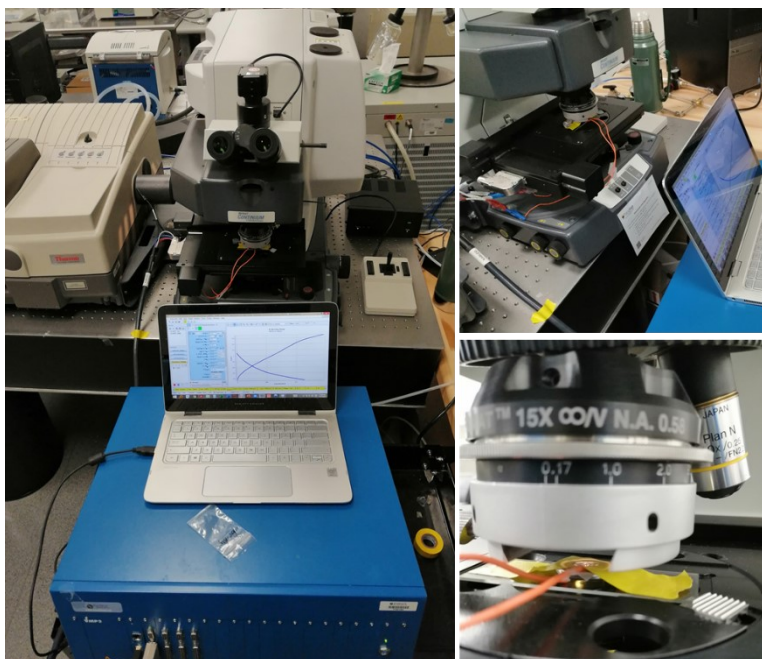


Figure S5.31 Set-up for *in situ* ATR-FTIR test during battery charging/discharging.

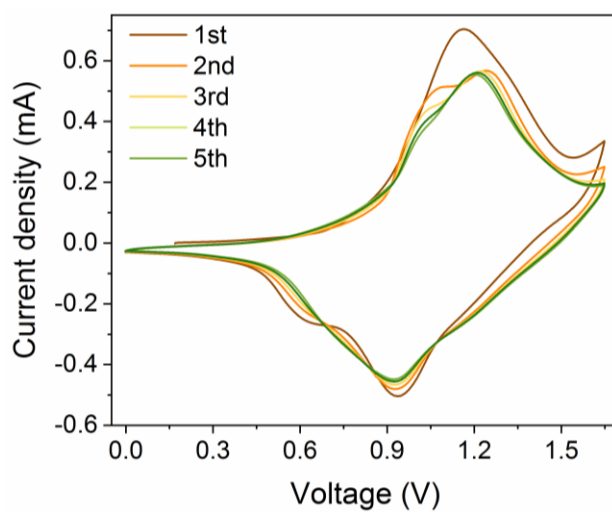


Figure S5.32 CV curves of polymer based ZIBs (PI-1/CNT//Zn_xMnO₂) in the first five cycles with a scan rate of 0.5 mV s⁻¹. The overlapping curves suggest excellent reversibility and cycling stability of PI-1/CNT-based ZIB.

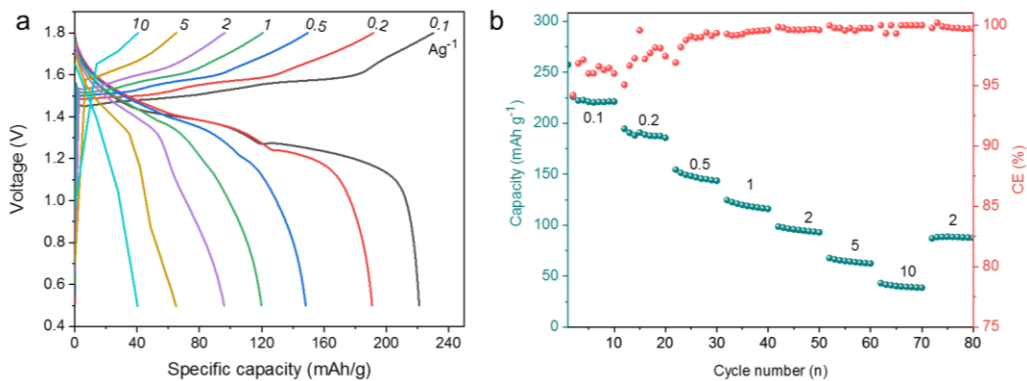


Figure S5.33 Electrochemical performance of Zn//MnO₂ battery. (a) Charge-discharge curves and (b) rate performance at different current densities.

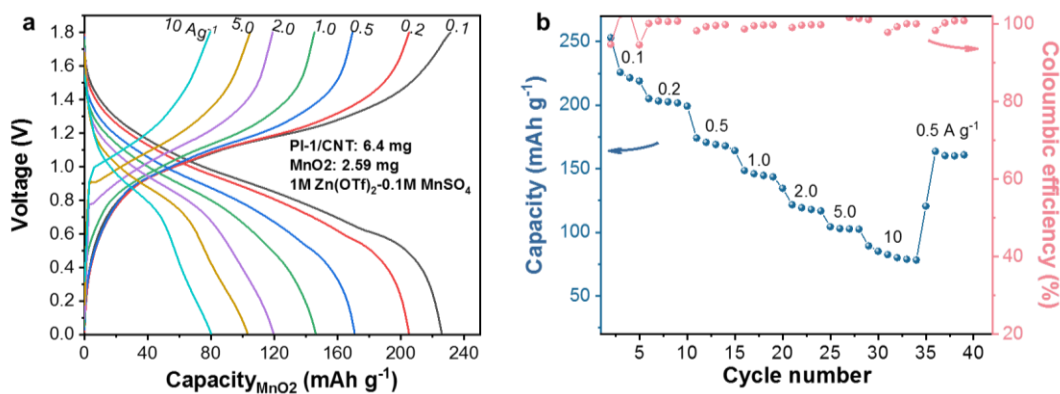


Figure S5.34 The electrochemical performance of rocking-chair PI-1/CNT//Zn_xMnO₂ full cells with a N/P mass ratio of ~2.5. (a) charge-discharge curves and (b) rate performance. Compared with excessive Zn anode (28.5 mg, Figure S33), the PI-1/CNT anode (6.4 mg) enables higher capacities of the cathode at all current densities from 0.1 to 10 A g⁻¹.

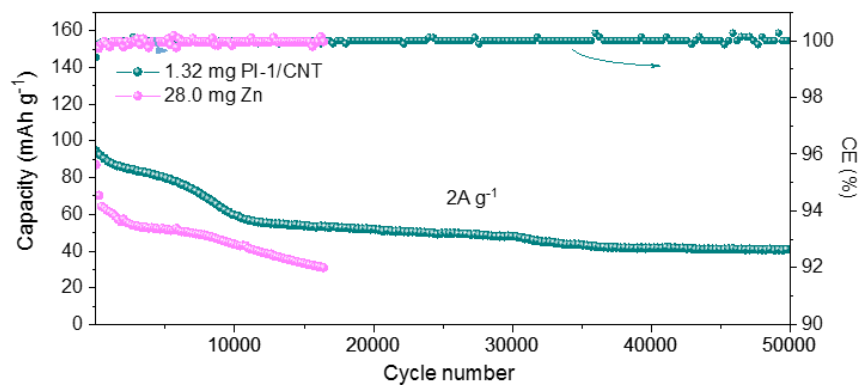


Figure S5.35 Cycling of PI-1/CNT//Zn_xMnO₂ and Zn//MnO₂ batteries at 2 A g⁻¹ with the same amount of MnO₂ (1.32 mg) but different amount of anode materials.

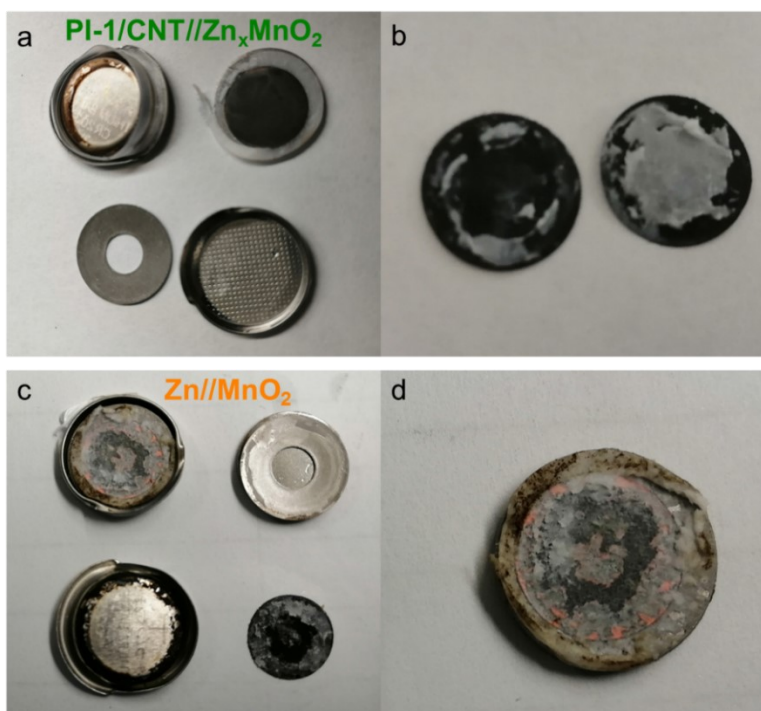


Figure S5.36 Digital photographs of disassembled ZIBs after long cycles. (a-b) PI-1/CNT//Zn_xMnO₂ battery after 50,000 cycles and (c-d) Zn//MnO₂ battery after 16,000 cycles.

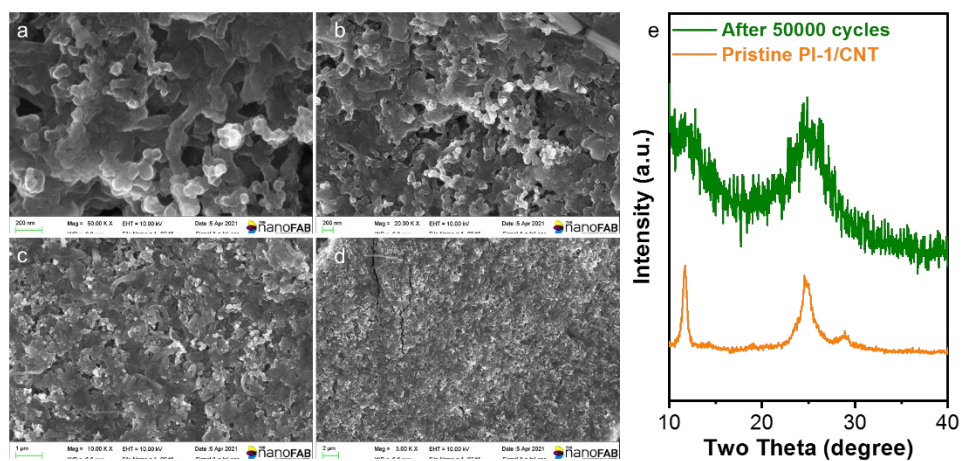


Figure S5.37 Structural characterization of after-50k-cycle PI-1/CNT electrode in the PI-1/CNT// Zn_xMnO_2 battery. (a-d) SEM images and (e) XRD patterns.

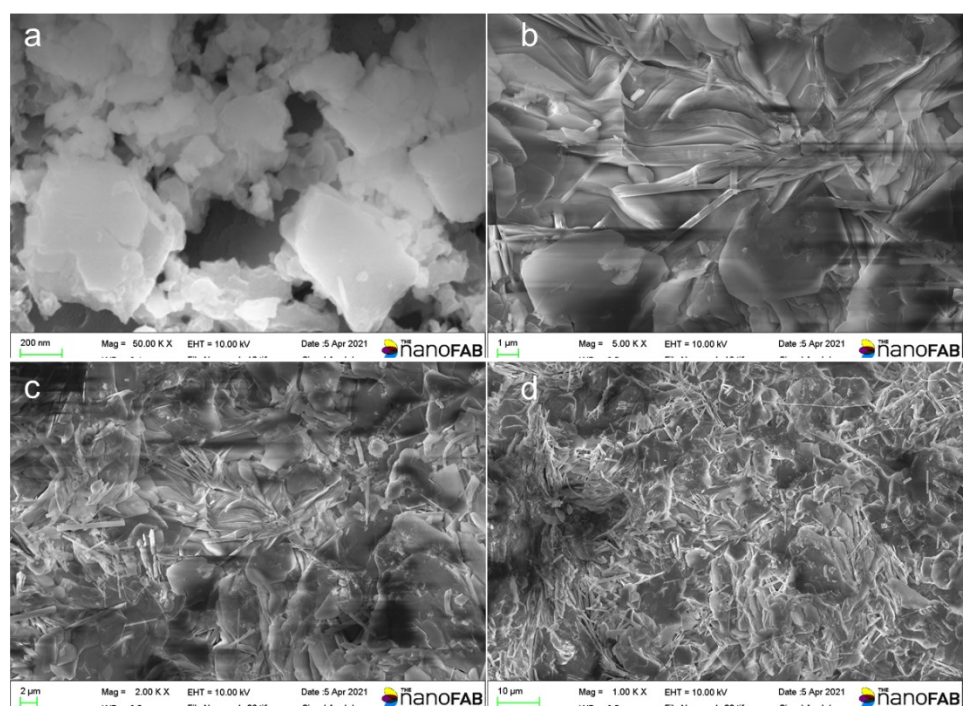


Figure S5.38 Structural characterization of Zn anode in the Zn// MnO_2 battery. (a-d) SEM images of the Zn anode after 16k cycles.

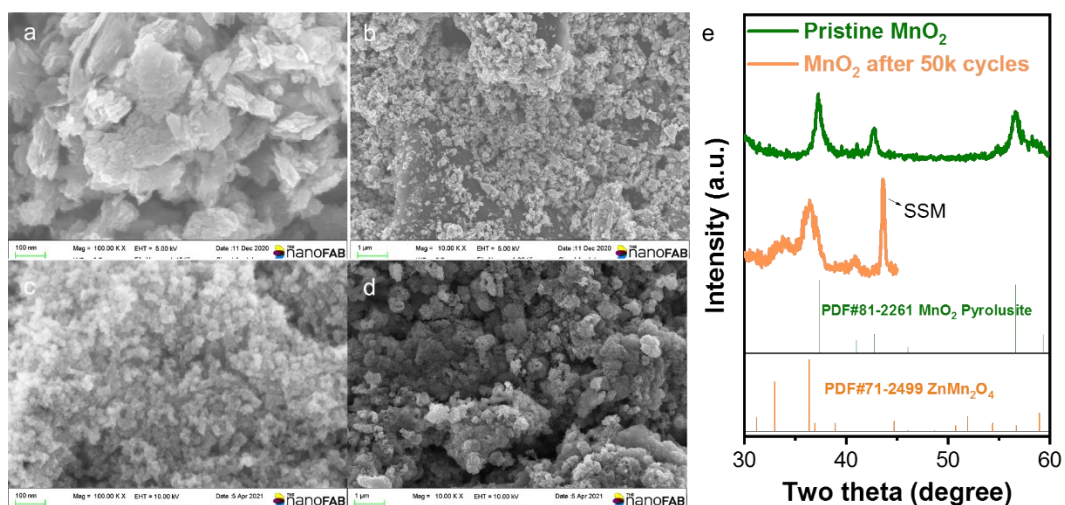


Figure S5.39 Structural characterization of cathode materials in the PI-1/CNT//Zn_xMnO₂ battery. SEM images of MnO₂ (a-b) before and (c-d) after 50000 cycles and (g) XRD patterns of pristine MnO₂ (green) and after 50,000 cycles (yellow).

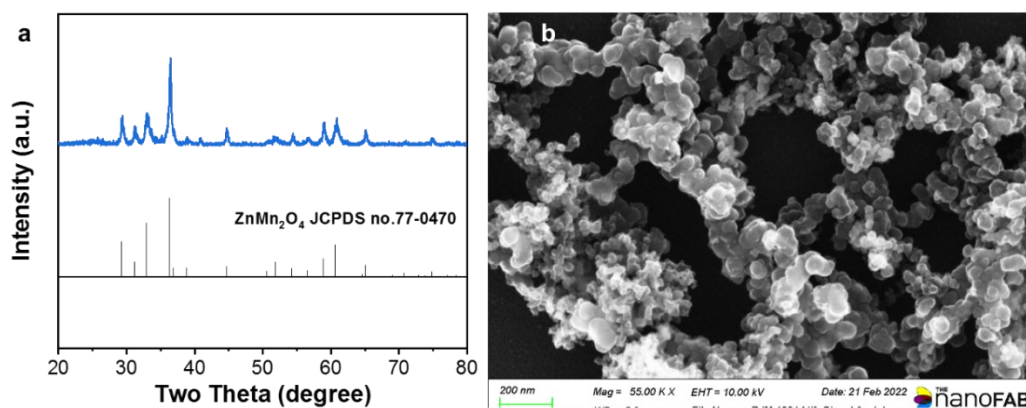


Figure S5.40 Characterization of ZnMn₂O₄. (a) the XRD pattern and (b) the SEM image.

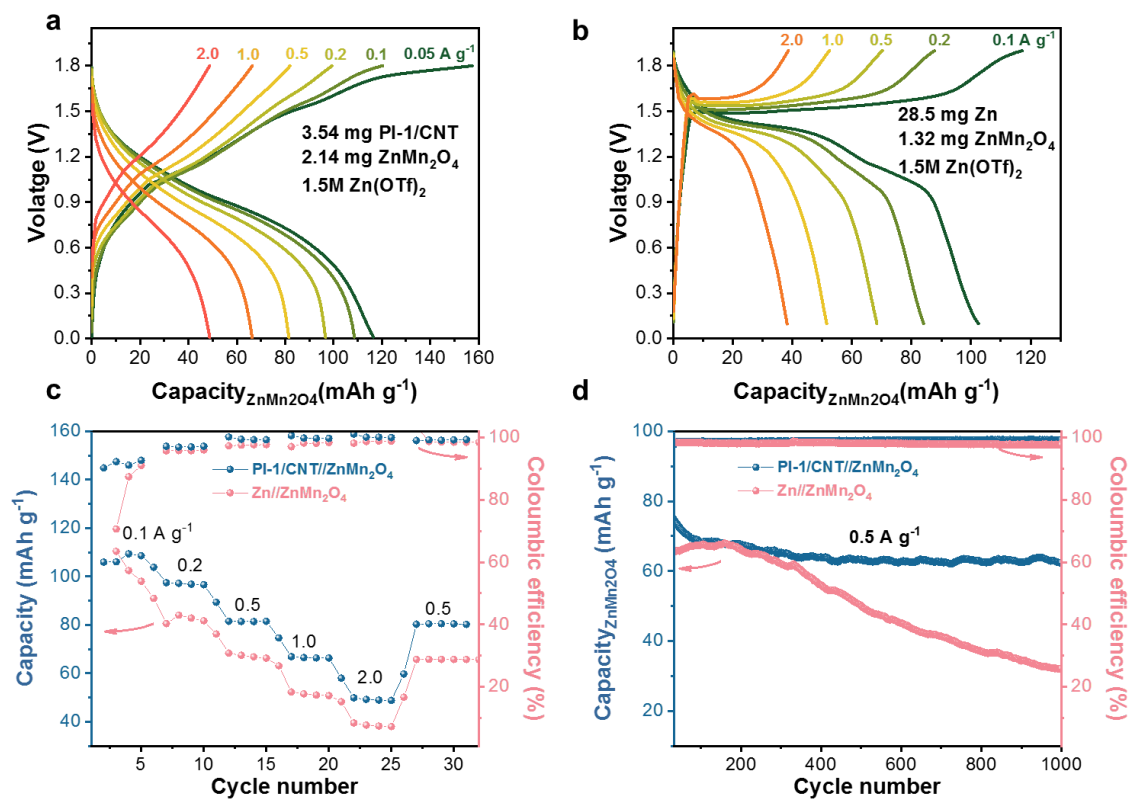


Figure S5.41 Electrochemical performance of PI-1/CNT//ZnMn₂O₄ and Zn//ZnMn₂O₄ batteries. (a-b) Charge-discharge curves of (a) PI-1/CNT//ZnMn₂O₄ cell and (b) Zn//ZnMn₂O₄ cell. (c) Rate performance at different current densities and (d) cycling performance at 0.5 A g⁻¹. The capacity is based on ZnMn₂O₄. 30 μ m Zn foil (28.5 mg) was used as the anode here for the assembly of Zn//ZnMn₂O₄ cell.

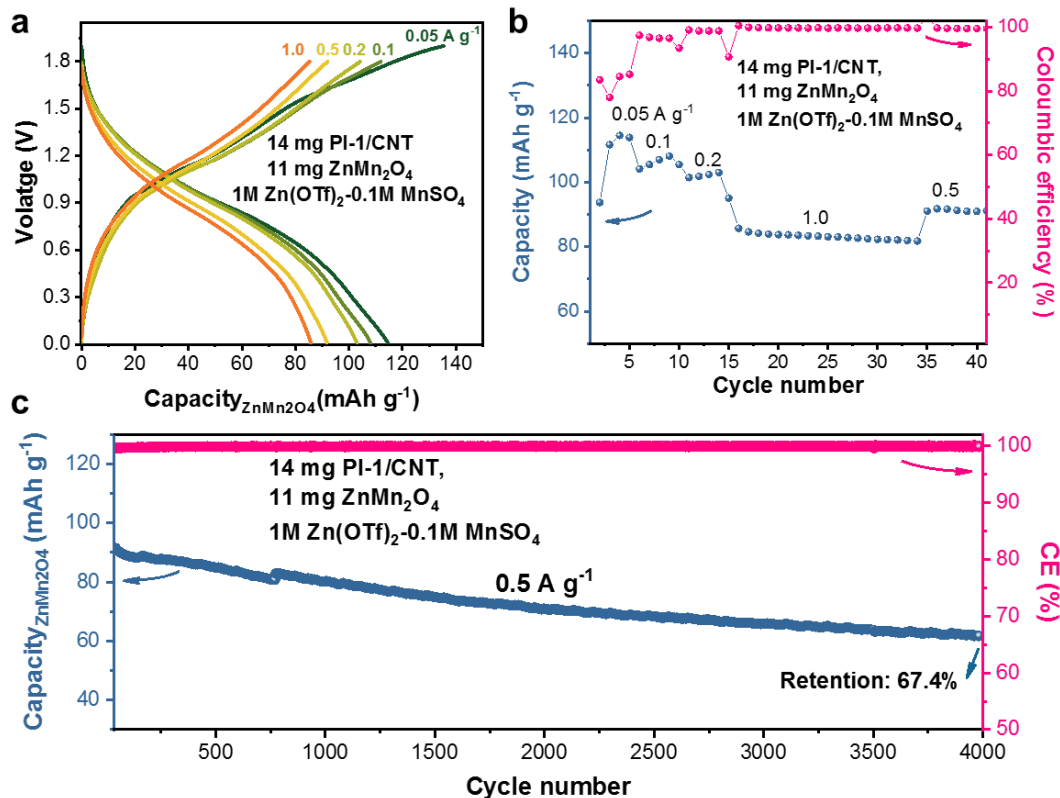


Figure S5.42 Electrochemical performance of PI-1/CNT//ZnMn₂O₄ full cell using high-loading, free-standing, current-collector-free, and binder-free electrodes. (a) Charge-discharge profiles, (b) rate performance, and (d) cycling performance at 0.5 A g⁻¹. The capacity is based on ZnMn₂O₄. The electrolyte is 100 μ L of 1M Zn(OTf)₂-0.1M MnSO₄. The free-standing ZnMn₂O₄ electrode was prepared in the same way as PI-1/CNT electrode by pressing using die mold with an area of 1.27 cm².

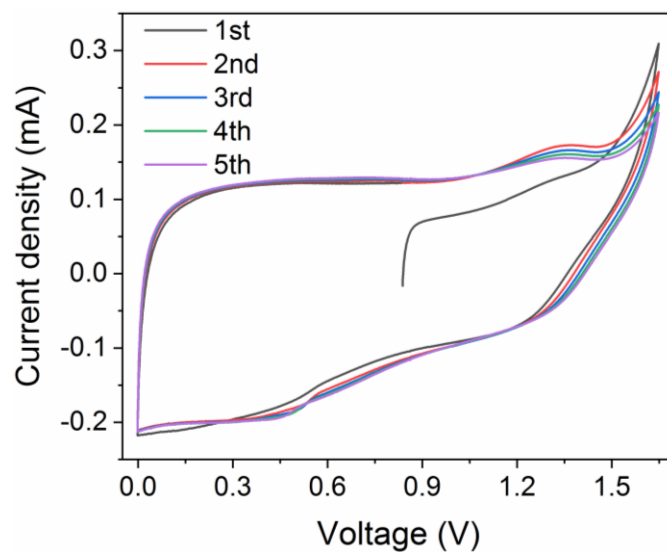


Figure S5.43 CV curves of PI-1/CNT//AC capacitor in the first five cycles with a scan rate of 0.5 mV s^{-1} . The overlapping curves indicate excellent reversibility of the PI-1/CNT-based ZIC.

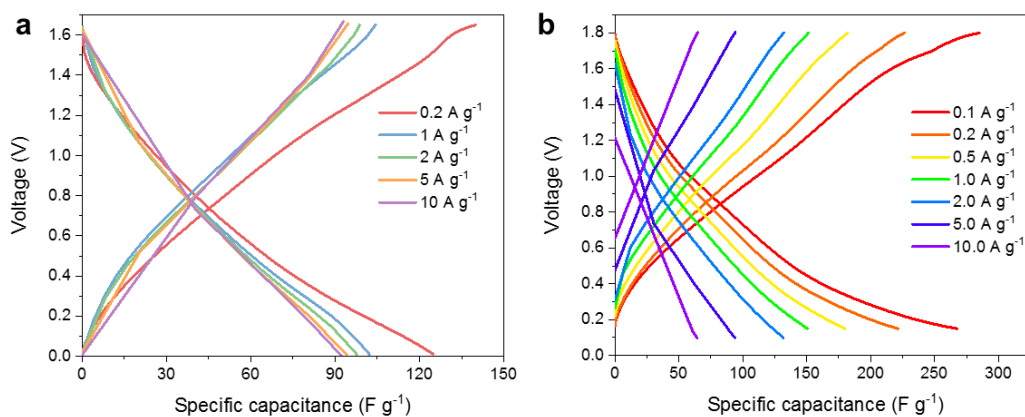


Figure S5.44 Charge-discharge profiles of (a) PI-1/CNT//AC and (b) Zn//AC capacitors under different current densities.

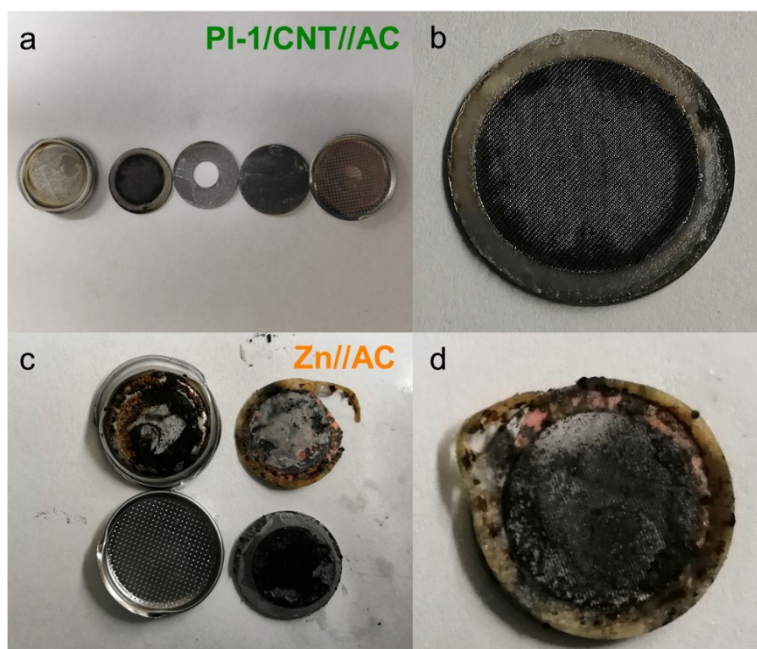


Figure S5.45 Digital photographs of disassembled ZICs after long cycles. (a-b) PI-1/CNT//AC capacitor after 500,000 cycles and (c-d) Zn//AC capacitor after 107,000 cycles.

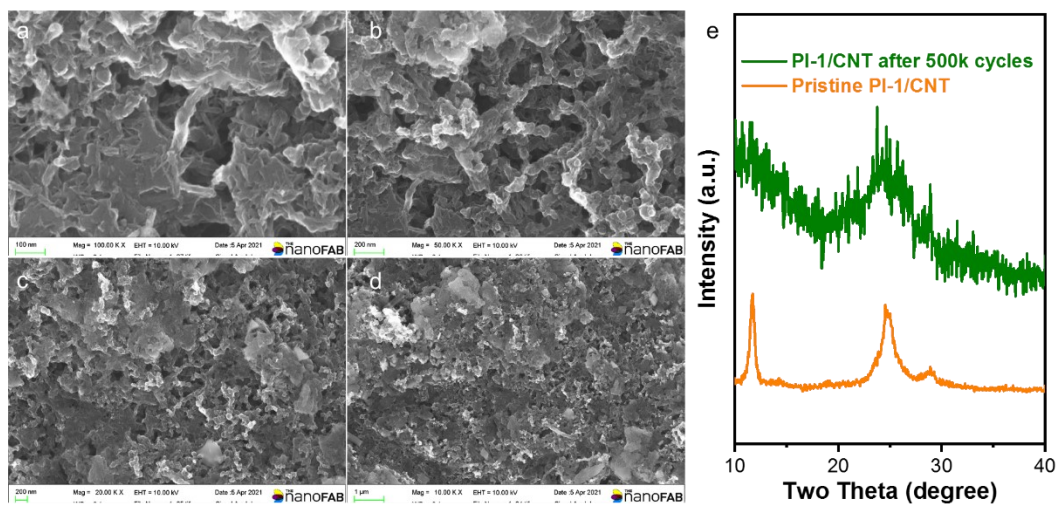


Figure S5.46 Structural characterization of after-500k-cycle PI-1/CNT electrode in the PI-1/CNT//AC capacitor. (a-d) SEM images and (e) XRD patterns.

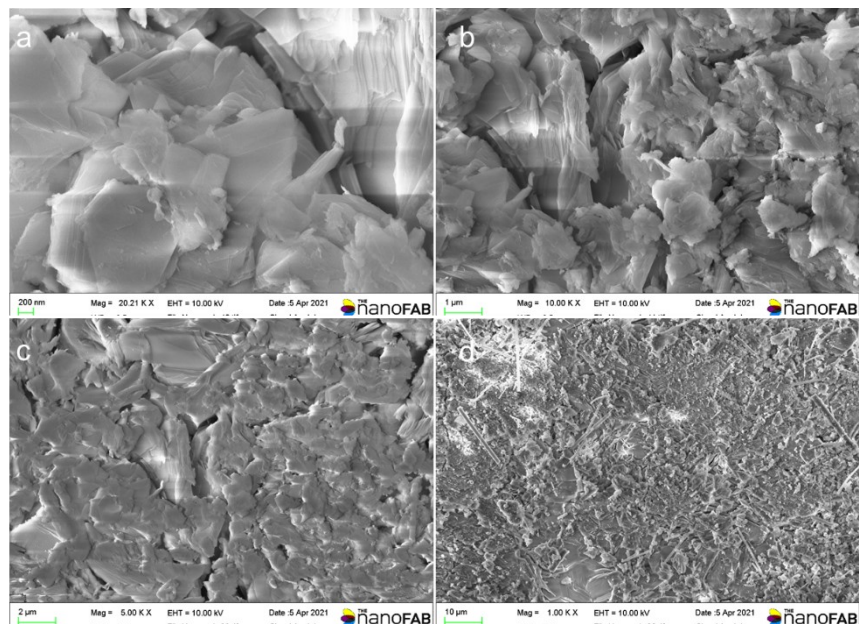


Figure S5.47 Structural characterization of after-cycling Zn anode in the Zn//AC capacitor. (a-d) SEM images of Zn anode.

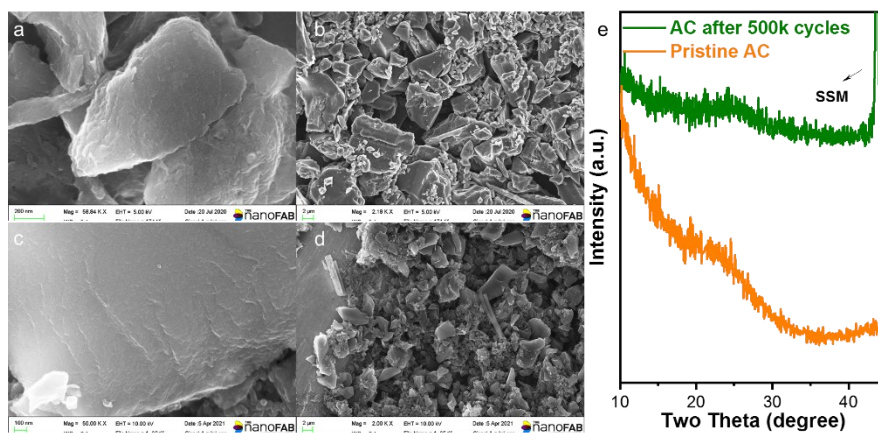


Figure S5.48 Structural characterization of pristine and after-500k-cycle AC cathode in the PI-1/CNT//AC capacitor. SEM images of AC (a-b) before and (c-d) after half million cycles. (e) XRD patterns of AC before (yellow line) and after half million cycles (green line).

Table S5.1 Performance comparison between electrode materials for zinc ion batteries

Materials	Loading (mg cm ⁻²)	Electrolyte	Rate performance (mAhg ⁻¹ @ Ag ⁻¹)	Cycling performance (%, cycles, Ag ⁻¹)
PI-1/CNT (This work)	1.20	1.5M Zn(OTf) ₂	58 @ 50	100%, 60000, 50Ag ⁻¹
			40 @ 100	75%, 1000000, 100 Ag ⁻¹
	4.08		84 @ 5	90%, 30000, 5 Ag ⁻¹
	19.7		70 @ 2	90%, 500, 1 Ag ⁻¹
	30.1		60 @ 1	83.1%, 100, 0.5 Ag ⁻¹
Organics				
C4Q ⁷⁴	2.5-10	3M Zn(OTf) ₂	172 @ 1	87%, 1000, 0.5 Ag ⁻¹
p-chloranil ²⁵⁰	1.8-3.0	1 M Zn(OTf) ₂	118 @ 0.217	70%, 200, 0.217 Ag ⁻¹
DTT ²⁴²	5	2M ZnSO ₄	97 @ 2	83.8%, 23000, 2 Ag ⁻¹
PTCDA ¹⁵⁹	2.5	2 M ZnCl ₂	76.9 @ 32	68.2%, 1000, 8 Ag ⁻¹
PANI ¹⁶⁰	1.5	1 M Zn(OTf) ₂	95 @ 5	94%, 200, 0.5 Ag ⁻¹ 92%, 3000, 5 Ag ⁻¹
PPy ¹⁶¹	N. A.	Zn(Ac) ₂ - KCl-PVA	37 @ 44.7	38%, 200, 4.4 Ag ⁻¹
PTO ¹⁶²	4-6	2M ZnSO ₄	113 @ 20	70%, 1000, 3Ag ⁻¹
poly(1,5-NAPD) ¹⁶³	2.7	2M ZnSO ₄	145 @ 14.8	91%, 10000, 10 Ag ⁻¹
TABQ ¹⁵⁰	1.3	1M ZnSO ₄	213 @ 5	85%, 1000, 5 Ag ⁻¹
TT-DQ ²⁵¹	N. A.	3M Zn(OTf) ₂	120 @ 50	91.8%, 200000, 40 Ag ⁻¹
Mn-based				
α-MnO ₂ ⁸⁷	1.0-5.0	2 M ZnSO ₄ + 0.1 M MnSO ₄	114 @ 3.08	92%, 5000, 1.54 Ag ⁻¹
β-MnO ₂ ⁵⁷	~2.0	3M Zn(OTf) ₂ + 0.1M Mn(OTf) ₂	100 @ 10	94%, 2000, 2Ag ⁻¹
α-MnO ₂ /CFP ⁵⁶	N. A.	2M ZnSO ₄ + 0.2 M MnSO ₄	50 @ 2	~100%, 10000, 2 Ag ⁻¹
δ-MnO ₂ ²⁵²	3-5	1 M ZnSO ₄ + 0.2 M MnSO ₄	113 @ 3	83.7%, 2000, 2 Ag ⁻¹
ZnMn ₂ O ₄ /C ¹⁰⁸	2.0	3M Zn(OTf) ₂	72 @ 2	94%, 500, 0.5Ag ⁻¹
Spinel-Mn ₃ O ₄ ²⁵³	2.0	1 M ZnSO ₄ + 1 M MnSO ₄	150 @ 0.5	92%, 500, 0.5Ag ⁻¹
δ-MnO ₂ ¹⁶⁴	N. A.	2M ZnSO ₄ + 0.1M MnSO ₄	124 @ 3	74%, 2000, 3Ag ⁻¹
γ-MnO ₂ ¹⁶⁵	2.0-3.0	3M ZnSO ₄ + 0.2 M MnSO ₄	80 @ 5	95%, 1000, 2Ag ⁻¹
Inverse opal MnO ₂ ²⁵⁴	1.5	2M ZnSO ₄ + 0.1M MnSO ₄	121 @ 2	100%, 5000, 2 A g ⁻¹

O-deficient σ-MnO₂⁹⁹	1.0	1 M ZnSO ₄ + 0.2 M MnSO ₄	100 @ 10	80%, 2000, 5 A g ⁻¹
V-based				
V₂O₅¹⁶⁶	1.5	saturated ZnSO ₄	108@10	82%, 6200, 10Ag ⁻¹
V₂O₅·1.6H₂O¹⁶⁷	2–3	3M Zn(OTf) ₂	251@20	95%, 5000, 10Ag ⁻¹
V₆O₁₃¹⁶⁸	1.0–1.5	3M Zn(OTf) ₂	144@24	90%, 2000, 4Ag ⁻¹
VO₂(B)²⁴¹	N. A.	3M Zn(OTf) ₂	171.4@51.2	91.2%, 300, 0.1A g ⁻¹
RGO/VO₂²⁵⁵	1.5	3M Zn(OTf) ₂	118.7@35	96%, 400, 1 A g ⁻¹
Na₂V₆O₁₆·3H₂O¹⁷⁰	~3	1 M ZnSO ₄	112 @20	80%, 1000, 14.44 A g ⁻¹
Cu_{0.1}V₂O₅·0.08H₂O¹⁷¹	N. A.	2 M ZnSO ₄	122 @ 20	88%, 10000, 10Ag ⁻¹
Zn_{0.3}V₂O₅·1.5H₂O⁷⁰	2.0	3M Zn(OTf) ₂	265.2 @ 10	96%, 20000, 10Ag ⁻¹
VN_{0.9}O_{0.15}¹⁶⁹	N. A.	3M Zn(OTf) ₂	124@102.4	95%, 1800, 4.5 Ag ⁻¹
Polyanions				
Na₃V₂(PO₄)₃²⁵⁶	N. A.	0.5 M Zn(Ac) ₂	58.2 @1	74%, 100, 0.05A g ⁻¹
Na₃V₂(PO₄)₃/C²⁵⁷	N. A.	0.5 M NaAc- Zn(AC) ₂	61.6@2	77%, 200, 0.05Ag ⁻¹
Na₃V₂(PO₄)₂F₃²³	10	2M Zn(OTf) ₂	33 @ 3	95%, 4000, 1 A g ⁻¹
Li₃V(PO₄)₃⁷⁸	8-10	4M Zn(OTf) ₂	121.9 @ 9	78.8%, 4000, 1.5 A g ⁻¹
PBA				
FeHCF⁶⁴	5.0	1 M Zn(OAc) ₂ / [Ch] OAc + 30 wt % H ₂ O	30 @ 0.06	94%, 10, 0.01A g ⁻¹
CuHCF²⁵⁸	> 5.0	0.02 M ZnSO ₄	43 @ 0.6	96%, 100, 0.06A g ⁻¹
CuHCF⁶²	N. A.	1 M ZnSO ₄	56 @ 0.02	77%, 20, 0.02 Ag ⁻¹
ZnHCF¹⁷²	8.0	3M ZnSO ₄	29.3 @ 1.2	80%, 200, 0.3 Ag ⁻¹
ZnHCF⁶³	8.0	1M ZnSO ₄	32 @ 1.2	76%, 100, 0.3 Ag ⁻¹
CoFe(CN)₆⁶⁵	N. A.	4M Zn(OTf) ₂	109 @ 6	100%, 2200, 3 Ag ⁻¹

Table S5.2 Performance comparison of Zn-free anode materials for rocking-chair type ZIBs

Materials	Loading (mg cm ⁻²)	Electrolyte	Voltage _{discharge} (vs. Zn ²⁺ /Zn)	Cap at low j (mAhg ⁻¹ @ Ag ⁻¹)	Cap at high j (mAhg ⁻¹ @Ag ⁻¹)	Cycling performance (% , cycles, Ag ⁻¹)
PI-1/CNT (This work)	1.2	1.5M Zn(OTf) ₂	0.36	128@0.05	58@ 50,	100%, 60000, 50
					40@100	75%, 1000000,100
	4.08			103@0.1	84 @ 5	90%, 30000, 5
	30.1			105@0.05	60 @ 1	83.1%, 100, 0.5
	50.0			106@0.02	61 @ 0.5	67.6 %, 100, 0.5
Mo ₆ S ₈ ³⁹	~15	0.1M ZnSO ₄	0.45–0.5 and 0.35	63@0.064	47 @0.256	~88%, 20, 0.0128
Mo ₆ S ₈ ³⁸	1	1M ZnSO ₄	0.36	79@0.045	58 @ 0.225	~95.2%, 150, 0.18
Zn ₂ Mo ₆ S ₈ ³⁷	5.1	0.1M ZnSO ₄	0.35	88@0.0064	57 @0.128	N. A.
h-MoO ₃ ⁴³	1.3	1M ZnSO ₄	0.36	120@0.2	55 @ 1	~100%, 100, 0.3 89.5%, 5000, 2
Zn _x Mo _{2.5+y} VO _{9+z} ⁴⁴	N. A.	0.5M Zn(Ac) ₂	0.25	~220@0.02	~180@0.02	~100%, 35, 0.02
TiS ₂ ⁴⁰	6.1	2M Zn(OTf) ₂	~0.25	N. A.	N. A.	33%, 50, 0.1
Na _{0.14} TiS ₂ ⁴⁰	5-6.0	2M Zn(OTf) ₂	~0.3	140@0.05	58 @ 2	77%, 5000, 0.5; 98%, 700, 0.2
H ₂ Ti ₃ O ₇ ²⁵⁹	4.0	1M ZnSO ₄	0.2	86@0.2	42 @ 2	105.5%, 4000, 0.6
Te ²⁶⁰	2.2	1M ZnSO ₄	0.61	376@0.1	N. A.	N. A.
Cu _{2-x} Se ²²⁰	~1.3	2M ZnSO ₄	0.42	210@0.1	40.1 @ 5	100%, 30000, 5
9,10-AQ ⁵³	2.0-5.0	1M ZnSO ₄ + 0.05M MnSO ₄	0.45	204.5@0.2	N. A.	~84.3%, 200, 0.2
PTCDI /rGO ⁵⁴	2.0-3.0	3M ZnSO ₄	~0.28, 0.38	127@0.05	121 @5	95%, 1200, 0.5 96%, 1500, 3
PTCDA ¹⁵⁹	2.5-12.3	2M ZnCl ₂	~0.55	122.9@0.2	76.9 @32	68.2%, 1000, 8
PI-COF ²²⁴	1.4	2M ZnSO ₄	0.5 V vs. Ag/AgCl	92@0.7	73.4 @7	85%, 4000, 10mVs ⁻¹

Table S5.3 Comparison of rocking-chair type ZIBs (energy density, power density, and life cycles)

Anode//Cathode	N/P ratio	Electrolyte	Power Density (W kg ⁻¹)	Energy Density (Wh kg ⁻¹)	Cycling performance (Capacity retention, cycles, rate)
PI-1/CNT// Zn _x MnO ₂ (This work)	1.0	1M Zn(OTf) ₂ + 0.1M MnSO ₄	45.5	50.51	~83%, 6000 cycles, 2 Ag ⁻¹ ~43%, 50000 cycles, 2 Ag ⁻¹
			91	47	
			227.5	45.5	
			455	44.4	
			880	41.8	
			2100	36.75	
			4200	31.7	
			6700	19.4	
Mo ₆ S ₈ // 1.5 m ZnI ₂ + 0.2 m I ₂ ³⁸	N. A. assuming N/P=1:1	1.1 M ZnSO ₄	48.9375	24.5	~90%, 350 cycles 0.6Ag ⁻¹
			97.875	24.4	
			190.125	23.9	
			364.5	21.9	
Zn ₂ Mo ₆ S ₈ // ZnPB ³⁷	5.5	0.1 M ZnSO ₄	249	22.8	~100%, 10 cycles
Na _{0.14} TiS ₂ // ZnMn ₂ O ₄ ₄₀	1.0	2M Zn(OTf) ₂	47.5	51	~74%, 100 cycles, 200 mAg ⁻¹
h-MoO ₃ // Zn _{0.2} MnO ₂ ⁴³	2.0	1 M ZnSO ₄	53.75	61	~100%, 1000, 1Ag ⁻¹ ~90%, 5000, 2Ag ⁻¹
			107	56.1	
			159.75	50.4	
			212	46.4	
			262.5	43.6	
			315	41.37	
			525	36.33	
			1050	29.4	
2625	15.75				
Cu _{2-x} Se// Zn _x MnO ₂ ²²⁰	1.1	2M ZnSO ₄ + 0.1M MnSO ₄	37.2093	69.4	~96.7%, 20000, 2Ag ⁻¹
			74.4186	55.8	
			182.558	39.5	
			358.14	28.6	
			706.977	18.9	
1767.44	11.4				
9,10-AQ// ZnMn ₂ O ₄ ⁵³	N. A. (capacity based on cathode mass)	1M ZnSO ₄ + 0.05M MnSO ₄	75	71.4	94.4%, 500 cycles, 200 mAg ⁻¹
			150	59.8	
			300	47.7	
			600	38	
			1200	30.7	
2400	23.3				
PTCDI/rGO// Zn-PB ₅₄	N/P=1:3	3M ZnSO ₄	47.5	44	75%, 150 cycles, 200 mAg ⁻¹
PI-COF// Zn _x MnO ₂ ²²⁴	~1.0	2M ZnSO ₄	346.14	52.5	80%, 2000 cycles, 100 mVs ⁻¹
			676.896	46.4	
			1338.41	40.12	
			1984.54	35.6	
			2584.51	32.7	
3076.8	27.3				

Table S5.4 Performance comparison of aqueous zinc ion hybrid supercapacitors

Anode//Cathode	Cathode loading (mg cm ⁻²)	Electrolyte	Rate performance	Cycling performance	Reference
PI-1/CNT//AC	1.4	1M ZnSO ₄	91.6 F g ⁻¹ /42 mAh g ⁻¹ @ 10 Ag ⁻¹	500000 cycles, 50%, 10 Ag ⁻¹	This work
	1.44	3M ZnSO ₄	40 F g ⁻¹ @ 200 Ag ⁻¹	300000 cycles, 93%, 200 Ag ⁻¹	
Zn//AC	0.7–0.8	2M ZnSO ₄	41 mAh g ⁻¹ @ 20 Ag ⁻¹	10000 cycles, 100%, 10 Ag ⁻¹	<i>Energy Storage Mater.</i> , 2018, 13, 96 ⁹²
Zn//AC	–	2M ZnSO ₄	45 mAh g ⁻¹ @ 0.6 Ag ⁻¹	10000 cycles, 100%, 0.3 Ag ⁻¹	<i>Adv. Mater.</i> , 2018, 31, 1806005 ⁹⁵
Zn//AC	6	2M ZnSO ₄	29 mAh g ⁻¹ @ 10 Ag ⁻¹	20000 cycles, 72%, 4 Ag ⁻¹	<i>Joule</i> , 2019, 3, 1289 ¹⁵⁵
Zn//BNC	2	1M ZnSO ₄	42.8 mAh g ⁻¹ @20 Ag ⁻¹	6500 cycles, 81.3%, 5 Ag ⁻¹	<i>Nano Energy</i> , 2019, 66, 104132 ⁹⁶
MnO₂//AC	1–20	2M Zn(OTf) ₂	20 mAh g ⁻¹ @1 Ag ⁻¹	5000 cycles, 93.4%, 1 Ag ⁻¹	<i>Energy Storage Mater.</i> , 2019, 20, 335 ²⁶¹
Zn//HNPC	1–1.2	1M ZnSO ₄	108.2 mAh g ⁻¹ @ 33.3 Ag ⁻¹	100000 cycles, 73.6%, 16.7 Ag ⁻¹	<i>Adv. Mater.</i> , 2019, 31, 1904948 ⁹⁸
Zn//N-HPC	1.0	2M ZnSO ₄	66.7 mAh g ⁻¹ @ 10 Ag ⁻¹	5000 cycles, 90.9%, 1 Ag ⁻¹	<i>Nano Res.</i> 2019, 12, 2935 ⁹⁴
Zn//aMEGO	–	3M Zn(OTf) ₂	100 F g ⁻¹ @20 Ag ⁻¹	80000 cycles, 93%, 8 Ag ⁻¹	<i>Adv. Energy Mater.</i> 2019, 9, 1902915 ¹⁴⁷
Zn//Ti₃C₂T_x-Rgo	~1	2M ZnSO ₄	40.3 F g ⁻¹ @6 Ag ⁻¹	75000 cycles, 95%, 5 Ag ⁻¹	<i>Adv. Electron. Mater.</i> 2019, 5, 1900537 ¹⁵⁸
Zn//AC	–	2M ZnSO ₄	150 F g ⁻¹ @20 Ag ⁻¹	10000 cycles, 99%, 10 Ag ⁻¹	<i>Adv. Energy Mater.</i> 2020, 10, 1902981 ³¹
Zn//PSC-A600	2	1M Zn(OTf) ₂	81.8 mAh g ⁻¹ @20 Ag ⁻¹	10000 cycles, 92.2%, 10 Ag ⁻¹	<i>Energy Storage Mater.</i> 2020, 28, 307 ⁹³
Zn//HHT-rGO	1.7–3.2	1M ZnSO ₄	159 F g ⁻¹ @100 mVs ⁻¹	20000 cycles, 97.8%, 2.5 Ag ⁻¹	<i>Adv. Mater.</i> 2020, 2007843 ¹²⁷
Zn//PC800	1.4–2.0	3M Zn(ClO ₄) ₂	78.4 mAh g ⁻¹ @20 Ag ⁻¹	30000 cycles, 99.2%, 20 Ag ⁻¹	<i>Adv. Energy Mater.</i> 2020, 10, 2001705 ¹²¹
Zn//HPAC	0.6	3M Zn(OTf) ₂	119 mAh g ⁻¹ @20 Ag ⁻¹	18000 cycles, 70%, 10 Ag ⁻¹	<i>Small</i> 2020, 16, 2003174 ¹²⁸
TiS₂//AC	–	2M ZnSO ₄	24 mAh g ⁻¹ @ 2 Ag ⁻¹	5000 cycles, 92%, 2 Ag ⁻¹	<i>Adv. Electron. Mater.</i> 2020, 6, 2000388 ²⁶²
Zn//AC	0.8	2M ZnCl ₂	159.7 F g ⁻¹ @20 Ag ⁻¹	100000 cycles, 95.1 %, 5 Ag ⁻¹	<i>Angew. Chem. Int. Ed.</i> 2021, 60, 990 ¹³⁶
TT-DQ	N. A.	3M Zn(OTf) ₂	120 mAh g ⁻¹ @ 50 Ag ⁻¹	200000 cycles, 91.8%, 40 Ag ⁻¹	<i>Adv. Mater.</i> 2021, 33, 2104148 ²⁵¹
Zn//AC-SA	1.9–10.0	3M ZnSO ₄	60 mAh g ⁻¹ @ 100 Ag ⁻¹	300000 cycles, 86.9, 45 Ag ⁻¹	<i>Energy Storage Mater.</i> 2022, 46, 233 ²⁰¹

Chapter 6 Upcycling Spent Alkaline Batteries into Rechargeable Zn Metal Batteries

A version of this Chapter has been published in *Nano Energy*:

Zhixiao Xu, Nianji Zhang, Xiaolei Wang, Upcycling spent alkaline batteries into rechargeable Zn metal batteries, *Nano Energy*, 2022, 102, 107724.

6.1 Introduction

Rechargeable aqueous zinc metal batteries (ZMBs) hold great potential for grid-level energy storage because of merits of Zn metals including large theoretical capacity of 820 mAh g⁻¹, proper redox potential of -0.764 V vs. standard hydrogen electrode, good air/water stability, low cost, and environmentally-friendliness.^{6, 9, 123, 263, 264} However, rechargeable ZMBs have not been commercialized yet due to issues from both anode and cathode side.^{5, 265} On one hand, Zn metal anodes show poor reversibility because of low Coulombic efficiency (CE), uncontrollable dendritic growth, metal corrosion, and hydrogen evolution.^{218, 265-267} That is why most reports use excessive Zn to counteract side reactions and extend battery life but this in turn will substantially decrease the cell-level energy densities.²¹⁸ On the other hand, cathode materials exhibit either low voltage platform or poor cycling performance, incapacitating ZMBs for practical applications. Among various cathode materials, Mn-based oxides with high voltage have received tremendous research interest but their short cycle life due to Mn dissolution awaits further improvement.^{61, 268} Overall, achieving high depth-of-discharge (DOD) of Zn, high-loading electrodes, lean electrolyte, and low N/P ratios is essential for practical applications of ZMBs,^{89, 132, 133, 201, 269} which however is still in the early stage.

Inspired by the fact that commercial Zn batteries including alkaline batteries and Zn-air batteries use zinc powders rather than zinc foils as the anode, we turn our attention to Zn powders to solve aforementioned challenges. Aside from that, alkaline batteries and Zn-carbon batteries have dominated the primary battery market for decades and been broadly used in portable electronics,^{270, 271} e.g. toys, calculators, and thermometers, but the status of their recycling (less than <50%) of electrode materials fails to meet sustainable development.^{270, 272} Recycling alkaline battery materials can not only preserve raw materials such as Zn, Mn, and Fe but also reduce hazardous wastes towards the environment.^{273, 274} The current recycling still focuses on hydrometallurgy and pyrometallurgy in which hydrometallurgical processes generally follow different steps of pre-treatment and subsequent leaching and separation of different metals by electrolysis, extraction or precipitation.²⁷⁵⁻²⁷⁷ Another emerging approach for treating spent alkaline batteries is upcycling towards other applications such as supercapacitors,²⁷⁸ catalysis,²⁷⁹ and micronutrient fertilizer.²⁸⁰ Despite the efforts made on re/upcycling alkaline batteries, there remains an urgent need for simple, economic, environmentally benign, and energy-saving approaches.

Here, for the first time, we report a “two-birds-one-stone” strategy to not only recycle alkaline battery electrode materials but also reshape them for rechargeable ZMBs workable under high loadings, high DOD, and low N/P ratios through a simple yet efficient thermal treatment. Through thermal reduction, the spent anode was regenerated as hexagonal prism-shaped Zn microcrystals while the cathode was thermally restored as a mixture of MnOOH and MnO₂ nanoflakes. The regenerated Zn anode shows high efficiency and long life in symmetric cells even under fast rates (8 mA cm⁻²) and high DOD (50%), far surpassing that of fresh Zn powder and commercial Zn foil. On the other hand, regenerated cathode delivers enhanced capacity, rate, and lifespan compared with pristine cathode materials. Moreover, the regenerated anode and cathode was paired under reasonable N/P ratios (3.8-8.2) and

high loadings ($8\sim 10\text{ mg cm}^{-2}$) to make rechargeable ZMBs with high efficiency, high energy density (94 Wh kg^{-1}) and high power density (1349 W kg^{-1}) based on both anode and cathode, promising for practical applications.

6.2 Experimental Section

6.2.1 Regeneration of anode and cathode materials.

Primary alkaline batteries (Duracell) were randomly selected from the battery recycling bin at the University of Alberta and then dismantled carefully by hand using tools to separate anode and cathode powders. These spent powders were firstly washed by water and then dried in the oven at $80\text{ }^{\circ}\text{C}$ overnight. For the anode regeneration, the recycled zinc powder was thermally reduced in the flowing H_2 (5%)/Ar (95%) mixture gas at $950\text{ }^{\circ}\text{C}$ for 2h with a ramp rate of $10\text{ }^{\circ}\text{C min}^{-1}$ in the tubular furnace in which the Zn vapor went through ethylene glycol and recrystallized in the liquid and then the solid powder was collected after centrifugation and stored in ethanol for future use. For the cathode regeneration, the spent cathode powder was directly oxidized in the air at different temperature from 300 to $500\text{ }^{\circ}\text{C}$ for 5h.

6.2.2 Characterization

The Rigaku XRD Ultima IV X-ray diffractometer with the Cu target (wavelength: 1.5406 \AA) was used for X-ray diffraction (XRD) analysis. The morphology of samples was observed on the field-emission scanning electron microscope (Zeiss Sigma FESEM) equipped with an EDX analyzer (Oxford AZtecSynergy) as well as sphere-aberrated transmission electron microscope (TEM, JEOL JEM-ARM200CF) equipped with Atomic Resolution S/TEM. The thermal property was measured by the thermogravimetric analyzer (TGA Q50). N_2 gas adsorption-desorption isotherm was obtained on the Autosorb iQ with samples degassed at $150\text{ }^{\circ}\text{C}$ for 10 h. The surface area of Reg400 was measured as $32\text{ m}^2\text{ g}^{-1}$.

6.2.3 Electrochemical measurement

The electrochemical performance was tested using CR2032-type coin cells assembled in the open atmosphere. The regenerated anode was fabricated by directly drop-coating regenerated Zn powder/ethanol suspension onto Cu foil and dried under infrared light immediately. This direct drop-coating method was also applied to the fresh Zn powder-based cells, but as-fabricated cells can only run for several cycles due to the large-sized particles of fresh Zn powders. As such, the fresh Zn-based cells were fabricated in a different way. Fresh Zn powder (90 wt%) was mixed with PVDF binder (10 wt%) in NMP to make the slurry and coated onto Cu foils, dried under infrared light followed by pressing using the hydraulic pressor (MTI). The cathode slurry was prepared by mixing 70 wt.% of regenerated Mn-based cathode, 10 wt.% of PVDF binder, and 20 wt.% of Super P conductive carbon in NMP under stirring overnight. The slurry was then coated onto stainless steel mesh via drop coating. After being dried under vacuum overnight, the MnO₂ cathode was used as the working electrode. The areal mass loading of MnO₂ active materials was controlled at 1.2~12 mg cm⁻². Zn foil (250 μm thickness), glassy fiber membrane (Whatman Grade A), 1M ZnSO₄+0.2 M MnSO₄ or 1M Zn(OTf)₂+0.1 M MnSO₄ was adopted as the reference/counter electrode, separator, and electrolyte respectively. Galvanostatic charge-discharge tests of half cells, symmetric cells, and full cells were carried out on the Neware battery testing system (CT-4008T-5V20mA-164 or CT-4008T-5V50mA-164).

For symmetric cells, two pieces of Zn/Cu electrodes with same amount of Zn was used for the symmetric cell construction. The cells were plated and stripped at different current densities (0.5-8 mA cm⁻²) between two electrodes for certain time (30-60 min) in every cycle. For comparison, commercial Zn foils (thickness: 30 μm and 100 μm) and fresh Zn powders were also applied as anodes for symmetric cells. The electrolyte is 3 M ZnSO₄ (100 μL) for symmetric cells.

For rechargeable full cells, regenerated anode and cathode was paired with controlled N/P capacity ratios (3.8-8.2) and high loadings (5-11 mg) to make full cells and 1M Zn(OTf)₂-0.1M MnSO₄ was employed as the electrolyte. For comparison, commercial Zn foils (100 μm thick, 95 mg) were also used as anodes for full cells fabrication. The N/P capacity ratio is controlled by fixing mass of anode and cathode materials. For example, to achieve a low N/P ratio of 3.8, we first fixed high-loading cathode as 10.5 mg, the amount of Zn anode was calculated as 9.8 mg, based on the calculation of $N/P = (9.8 * 820) / (10.5 * 200) = 3.8$. The capacity of cathode is set as 200 mAh g⁻¹ due to the mixed composition of MnO₂ and MnOOH.

6.2.4 Calculation

Calculation of Gravimetric/Areal Capacity

Gravimetric capacity:

$$Q_s = \frac{1000 * I * t}{m}$$

in which I, t, and m represents discharge current (A), discharge time (h), the mass (g) of active materials in the electrode, respectively.

Areal capacity:

$$Q_s = \frac{1000 * I * t}{A}$$

in which I, t, and A represents discharge current (A), discharge time (h), the area (cm²) of active materials in the electrode, respectively. A=1.13 cm²

Calculation of Gravimetric/Areal Energy and Power Densities

The gravimetric energy density E (Wh kg⁻¹) and power density P (Wkg⁻¹) of ZMBs were calculated based on the following equations:

$$E = \frac{1000 * \int IV(t) dt}{m}$$

$$P = \frac{I * V * 1000}{m}$$

in which $V(t)$, V , I , dt , and m represents discharge voltage (V), mid-point discharge voltage, current (A), differential time (h), the mass (g) of active materials in the electrode, respectively.

6.3 Results and discussion

One spent alkaline battery (Duracell) was selected as the study object. The battery was first dismantled, and its electrode materials were separated into spent anode and cathode (Figure S6.1). According to the commonly known reaction mechanism of alkaline batteries, zinc will react with MnO_2 to form ZnO and Mn_2O_3 .²⁷⁶ To regenerate ZnO into Zn , the spent anode should go through a reduction reaction whereas the spent cathode should go through an oxidation reaction to regenerate Mn_2O_3 into MnO_2 . Accordingly, a simple annealing method was adopted here for regenerating electrode materials, i.e., reductive hydrogen atmosphere for anode regeneration and oxidative air atmosphere for cathode regeneration. As control samples, fresh electrodes were also obtained from a new alkaline battery of the same brand.

6.3.1 Anode regeneration and structural characterization

The fresh, spent and regenerated anode materials were firstly investigated by XRD and SEM. As shown in the XRD patterns (**Figure 6.1a**), the fresh anode displays strong peaks of Zn and weak peaks of ZnO which may be produced during self-discharge. By contrast, the spent anode shows strong peaks of the hexagonal ZnO (JCPDS No. 89-0510) with a space group $P63/mc$ (No. 186) and weak peaks of Zn , verifying the conversion reaction from Zn to ZnO . After regeneration, however, all XRD peaks can be ascribed to hexagonal Zn (JCPDS No. 87-0713) with a space group $P63/mmc$ (No. 194),

which suggests the successful regeneration of the anode material. It is reported that (002) crystal plane of Zn metal benefits horizontal deposition and high reversibility during metal plating/stripping, superior to (101) and (100) crystal planes.²⁸¹ Accordingly, the intensity ratio of (002) to (101) is calculated for fresh and

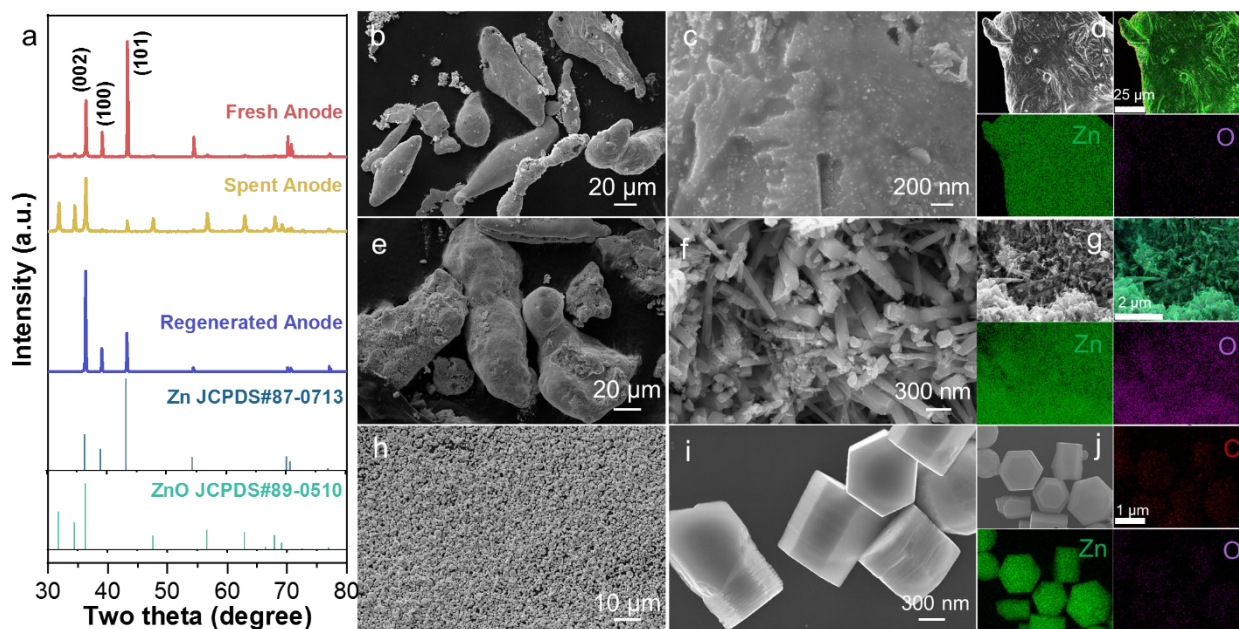


Figure 6.1 Structural characterization of anode materials. (a) XRD patterns of fresh, spent, and regenerated anode materials as well as standard cards. SEM images and EDX elemental mappings of fresh, spent, and regenerated anode materials. (b-d) fresh anode, (e-g) spent anode, and (h-j) regenerated anode.

regenerated Zn powders, in which the regenerated Zn powder affords a high value of 2.6, much higher than that of fresh Zn (0.49) and many commercial Zn foils,^{216, 282} suggesting the feasibility of using regenerated Zn powder anode for highly efficient ZMBs. The microstructures of fresh, spent, and regenerated anodes were observed by SEM and their elemental composition was mapped by energy dispersive x-ray analysis (EDX). As shown in **Figure 6.1b, c** and **Figure S6.2**, the fresh anode is composed of bulky particles with a lateral size around 10-100 μm, irregular microstructures, and

smooth surface. Zn elements dominate these particles with some surface oxygen element (**Figure 6.1d**). After use, the spent anode shows the same overall microstructure (**Figure 6.1e**) but a further look at the surface of the bulky particles reveals its change from smooth layers to aligned nanorods (**Figure 6.1f**). The change indicates the conversion from Zn layers to ZnO nanorods, which matches with XRD results and can be further confirmed by the elemental mapping images (**Figure 6.1g**). After regeneration, the anode microstructure manifests completely different morphology which is nanosheet-assembled micro-/nanoparticles with a shape of hexagonal prism or sphere in the size range of 1-3 μm (**Figure 6.1h, i**), matching well with (002) plane dominated XRD results. Typical hexagonal prisms have a base width of 600 nm and a height of 1 μm (**Figure 6.1i**). The corresponding EDX results (**Figure 6.1j** and **Figure S6.3**) show that Zn elements are major elements accompanied by some carbon and oxygen elements, implying that the regenerated Zn surface is covered with organic layer due to the use of ethylene glycol. The coating of organic layer was further confirmed by FTIR in which hydroxyl groups can be easily detected (**Figure S6.4**) as well as TEM and STEM mapping results in which carbon and oxygen elements uniformly distribute on the surface of regenerated Zn particles (**Figure S6.5-S6.6**). The hydroxyl-rich organic coating layer could provide zincophilic nucleation sites for Zn deposits.¹⁸

6.3.2 Cathode regeneration and structural characterization

Besides the anode materials, the fresh, spent and regenerated cathode materials were also characterized by XRD and SEM. The fresh cathode shows XRD peaks that belong to orthorhombic MnO_2 (JCPDS card no. 73-1539) and orthorhombic MnOOH (JCPDS card no. 74-1842), the latter of which may be generated during self-discharge (**Figure 6.2a**). Unexpectedly, these XRD peaks are

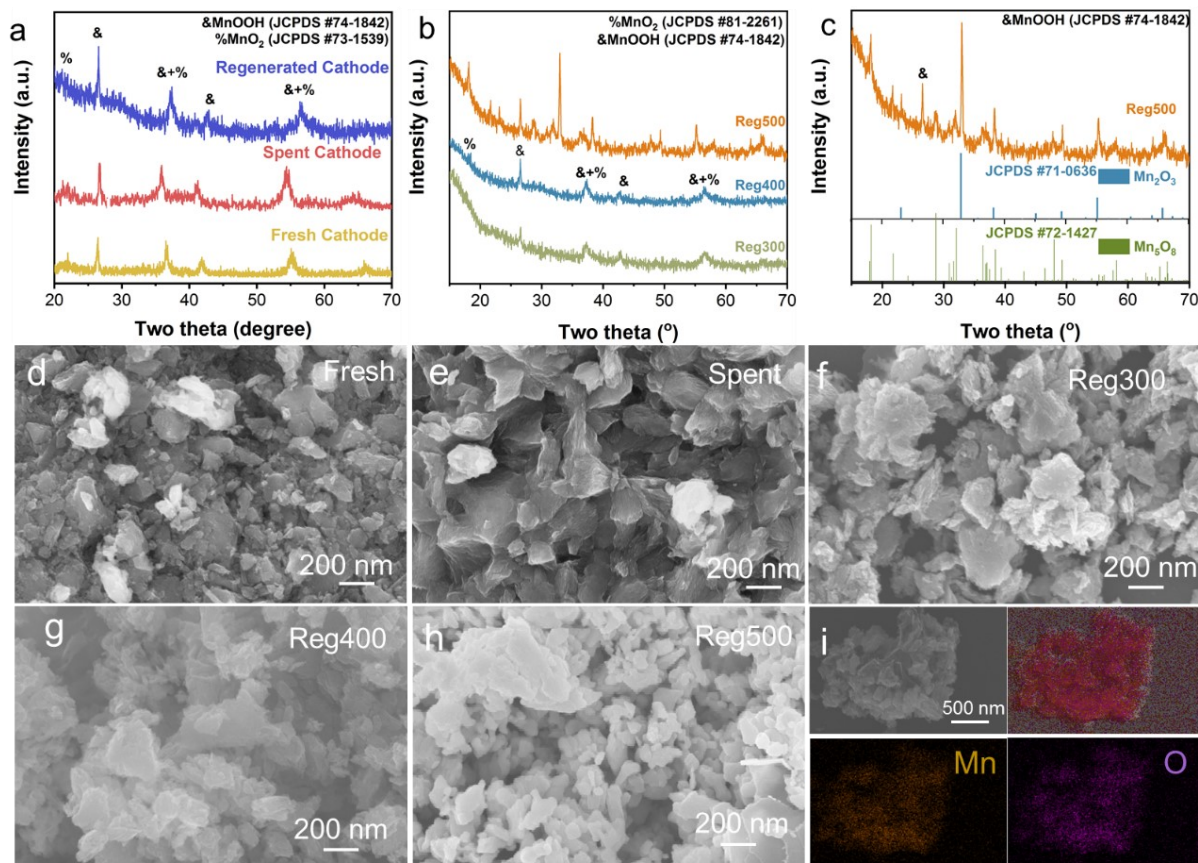


Figure 6.2 Cathode Regeneration and Structural Characterization. XRD patterns of (a) fresh, spent, and regenerated cathodes, and (b, c) regenerated cathode materials at different temperature and standard JCPDS cards. SEM images of (d) fresh cathode, (e) spent cathode, (f) Reg400, (g) Reg300, and (h) Reg500. (i) EDX elemental mappings of Reg400.

still dominant in the spent cathode except those MnO_2 peaks shift to lower angles, suggesting the increase of the interlayer distance, due probably to the ion insertion into MnO_2 after discharge. No peaks assignable to Mn_2O_3 can be detected in the spent cathode, falsifying the commonly believed reaction mechanism of the primary alkaline battery. Based on above results, rather than forming Mn_2O_3 and ZnO , we propose that MnO_2 will react with Zn to produce MnOOH and ZnO accompanied by some ion insertion into the MnO_2 . Cathode regeneration was carried out at different temperatures (300, 400, and 500 °C) in the air atmosphere and the corresponding samples were denoted as Reg300,

Reg400, and Reg500, respectively. After regeneration at low temperatures (Reg300 and Reg400), peaks belonging to MnO_2 shift back to higher angles in comparison to spent cathode, indicating the restoration of MnO_2 *via* contraction of the layered structure and the removal of inserted ions. Compared with Reg400, Reg300 shows lower degree of crystallization (**Figure 6.2b**) while Reg500 is composed of a mixture of MnOOH (Mn^{3+}), Mn_2O_3 (Mn^{3+}), and Mn_5O_8 ($\text{Mn}^{3.2+}$), suggesting a more oxidized process at a higher temperature (**Figure 6.2c**). SEM images show that the fresh cathode is composed of bulky particles assembled by irregular nanoparticles (**Figure 6.2d**) while the spent cathode shows more aggregated structure in which particles are interconnected (**Figure 6.2e** and **Figure S6.7**). By contrast, the regenerated cathodes (Reg300 and Reg400) exhibit nanoflake-shaped structure with a lateral size around 200-300 nm (**Figure 6.2f, g**). A higher temperature at 500 °C transforms assembled particles into discrete nanosheets with smaller sizes of 100-200 nm in Reg500 (**Figure 6.2h**). EDX mapping shows the uniform distribution of Mn and O in the Reg400 (**Figure 6.2i**). Thermal gravimetric analysis (**Figure S6.8**) shows that there are three main thermal events when heating the regenerated sample from room temperature to 900 °C in the air atmosphere, in the range of 170-200 °C, 500-600 °C, and 800-900 °C, corresponding to the MnO_2 formation, Mn_2O_3 and Mn_5O_8 formation, as well as Mn_3O_4 formation, respectively.^{283, 284} Overall, above results indicate the feasibility of our simple thermal reduction/oxidation approach toward the restoration and reshaping of spent anode and cathode materials in alkaline batteries.

6.3.3 Electrochemical performance and deposition morphology of regenerated anode

Next, the electrochemical performance of the regenerated anode was evaluated in symmetric cells. Zn/Cu electrodes were prepared by drop coating the regenerated Zn powder/ethanol suspension onto the commercial Cu foil followed by drying without binder. Two pieces of Zn/Cu electrodes were

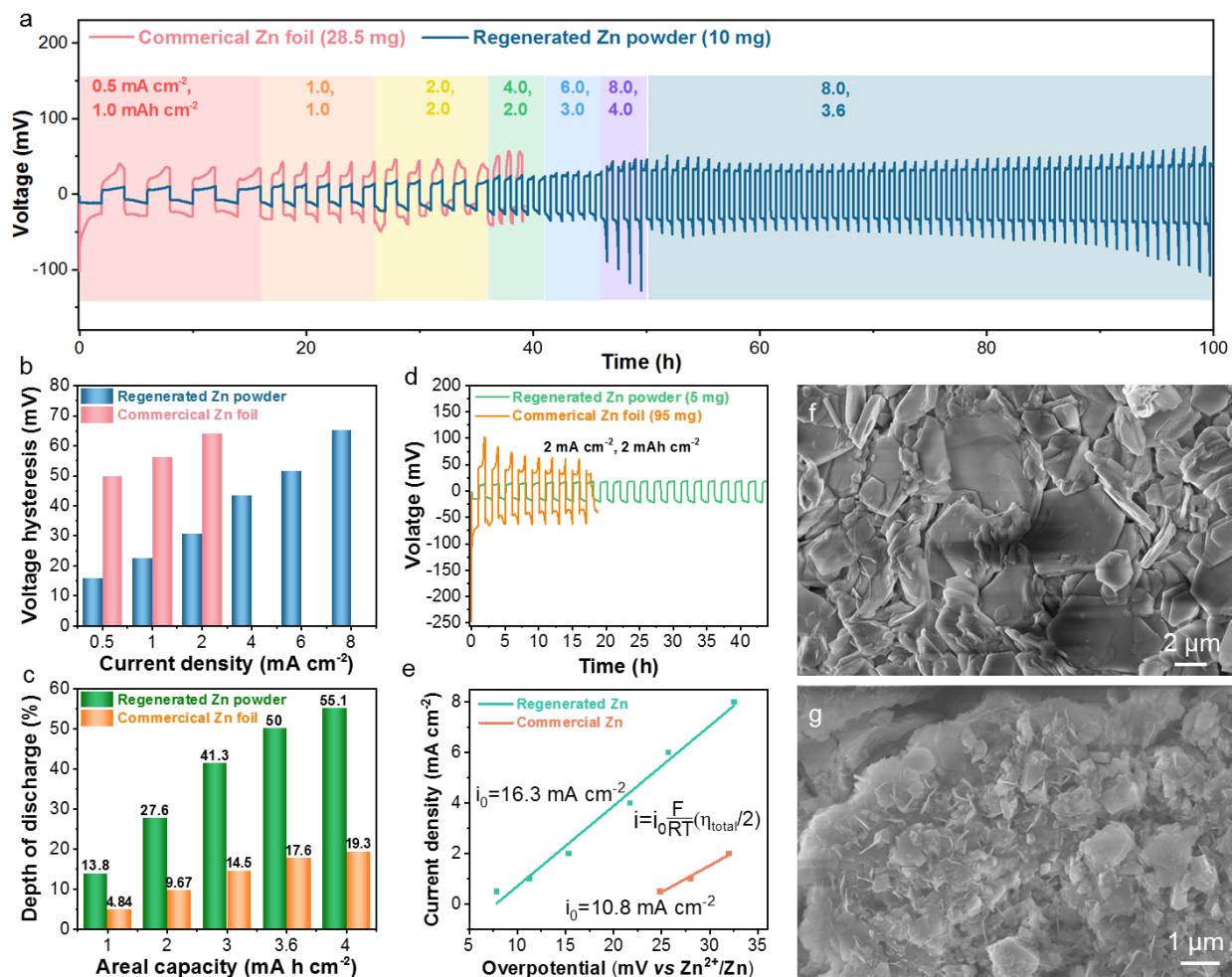


Figure 6.3 Electrochemical performance of regenerated Zn and commercial Zn anodes. (a) symmetric cells based on regenerated Zn powder (10 mg) and commercial Zn foils (28.5 mg) tested at different current rates and capacity, corresponding (b) voltage hysteresis, and (c) depth of discharge values. (d) Symmetric cells based on regenerated Zn powder (5 mg) and commercial Zn foils (95 mg) tested at 2 mA cm⁻² and 2 mAh cm⁻². (e) the plot of current density against overpotential. SEM images of after-cycle electrodes in symmetric cells: (f) regenerated Zn (after 100 h), and (g) commercial Zn (after 39 h).

assembled into symmetric cells and tested under different current densities and capacities. For comparison, the symmetric cells based on fresh Zn powder and commercial Zn foils were also tested under the same condition. **Figure 6.3a** shows the voltage profiles of the commercial Zn- and

regenerated Zn-based cells at different combinations of current densities and capacities including 0.5 mA cm⁻², 1.0 mA h cm⁻²; 1.0 mA cm⁻², 1.0 mA h cm⁻²; 2.0 mA cm⁻², 2.0 mA h cm⁻²; 4.0 mA cm⁻², 2.0 mA h cm⁻²; 6.0 mA cm⁻², 3.0 mA h cm⁻²; 8.0 mA cm⁻², 4.0 mA h cm⁻²; and 8.0 mA cm⁻², 3.6 mA h cm⁻². The regenerated Zn cell shows a superzincophilic feature with no nucleation overpotential in the first cycle, in stark contrast to a large overpotential of 75.3 mV in the commercial Zn cell (**Figure S6.9**). The superzincophilicity of regenerated Zn should be due to the coating of hydroxyl-rich organic layer on the hexagonal prism microstructure with exposed and oriented crystal planes. In following cycles with higher current rates and capacities, regenerated Zn cell keeps much lower voltage hysteresis values than those of commercial Zn cell (**Figure 6.3b**). Of note, due to the use of limited Zn (10 mg), the regenerated Zn electrode achieves a very high DOD of 13.8%, 27.6%, 41.3%, 50%, and 55.1% at the areal capacity of 1.0, 2.0, 3.0, 3.6, and 4.0 mAh cm⁻², respectively, much higher than that of the commercial one (**Figure 6.3c**). While the commercial Zn-based cell fails to work at 2.0 mA cm⁻² and 2.0 mAh cm⁻² after only ~30 h due to dendrites growth, the regenerated Zn cell can work well at higher rate of 8.0 mA cm⁻² and higher capacity of 3.6 mAh cm⁻² with longer lifespan of 100 h. At a DOD of 50%, the regenerated Zn cell can still run for more than 50 h. To the best of knowledge, this is hitherto one of the highest DOD values, much higher than previously reported values (**Table S6.1**).^{184, 186, 187, 215, 266} To further demonstrate the superiority of the regenerated Zn over commercial Zn, thicker Zn foils (100 μm, 95 mg) and less amount of regenerated Zn powder (5 mg) were employed for the symmetric cells working at 2.0 mA cm⁻² and 2.0 mAh cm⁻². The regenerated Zn- and the commercial Zn-based cell shows the first-cycle nucleation overpotential of 0 and 181.3 mV, respectively (**Figure S6.10**). Large voltage hysteresis of ~67.5 mV and short life of ~17 h is detected in the commercial Zn cell. By stark contrast, the regenerated Zn cell maintains a low voltage hysteresis of only ~36 mV for more than 40 h (**Figure 6.3d**). Besides commercial Zn

cells, the regenerated Zn cells are also better than the fresh Zn powder-based cells which can only work for less than 40 h at a relatively low DOD of 9.6%, a low rate of 0.5 mA cm^{-2} and a low capacity of 0.5 mAh cm^{-2} (**Figure S6.11**). Above results demonstrate the superiority of the regenerated Zn powder over commercial Zn foils and fresh Zn powder. To comprehend this superiority, the kinetics of Zn deposition was evaluated based on the exchange current density related to the Zn plating/stripping in Figure 3a. As shown in the **Figure 6.3e**, regenerated Zn electrode showcases an exchange current density of 16.3 mA cm^{-2} , larger than that of commercial Zn with a value of 10.8 mA cm^{-2} , indicating a faster deposition kinetics of the regenerated Zn.²⁰⁷ To further comprehend the superiority of regenerated Zn, after-cycle morphologies of the deposited Zn in different cells were captured via SEM. Densely packed and horizontally oriented hexagonal Zn plates can be observed in the regenerated Zn cell (**Figure 6.3f** and **Figure S6.12**) whereas the commercial Zn and fresh Zn cells both show flake-like dendrites (**Figure 6.3g** and **Figure S6.13-S6.14**). It is believed that the regenerated Zn powders covered with hydroxyl-rich organic layer enables superb zincophilic surface, the shape of hexagonal prism constructed by nanosheets offers abundant nucleation sites, and the geometric structure confines the plating of Zn along certain direction towards dense and horizontal layers.³¹ These results demonstrate that fast-rate, highly reversible, and deeply discharged Zn metal electrodes can be achieved *via* the regenerated and nanoengineered Zn powders, promising for full cell construction.

6.3.4 Electrochemical performance of regenerated cathode materials

Aside from the regenerated anode, the regenerated cathode was also evaluated in half cells for ZMBs with excessive Zn as the anode. For comparison, fresh cathode materials were also extracted from a new alkaline battery followed by thermal treatment. **Figure 6.4a** and **Figure S6.15** shows capacities

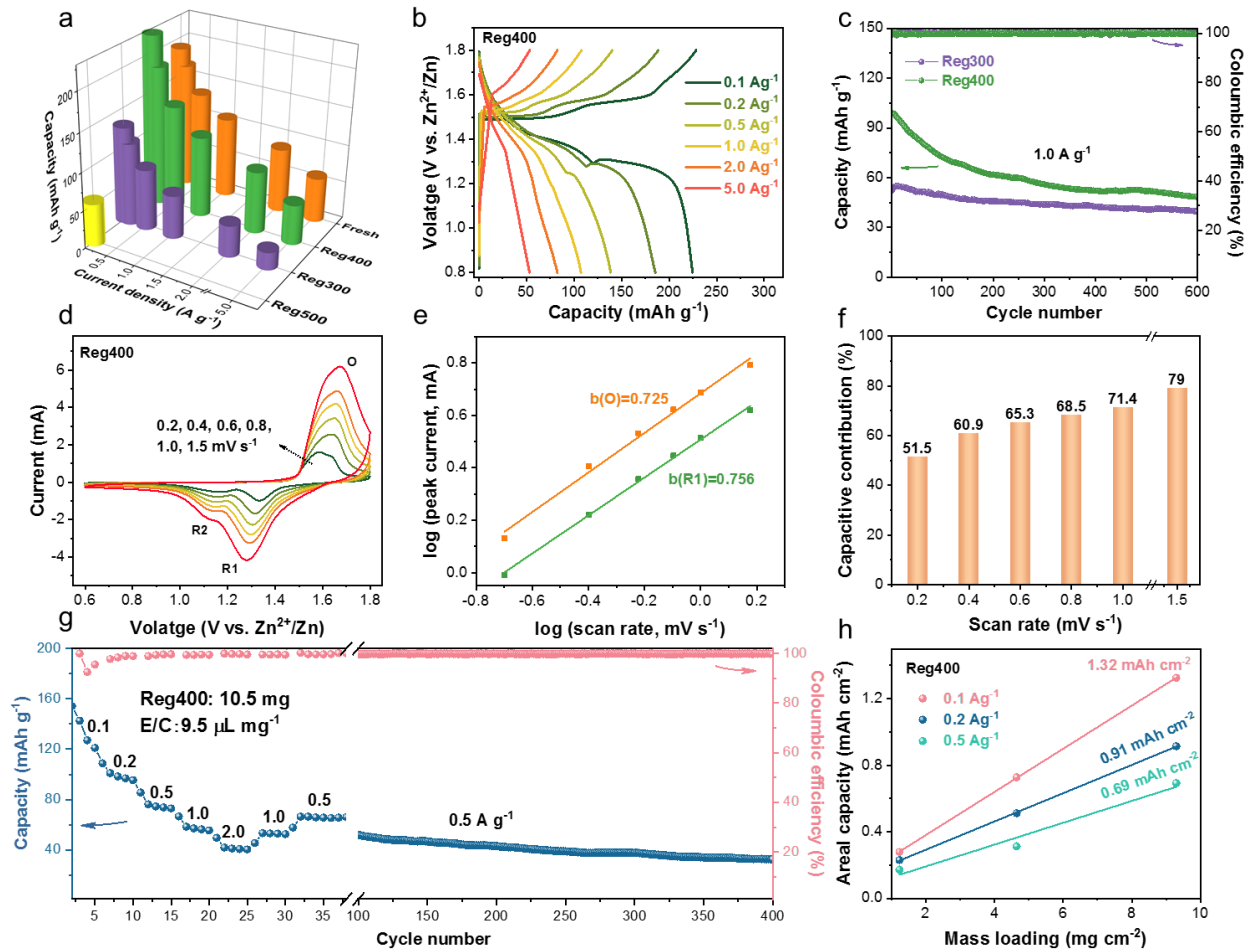


Figure 6.4 Electrochemical performance of regenerated cathodes. (a) 3D profiles of current densities-capacity-samples. (b) Charge-discharge profiles of Reg400. (c) Cycling performance of Reg400 and Reg300, and (d) CV profiles of Reg400 at diverse scan rates and derived (e) linear fitting of $\log(\text{current})$ against $\log(\text{scan rate})$ at redox peaks. (f) Capacitive contributions at different scan rates. (g) rate and cycling performance of Reg400 electrode under high loading and lean electrolyte. (h) Profiles of areal capacity against mass loading.

of Reg300, Reg400, Reg500, Fresh, and Fresh400 cathodes at different current rates. At a low rate of 0.1 A g^{-1} , the Reg300, Reg400, Reg500, Fresh, and Fresh400 cathode shows a capacity of 130, 225, 52, 120, and 188 mAh g^{-1} , separately. At higher rates of 0.2, 0.5, 1.0, 2.0, and 5.0 A g^{-1} , Reg400 delivers the capacity of 186, 139, 107, 83, and 53 mAh g^{-1} , respectively, much higher than those of

Reg300 and Reg500. Apparently, Reg400 shows best performance among regenerated cathode materials. Interestingly, capacities of Reg400 are also higher than those of fresh cathode at rates from 0.1 A g^{-1} to 1.0 A g^{-1} , suggesting the efficacy of thermal regeneration approach and holding potential for application. Charge-discharge curves of all samples present two discharge platforms (one at $\sim 1.4 \text{ V}$ and another at $\sim 1.27 \text{ V}$) at low rates indicating the co-storage of proton and zinc ions but only one platform at high rates due probably to proton storage given that the insertion of proton with small radius is much easier than that of zinc ions (**Figure 6.4b** and **Figure S6.16**). Reg400 can cycle at 0.1 A g^{-1} for 140 cycles with 100% capacity retention and at 1 A g^{-1} for 600 cycles with 50% capacity retention as well as $\sim 100\%$ CE values, suggesting good stability (**Figure S6.17** and **Figure 6.4c**).

The kinetic analysis of the Reg400 electrode was conducted by the cyclic voltammogram (CV) technique scanned at different rates. As shown in **Figure 6.4d**, there seems to be two couples of redox peaks at the low rate of 0.2 mV s^{-1} , placed at $1.62 \text{ V}/1.33 \text{ V}$ and $1.58 \text{ V}/1.15 \text{ V}$, named as O1/R1 and O2/R2 peaks, separately. However, with the increase of scan rates, O1 and O2 combines with each other and can hardly be distinguished so they are simplified as O peak. As scan rates increase, R1/R2 peak shifts negatively and O peak shifts positively but the voltage gap between O and R1/R2 remains low, suggesting a high reversibility and fast kinetics. Derived from the $i = av^b$ equation,^{148, 149} b values at different peaks can be obtained in which the $b=0.5$ indicates a diffusion-dominated process while $b=1.0$ suggests a capacitive-controlled reaction. The b value for the O and R1 peak was calculated to be 0.725 and 0.756, meaning that both diffusion and capacitive processes take part in the reaction (**Figure 6.4e**). These two processes were quantitatively clarified through the Dunn approach.^{148, 149} As the scan rate increases from 0.2 mV s^{-1} , to 0.4, 0.6, 0.8, 1.0, and 1.5 mV s^{-1} , the capacitive contribution raises from 51.5 to 60.9, 65.3, 68.5, 71.4, and 79% (**Figure 6.4f**). The results indicate rapid surface Faradic reactions contribute to the fast kinetics, which further suggests that proton

storage dominates at high rates according to discharge profiles. Based on above results, the charge storage mechanism of the cathode is believed to follow proton/ Zn^{2+} insertion/extraction. For practical power cells, high-loading electrodes are essential to increase cell-level energy densities and here we study three different levels of mass loading, including low-, medium-, and high-loadings (1.2 , 4.6 , and 9.3 mg cm^{-2}) for research and practical purposes.^{151, 201, 244} The electrolyte is fixed as $100 \mu\text{L}$ so the electrolyte-to-cathode (E/C) ratio drops as the loading mass rises. At 0.1 A g^{-1} , the 4.6 mg cm^{-2} electrode with a E/C ratio of 19.2 mL g^{-1} and the 9.3 mg cm^{-2} electrode with a E/C ratio of 9.5 mL g^{-1} retain 71% and 63% of capacity delivered by the 1.2 mg cm^{-2} electrode, respectively (**Figure 6.4g** and **Figure S6.18**). The high-loading electrode shows capacities of 142.6, 98.4, 74.6, 57.1, and 41.1 mAh g^{-1} at the rate of 0.1, 0.2, 0.5, 1.0, and 2.0 A g^{-1} , respectively. Under the harsh condition of lean electrolyte and high loading, the Reg400 cathode still manifests long cycle life with $\sim 50\%$ capacity retention and $\sim 100\%$ CE after 400 cycles at 0.5 A g^{-1} (**Figure 6.4g**). Profiles of areal capacity against mass loadings at different rates were plotted as **Figure 6.4h**, which displays linearly increased areal capacity with the elevation of mass loading until 9.3 mg cm^{-2} at rates from 0.1 to 0.5 A g^{-1} , meaning the limitation has not yet been reached in the loading mass at these rates. The highest areal capacity of 1.32 mAh cm^{-2} can be obtained by the 9.3 mg cm^{-2} electrode at 0.93 mA cm^{-2} . This electrode can also deliver high areal capacities of 0.91, 0.69, 0.53, and 0.38 mAh cm^{-2} at the rate of 1.86, 4.65, 9.29, and 18.6 mA cm^{-2} , respectively (**Figure S6.19**). Overall, high-loading Reg400 electrodes manifest high-rate capability and good stability, promising for practical application.

6.3.5 Regenerated anode and cathode for full cells

Encouraged by the good electrochemical performance of regenerated anode and cathode materials, we further assembled full cells based on regenerated electrodes under practical conditions including

high loadings and low N/P ratios. For comparison, commercial Zn foils were also used as anodes for the full cell construction with the same amount of cathode. **Figure 6.5a** compares the CV profiles of regenerated Zn and commercial Zn-based cell at a scan rate of 0.2 mV s^{-1} . Compared with commercial Zn cell, regenerated Zn cell has a more negative O peak (1.556V) and a more positive R1 peak (1.338 V) and the voltage gap between two peaks is 218 mV, which is smaller than that of commercial Zn cell (254 mV). This suggests the regenerated Zn anode enables a higher reversibility than the commercial Zn foil. This better reversibility of regenerated Zn cell is further demonstrated at all higher scan rates (**Figure 6.5b**) with smaller voltage gaps than those of commercial Zn cell (**Figure 6.5c**). Besides higher reversibility with smaller voltage gaps, the regenerated Zn cells also achieve higher capacities than commercial Zn cells at all current rates, as demonstrated in one cell with a cathode loading of 5.4 mg cm^{-2} and a N/P ratio of 8.2 (**Figure S6.20**) and another cell with a cathode loading of 9.3 mg cm^{-2} and a N/P ratio of 3.8 (**Figure 6.5d** and **Figure S6.21**), despite that commercial Zn cells are fabricated with higher N/P ratios (74 and 37). Take the latter cell with a N/P ratio of 3.8 as an example, the areal capacity can reach 1.40, 1.00, 0.82, 0.68, and 0.55 mAh cm^{-2} at the rate of 0.93, 1.86, 4.65, 9.29, and 18.6 mA cm^{-2} , higher than those of the commercial cell as mentioned earlier. Under the harsh condition of 9.3 mg cm^{-2} cathode loading, a N/P ratio of 3.8, and lean electrolyte of $4.93 \text{ } \mu\text{L}$ per milligram of anode and cathode, the regenerated Zn cell can run for more than 50 cycles at 4.65 mA cm^{-2} (**Figure S6.21f**). Based on the total mass of active anode and cathode, this regenerated cell still enables a high capacity of 77.0, 55.7, 45.6, 37.8, and 30.4 mAh g^{-1} at the rate of 51.7, 103, 259, 517, and 1034 mA g^{-1} , respectively (**Figure 6.5e**). The corresponding energy densities can be calculated as 94.0, 72.7, 59.4, 48.5, and 38.0 Wh kg^{-1} at power densities of 63.4, 139, 350, 692, and 1349 W kg^{-1} , surpassing most of previously reported ZMBs such as Zn//MnO₂,^{187, 203, 211} Zn//MnVO,¹⁸⁴ h-MoO₃//Zn_xMnO₂,⁴³ Cu_{2-x}Se//Zn_xMnO₂,²²⁰ AQ//ZnMn₂O₄,⁵³

and PI-1/CNT//Zn_xMnO₂²⁸⁵ (Table S6.2). Furthermore, cycled cells were disassembled and electrodes were extracted to study the failure mechanism. After cycling, commercial Zn shows a larger amount of dendrites (zinc sulfate hydroxide) than regenerated Zn (Figure S6.22), showing the superiority of regenerated Zn anode. On the other hand, the cathode transformed to small nanoparticles after cycling, indicating a reconstruction process during interaction with zinc ions and proton, which should be responsible for the capacity decay (Figure S6.23).

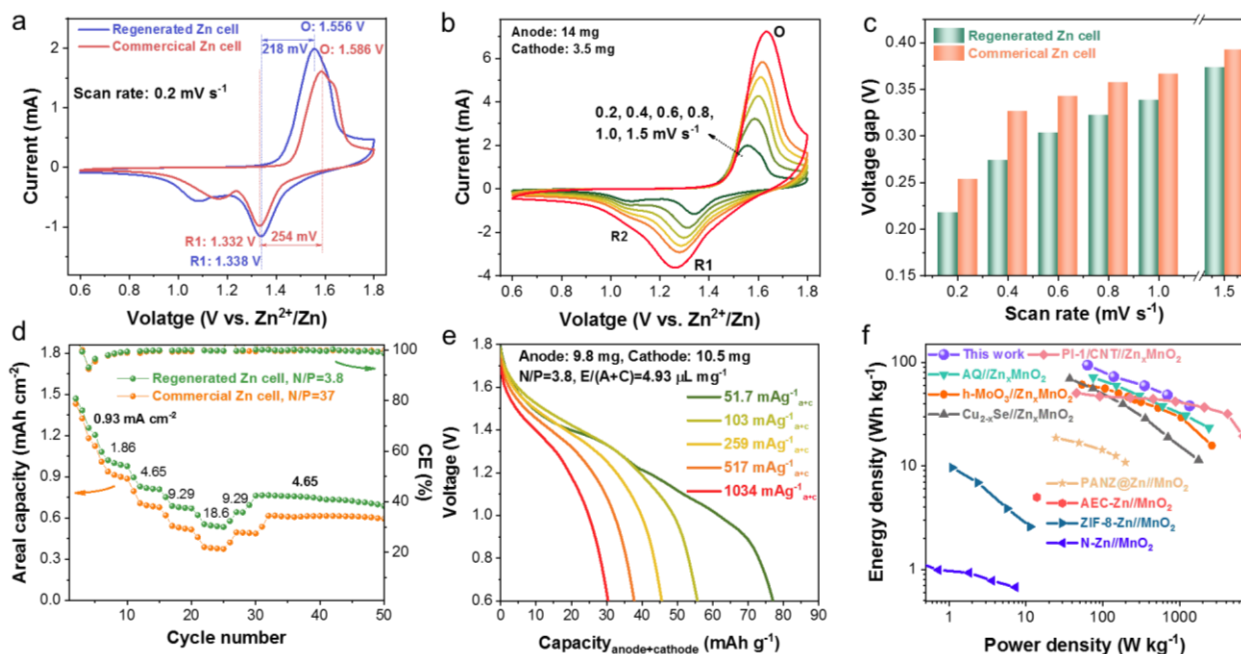


Figure 6.5 Full cells based on regenerated anodes and cathodes. (a) CV curves of regenerated Zn cell and commercial Zn cell at a scan rate of 0.2 mV s⁻¹. (b) CV profiles of regenerated electrodes-based cell at different rates from 0.2 to 1.5 mV s⁻¹. (c) Voltage gaps between O and R1 peaks in two cells at different rates. (d) Rate performance of regenerated and commercial cells with high-loading cathodes and different N/P ratios. (e) Discharge profiles of regenerated Zn cell based on total mass of regenerated anode and cathode materials. (f) Ragone plots of our regenerated Zn cell and previously reported ZMBs and ZIBs.

6.4 Summary

In conclusion, for the first time, spent alkaline battery electrodes have been successfully recycled and reshaped for rechargeable zinc metal batteries with application potentials through a simple yet efficient thermal treatment. Regenerated Zn anode with zincophilic hydroxyl layers and hexagonal prism shapes manifest near-zero nucleation overpotential and high reversibility even at fast rates and deep discharge surpassing commercial Zn foils while the regenerated cathode containing MnO₂ and MnOOH shows higher capacity than pristine ones. The pairing of two electrodes enables high energy and power densities (94 Wh kg⁻¹, 1349 W kg⁻¹) at the cell level even under harsh conditions including high loadings of ~9.3 mg cm⁻², a low N/P ratio of 3.8, and lean electrolyte of 4.93 μL mg⁻¹_{anode+cathode}. The study about the solvent effect on Zn powder regeneration and about the electrolyte engineering on full cell performance are under investigation in the lab. This “two birds one stone” strategy is of great significance towards the sustainable development and clean energy deployment and opens a new chapter towards battery recycling and upcycling.

6.5 Supporting Information

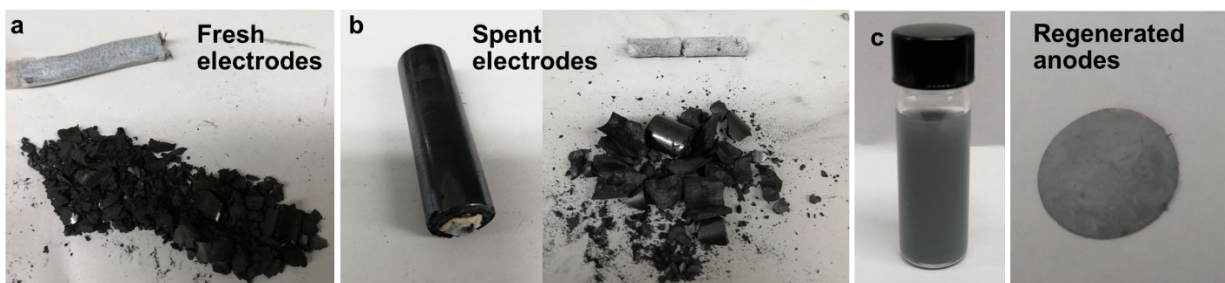


Figure S6.1 Digital photos of fresh, spent, and regenerated electrode materials. (a) fresh electrodes, (b) spent electrodes, (c) regenerated Zn powder in ethanol and coated on Cu foil.

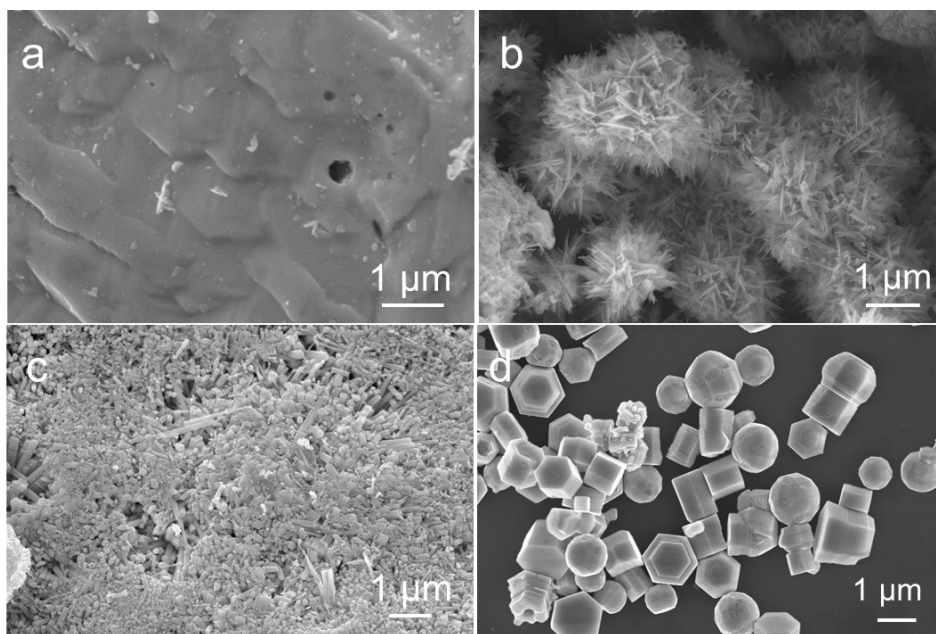


Figure S6.2 SEM images of (a, b) fresh anode, (c) spent anode, and (d) regenerated anode. (b) shows the side product of fresh Zn anode due to the formation of ZnO during self-discharge.

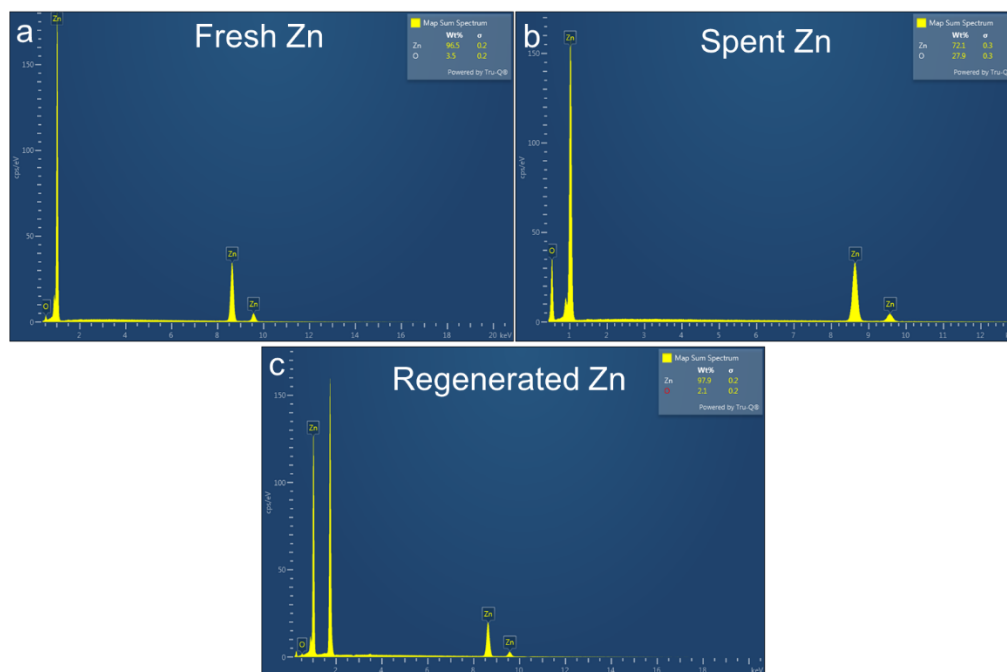


Figure S6.3 EDX point analysis of fresh, spent, and regenerated anode materials. The result shows the amount of O element follows the order: Regenerated Zn < Fresh Zn < Spent Zn, matching well with elemental mapping results. Of note the Si signal in regenerated Zn is from Si wafer.

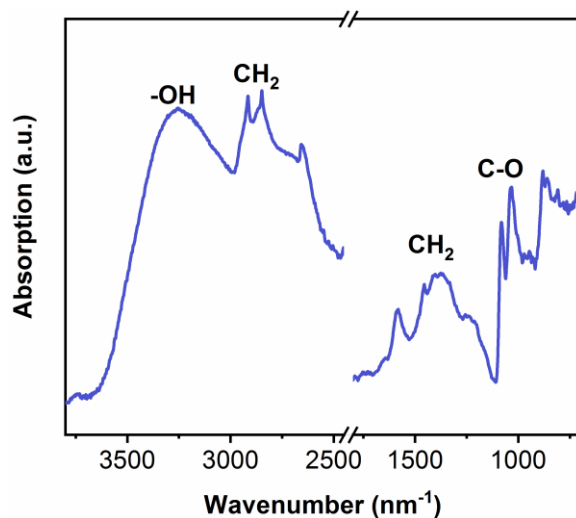


Figure S6.4 ATR-FTIR spectrum of regenerated Zn powder. Characteristic peaks belonging to ethylene glycol could be detected, indicating the adsorption of hydroxyl-rich organic layer on the surface of regenerated Zn.

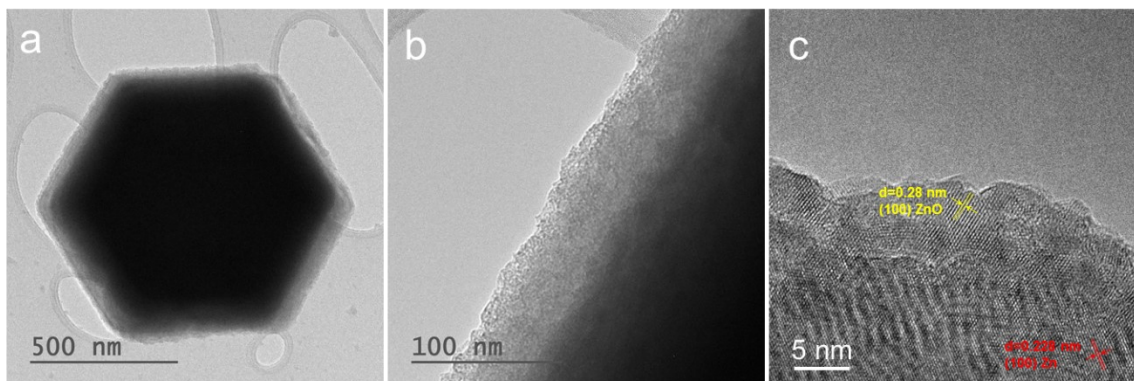


Figure S6.5 TEM images of regenerated Zn powder. (a-b) TEM images and (c) HRTEM image. Lattice fringes of 0.228 nm and 0.28 nm can be detected at the side of the hexagonal prism which can be ascribed to the (100) crystal planes of Zn and ZnO, respectively. The HRTEM image confirms the side of the hexagonal prism belongs to the (100) crystal plane of Zn and the unavoidable surface oxidation of Zn due to exposure to the air atmosphere.

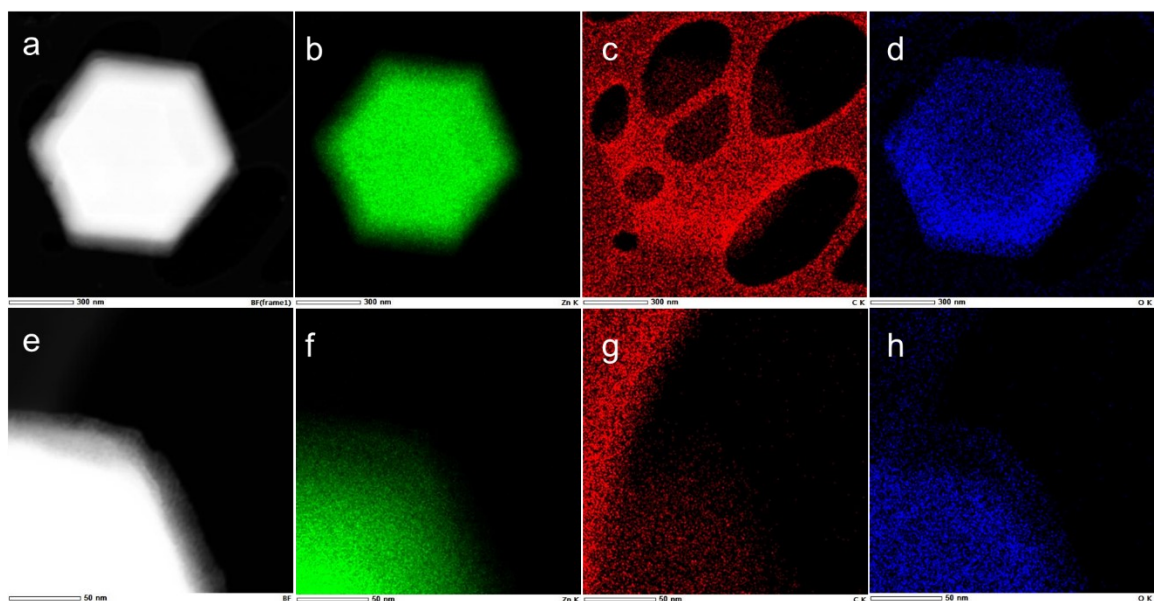


Figure S6.6 STEM elemental mapping of regenerated Zn. (a, e) STEM image and corresponding mapping of (b, f) Zn, (c, g) C, and (d, h) O elements. The uniform distribution of carbon and oxygen elements on regenerated Zn confirms the coating of hydroxyl-rich organic layer.

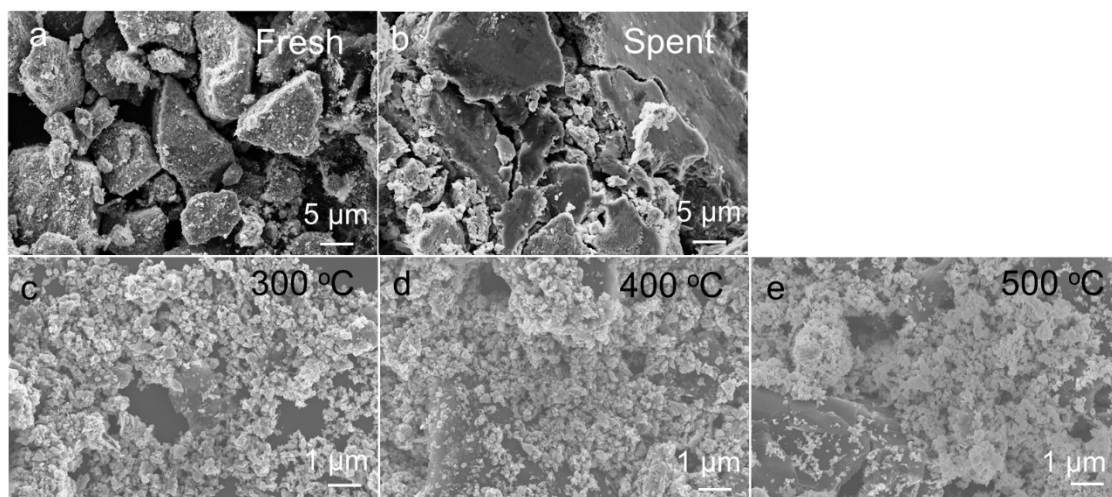


Figure S6.7 SEM images of (a) fresh, (b) spent, and (c-e) regenerated cathode materials, (c) Reg300, (d) Reg400, and (e) Reg500.

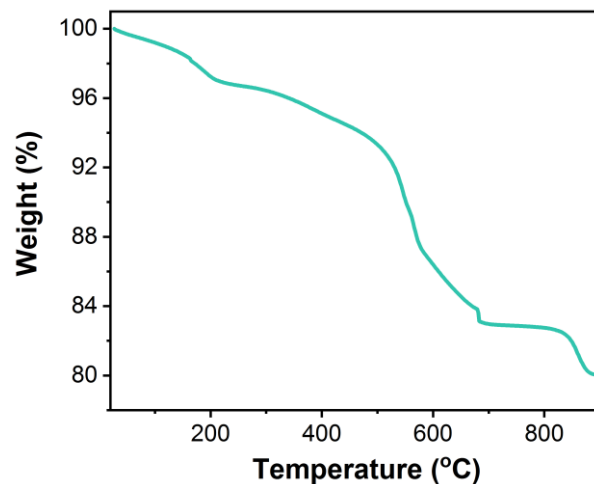


Figure S6.8 TGA curve of the regenerated cathode materials (Reg400).

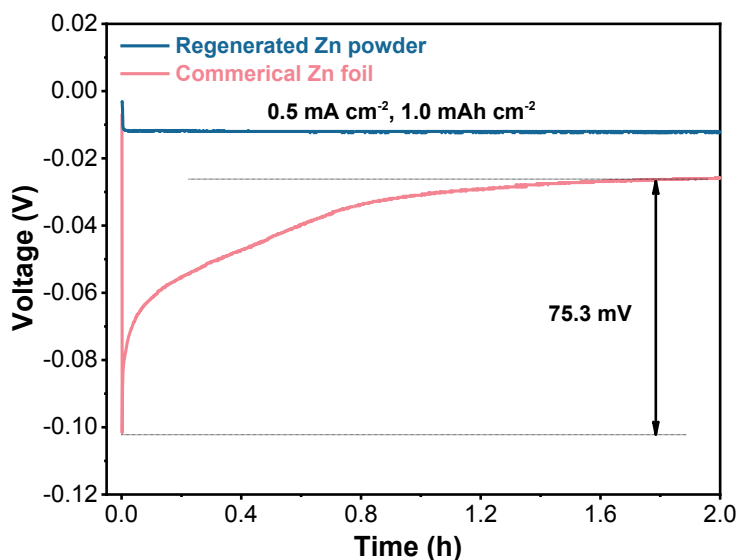


Figure S6.9 The first cycle of the symmetric cells in Figure 6.3a showing the zero nucleation overpotential of the regenerated Zn cell and high overpotential of commercial Zn cell with a value of 75.3 mV. The zero nucleation overpotential indicates the superzincophilic feature of the regenerated Zn powder.

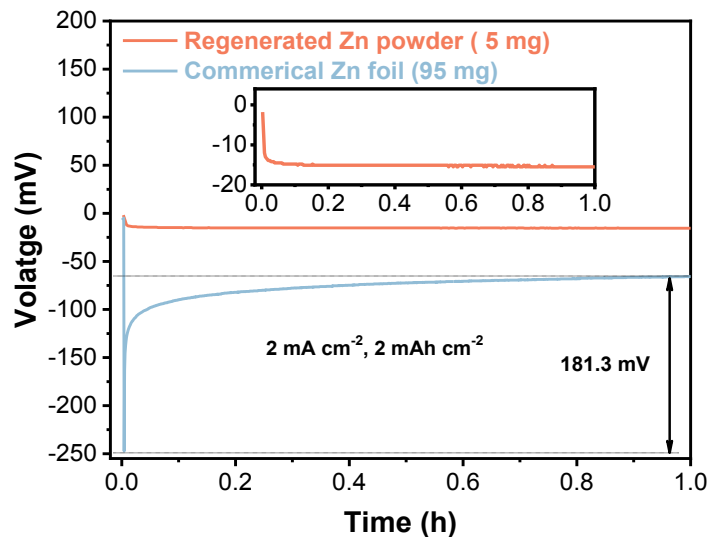


Figure S6.10 The first cycle of the symmetric cells in Figure 6.3d showing the zero nucleation overpotential of the regenerated Zn cell and high overpotential of commercial Zn cell with a value of 181.3 mV. The zero nucleation overpotential indicates the superzincophilic feature of the regenerated Zn powder.

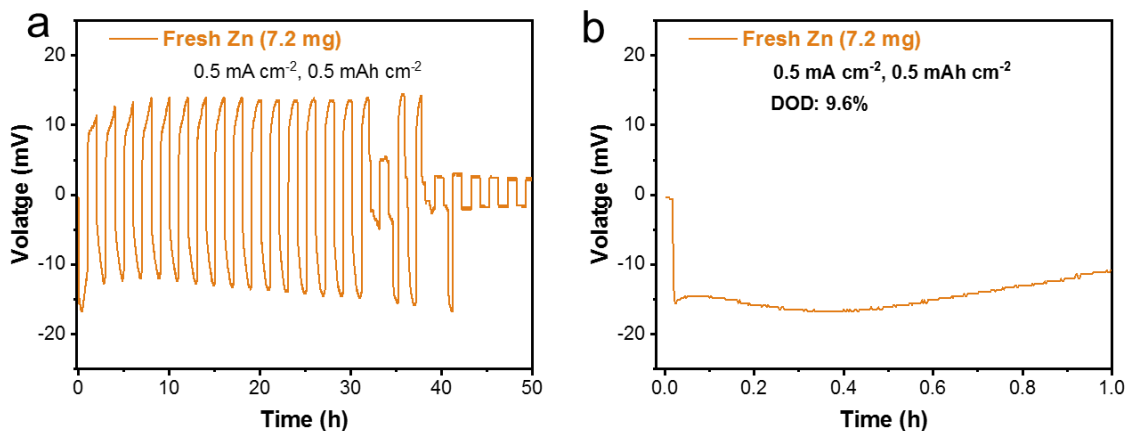


Figure S6.11 Symmetric cells based on fresh Zn powders (7.2 mg). (a) Voltage-time curves in 50 h and (b) first cycle profile. The DOD of the fresh Zn anode is 9.6%.

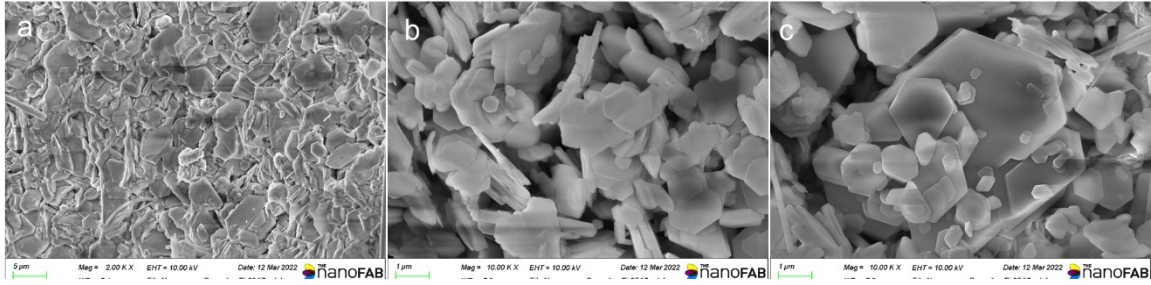


Figure S6.12 SEM images of the regenerated Zn anode after symmetric-cell tests (100h) in Figure 6.3a.

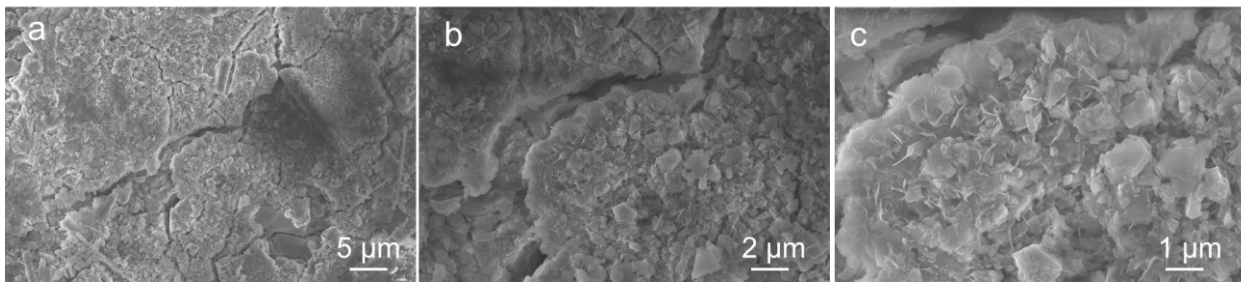


Figure S6.13 SEM images of the commercial Zn anode after symmetric-cell tests (~40h) in Figure 6.3a.

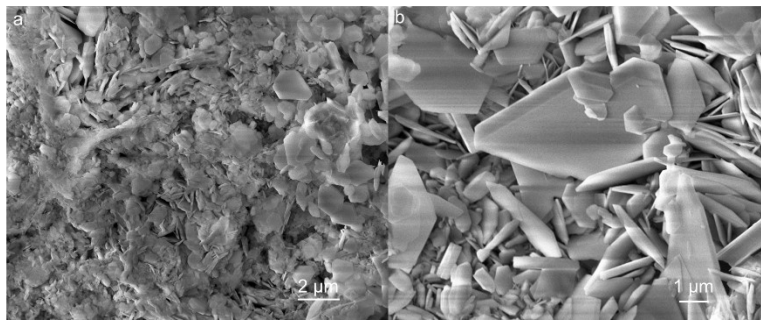


Figure S6.14 SEM images of the fresh Zn anode after being plated with 1.0 mAh cm^{-2} of Zn after several cycles.

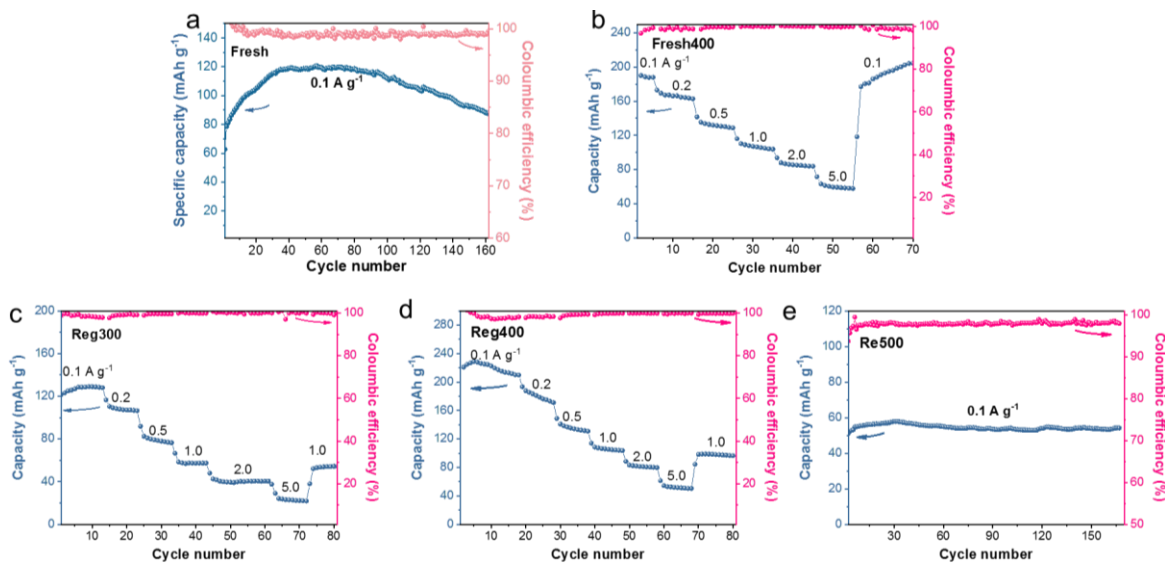


Figure S6.15 Rate performance of fresh and regenerated cathodes. (a) Fresh, (b) Fresh400, (c) Reg300, (d) Reg400, and (e) Reg500.

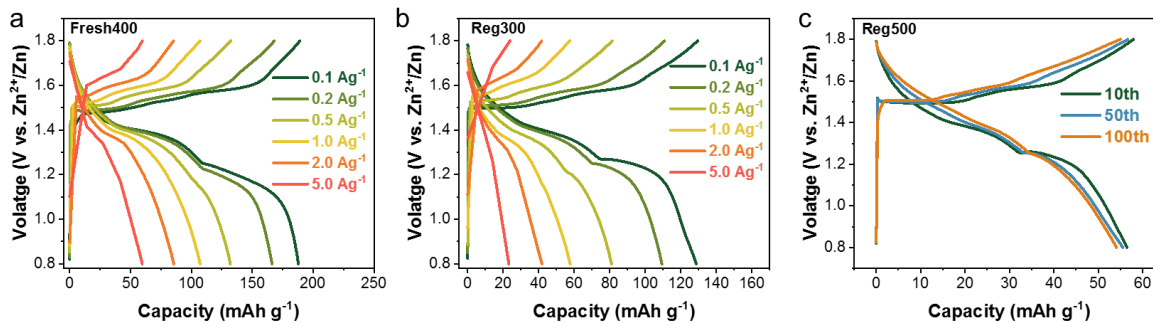


Figure S6.16 Charge-discharge curves of (a) Fresh400 cathode, (b) Reg300, and (c) Reg500.

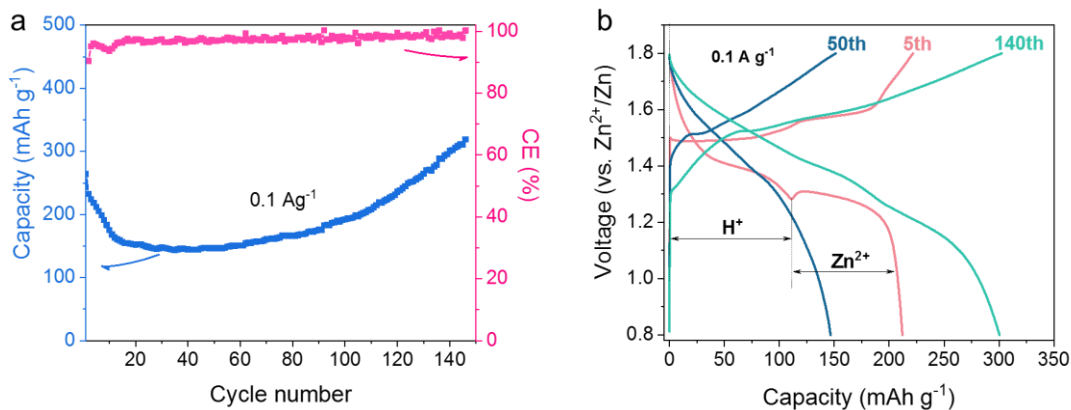


Figure S6.17 Cycling performance of Reg400. (a) Cycling profile at 0.1 Ag^{-1} , (b) Charge/discharge curves at different cycle showing change in the discharge platforms including both proton and Zn^{2+} insertion.

The possible reason for the decay in first few cycles (Figure S6.17a) is the cathode metal dissolution and transformation into porous structures with larger surface area which provides sites to adsorb and store zinc ions to form double-layer electrical capacitance. Accordingly, the increased capacitive behavior increases the cathode capacity. This agrees with the charge-discharge curves shown in Figure S6.17b, in which there are two voltage plateaus belonging to proton and zinc ions storage in the 5th cycle, and at the 50th cycle, two plateaus merge into one and the Zn^{2+} plateau almost disappears, indicating the structural transformation and the surface pseudocapacitive behavior, and at the 100th cycle, a larger amount of capacity can be achieved with obvious pseudocapacitive slopes.

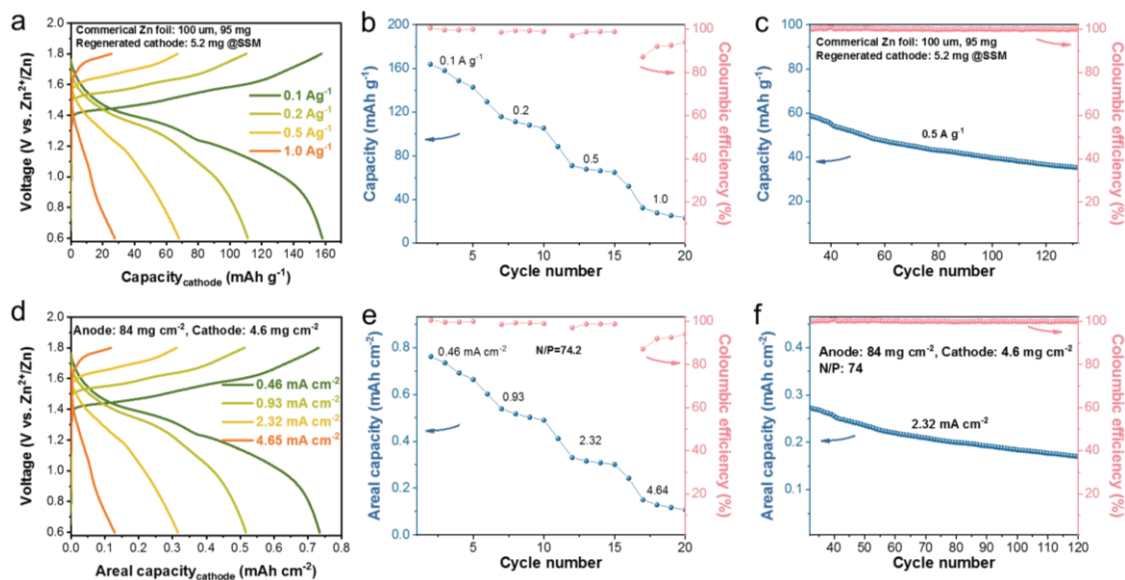


Figure S6.18 Electrochemical performance of commercial anode (84 mg cm⁻²) and regenerated cathode (4.6 mg cm⁻²) with a N/P of 74 for rechargeable full cells. (a, d) charge-discharge curves, (b, e) rate performance, and (c, f) cycling performance. The capacity is based on (a-c) mass (gravimetric capacity) and (d-f) area (areal capacity).

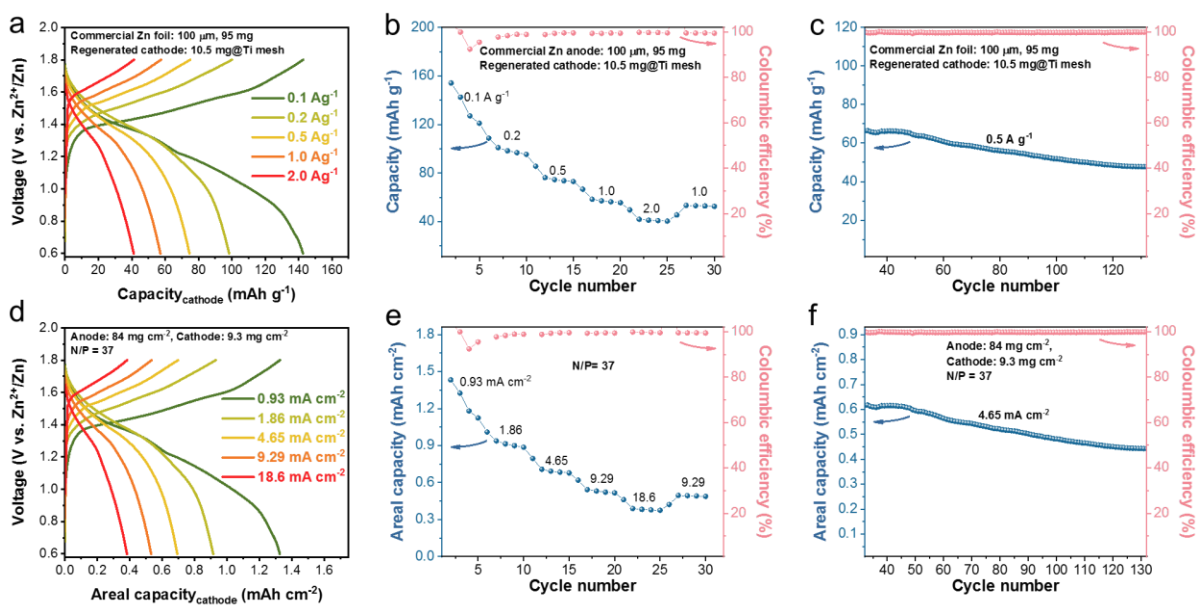


Figure S6.19 Electrochemical performance of commercial anode (84 mg cm⁻²) and cathode (9.3 mg cm⁻²) with a N/P of 37 for rechargeable full cells. (a, d) charge-discharge curves, (b, e) rate performance, and (c, f) cycling performance. The capacity is based on (a-c) mass (gravimetric capacity) and (d-f) area (areal capacity).

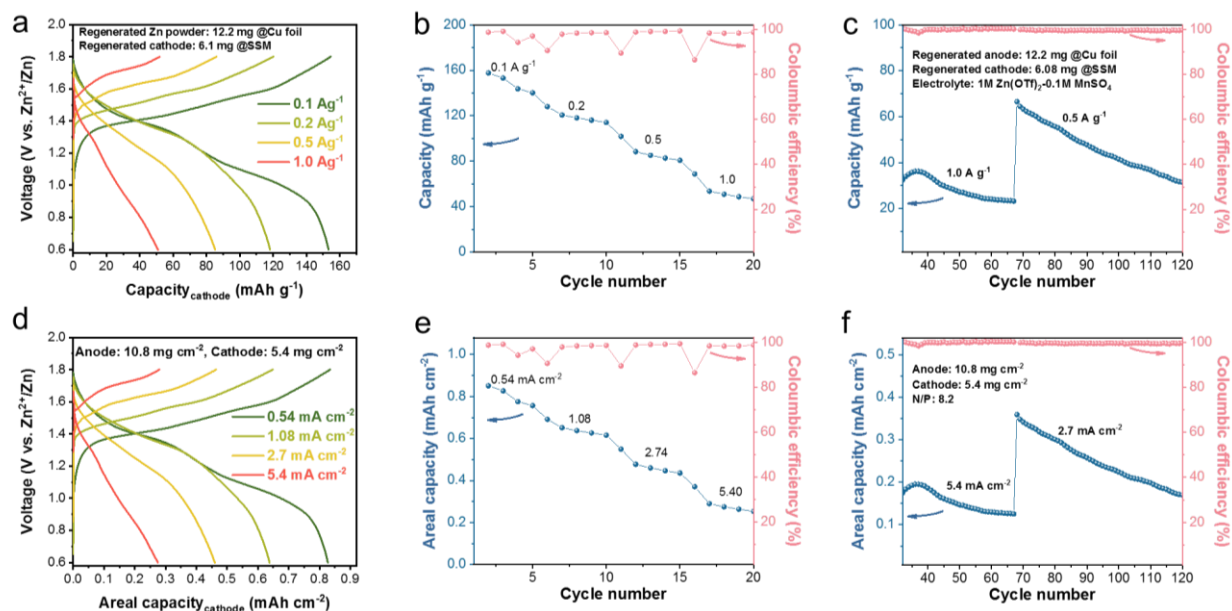


Figure S6.20 Electrochemical performance of regenerated anode (10.8 mg cm^{-2}) and cathode (5.4 mg cm^{-2}) with a N/P of 8.2 for rechargeable full cells. (a, d) charge-discharge curves, (b, e) rate performance, and (c, f) cycling performance. The capacity is based on (a-c) mass (gravimetric capacity) and (d-f) area (areal capacity).

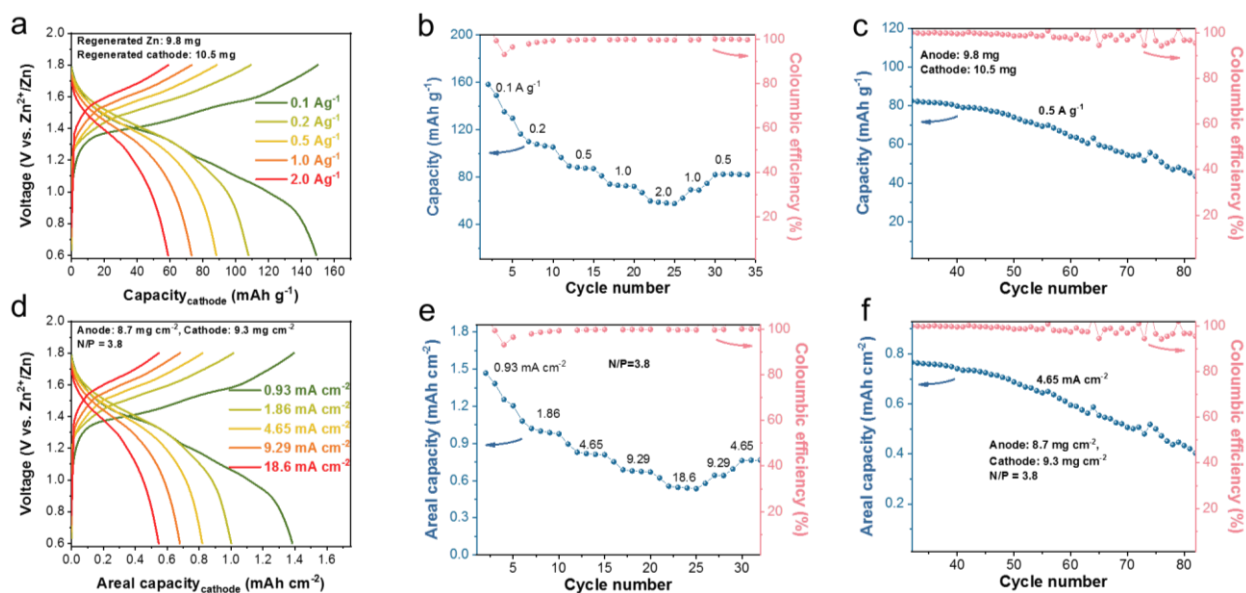


Figure S6.21 Electrochemical performance of regenerated anode (8.7 mg cm^{-2}) and cathode (9.3 mg cm^{-2}) with a N/P of 3.8 for rechargeable full cells. (a, d) charge-discharge curves, (b, e) rate performance, and (c, f) cycling performance. The capacity is based on (a-c) mass (gravimetric capacity) and (d-f) area (areal capacity).

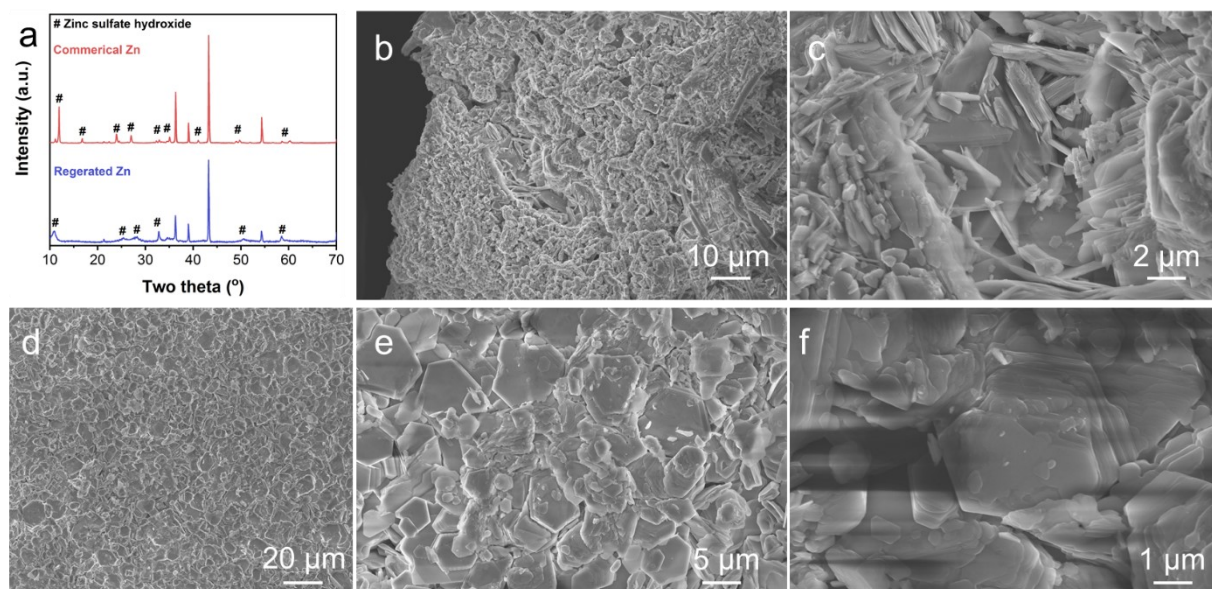


Figure S6.22 Characterization of anodes after cycling. (a) XRD patterns and (b-f) SEM images of (b, c) commercial Zn and (d-f) regenerated Zn anode.

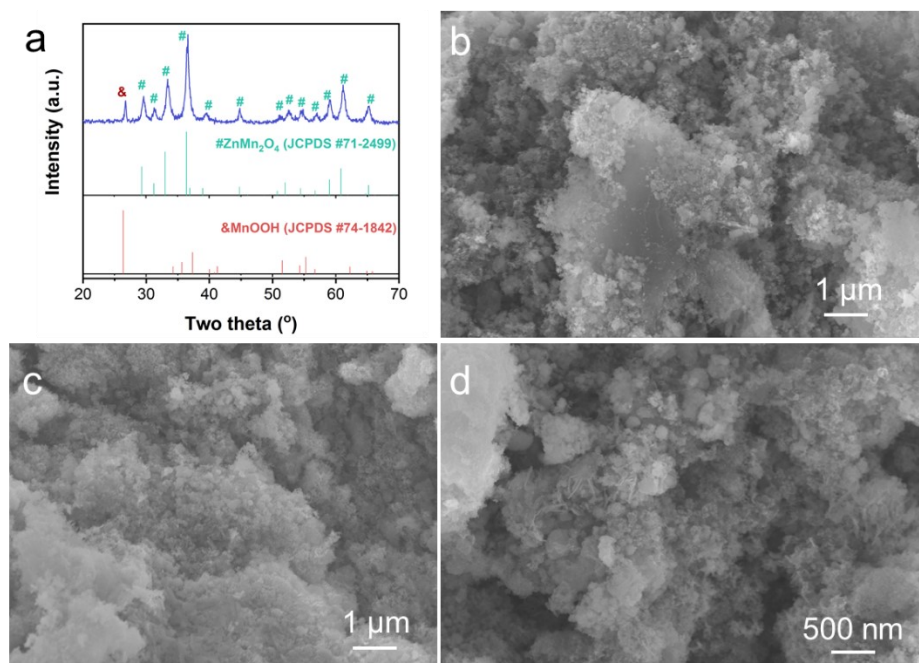


Figure S6.23 Characterization of high-loading cathode in the regenerated full cell after cycling. (a) XRD patterns and (b-d) SEM images.

Table S6.1 Comparison of DOD values of reported Zn metal in symmetric cells and full cells

Anode	Cathode	Rate (A g ⁻¹)	DOD of Zn (%)	Life cycle	Reference
Regenerated Zn powder	Zn	0.5~8 mA cm ⁻²	13.8-55.1%	100 h	This work
	MnO ₂	0.1~2.0	7.8~19.6	80	
N-Zn	MnO ₂	1.0	0.079	2000	<i>Adv. Sci.</i> , 2021, 2103952 ²¹¹
C-750/Zn	MnO ₂	0.3	0.328	5000	<i>Adv. Energy Mater.</i> 2020, 10, 1904215 ²⁰³
NGO-Zn	LiMn ₂ O ₄	0.14	1.88	600	<i>ACS Appl. Energy Mater.</i> 2021, 4, 6, 6364 ²⁰²
AEC-Zn	AEC-Zn	8.85 mA cm ⁻²	60	250 h	<i>Adv. Funct. Mater.</i> 2021, 31, 2001867 ¹⁸⁷
	MnO ₂	0.62	0.53	300	
MOF/Zn	MnO ₂	0.5	6.8	180	<i>Angew. Chem. Int. Ed.</i> 2020, 59 9377 ²⁶
Zn In	AC	2.0	0.24	5000	<i>Small</i> 2020, 16, 2001736 ²¹⁴
Cu-Zn alloy/Zn	MnO ₂	3.08	0.18	500	<i>Energy Storage Mater.</i> 2020, 27, 205 ²⁰⁴
Zn@GF	PB	0.1	3.33	150	<i>Electrochim. Acta</i> 2017, 244, 172 ¹⁹⁰
Zn with CNF interlayer	MnO ₂	1	1.58	400	<i>Chem. Eng. J.</i> 2021, 425, 131862 ²⁰⁹
Zn (4 m Zn(BF ₄) ₂ /EG)	Zn	0.5 mA cm ⁻²	50	200 h	<i>Nat. Sustain.</i> 2021, ²¹⁵
	V ₂ O ₅	1.0	22.26	800	
PAN@Zn	MnO ₂	0.5	10	400	<i>Adv. Sci.</i> 2021, 8, 2100309 ¹⁸⁴
Zn@ZIF-8- 500	AC	4.0	3.6	20000	<i>Joule</i> 3, 2019, 1289 ¹⁵⁵
	I ₂ /C	2.0	6.0	1600	
Zn/CNT/CC	CNT/MnO _x @PEDOT	20 mA cm ⁻²	12	1000	<i>Adv. Mater.</i> 2019, 31,1903675 ²⁸
Zn (NC/GF)	Zn		42.7	48 h	<i>Nano research.</i> 2021. ²⁸⁶

Table S6.2 Comparison of full cells with regards to discharge voltage, power density, and energy density

Cell	Voltage (V)	Power density (W kg ⁻¹)	Energy density (Wh kg ⁻¹)	Reference
Zn//MnO₂-MnOOH	1.29	63.39	94.04	This work
	1.35	139.05	72.73	
	1.35	350.43	59.46	
	1.34	691.75	48.47	
	1.30	1349.37	37.95	
h-MoO ₃ //Zn _{0.2} MnO ₂	1.075	53.75	61	<i>J. Mater. Chem. A</i> 2020, 8, 9006 ⁴³
	1.07	107	56.07	
	1.065	159.75	50.37	
	1.06	212	46.43	
	1.05	262.5	43.58	
	1.05	315	41.37	
	1.05	525	36.33	
	1.05	1050	29.4	
Cu _{2-x} Se//Zn _x MnO ₂	0.8	37.21	69.40	<i>Adv. Funct. Mater.</i> 2020, 31, 2005092 ²²⁰
	0.8	74.42	55.81	
	0.785	182.56	39.47	
	0.77	358.14	28.65	
	0.76	706.98	18.95	
	0.76	1767.44	11.38	
AQ// ZnMn ₂ O ₄	0.75	75	71.4	<i>Mater. Today Energy</i> 2019, 13, 323 ⁵³
	0.75 (assumed)	150	59.78	
	0.75 (assumed)	300	47.74	
	0.75 (assumed)	600	37.99	
	0.75 (assumed)	1200	30.68	
	0.75 (assumed)	2400	23.29	
PI-1/CNT//Zn _x MnO ₂	0.91	91	47	<i>Adv. Mater.</i> 2022, 34, 2200077 ²⁸⁵
	0.90	227.5	45.5	
	0.90	455	44.4	
	0.90	880	41.8	
	0.90	2100	36.75	
	0.85	4200	31.7	
N-Zn//MnO ₂	1.25	0.36	1.20	<i>Adv. Sci.</i> 2022, 9, 2103952 ²¹¹
	1.30	0.73	0.99	
	1.30	1.82	0.93	
	1.30	3.64	0.78	
	1.35	7.27	0.68	
ZIF-8//MnO ₂	1.32	1.10	9.63	<i>Adv. Energy Mater.</i> 2020, 10, 1904215 ²⁰³
	1.35	2.37	6.91	
	1.35	5.70	3.89	
	1.30	11.40	2.59	
AEC-Zn//MnO ₂	1.33	13.94	4.98	<i>Adv. Funct. Mater.</i> 2020, 31, 2001867 ¹⁸⁷
PANZ@Zn//MnVO	0.7	24.59	18.64	<i>Adv. Sci.</i> 2021, 8, 2100309 ¹⁸⁴
	0.7	49.18	16.72	
	0.6	98.36	14.26	

Chapter 7 Conclusions and Perspective

7.1 Conclusions

Aqueous Zn-based energy storage devices hold great potential for grid-level energy storage due to merits of zinc metals including high capacity, high safety, water/air compatibility, a suitable redox potential, and high abundance. However, the reversibility of zinc metal anode is challenged by dendrite growth, low CE, metal corrosion, and hydrogen evolution while no cathodes meet the demand of long life, high voltage, and high capacity simultaneously under the high-loading condition. Furthermore, practical Zn batteries/capacitors require limited Zn use, high-loading cathodes, lean electrolyte, and low N/P ratios, which however, is hardly reported in most research. In this thesis, research reports on Zn anodes, cathodes, and electrolytes have been comprehensively summarized. To further improve the performance of zinc batteries and capacitors as well as achieve sustainable development, this thesis proposes one work on extreme zinc metal supercapacitors via electrolyte and binder engineering, two works on making reversible anodes with one focused on carbon-based Zn host and another one on Zn-free polymer anode, and final work on upcycling waste alkaline batteries into secondary Zn-MnO₂ batteries.

My first project systematically investigates the influence of binder, electrolyte, loading mass, and high/low temperature on capacitor performance. In this project, activated carbon, aqueous binder, and concentrated electrolyte were integrated to enable optimized ZICs working under extreme conditions including ultrafast rate (200 Ag⁻¹), ultralong cycles (300,000 cycles), high loadings (10 mg cm⁻²), and wide temperatures (-60-60 °C). However, in this project, the use of excessive Zn and high N/P ratios jeopardizes energy and power densities at the cell level.

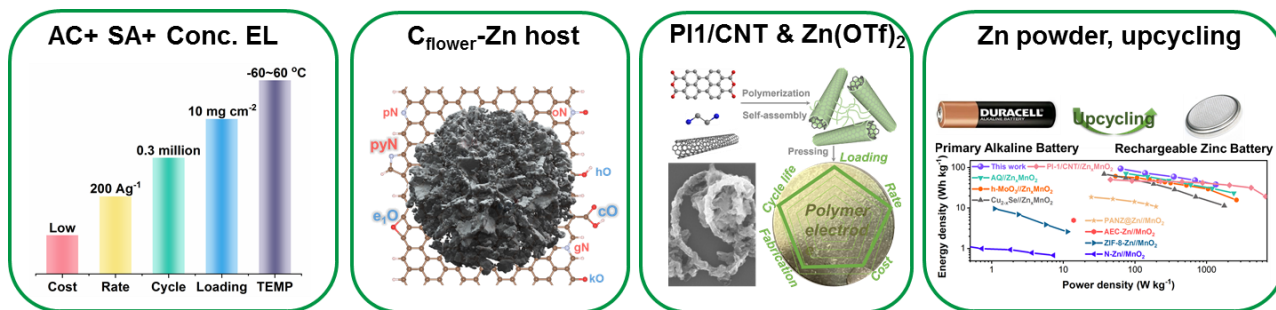
The second project proposes one way of obtaining limited Zn use in cells by confining zinc deposition/dissolution inside a 3D carbon host. Starting from DFT calculation of binding energy

between different dopants and zinc atoms, suitable monomers were chosen to make corresponding polymers, and the assembled polymer morphology has been tuned through adjusting polymerization conditions. Followed by carbonization, polymers were converted to carbon as zinc hosts. Among different carbons, the flower-shaped carbon host with micro-sized hierarchical structure and zincophilic oxygen/nitrogen dopants enables high plating/stripping efficiency up to 99% as well as extended lifespan and faster rate performance in full cells under low N/P ratios including both zinc batteries and capacitors, surpassing hostless Zn anodes.

Alternatively, the third project demonstrates a Zn-free polymer anode of low redox potential vs. Zn potential, near-theoretical capacity, ultrafast rate (100 A g^{-1}), durable (100,000,000 cycles), ultrahigh-loading (50 mg cm^{-2}) capability. Impressively, free-standing, binder-free, and current collector-free polymer electrodes can be easily manufactured through a pressing technique. When this polymer electrode is coupled with cathode materials to make full cells under low N/P ratios, corresponding batteries and capacitors demonstrate unprecedented power density and long life. Along with the sustainability, low cost, and the excellent thermal stability of polyimide, this polymer electrode shows great promise for constructing aqueous batteries/capacitors for stationary energy storage.

The fourth project regenerates Zn powders from spent alkaline batteries to act as efficient anode materials for rechargeable Zn batteries. The symmetrical cells based on limited Zn powders can work under high DOD and fast rates (8 mA cm^{-2}), superior to fresh Zn powder- and commercial thick Zn foil-based cells. The superior performance can be attributed to the coating of organic zincophilic interlayers and orientation of crystal planes in ethylene glycol solvent during thermal reduction. Meanwhile, cathode waste has also been restored to supersede fresh cathode materials with respect to specific capacity, rate, and cycle life. Under practical conditions of limited Zn, low N/P ratios,

high-loading cathodes, and lean electrolyte, full cells based on regenerated anode and cathode materials show good performance, surpassing commercial Zn foil-based cells.



Practical testing conditions for four projects

	Application	Limited anode	High-loading electrodes	Low N/P ratios	Lean electrolyte	Wide temperature
1 st project	Capacitor	No	Yes 10 mg cm ⁻²	No	Yes 8.8 μL mg ⁻¹	Yes
2 nd project	Battery & Capacitor	Yes 1-10 mAh	No	Yes N/P=1-3	No	No
3 rd project	Battery & Capacitor	Yes	Yes 10-50 mg cm ⁻²	Yes N/P=1.0	Yes 1.6 μL mg ⁻¹	No
4 th project	Battery	Yes 8.7 mg cm ⁻²	Yes 9.3 mg cm ⁻²	Yes N/P=3.8	Yes 9.5 μL mg ⁻¹	No

Figure 7.1 Summary of research projects about electrode and electrolyte engineering towards practical zinc batteries and capacitors

7.2 Perspective

Despite tremendous reports on zinc anodes, cathodes, electrolytes, and binders, there remains a large gap between research outputs and practical applications, especially when it comes to cell-level performance and practical testing conditions like limited Zn use, high-loading cathodes, low N/P ratios, lean electrolyte, and wide-temperature operation. Also, most of previous work test electrode performance in the format of coin cells rather than pouch cells, prismatic cells, and cylinder cells which show more promise for large-scale energy storage.

Limited Zn use. To achieve limited use of Zn, there are generally four ways, including deposited Zn on hosts/substrates, zinc-free anodes, zinc powders, and ultrathin zinc foils (less than 10 μm). In this thesis, former three ways have been demonstrated and future work can be done as follows:

For the 3D carbon hosted zinc anode project, more work can be done on first, other 3D carbons derived from polymers with different combinations of monomers, 3D carbons derived from covalent (metal) organic frameworks with different metal-carbon species, and 3D carbons derived from other carbon-containing sources; second, 3D carbon-based nanohybrid host, such as ZnO/carbon and Ag/carbon host which show excellent zincophilicity; third, anode-free carbon or carbon-based composite host to further enhance cell-level energy densities.

For the Zn-free polymer anode project, future work can be done on the rational preparation of polymers via molecular engineering to introduce different functional groups, benzene rings, and linear chains to investigate the influence of these structures on zinc ions/proton storage. Specifically, the introduction of additional carbonyl groups, longer flexible chains, and more conjugated structure in the polymer chain. Besides, the control of polymer morphology and study the morphological effect on battery performance is another direction worth exploring.

For Zn powder anode project, more work can be done on the change of solvent during powder regeneration and study its influence on crystal structure, micro-/nanostructure of zinc powder and the corresponding electrochemical reversibility in both mildly acidic and alkaline electrolyte. Along with electrolyte engineering, the zinc powder can be further applied for other Zn-based energy storage systems including rechargeable Zn-Ni batteries, Zn-air batteries, and Zn-LiMn₂O₄ batteries.

High-loading cathodes. Increasing loading mass generally decreases the specific capacity, rate and cycling performance of electrode materials due to impeded ionic/electronic transfer and severe volumetric changes. The achievement of high-loading cathodes depends on suitable binders and

electrode structures. Suitable binders should be capable of anchoring electrode materials with strong mechanical properties that will not peel off from current collectors even under high loadings, such as the sodium alginate binder in my first project. Electrode structures with high porosity but low tortuosity is preferred when designing thick electrodes, for example, free-standing polymer electrode in my third project in which carbon nanotubes go through the whole electrode functioning as not only efficient ionic and electronic conductors but also effective binder ensuring seamless contact between the active material and the conductive agent.

Low N/P ratios and lean electrolyte. Limited use of Zn and increased cathode loadings can lower N/P ratios to an ideal value of 1, which can hardly be achieved for Zn metal-based devices. Most previous reports use high N/P ratios up to 10-100, which is unrealistic for practical applications. To achieve lean electrolyte use, conductive carbon amount in the electrodes should be lowered and ultrathin separators with high electrolyte holding capability should be designed so that limited electrolyte can still reach active electrode materials rather than being wasted on wetting conductive agents and separators.

Wide-temperature operation. Cold and hot temperatures need to be considered when designing energy storage devices due to ever changing climate. Cold temperatures will increase internal resistance of ionic and electronic transfer lowering rate and cycle life of energy storage devices while hot temperatures will accelerate water decomposition and other side reactions. Achieving wide-temperature operation relies on the rational design of electrode and electrolyte with high stability and high ionic/electrical conductivity under both low and high temperatures.

References

1. Pomerantseva, E., Bonaccorso, F., Feng, X., Cui, Y., and Gogotsi, Y. (2019). Energy storage: The future enabled by nanomaterials. *Science* *366*, eaan8285.
2. Wang, Z.L. (2017). Catch wave power in floating nets. *Nature News* *542*, 159.
3. Chu, S., Cui, Y., and Liu, N. (2017). The path towards sustainable energy. *Nat. Mater.* *16*, 16-22.
4. Sun, Y., Liu, N., and Cui, Y. (2016). Promises and challenges of nanomaterials for lithium-based rechargeable batteries. *Nat. Energy* *1*, 16071.
5. Blanc, L.E., Kundu, D., and Nazar, L.F. (2020). Scientific Challenges for the Implementation of Zn-Ion Batteries. *Joule* *4*, 771-799.
6. Jia, X., Liu, C., Neale, Z.G., Yang, J., and Cao, G. (2020). Active Materials for Aqueous Zinc Ion Batteries: Synthesis, Crystal Structure, Morphology, and Electrochemistry. *Chem. Rev.* *120*, 7795-7866.
7. Zampardi, G., and La Mantia, F. (2022). Open challenges and good experimental practices in the research field of aqueous Zn-ion batteries. *Nat. Commun.* *13*, 687.
8. Xu, Z., Zhang, N., and Wang, X. (2022). Upcycling spent alkaline batteries into rechargeable zinc metal batteries. *Nano Energy* *102*, 107724.
9. Chao, D., Zhou, W., Xie, F., Ye, C., Li, H., Jaroniec, M., and Qiao, S.-Z. (2020). Roadmap for advanced aqueous batteries: From design of materials to applications. *Sci. Adv.* *6*, eaba4098.
10. Wan, F., Zhou, X., Lu, Y., Niu, Z., and Chen, J. (2020). Energy Storage Chemistry in Aqueous Zinc Metal Batteries. *ACS Energy Lett.* *5*, 3569-3590.
11. Dong, L., Yang, W., Yang, W., Li, Y., Wu, W., and Wang, G. (2019). Multivalent metal ion hybrid capacitors: A review with a focus on zinc-ion hybrid capacitors. *J. Mater. Chem. A* *7*, 13810-13832.
12. Li, Z., An, Y., Dong, S., Chen, C., Wu, L., Sun, Y., and Zhang, X. (2020). Progress on zinc ion hybrid supercapacitors: Insights and challenges. *Energy Storage Mater.* *31*, 252-266.
13. Wang, H., Wang, M., and Tang, Y. (2018). A novel zinc-ion hybrid supercapacitor for long-life and low-cost energy storage applications. *Energy Storage Mater.* *13*, 1-7.
14. Tian, Y., An, Y., Wei, C., Xi, B., Xiong, S., Feng, J., and Qian, Y. (2020). Recent Advances and Perspectives of Zn-Metal Free "Rocking-Chair"-Type Zn-Ion Batteries. *Adv. Energy Mater.* *11*, 2002529.
15. Shin, J., Lee, J., Park, Y., and Choi, J.W. (2020). Aqueous zinc ion batteries: focus on zinc metal anodes. *Chem. Sci.* *11*, 2028-2044.
16. Zhang, Q., Luan, J., Tang, Y., Ji, X., and Wang, H. (2020). Interfacial Design of Dendrite-Free Zinc Anodes for Aqueous Zinc-Ion Batteries. *Angew. Chem. Int. Ed.* *59*, 13180-13191.

17. Yang, Q., Liang, G., Guo, Y., Liu, Z., Yan, B., Wang, D., Huang, Z., Li, X., Fan, J., and Zhi, C. (2019). Do Zinc Dendrites Exist in Neutral Zinc Batteries: A Developed Electrohealing Strategy to In Situ Rescue In-Service Batteries. *Adv. Mater.* *31*, 1903778.
18. Zhao, Z., Zhao, J., Hu, Z., Li, J., Li, J., Zhang, Y., Wang, C., and Cui, G. (2019). Long-life and deeply rechargeable aqueous Zn anodes enabled by a multifunctional brightener-inspired interphase. *Energy Environ. Sci.* *12*, 1938-1949.
19. Shen, C., Li, X., Li, N., Xie, K., Wang, J.-g., Liu, X., and Wei, B. (2018). Graphene-Boosted, High-Performance Aqueous Zn-Ion Battery. *ACS Appl. Mater. Interfaces* *10*, 25446-25453.
20. Bai, M., Xie, K., Yuan, K., Zhang, K., Li, N., Shen, C., Lai, Y., Vajtai, R., Ajayan, P., and Wei, B. (2018). A Scalable Approach to Dendrite-Free Lithium Anodes via Spontaneous Reduction of Spray-Coated Graphene Oxide Layers. *Adv. Mater.* *30*, 1801213.
21. Dong, L., Yang, W., Yang, W., Tian, H., Huang, Y., Wang, X., Xu, C., Wang, C., Kang, F., and Wang, G. (2020). Flexible and conductive scaffold-stabilized zinc metal anodes for ultralong-life zinc-ion batteries and zinc-ion hybrid capacitors. *Chem. Eng. J.* *384*, 123355.
22. Yin, Y., Wang, S., Zhang, Q., Song, Y., Chang, N., Pan, Y., Zhang, H., and Li, X. (2020). Dendrite-Free Zinc Deposition Induced by Tin-Modified Multifunctional 3D Host for Stable Zinc-Based Flow Battery. *Adv. Mater.* *32*, 1906803.
23. Li, W., Wang, K., Cheng, S., and Jiang, K. (2018). A long-life aqueous Zn-ion battery based on Na₃V₂(PO₄)₂F₃ cathode. *Energy Storage Mater.* *15*, 14-21.
24. Li, W., Wang, K.L., Zhou, M., Zhan, H.C., Cheng, S.J., and Jiang, K. (2018). Advanced Low-Cost, High-Voltage, Long-Life Aqueous Hybrid Sodium/Zinc Batteries Enabled by a Dendrite-Free Zinc Anode and Concentrated Electrolyte. *ACS Appl. Mater. Interfaces* *10*, 22059-22066.
25. Kang, L., Cui, M., Jiang, F., Gao, Y., Luo, H., Liu, J., Liang, W., and Zhi, C. (2018). Nanoporous CaCO₃ Coatings Enabled Uniform Zn Stripping/Plating for Long-Life Zinc Rechargeable Aqueous Batteries. *Adv. Energy Mater.* *8*, 1801090.
26. Yang, H., Chang, Z., Qiao, Y., Deng, H., Mu, X., He, P., and Zhou, H. (2020). Constructing a Super-Saturated Electrolyte Front Surface for Stable Rechargeable Aqueous Zinc Batteries. *Angew. Chem. Int. Ed.* *59*, 9377-9381.
27. Zheng, J., Zhao, Q., Tang, T., Yin, J., Quilty, C.D., Renderos, G.D., Liu, X., Deng, Y., Wang, L., Bock, D.C., *et al.* (2019). Reversible epitaxial electrodeposition of metals in battery anodes. *Science* *366*, 645-648.

28. Zeng, Y., Zhang, X., Qin, R., Liu, X., Fang, P., Zheng, D., Tong, Y., and Lu, X. (2019). Dendrite-Free Zinc Deposition Induced by Multifunctional CNT Frameworks for Stable Flexible Zn-Ion Batteries. *Adv. Mater.* *31*, 1903675.
29. Li, C., Shi, X., Liang, S., Ma, X., Han, M., Wu, X., and Zhou, J. (2020). Spatially homogeneous copper foam as surface dendrite-free host for zinc metal anode. *Chem. Eng. J.* *379*, 122248.
30. Parker, J.F., Chervin, C.N., Pala, I.R., Machler, M., Burz, M.F., Long, J.W., and Rolison, D.R. (2017). Rechargeable nickel–3D zinc batteries: An energy-dense, safer alternative to lithium-ion. *Science* *356*, 415.
31. An, G.-H., Hong, J., Pak, S., Cho, Y., Lee, S., Hou, B., and Cha, S. (2020). 2D Metal Zn Nanostructure Electrodes for High-Performance Zn Ion Supercapacitors. *Adv. Energy Mater.* *10*, 1902981.
32. Li, H., Han, C., Huang, Y., Huang, Y., Zhu, M., Pei, Z., Xue, Q., Wang, Z., Liu, Z., Tang, Z., *et al.* (2018). An extremely safe and wearable solid-state zinc ion battery based on a hierarchical structured polymer electrolyte. *Energy Environ. Sci.* *11*, 941-951.
33. Zeng, Y., Zhang, X., Meng, Y., Yu, M., Yi, J., Wu, Y., Lu, X., and Tong, Y. (2017). Achieving Ultrahigh Energy Density and Long Durability in a Flexible Rechargeable Quasi-Solid-State Zn–MnO₂ Battery. *Adv. Mater.* *29*, 1700274.
34. Zhang, Q., Luan, J., Fu, L., Wu, S., Tang, Y., Ji, X., and Wang, H. (2019). The Three-Dimensional Dendrite-Free Zinc Anode on a Copper Mesh with a Zinc-Oriented Polyacrylamide Electrolyte Additive. *Angew. Chem. Int. Ed.* *58*, 15841-15847.
35. Kang, Z., Wu, C., Dong, L., Liu, W., Mou, J., Zhang, J., Chang, Z., Jiang, B., Wang, G., Kang, F., *et al.* (2019). 3D Porous Copper Skeleton Supported Zinc Anode toward High Capacity and Long Cycle Life Zinc Ion Batteries. *ACS Sustain. Chem. Eng.* *7*, 3364-3371.
36. Gocke, E., Schramm, W., Dolscheid, P., and Schöllhorn, R. (1987). Molybdenum cluster chalcogenides Mo₆X₈: Electrochemical intercalation of closed shell ions Zn²⁺, Cd²⁺, and Na. *J. Solid State Chem.* *70*, 71-81.
37. Chae, M.S., Heo, J.W., Lim, S.-C., and Hong, S.-T. (2016). Electrochemical Zinc-Ion Intercalation Properties and Crystal Structures of ZnMo₆S₈ and Zn₂Mo₆S₈ Chevrel Phases in Aqueous Electrolytes. *Inorg. Chem.* *55*, 3294-3301.
38. Cheng, Y., Luo, L., Zhong, L., Chen, J., Li, B., Wang, W., Mao, S.X., Wang, C., Sprenkle, V.L., Li, G., *et al.* (2016). Highly Reversible Zinc-Ion Intercalation into Chevrel Phase Mo₆S₈ Nanocubes and Applications for Advanced Zinc-Ion Batteries. *ACS Appl. Mater. Interfaces* *8*, 13673-13677.
39. Chae, M.S., and Hong, S.-T. (2019). Prototype System of Rocking-Chair Zn-Ion Battery Adopting Zinc Chevrel Phase Anode and Rhombohedral Zinc Hexacyanoferrate Cathode. *Batteries* *5*, 3.

40. Li, W., Wang, K., Cheng, S., and Jiang, K. (2019). An Ultrastable Presodiated Titanium Disulfide Anode for Aqueous “Rocking-Chair” Zinc Ion Battery. *Adv. Energy Mater.* *9*, 1900993.
41. Naveed, A., Yang, H., Shao, Y., Yang, J., Yanna, N., Liu, J., Shi, S., Zhang, L., Ye, A., He, B., *et al.* (2019). A Highly Reversible Zn Anode with Intrinsically Safe Organic Electrolyte for Long-Cycle-Life Batteries. *Adv. Mater.* *31*, 1900668.
42. Liu, W., Hao, J., Xu, C., Mou, J., Dong, L., Jiang, F., Kang, Z., Wu, J., Jiang, B., and Kang, F. (2017). Investigation of zinc ion storage of transition metal oxides, sulfides, and borides in zinc ion battery systems. *Chem. Commun.* *53*, 6872-6874.
43. Xiong, T., Zhang, Y., Wang, Y., Lee, W.S.V., and Xue, J. (2020). Hexagonal MoO₃ as a zinc intercalation anode towards zinc metal-free zinc-ion batteries. *J. Mater. Chem. A* *8*, 9006-9012.
44. Kaveevivitchai, W., and Manthiram, A. (2016). High-capacity zinc-ion storage in an open-tunnel oxide for aqueous and nonaqueous Zn-ion batteries. *J. Mater. Chem. A* *4*, 18737-18741.
45. Kaveevivitchai, W., and Jacobson, A.J. (2016). High Capacity Rechargeable Magnesium-Ion Batteries Based on a Microporous Molybdenum–Vanadium Oxide Cathode. *Chem. Mater.* *28*, 4593-4601.
46. Li, H., McRae, L., Firby, C.J., and Elezzabi, A.Y. (2019). Rechargeable Aqueous Electrochromic Batteries Utilizing Ti-Substituted Tungsten Molybdenum Oxide Based Zn²⁺ Ion Intercalation Cathodes. *Adv. Mater.* *31*, 1807065.
47. Lu, Y., Zhang, Q., Li, L., Niu, Z., and Chen, J. (2018). Design Strategies toward Enhancing the Performance of Organic Electrode Materials in Metal-Ion Batteries. *Chem* *4*, 2786-2813.
48. Peng, H., Yu, Q., Wang, S., Kim, J., Rowan, A.E., Nanjundan, A.K., Yamauchi, Y., and Yu, J. (2019). Molecular Design Strategies for Electrochemical Behavior of Aromatic Carbonyl Compounds in Organic and Aqueous Electrolytes. *Adv. Sci.* *6*, 1900431.
49. Cui, J., Guo, Z., Yi, J., Liu, X., Wu, K., Liang, P., Li, Q., Liu, Y., Wang, Y., Xia, Y., *et al.* (2020). Organic Cathode Materials for Rechargeable Zinc Batteries: Mechanisms, Challenges, and Perspectives. *ChemSusChem* *13*, 2160-2185.
50. Huang, J., Dong, X., Guo, Z., and Wang, Y. (2020). Progress of Organic Electrodes in Aqueous Electrolyte for Energy Storage and Conversion. *Angewandte Chemie* *59*, 18322-18333.
51. Poizot, P., Gaubicher, J., Renault, S., Dubois, L., Liang, Y., and Yao, Y. (2020). Opportunities and Challenges for Organic Electrodes in Electrochemical Energy Storage. *Chem. Rev.* *120*, 6490-6557.
52. Lu, Y., and Chen, J. (2020). Prospects of organic electrode materials for practical lithium batteries. *Nat. Rev. Chem.* *4*, 127-142.

53. Yan, L., Zeng, X., Li, Z., Meng, X., Wei, D., Liu, T., Ling, M., Lin, Z., and Liang, C. (2019). An innovation: Dendrite free quinone paired with ZnMn₂O₄ for zinc ion storage. *Mater. Today Energy* *13*, 323-330.
54. Liu, N., Wu, X., Zhang, Y., Yin, Y., Sun, C., Mao, Y., Fan, L., and Zhang, N. (2020). Building High Rate Capability and Ultrastable Dendrite-Free Organic Anode for Rechargeable Aqueous Zinc Batteries. *Adv. Sci.* *7*, 2000146.
55. Li, H., Ma, L., Han, C., Wang, Z., Liu, Z., Tang, Z., and Zhi, C. (2019). Advanced rechargeable zinc-based batteries: Recent progress and future perspectives. *Nano Energy* *62*, 550-587.
56. Sun, W., Wang, F., Hou, S., Yang, C., Fan, X., Ma, Z., Gao, T., Han, F., Hu, R., Zhu, M., *et al.* (2017). Zn/MnO₂ Battery Chemistry With H(+) and Zn(2+) Coinsertion. *J. Am. Chem. Soc.* *139*, 9775-9778.
57. Zhang, N., Cheng, F.Y., Liu, J.X., Wang, L.B., Long, X.H., Liu, X.S., Li, F.J., and Chen, J. (2017). Rechargeable aqueous zinc-manganese dioxide batteries with high energy and power densities. *Nat. Commun.* *8*, 405.
58. Huang, J.H., Wang, Z., Hou, M.Y., Dong, X.L., Liu, Y., Wang, Y.G., and Xia, Y.Y. (2018). Polyaniline-intercalated manganese dioxide nanolayers as a high-performance cathode material for an aqueous zinc-ion battery. *Nat. Commun.* *9*, 2906.
59. Soundharrajan, V., Sambandam, B., Kim, S., Mathew, V., Jo, J., Kim, S., Lee, J., Islam, S., Kim, K., Sun, Y.-K., *et al.* (2018). Aqueous Magnesium Zinc Hybrid Battery: An Advanced High-Voltage and High-Energy MgMn₂O₄ Cathode. *ACS Energy Lett.* *3*, 1998-2004.
60. Wu, B., Zhang, G., Yan, M., Xiong, T., He, P., He, L., Xu, X., and Mai, L. (2018). Graphene Scroll-Coated alpha-MnO₂ Nanowires as High-Performance Cathode Materials for Aqueous Zn-Ion Battery. *Small* *14*, e1703850.
61. Zhao, Y., Zhu, Y., and Zhang, X. (2020). Challenges and perspectives for manganese-based oxides for advanced aqueous zinc-ion batteries. *InfoMat* *2*, 237-260.
62. Jia, Z., Wang, B., and Wang, Y. (2015). Copper hexacyanoferrate with a well-defined open framework as a positive electrode for aqueous zinc ion batteries. *Mater. Chem. Phys.* *149-150*, 601-606.
63. Zhang, L., Chen, L., Zhou, X., and Liu, Z. (2015). Towards High-Voltage Aqueous Metal-Ion Batteries Beyond 1.5 V: The Zinc/Zinc Hexacyanoferrate System. *Adv. Energy Mater.* *5*, 1400930
64. Liu, Z., Pulletikurthi, G., and Endres, F. (2016). A Prussian Blue/Zinc Secondary Battery with a Bio-Ionic Liquid-Water Mixture as Electrolyte. *ACS Appl. Mater. Interfaces* *8*, 12158-12164.
65. Ma, L., Chen, S., Long, C., Li, X., Zhao, Y., Liu, Z., Huang, Z., Dong, B., Zapien, J.A., and Zhi, C. (2019). Achieving High-Voltage and High-Capacity Aqueous Rechargeable Zinc Ion Battery by Incorporating Two-Species Redox Reaction. *Adv. Energy Mater.* *9*, 1902446.

66. Yang, Q., Mo, F., Liu, Z., Ma, L., Li, X., Fang, D., Chen, S., Zhang, S., and Zhi, C. (2019). Activating Coordinated Iron of Iron Hexacyanoferrate for Zn Hybrid-Ion Batteries with 10 000-Cycle Lifespan and Superior Rate Capability. *Adv. Mater.* *31*, 1901521.
67. Yan, M.Y., He, P., Chen, Y., Wang, S.Y., Wei, Q.L., Zhao, K.N., Xu, X., An, Q.Y., Shuang, Y., Shao, Y.Y., *et al.* (2018). Water-Lubricated Intercalation in V₂O₅ center dot nH₂O for High-Capacity and High-Rate Aqueous Rechargeable Zinc Batteries. *Adv. Mater.* *30*, 1703725.
68. Zhang, N., Dong, Y., Jia, M., Bian, X., Wang, Y.Y., Qiu, M.D., Xu, J.Z., Liu, Y.C., Jiao, L.F., and Cheng, F.Y. (2018). Rechargeable Aqueous Zn-V₂O₅ Battery with High Energy Density and Long Cycle Life. *ACS Energy Lett.* *3*, 1366-1372.
69. Ma, L., Li, N., Long, C., Dong, B., Fang, D., Liu, Z., Zhao, Y., Li, X., Fan, J., Chen, S., *et al.* (2019). Achieving Both High Voltage and High Capacity in Aqueous Zinc-Ion Battery for Record High Energy Density. *Adv. Funct. Mater.* *29*, 1906142.
70. Wang, L., Huang, K.-W., Chen, J., and Zheng, J. (2019). Ultralong cycle stability of aqueous zinc-ion batteries with zinc vanadium oxide cathodes. *Sci. Adv.* *5*, eaax4279.
71. Pan, Z., Yang, J., Yang, J., Zhang, Q., Zhang, H., Li, X., Kou, Z., Zhang, Y., Chen, H., Yan, C., *et al.* (2020). Stitching of Zn₃(OH)₂V₂O₇·2H₂O 2D Nanosheets by 1D Carbon Nanotubes Boosts Ultrahigh Rate for Wearable Quasi-Solid-State Zinc-Ion Batteries. *ACS Nano* *14*, 842-853.
72. Wan, F., Zhang, L., Wang, X., Bi, S., Niu, Z., and Chen, J. (2018). An Aqueous Rechargeable Zinc-Organic Battery with Hybrid Mechanism. *Adv. Funct. Mater.* *28*, 1804975.
73. Nam, K.W., Kim, H., Beldjoudi, Y., Kwon, T.-w., Kim, D.J., and Stoddart, J.F. (2020). Redox-Active Phenanthrenequinone Triangles in Aqueous Rechargeable Zinc Batteries. *J. Am. Chem. Soc.* *142*, 2541-2548.
74. Zhao, Q., Huang, W.W., Luo, Z.Q., Liu, L.J., Lu, Y., Li, Y.X., Li, L., Hu, J.Y., Ma, H., and Chen, J. (2018). High-capacity aqueous zinc batteries using sustainable quinone electrodes. *Sci. Adv.* *4*, eaao1761.
75. Wang, X., Wang, F., Wang, L., Li, M., Wang, Y., Chen, B., Zhu, Y., Fu, L., Zha, L., Zhang, L., *et al.* (2016). An Aqueous Rechargeable Zn//Co₃O₄ Battery with High Energy Density and Good Cycling Behavior. *Adv. Mater.* *28*, 4904-4911.
76. Zeng, Y.X., Lai, Z.Z., Han, Y., Zhang, H.Z., Xie, S.L., and Lu, X.H. (2018). Oxygen-Vacancy and Surface Modulation of Ultrathin Nickel Cobaltite Nanosheets as a High-Energy Cathode for Advanced Zn-Ion Batteries. *Adv. Mater.* *30*, e1802396.
77. Liu, J., Xu, P., Liang, J., Liu, H., Peng, W., Li, Y., Zhang, F., and Fan, X. (2020). Boosting aqueous zinc-ion storage in MoS₂ via controllable phase. *Chem. Eng. J.* *389*, 124405.

78. Wang, F., Hu, E., Sun, W., Gao, T., Ji, X., Fan, X., Han, F., Yang, X.-Q., Xu, K., and Wang, C. (2018). A rechargeable aqueous Zn²⁺-battery with high power density and a long cycle-life. *Energy Environ. Sci.* *11*, 3168-3175.
79. Gross, M.M., and Manthiram, A. (2018). Rechargeable Zinc-Aqueous Polysulfide Battery with a Mediator-Ion Solid Electrolyte. *ACS Appl. Mater. Interfaces* *10*, 10612-10617.
80. Zhao, Y., Wang, D., Li, X., Yang, Q., Guo, Y., Mo, F., Li, Q., Peng, C., Li, H., and Zhi, C. (2020). Initiating a Reversible Aqueous Zn/Sulfur Battery through a “Liquid Film”. *Adv. Mater.* *32*, 2003070.
81. Wang, G., Kohn, B., Scheler, U., Wang, F., Oswald, S., Löffler, M., Tan, D., Zhang, P., Zhang, J., and Feng, X. (2020). A High-Voltage, Dendrite-Free, and Durable Zn–Graphite Battery. *Adv. Mater.* *32*, 1905681.
82. Xu, C., Li, B., Du, H., and Kang, F. (2012). Energetic Zinc Ion Chemistry: The Rechargeable Zinc Ion Battery. *Angew. Chem. Int. Ed.* *51*, 933-935.
83. Alfuruqi, M.H., Mathew, V., Gim, J., Kim, S., Song, J., Baboo, J.P., Choi, S.H., and Kim, J. (2015). Electrochemically Induced Structural Transformation in a γ -MnO₂ Cathode of a High Capacity Zinc-Ion Battery System. *Chem. Mater.* *27*, 3609-3620.
84. Han, S.-D., Kim, S., Li, D., Petkov, V., Yoo, H.D., Phillips, P.J., Wang, H., Kim, J.J., More, K.L., Key, B., *et al.* (2017). Mechanism of Zn Insertion into Nanostructured δ -MnO₂: A Nonaqueous Rechargeable Zn Metal Battery. *Chem. Mater.* *29*, 4874-4884.
85. Lee, J., Ju, J.B., Cho, W.I., Cho, B.W., and Oh, S.H. (2013). Todorokite-type MnO₂ as a zinc-ion intercalating material. *Electrochim. Acta* *112*, 138-143.
86. Yuan, C., Zhang, Y., Pan, Y., Liu, X., Wang, G., and Cao, D. (2014). Investigation of the intercalation of polyvalent cations (Mg²⁺, Zn²⁺) into λ -MnO₂ for rechargeable aqueous battery. *Electrochim. Acta* *116*, 404-412.
87. Pan, H., Shao, Y., Yan, P., Cheng, Y., Han, K.S., Nie, Z., Wang, C., Yang, J., Li, X., Bhattacharya, P., *et al.* (2016). Reversible aqueous zinc/manganese oxide energy storage from conversion reactions. *Nat. Energy* *1*, 16039.
88. Tie, Z., Liu, L., Deng, S., Zhao, D., and Niu, Z. (2020). Proton Insertion Chemistry of a Zinc–Organic Battery. *Angew. Chem. Int. Ed.* *59*, 4920-4924.
89. Chao, D., Zhou, W., Ye, C., Zhang, Q., Chen, Y., Gu, L., Davey, K., and Qiao, S.-Z. (2019). An Electrolytic Zn–MnO₂ Battery for High-Voltage and Scalable Energy Storage. *Angew. Chem. Int. Ed.* *58*, 7823-7828.

90. Zhong, C., Liu, B., Ding, J., Liu, X., Zhong, Y., Li, Y., Sun, C., Han, X., Deng, Y., Zhao, N., *et al.* (2020). Decoupling electrolytes towards stable and high-energy rechargeable aqueous zinc–manganese dioxide batteries. *Nat. Energy* *5*, 440-449.
91. Liu, C., Chi, X., Han, Q., and Liu, Y. (2020). A High Energy Density Aqueous Battery Achieved by Dual Dissolution/Deposition Reactions Separated in Acid-Alkaline Electrolyte. *Adv. Energy Mater.* *10*, 1903589.
92. Dong, L., Ma, X., Li, Y., Zhao, L., Liu, W., Cheng, J., Xu, C., Li, B., Yang, Q.-H., and Kang, F. (2018). Extremely safe, high-rate and ultralong-life zinc-ion hybrid supercapacitors. *Energy Storage Mater.* *13*, 96-102.
93. Li, Z., Chen, D., An, Y., Chen, C., Wu, L., Chen, Z., Sun, Y., and Zhang, X. (2020). Flexible and anti-freezing quasi-solid-state zinc ion hybrid supercapacitors based on pencil shavings derived porous carbon. *Energy Storage Mater.* *28*, 307-314.
94. Liu, P., Gao, Y., Tan, Y., Liu, W., Huang, Y., Yan, J., and Liu, K. (2019). Rational design of nitrogen doped hierarchical porous carbon for optimized zinc-ion hybrid supercapacitors. *Nano Res.* *12*, 2835-2841.
95. Zhang, P., Li, Y., Wang, G., Wang, F., Yang, S., Zhu, F., Zhuang, X., Schmidt, O.G., and Feng, X. (2019). Zn-Ion Hybrid Micro-Supercapacitors with Ultrahigh Areal Energy Density and Long-Term Durability. *Adv. Mater.* *31*, 1806005.
96. Lu, Y., Li, Z., Bai, Z., Mi, H., Ji, C., Pang, H., Yu, C., and Qiu, J. (2019). High energy-power Zn-ion hybrid supercapacitors enabled by layered B/N co-doped carbon cathode. *Nano Energy* *66*, 104132.
97. Liu, P., Liu, W., Huang, Y., Li, P., Yan, J., and Liu, K. (2020). Mesoporous hollow carbon spheres boosted, integrated high performance aqueous Zn-Ion energy storage. *Energy Storage Mater.* *25*, 858-865.
98. Zhang, H., Liu, Q., Fang, Y., Teng, C., Liu, X., Fang, P., Tong, Y., and Lu, X. (2019). Boosting Zn-Ion Energy Storage Capability of Hierarchically Porous Carbon by Promoting Chemical Adsorption. *Adv. Mater.* *31*, e1904948.
99. Xiong, T., Yu, Z.G., Wu, H., Du, Y., Xie, Q., Chen, J., Zhang, Y.-W., Pennycook, S.J., Lee, W.S.V., and Xue, J. (2019). Defect Engineering of Oxygen-Deficient Manganese Oxide to Achieve High-Performing Aqueous Zinc Ion Battery. *Adv. Energy Mater.* *9*, 1803815.
100. Ye, Z., Cao, Z., Lam Chee, M.O., Dong, P., Ajayan, P.M., Shen, J., and Ye, M. (2020). Advances in Zn-ion batteries via regulating liquid electrolyte. *Energy Storage Mater.* *32*, 290-305.
101. Han, S.-D., Rajput, N.N., Qu, X., Pan, B., He, M., Ferrandon, M.S., Liao, C., Persson, K.A., and Burrell, A.K. (2016). Origin of Electrochemical, Structural, and Transport Properties in Nonaqueous Zinc Electrolytes. *ACS Appl. Mater. Interfaces* *8*, 3021-3031.

102. Senguttuvan, P., Han, S.-D., Kim, S., Lipson, A.L., Tepavcevic, S., Fister, T.T., Bloom, I.D., Burrell, A.K., and Johnson, C.S. (2016). A High Power Rechargeable Nonaqueous Multivalent Zn/V₂O₅ Battery. *Adv. Energy Mater.* *6*, 1600826.
103. Kundu, D., Hosseini Vajargah, S., Wan, L., Adams, B., Prendergast, D., and Nazar, L.F. (2018). Aqueous vs. nonaqueous Zn-ion batteries: consequences of the desolvation penalty at the interface. *Energy Environ. Sci.* *11*, 881-892.
104. Wang, F., Sun, W., Shadike, Z., Hu, E., Ji, X., Gao, T., Yang, X.-Q., Xu, K., and Wang, C. (2018). How Water Accelerates Bivalent Ion Diffusion at the Electrolyte/Electrode Interface. *Angew. Chem. Int. Ed.* *57*, 11978-11981.
105. Kasiri, G., Trócoli, R., Bani Hashemi, A., and La Mantia, F. (2016). An electrochemical investigation of the aging of copper hexacyanoferrate during the operation in zinc-ion batteries. *Electrochim. Acta* *222*, 74-83.
106. Chae, M.S., Heo, J.W., Kwak, H.H., Lee, H., and Hong, S.-T. (2017). Organic electrolyte-based rechargeable zinc-ion batteries using potassium nickel hexacyanoferrate as a cathode material. *J. Power Sources* *337*, 204-211.
107. Peng, Z., Wei, Q., Tan, S., He, P., Luo, W., An, Q., and Mai, L. (2018). Novel layered iron vanadate cathode for high-capacity aqueous rechargeable zinc batteries. *Chem. Commun.* *54*, 4041-4044.
108. Zhang, N., Cheng, F., Liu, Y., Zhao, Q., Lei, K., Chen, C., Liu, X., and Chen, J. (2016). Cation-Deficient Spinel ZnMn₂O₄ Cathode in Zn(CF₃SO₃)₂ Electrolyte for Rechargeable Aqueous Zn-Ion Battery. *J. Am. Chem. Soc.* *138*, 12894-12901.
109. Wan, F., Zhang, Y., Zhang, L., Liu, D., Wang, C., Song, L., Niu, Z., and Chen, J. (2019). Reversible Oxygen Redox Chemistry in Aqueous Zinc-Ion Batteries. *Angew. Chem. Int. Ed.* *58*, 7062-7067.
110. Wang, F., Borodin, O., Gao, T., Fan, X., Sun, W., Han, F., Faraone, A., Dura, J.A., Xu, K., and Wang, C. (2018). Highly reversible zinc metal anode for aqueous batteries. *Nat Mater* *17*, 543-549.
111. Mitha, A., Yazdi, A.Z., Ahmed, M., and Chen, P. (2018). Surface Adsorption of Polyethylene Glycol to Suppress Dendrite Formation on Zinc Anodes in Rechargeable Aqueous Batteries. *ChemElectroChem* *5*, 2409-2418.
112. Xu, W., Zhao, K., Huo, W., Wang, Y., Yao, G., Gu, X., Cheng, H., Mai, L., Hu, C., and Wang, X. (2019). Diethyl ether as self-healing electrolyte additive enabled long-life rechargeable aqueous zinc ion batteries. *Nano Energy* *62*, 275-281.
113. Ma, L., Chen, S., Li, H., Ruan, Z., Tang, Z., Liu, Z., Wang, Z., Huang, Y., Pei, Z., Zapien, J.A., *et al.* (2018). Initiating a mild aqueous electrolyte Co₃O₄/Zn battery with 2.2 V-high voltage and 5000-cycle lifespan by a Co(III) rich-electrode. *Energy Environ. Sci.* *11*, 2521-2530.

114. Wan, F., Zhang, L., Dai, X., Wang, X., Niu, Z., and Chen, J. (2018). Aqueous rechargeable zinc/sodium vanadate batteries with enhanced performance from simultaneous insertion of dual carriers. *Nat. Commun.* *9*, 1656.
115. Wang, J.M., Zhang, L., Zhang, C., and Zhang, J.Q. (2001). Effects of bismuth ion and tetrabutylammonium bromide on the dendritic growth of zinc in alkaline zincate solutions. *J. Power Sources* *102*, 139-143.
116. Hou, Z., Zhang, X., Li, X., Zhu, Y., Liang, J., and Qian, Y. (2017). Surfactant widens the electrochemical window of an aqueous electrolyte for better rechargeable aqueous sodium/zinc battery. *J. Mater. Chem. A* *5*, 730-738.
117. Wu, K., Huang, J., Yi, J., Liu, X., Liu, Y., Wang, Y., Zhang, J., and Xia, Y. (2020). Recent Advances in Polymer Electrolytes for Zinc Ion Batteries: Mechanisms, Properties, and Perspectives. *Adv. Energy Mater.* *10*, 1903977.
118. Dunn, B., Kamath, H., and Tarascon, J.-M. (2011). Electrical energy storage for the grid: a battery of choices. *Science* *334*, 928-935.
119. Posada, J.O.G., Rennie, A.J.R., Villar, S.P., Martins, V.L., Marinaccio, J., Barnes, A., Glover, C.F., Worsley, D.A., and Hall, P.J. (2017). Aqueous batteries as grid scale energy storage solutions. *Renew. Sust. Energ. Rev.* *68*, 1174-1182.
120. Xing, Z., Wang, S., Yu, A., and Chen, Z. (2018). Aqueous intercalation-type electrode materials for grid-level energy storage: Beyond the limits of lithium and sodium. *Nano Energy* *50*, 229-244.
121. Yin, J., Zhang, W., Wang, W., Alhebshi, N.A., Salah, N., and Alshareef, H.N. (2020). Electrochemical Zinc Ion Capacitors Enhanced by Redox Reactions of Porous Carbon Cathodes. *Adv. Energy Mater.* *10*, 2001705.
122. Song, M., Tan, H., Chao, D.L., and Fan, H.J. (2018). Recent Advances in Zn-Ion Batteries. *Adv. Funct. Mater.* *28*, 1802564.
123. Xu, Z., Deng, W., and Wang, X. (2021). 3D Hierarchical Carbon-Rich Micro-/Nanomaterials for Energy Storage and Catalysis. *Electrochem. Energ. Rev.* *4*, 269-335.
124. Kundu, D., Adams, B.D., Duffort, V., Vajargah, S.H., and Nazar, L.F. (2016). A high-capacity and long-life aqueous rechargeable zinc battery using a metal oxide intercalation cathode. *Nat. Energy* *1*, 16119.
125. Yin, J., Zhang, W., Alhebshi, N.A., Salah, N., and Alshareef, H.N. (2021). Electrochemical Zinc Ion Capacitors: Fundamentals, Materials, and Systems. *Adv. Energy Mater.* *11*, 2100201.
126. Lee, Y.-G., and An, G.-H. (2020). Synergistic Effects of Phosphorus and Boron Co-Incorporated Activated Carbon for Ultrafast Zinc-Ion Hybrid Supercapacitors. *ACS Appl. Mater. Interfaces* *12*, 41342-41349.

127. Shao, Y., Sun, Z., Tian, Z., Li, S., Wu, G., Wang, M., Tong, X., Shen, F., Xia, Z., Tung, V., *et al.* (2020). Regulating Oxygen Substituents with Optimized Redox Activity in Chemically Reduced Graphene Oxide for Aqueous Zn-Ion Hybrid Capacitor. *Adv. Funct. Mater.* *31*, 2007843.
128. Zhou, Z., Zhou, X., Zhang, M., Mu, S., Liu, Q., and Tang, Y. (2020). In Situ Two-Step Activation Strategy Boosting Hierarchical Porous Carbon Cathode for an Aqueous Zn-Based Hybrid Energy Storage Device with High Capacity and Ultra-Long Cycling Life. *Small* *16*, 2003174.
129. Deng, X., Li, J., Shan, Z., Sha, J., Ma, L., and Zhao, N. (2020). A N, O co-doped hierarchical carbon cathode for high-performance Zn-ion hybrid supercapacitors with enhanced pseudocapacitance. *J. Mater. Chem. A* *8*, 11617-11625.
130. Chen, R., Yu, M., Sahu, R.P., Puri, I.K., and Zhitomirsky, I. (2020). The Development of Pseudocapacitor Electrodes and Devices with High Active Mass Loading. *Adv. Energy Mater.* *10*, 1903848.
131. Wu, X., Xia, S., Huang, Y., Hu, X., Yuan, B., Chen, S., Yu, Y., and Liu, W. (2019). High-Performance, Low-Cost, and Dense-Structure Electrodes with High Mass Loading for Lithium-Ion Batteries. *Adv. Funct. Mater.* *29*, 1903961.
132. Li, M., Zhang, Y., Bai, Z., Liu, W.W., Liu, T., Gim, J., Jiang, G., Yuan, Y., Luo, D., Feng, K., *et al.* (2018). A Lithium–Sulfur Battery using a 2D Current Collector Architecture with a Large-Sized Sulfur Host Operated under High Areal Loading and Low E/S Ratio. *Adv. Mater.* *30*, 1804271.
133. Wu, F., Liu, M., Li, Y., Feng, X., Zhang, K., Bai, Y., Wang, X., and Wu, C. (2021). High-Mass-Loading Electrodes for Advanced Secondary Batteries and Supercapacitors. *Electrochem. Energ. Rev.* *4*, 382-446.
134. Chen, M., Zhang, Y., Xing, G., Chou, S.-L., and Tang, Y. (2021). Electrochemical energy storage devices working in extreme conditions. *Energy Environ. Sci.* *14*, 3323-3351.
135. Li, F., and Hu, X. (2021). Zinc Metal Energy Storage Devices under Extreme Conditions of Low Temperatures. *Batteries Supercaps* *4*, 389-406.
136. Wang, C., Pei, Z., Meng, Q., Zhang, C., Sui, X., Yuan, Z., Wang, S., and Chen, Y. (2021). Toward Flexible Zinc-Ion Hybrid Capacitors with Superhigh Energy Density and Ultralong Cycling Life: The Pivotal Role of ZnCl₂ Salt-Based Electrolytes. *Angew. Chem. Int. Ed.* *60*, 990-997.
137. Liu, Z., Wang, D., Tang, Z., Liang, G., Yang, Q., Li, H., Ma, L., Mo, F., and Zhi, C. (2019). A mechanically durable and device-level tough Zn-MnO₂ battery with high flexibility. *Energy Storage Mater.* *23*, 636-645.
138. Xu, Z., Xu, L., Xu, Z., Deng, Z., and Wang, X. (2021). N, O - Codoped Carbon Nanosheet Array Enabling Stable Lithium Metal Anode. *Adv. Funct. Mater.* *31*, 2102354.

139. Xu, Z., Lu, D., Ma, L., Lu, C., Xi, X., Zhang, G., Liu, R., and Wu, D. (2019). Hierarchically ordered carbon tube-sheet superstructure via template-directed self-assembly of polyimide. *Chem. Eng. J.* *364*, 201-207.
140. Xu, Z., Zhuang, X., Yang, C., Cao, J., Yao, Z., Tang, Y., Jiang, J., Wu, D., and Feng, X. (2016). Nitrogen-Doped Porous Carbon Superstructures Derived from Hierarchical Assembly of Polyimide Nanosheets. *Adv. Mater.* *28*, 1981-1987.
141. Bresser, D., Buchholz, D., Moretti, A., Varzi, A., and Passerini, S. (2018). Alternative binders for sustainable electrochemical energy storage – the transition to aqueous electrode processing and bio-derived polymers. *Energy Environ. Sci.* *11*, 3096-3127.
142. Cholewinski, A., Si, P., Uceda, M., Pope, M., and Zhao, B. (2021). Polymer Binders: Characterization and Development toward Aqueous Electrode Fabrication for Sustainability. *Polymers* *13*, 631.
143. Tran, H.Y., Wohlfahrt-Mehrens, M., and Dsoke, S. (2017). Influence of the binder nature on the performance and cycle life of activated carbon electrodes in electrolytes containing Li-salt. *J. Power Sources* *342*, 301-312.
144. Kovalenko, I., Zdyrko, B., Magasinski, A., Hertzberg, B., Milicev, Z., Burtovyy, R., Luzinov, I., and Yushin, G. (2011). A Major Constituent of Brown Algae for Use in High-Capacity Li-Ion Batteries. *Science* *334*, 75-79.
145. Ding, Y., Zhong, X., Yuan, C., Duan, L., Zhang, L., Wang, Z., Wang, C., and Shi, F. (2021). Sodium Alginate Binders for Bivalency Aqueous Batteries. *ACS Appl. Mater. Interfaces* *13*, 20681-20688.
146. Li, M., Wang, C., Chen, Z., Xu, K., and Lu, J. (2020). New Concepts in Electrolytes. *Chem. Rev.* *120*, 6783-6819.
147. Wu, S., Chen, Y., Jiao, T., Zhou, J., Cheng, J., Liu, B., Yang, S., Zhang, K., and Zhang, W. (2019). An Aqueous Zn-Ion Hybrid Supercapacitor with High Energy Density and Ultrastability up to 80 000 Cycles. *Adv. Energy Mater.* *9*, 1902915.
148. Augustyn, V., Come, J., Lowe, M.A., Kim, J.W., Taberna, P.-L., Tolbert, S.H., Abruña, H.D., Simon, P., and Dunn, B. (2013). High-rate electrochemical energy storage through Li⁺ intercalation pseudocapacitance. *Nat. Mater.* *12*, 518-522.
149. Kim, H.-S., Cook, J.B., Lin, H., Ko, Jesse S., Tolbert, Sarah H., Ozolins, V., and Dunn, B. (2017). Oxygen vacancies enhance pseudocapacitive charge storage properties of MoO_{3-x}. *Nat. Mater.* *16*, 454-460.
150. Lin, Z., Shi, H.-Y., Lin, L., Yang, X., Wu, W., and Sun, X. (2021). A high capacity small molecule quinone cathode for rechargeable aqueous zinc-organic batteries. *Nat. Commun.* *12*, 4424.

151. Sun, H., Mei, L., Liang, J., Zhao, Z., Lee, C., Fei, H., Ding, M., Lau, J., Li, M., Wang, C., *et al.* (2017). Three-dimensional holey-graphene/niobia composite architectures for ultrahigh-rate energy storage. *Science* *356*, 599.
152. Sun, T., Yuan, X., Wang, K., Zheng, S., Shi, J., Zhang, Q., Cai, W., Liang, J., and Tao, Z. (2021). An ultralow-temperature aqueous zinc-ion battery. *J. Mater. Chem. A* *9*, 7042-7047.
153. Zhang, Q., Ma, Y., Lu, Y., Li, L., Wan, F., Zhang, K., and Chen, J. (2020). Modulating electrolyte structure for ultralow temperature aqueous zinc batteries. *Nat. Commun.* *11*, 4463.
154. Yang, Q., Huang, Z., Li, X., Liu, Z., Li, H., Liang, G., Wang, D., Huang, Q., Zhang, S., Chen, S., *et al.* (2019). A Wholly Degradable, Rechargeable Zn-Ti₃C₂ MXene Capacitor with Superior Anti-Self-Discharge Function. *ACS Nano* *13*, 8275-8283.
155. Wang, Z., Huang, J., Guo, Z., Dong, X., Liu, Y., Wang, Y., and Xia, Y. (2019). A Metal-Organic Framework Host for Highly Reversible Dendrite-free Zinc Metal Anodes. *Joule* *3*, 1289-1300.
156. Jian, Z., Yang, N., Vogel, M., Leith, S., Schulte, A., Schönherr, H., Jiao, T., Zhang, W., Müller, J., Butz, B., *et al.* (2020). Flexible Diamond Fibers for High-Energy-Density Zinc-Ion Supercapacitors. *Adv. Energy Mater.* *10*, 2002202.
157. He, H., Lian, J., Chen, C., Xiong, Q., and Zhang, M. (2021). Super hydrophilic carbon fiber film for freestanding and flexible cathodes of zinc-ion hybrid supercapacitors. *Chem. Eng. J.* *421*, 129786.
158. Wang, Q., Wang, S., Guo, X., Ruan, L., Wei, N., Ma, Y., Li, J., Wang, M., Li, W., and Zeng, W. (2019). MXene-Reduced Graphene Oxide Aerogel for Aqueous Zinc-Ion Hybrid Supercapacitor with Ultralong Cycle Life. *Adv. Electron. Mater.* *5*, 1900537.
159. Zhang, H., Fang, Y., Yang, F., Liu, X., and Lu, X. (2020). Aromatic organic molecular crystal with enhanced π - π stacking interaction for ultrafast Zn-ion storage. *Energy Environ. Sci.* *13*, 2515-2523.
160. Shi, H.-Y., Ye, Y.-J., Liu, K., Song, Y., and Sun, X. (2018). A Long-Cycle-Life Self-Doped Polyaniline Cathode for Rechargeable Aqueous Zinc Batteries. *Angew. Chem. Int. Ed.* *57*, 16359-16363.
161. Wang, J., Liu, J., Hu, M., Zeng, J., Mu, Y., Guo, Y., Yu, J., Ma, X., Qiu, Y., and Huang, Y. (2018). A flexible, electrochromic, rechargeable Zn//PPy battery with a short circuit chromatic warning function. *J. Mater. Chem. A* *6*, 11113-11118.
162. Guo, Z.W., Ma, Y.Y., Dong, X.L., Huang, J.H., Wang, Y.G., and Xia, Y.Y. (2018). An Environmentally Friendly and Flexible Aqueous Zinc Battery Using an Organic Cathode. *Angew. Chem. Int. Ed.* *57*, 11737-11741.
163. Zhao, Y., Wang, Y., Zhao, Z., Zhao, J., Xin, T., Wang, N., and Liu, J. (2020). Achieving high capacity and long life of aqueous rechargeable zinc battery by using nanoporous-carbon-supported poly(1,5-naphthalenediamine) nanorods as cathode. *Energy Storage Mater.* *28*, 64-72.

164. Wang, J., Wang, J.-G., Liu, H., Wei, C., and Kang, F. (2019). Zinc ion stabilized MnO₂ nanospheres for high capacity and long lifespan aqueous zinc-ion batteries. *J. Mater. Chem. A* *7*, 13727-13735.
165. Jiao, Y., Kang, L., Berry-Gair, J., McColl, K., Li, J., Dong, H., Jiang, H., Wang, R., Corà, F., Brett, D.J.L., *et al.* (2020). Enabling stable MnO₂ matrix for aqueous zinc-ion battery cathodes. *J. Mater. Chem. A* *8*, 22075-22082.
166. Qin, H., Chen, L., Wang, L., Chen, X., and Yang, Z. (2019). V₂O₅ hollow spheres as high rate and long life cathode for aqueous rechargeable zinc ion batteries. *Electrochim. Acta* *306*, 307-316.
167. Wang, X., Ma, L., Zhang, P., Wang, H., Li, S., Ji, S., Wen, Z., and Sun, J. (2020). Vanadium pentoxide nanosheets as cathodes for aqueous zinc-ion batteries with high rate capability and long durability. *Appl. Surf. Sci.* *502*, 144207.
168. Shin, J., Choi, D.S., Lee, H.J., Jung, Y., and Choi, J.W. (2019). Hydrated Intercalation for High-Performance Aqueous Zinc Ion Batteries. *Adv. Energy Mater.* *9*, 1900083.
169. Ding, J., Du, Z., Li, B., Wang, L., Wang, S., Gong, Y., and Yang, S. (2019). Unlocking the Potential of Disordered Rocksalts for Aqueous Zinc-Ion Batteries. *Adv. Mater.* *31*, 1904369.
170. Soundharajan, V., Sambandam, B., Kim, S., Alfaruqi, M.H., Putro, D.Y., Jo, J., Kim, S., Mathew, V., Sun, Y.-K., and Kim, J. (2018). Na₂V₆O₁₆·3H₂O Barnesite Nanorod: An Open Door to Display a Stable and High Energy for Aqueous Rechargeable Zn-Ion Batteries as Cathodes. *Nano Lett.* *18*, 2402-2410.
171. Yang, Y., Tang, Y., Liang, S., Wu, Z., Fang, G., Cao, X., Wang, C., Lin, T., Pan, A., and Zhou, J. (2019). Transition metal ion-preintercalated V₂O₅ as high-performance aqueous zinc-ion battery cathode with broad temperature adaptability. *Nano Energy* *61*, 617-625.
172. Zhang, L., Chen, L., Zhou, X., and Liu, Z. (2015). Morphology-Dependent Electrochemical Performance of Zinc Hexacyanoferrate Cathode for Zinc-Ion Battery. *Sci. Rep.* *5*, 18263.
173. Chen, W., Li, G., Pei, A., Li, Y., Liao, L., Wang, H., Wan, J., Liang, Z., Chen, G., Zhang, H., *et al.* (2018). A manganese–hydrogen battery with potential for grid-scale energy storage. *Nat. Energy* *3*, 428-435.
174. Zhang, Y., Wu, Y., You, W., Tian, M., Huang, P.-W., Zhang, Y., Sun, Z., Ma, Y., Hao, T., and Liu, N. (2020). Deeply Rechargeable and Hydrogen-Evolution-Suppressing Zinc Anode in Alkaline Aqueous Electrolyte. *Nano Lett.* *20*, 4700-4707.
175. Lim, M.B., Lambert, T.N., and Chalamala, B.R. (2021). Rechargeable alkaline zinc–manganese oxide batteries for grid storage: Mechanisms, challenges and developments. *Mater. Sci. Eng. R Rep.* *143*, 100593.
176. Li, B., Nie, Z., Vijayakumar, M., Li, G., Liu, J., Sprenkle, V., and Wang, W. (2015). Ambipolar zinc-polyiodide electrolyte for a high-energy density aqueous redox flow battery. *Nat. Commun.* *6*, 6303.

177. Wang, C.H., Lai, Q.Z., Feng, K., Xu, P.C., Li, X.F., and Zhang, H.M. (2018). From zeolite-type metal organic framework to porous nano-sheet carbon: High activity positive electrode material for bromine-based flow batteries. *Nano Energy* 44, 240-247.
178. Sun, W., Wang, F., Zhang, B., Zhang, M., Küpers, V., Ji, X., Theile, C., Bieker, P., Xu, K., Wang, C., *et al.* (2021). A rechargeable zinc-air battery based on zinc peroxide chemistry. *Science* 371, 46-51.
179. Park, J., Park, M., Nam, G., Lee, J.-s., and Cho, J. (2015). All-Solid-State Cable-Type Flexible Zinc–Air Battery. *Adv. Mater.* 27, 1396-1401.
180. Cao, L., Li, D., Pollard, T., Deng, T., Zhang, B., Yang, C., Chen, L., Vatamanu, J., Hu, E., Hourwitz, M.J., *et al.* (2021). Fluorinated interphase enables reversible aqueous zinc battery chemistries. *Nat. Nanotechnol.* 16, 902-910.
181. Liu, W., Liu, P., and Mitlin, D. (2020). Review of Emerging Concepts in SEI Analysis and Artificial SEI Membranes for Lithium, Sodium, and Potassium Metal Battery Anodes. *Adv. Energy Mater.* 10, 2002297.
182. Xu, Z., Yang, J., Zhang, T., Sun, L., Nuli, Y., Wang, J., and Hirano, S.-i. (2019). Stable Na Metal Anode Enabled by a Reinforced Multistructural SEI Layer. *Adv. Funct. Mater.* 29, 1901924.
183. Zheng, J., Bock, D.C., Tang, T., Zhao, Q., Yin, J., Tallman, K.R., Wheeler, G., Liu, X., Deng, Y., Jin, S., *et al.* (2021). Regulating electrodeposition morphology in high-capacity aluminium and zinc battery anodes using interfacial metal–substrate bonding. *Nat. Energy* 6, 398-406.
184. Chen, P., Yuan, X., Xia, Y., Zhang, Y., Fu, L., Liu, L., Yu, N., Huang, Q., Wang, B., Hu, X., *et al.* (2021). An Artificial Polyacrylonitrile Coating Layer Confining Zinc Dendrite Growth for Highly Reversible Aqueous Zinc-Based Batteries. *Adv. Sci.* 8, 2100309.
185. Bhojate, S., Mhin, S., Jeon, J.-e., Park, K., Kim, J., and Choi, W. (2020). Stable and High-Energy-Density Zn-Ion Rechargeable Batteries Based on a MoS₂-Coated Zn Anode. *ACS Appl. Mater. Interfaces.* 12, 27249–27257.
186. Liang, P., Yi, J., Liu, X., Wu, K., Wang, Z., Cui, J., Liu, Y., Wang, Y., Xia, Y., and Zhang, J. (2020). Highly Reversible Zn Anode Enabled by Controllable Formation of Nucleation Sites for Zn-Based Batteries. *Adv. Funct. Mater.* 30, 1908528.
187. Zhao, R., Yang, Y., Liu, G., Zhu, R., Huang, J., Chen, Z., Gao, Z., Chen, X., and Qie, L. (2021). Redirected Zn Electrodeposition by an Anti-Corrosion Elastic Constraint for Highly Reversible Zn Anodes. *Adv. Funct. Mater.* 31, 2001867.
188. An, Y., Tian, Y., Li, Y., Wei, C., Tao, Y., Liu, Y., Xi, B., Xiong, S., Feng, J., and Qian, Y. (2020). Heteroatom-doped 3D porous carbon architectures for highly stable aqueous zinc metal batteries and non-aqueous lithium metal batteries. *Chem. Eng. J.* 400, 125843.

189. Xie, F., Li, H., Wang, X., Zhi, X., Chao, D., Davey, K., and Qiao, S.-Z. (2021). Mechanism for Zincophilic Sites on Zinc-Metal Anode Hosts in Aqueous Batteries. *Adv. Energy Mater.* *11*, 2003419.
190. Wang, L.-P., Li, N.-W., Wang, T.-S., Yin, Y.-X., Guo, Y.-G., and Wang, C.-R. (2017). Conductive graphite fiber as a stable host for zinc metal anodes. *Electrochim. Acta* *244*, 172-177.
191. Liu, S., Wang, A., Li, Q., Wu, J., Chiou, K., Huang, J., and Luo, J. (2018). Crumpled Graphene Balls Stabilized Dendrite-free Lithium Metal Anodes. *Joule* *2*, 184-193.
192. Kresse, G., and Furthmüller, J. (1996). Efficient iterative schemes for ab initio total-energy calculations using a plane-wave basis set. *Phys. Rev. B: Condens. Matter* *54*, 11169-11186.
193. Perdew, J.P., Burke, K., and Ernzerhof, M. (1996). Generalized Gradient Approximation Made Simple. *Phys. Rev. Lett.* *77*, 3865-3868.
194. Hammer, B., Hansen, L.B., and Nørskov, J.K. (1999). Improved adsorption energetics within density-functional theory using revised Perdew-Burke-Ernzerhof functionals. *Phys. Rev. B: Condens. Matter* *59*, 7413-7421.
195. Methfessel, M., and Paxton, A.T. (1989). High-precision sampling for Brillouin-zone integration in metals. *Phys. Rev. B: Condens. Matter* *40*, 3616-3621.
196. Grimme, S. (2006). Semiempirical GGA-type density functional constructed with a long-range dispersion correction. *J. Comput. Chem.* *27*, 1787-1799.
197. Seo, M.H., Choi, S.M., Lim, E.J., Kwon, I.H., Seo, J.K., Noh, S.H., Kim, W.B., and Han, B. (2014). Toward New Fuel Cell Support Materials: A Theoretical and Experimental Study of Nitrogen-Doped Graphene. *ChemSusChem* *7*, 2609-2620.
198. Zuo, T.-T., Wu, X.-W., Yang, C.-P., Yin, Y.-X., Ye, H., Li, N.-W., and Guo, Y.-G. (2017). Graphitized Carbon Fibers as Multifunctional 3D Current Collectors for High Areal Capacity Li Anodes. *Adv. Mater.* *29*, 1700389.
199. Hu, Z., Li, Z., Xia, Z., Jiang, T., Wang, G., Sun, J., Sun, P., Yan, C., and Zhang, L. (2019). PECVD-derived graphene nanowall/lithium composite anodes towards highly stable lithium metal batteries. *Energy Storage Mater.* *22*, 29-39.
200. Tian, Y., An, Y., Wei, C., Xi, B., Xiong, S., Feng, J., and Qian, Y. (2019). Flexible and Free-Standing Ti₃C₂T_x MXene@Zn Paper for Dendrite-Free Aqueous Zinc Metal Batteries and Nonaqueous Lithium Metal Batteries. *ACS Nano* *13*, 11676-11685.
201. Xu, Z., Ma, R., and Wang, X. (2022). Ultrafast, long-life, high-loading, and wide-temperature zinc ion supercapacitors. *Energy Storage Mater.* *46*, 233-242.

202. Hao, Y., Zhou, J., Wei, G., Liu, A., Zhang, Y., Mei, Y., Lu, B., Luo, M., and Xie, M. (2021). Artificial N-doped Graphene Protective Layer Enables Stable Zn Anode for Aqueous Zn-ion Batteries. *ACS Appl. Energy Mater.* *4*, 6364-6373.
203. Yuksel, R., Buyukcakir, O., Seong, W.K., and Ruoff, R.S. (2020). Metal-Organic Framework Integrated Anodes for Aqueous Zinc-Ion Batteries. *Adv. Energy Mater.* *10*, 1904215.
204. Cai, Z., Ou, Y., Wang, J., Xiao, R., Fu, L., Yuan, Z., Zhan, R., and Sun, Y. (2020). Chemically resistant Cu-Zn/Zn composite anode for long cycling aqueous batteries. *Energy Storage Mater.* *27*, 205-211.
205. Hou, T.-Z., Chen, X., Peng, H.-J., Huang, J.-Q., Li, B.-Q., Zhang, Q., and Li, B. (2016). Design Principles for Heteroatom-Doped Nanocarbon to Achieve Strong Anchoring of Polysulfides for Lithium-Sulfur Batteries. *Small* *12*, 3283-3291.
206. Chen, X., Chen, X.-R., Hou, T.-Z., Li, B.-Q., Cheng, X.-B., Zhang, R., and Zhang, Q. (2019). Lithiophilicity chemistry of heteroatom-doped carbon to guide uniform lithium nucleation in lithium metal anodes. *Sci. Adv.* *5*, eaau7728.
207. Xie, X., Liang, S., Gao, J., Guo, S., Guo, J., Wang, C., Xu, G., Wu, X., Chen, G., and Zhou, J. (2020). Manipulating the ion-transfer kinetics and interface stability for high-performance zinc metal anodes. *Energy Environ. Sci.* *13*, 503-510.
208. Tian, Y., An, Y., Liu, C., Xiong, S., Feng, J., and Qian, Y. (2021). Reversible zinc-based anodes enabled by zincophilic antimony engineered MXene for stable and dendrite-free aqueous zinc batteries. *Energy Storage Mater.* *41*, 343-353.
209. Liang, Y., Wang, Y., Mi, H., Sun, L., Ma, D., Li, H., He, C., and Zhang, P. (2021). Functionalized carbon nanofiber interlayer towards dendrite-free, Zn-ion batteries. *Chem. Eng. J.* *425*, 131862.
210. Yang, Q., Li, L., Hussain, T., Wang, D., Hui, L., Guo, Y., Liang, G., Li, X., Chen, Z., Huang, Z., *et al.* (2021). Stabilizing Interface pH by N-Modified Graphdiyne for Dendrite-Free and High-Rate Aqueous Zn-Ion Batteries. *Angew. Chem. Int. Ed.* *61*, e202112304.
211. Jia, H., Qiu, M., Lan, C., Liu, H., Dirican, M., Fu, S., and Zhang, X. (2022). Advanced Zinc Anode with Nitrogen-Doping Interface Induced by Plasma Surface Treatment. *Adv. Sci.* *9*, 2103952.
212. Jin, H., Dai, S., Xie, K., Luo, Y., Liu, K., Zhu, Z., Huang, L., Huang, L., and Zhou, J. (2022). Regulating Interfacial Desolvation and Deposition Kinetics Enables Durable Zn Anodes with Ultrahigh Utilization of 80. *Small* *18*, e2106441.
213. Chen, Y., Li, J., Zhang, S., Cui, J., and Shao, M. (2020). Highly Reversible Zinc Anode Enhanced by Ultrathin MnO₂ Cathode Material Film for High - Performance Zinc - Ion Batteries. *Adv. Mater. Interfaces* *7*, 2000510.

214. Han, D., Wu, S., Zhang, S., Deng, Y., Cui, C., Zhang, L., Long, Y., Li, H., Tao, Y., Weng, Z., *et al.* (2020). A Corrosion-Resistant and Dendrite-Free Zinc Metal Anode in Aqueous Systems. *Small* 16, 2001736.
215. Han, D., Cui, C., Zhang, K., Wang, Z., Gao, J., Guo, Y., Zhang, Z., Wu, S., Yin, L., Weng, Z., *et al.* (2021). A non-flammable hydrous organic electrolyte for sustainable zinc batteries. *Nat. Sustain.* 5, 205-213.
216. Yufit, V., Tariq, F., Eastwood, D.S., Biton, M., Wu, B., Lee, P.D., and Brandon, N.P. (2019). Operando Visualization and Multi-scale Tomography Studies of Dendrite Formation and Dissolution in Zinc Batteries. *Joule* 3, 485-502.
217. Parker, J.F., Ko, J.S., Rolison, D.R., and Long, J.W. (2018). Translating Materials-Level Performance into Device-Relevant Metrics for Zinc-Based Batteries. *Joule* 2, 2519-2527.
218. Xu, Z., Jin, S., Zhang, N., Deng, W., Seo, M.H., and Wang, X. (2022). Efficient Zn Metal Anode Enabled by O,N-Codoped Carbon Microflowers. *Nano Lett.* 22, 1350-1357.
219. Mei, J., Wang, J., Gu, H., Du, Y., Wang, H., Yamauchi, Y., Liao, T., Sun, Z., and Yin, Z. (2021). Nano Polymorphism-Enabled Redox Electrodes for Rechargeable Batteries. *Adv. Mater.* 33, 2004920.
220. Yang, Y., Xiao, J., Cai, J., Wang, G., Du, W., Zhang, Y., Lu, X., and Li, C.C. (2020). Mixed - Valence Copper Selenide as an Anode for Ultralong Lifespan Rocking - Chair Zn - Ion Batteries: An Insight into its Intercalation/Extraction Kinetics and Charge Storage Mechanism. *Adv. Funct. Mater.* 31, 2005092.
221. Chen, L., Li, W., Guo, Z., Wang, Y., Wang, C., Che, Y., and Xia, Y. (2015). Aqueous Lithium-Ion Batteries Using O₂ Self-Elimination Polyimides Electrodes. *J. Electrochem. Soc.* 162, A1972-A1977.
222. Wang, Y., Cui, X., Zhang, Y., Zhang, L., Gong, X., and Zheng, G. (2016). Achieving High Aqueous Energy Storage via Hydrogen-Generation Passivation. *Adv. Mater.* 28, 7626-7632.
223. Wu, D., Zhang, G., Lu, D., Ma, L., Xu, Z., Xi, X., Liu, R., Liu, P., and Su, Y. (2018). Perylene diimide-diamine/carbon black composites as high performance lithium/sodium ion battery cathodes. *J. Mater. Chem. A* 6, 13613-13618.
224. Yu, M., Chandrasekhar, N., Raghupathy, R.K.M., Ly, K.H., Zhang, H., Dmitrieva, E., Liang, C., Lu, X., Kühne, T.D., Mirhosseini, H., *et al.* (2020). A High-Rate Two-Dimensional Polyarylimide Covalent Organic Framework Anode for Aqueous Zn-Ion Energy Storage Devices. *J. Am. Chem. Soc.* 142, 19570-19578.
225. Abraham, M.J., Murtola, T., Schulz, R., Páll, S., Smith, J. C., Hess, B., Lindahl, E., Abraham, M.J., Murtola, T., Schulz, R., Páll, S., Smith, J.C., Hess, B., and Lindahl, E. (2015). Gromacs: High performance molecular simulations through multi-level parallelism from laptops to supercomputers. *SoftwareX* 1-2, 19-25.

226. Pronk, S., Páll, S., Schulz, R., Larsson, P., Bjelkmar, P., Apostolov, R., Shirts, M.R., Smith, J.C., Kasson, P.M., Van Der Spoel, D., *et al.* (2013). GROMACS 4.5: a high-throughput and highly parallel open source molecular simulation toolkit. *Bioinformatics* *29*, 845-854.
227. Nosé, S. (1984). A molecular dynamics method for simulations in the canonical ensemble. *Mol. Phys.* *52*, 255-268.
228. Hoover, W.G. (1985). Canonical dynamics: Equilibrium phase-space distributions. *Phys. Rev. A* *31*, 1695-1697.
229. Hockney, R.W., Goel, S.P., and Eastwood, J.W. (1974). Quiet high-resolution computer models of a plasma. *J. Comp. Phys.* *14*, 148-158.
230. Hess, B., Bekker, H., Berendsen, H.J.C., and Fraaije, J.G.E.M. (1997). LINCS: A linear constraint solver for molecular simulations. *J. Comp. Chem* *18*, 1463-1472.
231. Darden, T., York, D., and Pedersen, L. (1993). Particle mesh Ewald: An $N \cdot \log(N)$ method for Ewald sums in large systems. *J. Chem. Phys.* *98*, 10089-10092.
232. Babu, C.S., and Lim, C. (2006). Empirical Force Fields for Biologically Active Divalent Metal Cations in Water. *J. Phys. Chem. A* *110*, 691-699.
233. Cannon, W.R., Pettitt, B.M., and McCammon, J.A. (1994). Sulfate anion in water: Model structural, thermodynamic, and dynamic properties. *J. Phys. Chem.* *98*, 6225-6230.
234. Lopes, J.N.C., and Pádua, A.A.H. (2004). Molecular force field for ionic liquids composed of triflate or bistriflylimide anions. *J. Phys. Chem. B* *108*, 16893-16898.
235. Jorgensen, W.L., Maxwell, D.S., and Tirado-Rives, J. (1996). Development and testing of the OPLS all-atom force field on conformational energetics and properties of organic liquids. *J. Am. Chem. Soc.* *118*, 11225-11236.
236. Wang, Z., Yang, Y., Olmsted, D.L., Asta, M., and Laird, B.B. (2014). Evaluation of the constant potential method in simulating electric double-layer capacitors. *J. Chem. Phys.* *141*, 1-8.
237. Chen, H., Xu, H., Wang, S., Huang, T., Xi, J., Cai, S., Guo, F., Xu, Z., Gao, W., and Gao, C. (2017). Ultrafast all-climate aluminum-graphene battery with quarter-million cycle life. *Sci. Adv.* *3*, eaao7233.
238. Wu, X., Hong, J.J., Shin, W., Ma, L., Liu, T., Bi, X., Yuan, Y., Qi, Y., Surta, T.W., Huang, W., *et al.* (2019). Diffusion-free Grotthuss topochemistry for high-rate and long-life proton batteries. *Nat. Energy* *4*, 123-130.
239. Shen, X., Sun, T., Yang, L., Krasnoslobodtsev, A., Sabirianov, R., Sealy, M., Mei, W.-N., Wu, Z., and Tan, L. (2021). Ultra-fast charging in aluminum-ion batteries: electric double layers on active anode. *Nat. Commun.* *12*, 820.

240. Wang, X., Li, G., Seo, M.H., Hassan, F.M., Hoque, M.A., and Chen, Z. (2015). Sulfur Atoms Bridging Few-Layered MoS₂ with S-Doped Graphene Enable Highly Robust Anode for Lithium-Ion Batteries. *Adv. Energy Mater.* *5*, 1501106.
241. Ding, J.W., Du, Z.G., Gu, L.Q., Li, B., Wang, L.Z., Wang, S.W., Gong, Y.J., and Yang, S.B. (2018). Ultrafast Zn²⁺ Intercalation and Deintercalation in Vanadium Dioxide. *Adv. Mater.* *30*, e1800762.
242. Wang, Y., Wang, C., Ni, Z., Gu, Y., Wang, B., Guo, Z., Wang, Z., Bin, D., Ma, J., and Wang, Y. (2020). Binding Zinc Ions by Carboxyl Groups from Adjacent Molecules toward Long-Life Aqueous Zinc-Organic Batteries. *Adv. Mater.* *32*, e2000338.
243. Yang, W., Du, X., Zhao, J., Chen, Z., Li, J., Xie, J., Zhang, Y., Cui, Z., Kong, Q., Zhao, Z., *et al.* (2020). Hydrated Eutectic Electrolytes with Ligand-Oriented Solvation Shells for Long-Cycling Zinc-Organic Batteries. *Joule* *4*, 1557-1574.
244. Park, S.-H., King, P.J., Tian, R., Boland, C.S., Coelho, J., Zhang, C., McBean, P., McEvoy, N., Kremer, M.P., Daly, D., *et al.* (2019). High areal capacity battery electrodes enabled by segregated nanotube networks. *Nat. Energy* *4*, 560-567.
245. Lu, Y., Cai, Y., Zhang, Q., and Chen, J. (2021). Insights into Redox Processes and Correlated Performance of Organic Carbonyl Electrode Materials in Rechargeable Batteries. *Adv. Mater.* *34*, 2104150.
246. Wang, W., Kale, V.S., Cao, Z., Kandambeth, S., Zhang, W., Ming, J., Parvatkar, P.T., Abou-Hamad, E., Shekhah, O., Cavallo, L., *et al.* (2020). Phenanthroline Covalent Organic Framework Electrodes for High-Performance Zinc-Ion Supercapattery. *ACS Energy Lett.* *5*, 2256-2264.
247. Wang, H., Ye, W., Yang, Y., Zhong, Y., and Hu, Y. (2021). Zn-ion hybrid supercapacitors: Achievements, challenges and future perspectives. *Nano Energy* *85*, 105942.
248. Dong, X., Guo, Z., Guo, Z., Wang, Y., and Xia, Y. (2018). Organic Batteries Operated at -70°C. *Joule* *2*, 902-913.
249. Israelachvili, J.N. (2011). *Intermolecular and surface forces* (Academic press).
250. Kundu, D., Oberholzer, P., Glaros, C., Bouzid, A., Tervoort, E., Pasquarello, A., and Niederberger, M. (2018). Organic Cathode for Aqueous Zn-Ion Batteries: Taming a Unique Phase Evolution toward Stable Electrochemical Cycling. *Chem. Mater.* *30*, 3874-3881.
251. Song, Z., Miao, L., Ruhlmann, L., Lv, Y., Zhu, D., Li, L., Gan, L., and Liu, M. (2021). Self-Assembled Carbon Superstructures Achieving Ultra-Stable and Fast Proton-Coupled Charge Storage Kinetics. *Adv. Mater.* *33*, 2104148.
252. Qiu, N., Chen, H., Yang, Z., Sun, S., and Wang, Y. (2018). Low-cost birnessite as a promising cathode for high-performance aqueous rechargeable batteries. *Electrochim. Acta* *272*, 154-160.

253. Wang, L., Cao, X., Xu, L., Chen, J., and Zheng, J. (2018). Transformed Akhtenskite MnO₂ from Mn₃O₄ as Cathode for a Rechargeable Aqueous Zinc Ion Battery. *ACS Sustain. Chem. Eng.* *6*, 16055-16063.
254. Ren, H., Zhao, J., Yang, L., Liang, Q., Madhavi, S., and Yan, Q. (2019). Inverse opal manganese dioxide constructed by few-layered ultrathin nanosheets as high-performance cathodes for aqueous zinc-ion batteries. *Nano Res.* *12*, 1347-1353.
255. Dai, X., Wan, F., Zhang, L., Cao, H., and Niu, Z. (2019). Freestanding graphene/VO₂ composite films for highly stable aqueous Zn-ion batteries with superior rate performance. *Energy Storage Mater.* *17*, 143-150.
256. Li, G., Yang, Z., Jiang, Y., Jin, C., Huang, W., Ding, X., and Huang, Y. (2016). Towards polyvalent ion batteries: A zinc-ion battery based on NASICON structured Na₃V₂(PO₄)₃. *Nano Energy* *25*, 211-217.
257. Li, G., Yang, Z., Jiang, Y., Zhang, W., and Huang, Y. (2016). Hybrid aqueous battery based on Na₃V₂(PO₄)₃/C cathode and zinc anode for potential large-scale energy storage. *J. Power Sources* *308*, 52-57.
258. Trócoli, R., and La Mantia, F. (2015). An Aqueous Zinc-Ion Battery Based on Copper Hexacyanoferrate. *ChemSusChem* *8*, 481-485.
259. Liu, Y., Zhou, X., Wang, X., Chen, G., Liu, R., Ma, Y., Bai, Y., and Yuan, G. (2021). Hydrated titanate acid as an ultralow-potential anode for aqueous zinc-ion full batteries. *Chem. Eng. J.* *420*, 129629.
260. Chen, Z., Li, C., Yang, Q., Wang, D., Li, X., Huang, Z., Liang, G., Chen, A., and Zhi, C. (2021). Conversion-Type Nonmetal Elemental Tellurium Anode with High Utilization for Mild/Alkaline Zinc Batteries. *Adv. Mater.* *33*, 2105426.
261. Ma, X., Cheng, J., Dong, L., Liu, W., Mou, J., Zhao, L., Wang, J., Ren, D., Wu, J., Xu, C., *et al.* (2019). Multivalent ion storage towards high-performance aqueous zinc-ion hybrid supercapacitors. *Energy Storage Mater.* *20*, 335-342.
262. Wang, Q., Wang, S., Li, J., Ruan, L., Wei, N., Huang, L., Dong, Z., Cheng, Q., Xiong, Y., and Zeng, W. (2020). A Novel Aqueous Zinc-Ion Hybrid Supercapacitor Based on TiS₂ (De)Intercalation Battery-Type Anode. *Adv. Electron. Mater.* *6*, 2000388.
263. Lu, Y., Zhang, H., Liu, H., Nie, Z., Xu, F., Zhao, Y., Zhu, J., and Huang, W. (2021). Electrolyte Dynamics Engineering for Flexible Fiber-Shaped Aqueous Zinc-Ion Battery with Ultralong Stability. *Nano Lett.* *21*, 9651-9660.
264. Geng, L., Meng, J., Wang, X., Han, C., Han, K., Xiao, Z., Huang, M., Xu, P., Zhang, L., Zhou, L., *et al.* (2022). Eutectic Electrolyte with Unique Solvation Structure for High-Performance Zinc-Ion Batteries. *Angew. Chem. Int. Ed.* *61*, e202206717.

265. Li, H., Guo, C., Zhang, T., Xue, P., Zhao, R., Zhou, W., Li, W., Elzatahry, A., Zhao, D., and Chao, D. (2022). Hierarchical Confinement Effect with Zincophilic and Spatial Traps Stabilized Zn-Based Aqueous Battery. *Nano Lett.* *22*, 4223-4231.
266. Cao, P., Zhou, X., Wei, A., Meng, Q., Ye, H., Liu, W., Tang, J., and Yang, J. (2021). Fast-Charging and Ultrahigh-Capacity Zinc Metal Anode for High-Performance Aqueous Zinc-Ion Batteries. *Adv. Funct. Mater.* *31*, 2100398.
267. Xiao, P., Xue, L., Guo, Y., Hu, L., Cui, C., Li, H., and Zhai, T. (2021). On-site building of a Zn²⁺-conductive interfacial layer via short-circuit energization for stable Zn anode. *Sci. Bull.* *66*, 545-552.
268. Fu, Y.Q., Wei, Q.L., Zhang, G.X., Wang, X.M., Zhang, J.H., Hu, Y.F., Wang, D.N., Zuin, L.C., Zhou, T., Wu, Y.C., *et al.* (2018). High-Performance Reversible Aqueous Zn-Ion Battery Based on Porous MnOx Nanorods Coated by MOF-Derived N-Doped Carbon. *Adv. Energy Mater.* *8*, 1801445.
269. Ding, Y., Zhang, Q., Rui, K., Xu, F., Lin, H., Yan, Y., Li, H., Zhu, J., and Huang, W. (2020). Ultrafast Microwave Activating Polarized Electron for Scalable Porous Al toward High-Energy-Density Batteries. *Nano Lett.* *20*, 8818-8824.
270. Espinosa, D.C.R., Bernardes, A.M., and Tenório, J.A.S. (2004). An overview on the current processes for the recycling of batteries. *J. Power Sources* *135*, 311-319.
271. Yeşiltepe, S., Buğdaycı, M., Yücel, O., and Şeşen, M.K. (2019). Recycling of Alkaline Batteries via a Carbothermal Reduction Process. *Batteries* *5*, 35.
272. Bernardes, A.M., Espinosa, D.C.R., and Tenório, J.A.S. (2004). Recycling of batteries: a review of current processes and technologies. *J. Power Sources* *130*, 291-298.
273. Xu, P., Tan, D.H.S., and Chen, Z. (2021). Emerging trends in sustainable battery chemistries. *Trends Chem* *3*, 620-630.
274. Hu, X., Robles, A., Vikström, T., Väänänen, P., Zackrisson, M., and Ye, G. (2021). A novel process on the recovery of zinc and manganese from spent alkaline and zinc-carbon batteries. *J. Hazard. Mater.* *411*, 124928.
275. Morcali, M.H. (2015). Reductive atmospheric acid leaching of spent alkaline batteries in H₂SO₄/Na₂SO₃ solutions. *Int. J. Miner. Metall.* *22*, 674-681.
276. Buzatu, T., Popescu, G., Birloaga, I., and Săceanu, S. (2013). Study concerning the recovery of zinc and manganese from spent batteries by hydrometallurgical processes. *Waste Manage.* *33*, 699-705.
277. Buzatu, M., Săceanu, S., Ghica, V.G., Iacob, G., and Buzatu, T. (2013). Simultaneous recovery of Zn and MnO₂ from used batteries, as raw materials, by electrolysis. *Waste Manage.* *33*, 1764-1769.
278. Farzana, R., Hassan, K., and Sahajwalla, V. (2019). Manganese oxide synthesized from spent Zn-C battery for supercapacitor electrode application. *Sci. Rep.* *9*, 8982.

279. Gallegos, M.V., Falco, L.R., Peluso, M.A., Sambeth, J.E., and Thomas, H.J. (2013). Recovery of manganese oxides from spent alkaline and zinc-carbon batteries. An application as catalysts for VOCs elimination. *Waste Manage.* *33*, 1483-1490.
280. Gabal, M.A., Al-luhaibi, R.S., and Al Angari, Y.M. (2014). Recycling spent zinc-carbon batteries through synthesizing nano-crystalline Mn-Zn ferrites. *Powder Technol.* *258*, 32-37.
281. Zhou, M., Guo, S., Li, J., Luo, X., Liu, Z., Zhang, T., Cao, X., Long, M., Lu, B., Pan, A., *et al.* (2021). Surface-Preferred Crystal Plane for a Stable and Reversible Zinc Anode. *Adv. Mater.* *33*, 2100187.
282. Deng, W., Zhang, N., and Wang, X. (2022). Hybrid interlayer enables dendrite-free and deposition-modulated zinc anodes. *Chem. Eng. J.* *432*, 134378.
283. Pérez-Garibay, R., González-García, A.P., Fuentes-Aceituno, J.C., Rendón-Ángeles, J.C., and Bello-Teodoro, S. (2016). Synthesis of Mn₂O₃ from Manganese Sulfated Leaching Solutions. *Ind. Eng. Chem. Res.* *55*, 9468-9475.
284. Lee, J.A., Newnham, C.E., Stone, F.S., and Tye, F.L. (1980). Thermal decomposition of manganese oxyhydroxide. *J. Solid State Chem.* *31*, 81-93.
285. Xu, Z., Li, M., Sun, W., Tang, T., Lu, J., and Wang, X. (2022). An Ultrafast, Durable, and High-Loading Polymer Anode for Aqueous Zinc-Ion Batteries and Supercapacitors. *Adv. Mater.* *34*, e2200077.
286. Yang, X., Li, W., Lv, J., Sun, G., Shi, Z., Su, Y., Lian, X., Shao, Y., Zhi, A., Tian, X., *et al.* (2021). In situ separator modification via CVD-derived N-doped carbon for highly reversible Zn metal anodes. *Nano Res.* *15*, 9785-9791.